PLEXUS-SPECIFIC MICRO-VASCULAR PATHOLOGIES DEFINED BY OPTICAL COHERENCE TOMOGRAPHIC ANGIOGRAPHY

by

Jie Wang

A DISSERTATION

Presented to the

Department of Biomedical Engineering

within the Oregon Health & Science University

School of Medicine

in partial fulfillment of

the requirements for the degree of

Doctor of Philosophy

December 2022

© Copyright 2022by Jie Wang
All Rights Reserved

Doctor of Philosophy
School of Medicine
Oregon Health & Science University

CERTIFICATE OF APPROVAL

This is to certify that the PhD dissertation of
Jie Wang
has been approved.

Yali Jia, PhD
Advisor

Yong Hwang Chang, PhD
Chair

J. Peter Campbell, MD, MPH
Committee Member

Meysam Asgari, PhD
Committee Member

David Huang, MD, PhD
Committee Member

TABLE OF CONTENTS

List of Figures iv

List of Tables xi

List of Abbreviations xii

1 Introduction 1

1.1 Retina structural and vascular anatomical terminology . . . 1

1.2 Two critical vascular biomarkers in retinal vascular diseases . . . 3

1.3 Currently available imaging modalities . . . 3

1.4 Optical coherence tomographic angiography and its major artifacts . . . 6

1.5 Artificial intelligence for aiding optical coherence tomographic angiography-based vascular biomarker detection and quantification . . . 8

1.6 Outline . . . 9

2 Optical coherence tomographic angiography reading toolkit 10

2.1 Retinal layers segmentation and intelligent manual correction . . . 10

2.2 User interface and case report . . . 12

3 Signal attenuation-compensated projection-resolved optical coherence tomographic angiography 14

3.1 Abstract . . . 14

3.2 Introduction . . . 14

3.3 Data acquisition and pre-processing . . . 16

3.4 Method . . . 18

3.4.1 Optical coherence tomogeaphic angiography signal attenuation compensation . . . 18

3.4.2 Large vessel shadow compensation . . . 20

3.4.3 Implementation . . . 21

3.5 Results . . . 21

3.5.1 Evaluation on healthy eyes . . . 21

3.5.2 Preservation on challenging scan affected by shadow artifacts . . . 27

3.5.3 Preservation on choroidal neovascularization . . . 28

3.5.4 Platform independence . . . 29

3.6 Discussion and conclusion . . . 30

4 Robust non-perfusion area Detection in three retinal plexuses using convolutional neural network in optical coherence tomographic angiography 33

4.1 Abstract . . . 33

4.2 Introduction . . . 33

4.3 Dataset . . . 34

4.4 Non-perfusion area Detection using a convolutional neural network . . . 35

4.4.1 Artifact included challenges in detecting non-perfusion area . . . 35

4.4.2 Detecting non-perfusion area using convolutional neural network . . . 36
4.4.3 Training . . . 37
4.5 Results . . . 39
4.5.1 Effect of signal attenuation . . . 39
4.5.2 Effect of artifacts in clinical dataset . . . 43
4.5.3 Performance on clinical DR scans . . . 45
4.5.4 Repeatability Assessment . . . 47
4.6 Discussion and conclusion . . . 48

5 Automated diagnosis and segmentation of choroidal neovascularization in optical coherence tomographic angiography using deep learning 51
5.1 Abstract . . . 51
5.2 Introduction . . . 51
5.3 Data acquisition and preprocessing . . . 54
5.4 Choroidal neovascularization identification and segmentation using convolutional neural networks . . 57
5.4.1 Algorithm outline . . . 57
5.4.2 Choroidal neovascularization membrane segmentation using convolutional neural network . . 58
5.4.3 Choroidal neovascularization vessel segmentation using convolutional neural network 60
5.4.4 Training . . . 61
5.5 Results . . . 63
5.5.1 Choroidal neovascularization diagnostic accuracy . . . 63
5.5.2 Choroidal neovascularization segmentation accuracy . . . 64
5.6 Discussion and conclusion . . . 69

6 Deep learning for diagnosing and segmenting choroidal neovascularization in optical coherence tomographic angiography in a large real-world dataset 73
6.1 Abstract . . . 73
6.2 Introduction . . . 73
6.3 Methods . . . 76
6.3.1 Dataset . . . 76
6.3.2 Preprocessing . . . 77
6.3.3 Ground truth label generation . . . 77
6.3.4 Deep learning model for choroidal neovascularization diagnosis and segmentation 78
6.3.5 Implementation . . . 79
6.4 Results . . . 81
6.4.1 Study population . . . 81
6.4.2 Overall performance evaluation of choroidal neovascularization diagnosis and membrane segmentation . . . 81
6.4.3 Performance of choroidal neovascularization diagnosis and membrane segmentation on different scan sizes . . . 84
6.4.4 Performance of choroidal neovascularization diagnosis and membrane segmentation on different diseases . . . 84

6.4.5 Clinical application . . . 87
6.5 Discussion and conclusion . . . 87

7 Invariant features-based automated registration and montage for wide-field optical coherence tomographic angiography 92
7.1 Abstract . . . 92
7.2 Introduction . . . 92
7.3 Data acquisition and preprocessing . . . 94
7.4 Methods . . . 95
7.4.1 Algorithm overview and data pre-processing . . . 96
7.4.2 Invariant features-based registration and montage . . . 96
7.4.3 Flow signal compensation and seamless blending . . . 101
7.4.4 Bundle processing . . . 104
7.5 Results . . . 105
7.6 Discussion and conclusion . . . 110

8 Future work and Conclusion 113
8.1 Future improvements of technology . . . 113
8.2 Conclusion . . . 114

9 References 115

List of Figures

1.1 (A) Cross-section of a human eye and location of retina; (B) Retinal histology. The inner retina consists of the inner limiting membrane (ILM) through to the outer boundary of outer plexiform layer (OPL). The outer retina consists of outer boundary of OPL through to the Bruch's membrane (BM). 1

1.2 Anatomic cross-sectional retinal structure and location of the vascular plexuses in the human retina at the macula. The vessels are illustrated in red. Four vascular networks including the nerve fiber layer plexus (NFLP), ganglion cell layer plexus (GCLP), intermediate capillary plexus (ICP), and deep capillary plexus (DCP). superficial vascular complex (SVC) consists of NFLP and GCLP, and deep vascular complex (DVC) consists of ICP and DCP 2

1.3 Color fundus photograph of a healthy eye (A) and an eye diagnosed with neovascular age-related macular degeneration (AMD) (B). Retinal pathologies, e.g. hemorrhages, drusen, can be visualized with color fundus photography (B) 4

1.4 fluorescein angiograph (FA) of an eye diagnosied with diabetic retinopathy (DR)(A), and an eye diagnosed with neovascular age-related macular degeneration (AMD) (B). The profile of retinal pathologies of macular ischemia (A) and choroidal neovascularization (CNV) (B) can be imaged with FA, but the visualization of pathological details is limited due to the low image resolution 5

1.5 Optical coherence tomography captured 3D retinal structure (A) showing well arranged anatomic retinal nerve layers in a healthy eye and depth-resolved retinal structural pathologies, e.g. diabetic macular edema (C), in an eye diagnosed with diabetic retinopathy 6

1.6 The principle of motion contrast in optical coherence tomographic angiography (OCTA) is explained using video frames. In frames 1 and 2, tennis balls falling out of a tube represent red blood cells. Motion contrast is generated by subtracting the two frames from each other, which accentuates the moving parts in the image while removing the stationary parts (right). Note both the tennis balls (representing flowing blood) and the shadows they cast on the wall (representing projection artifacts) are highlighted. 7

1.7 optical coherence tomographic angiography (OCTA) from an healthy eye (row 1) and an eye diagnosed with diabetic retinopathy shows macular ischemia in slab-specific *en face* angiograms of the superficial vascular complex (SVC), intermediate capillary plexus (ICP), deep capillary plexus (DCP) in the inner retina, and choroidal neovascularization (CNV) in the outer retina. Macular ischemia is highlighted by the green arrows, and CNV is highlighted by the blue arrow. 8

2.1 Procedure for detecting plexus-specific micro-vascular pathologies defined by optical coherence tomographic angiography. (A) Color coded uncorrected flow signal volume overlaid on the structural volume, (B) Color coded uncorrected flow signal volume overlaid on the structural volume and illustration of retinal layers segmentation, (C) Color coded projection-resolved flow signal volume overlaid on the structural volume and illustration of retinal layer segmentation, (D) plexus-specific optical coherence tomographic angiography (OCTA) angiograms of the superficial vascular complex (SVC), intermediate capillary plexus (ICP), deep capillary plexus (DCP), and outer retina. 10

2.2 Anatomic slab segmentation in a healthy eye (row 1, age matched with A2), an eye with age-related macular degeneration (AMD)(row 2), and a diabetic retinopathy (DR) eye with diabetic macular edema (DME). Column A: cross-sectional structural optical coherence tomography (OCT). Column B: gradient images of column A. Gradients vanish in some pathological areas in the AMD eye (B2). Column C: cross-sectional structural OCT with boundaries detected through a graph search algorithm[1] (colored dotted lines). Red arrows in C2 indicate mis-segmented regions. Such processing failures can lead to difficulty in interpreting images and generate errors in structural OCT and optical coherence tomographic angiography (OCTA). 11

2.3 Demonstration of semi-automated layer correction. (A1) Uncorrected layer segmentation, (A2) Manual correction of outer plexiform layer (OPL) / outer nuclear layer (ONL) segmentation, two stars are anchors used for segmentation correction; (B) Enface segmentation map on key frames;(C) *En face* segmentation map after manual correction propagation. The yellow line in B and C indicate the B-scan position of A. 12

2.4 The user interface of optical coherence tomographic angiography (OCTA) reading toolkit software . . 13

2.5 Case report. (A) superficial vascular complex (SVC) defined as the anterior 80% of the ganglion cell complex (GCC); (B)intermediate capillary plexus (ICP) defined as the outer 20% of the GCC and inner 50% of the inner nuclear layer (INL); (C) deep capillary plexus (DCP) defined as the outer 50% of the INL and the outer plexiform layer (OPL); (D) Inner retina: defined as the boundary of vitreous inner limiting membrane (ILM) to the low boundary of OPL; (E) The outer retina is defined as the lower boundary of OPL to Bruch's membrane (BM); (F) choriocapillaris (CC) is defined as the region between BM and BM+$10um$; (G) Mean projection of OCT volume; (H) cross-sectional OCT overlaid with color-coded PR-OCTA signal (violet: inner retinal; yellow: pathological outer retinal; red: choroidal) at the position indicated by the yellow line in (A). 13

3.1 Uncorrected optical coherence tomographic angiography (OCTA) exhibiting projection artifacts. (A) Cross-sectional structural optical coherence tomography (OCT) overlaid with color coded OCTA flow in the inner retina (violet), outer retina (yellow), and choroid (red). (A1) Magnification of the region within the green box in A. *En face* images are produced by maximum projection over the relevant regions to show the superficial vascular complex (SVC) (B), intermediate capillary plexus (ICP) (C), deep capillary plexus (DCP) (D), outer retina (E), and choriocapillaris (CC) (F). Vascular patterns from the SVC are clearly duplicated in each of the deeper regions. SVC is defined as the anterior 80% of the ganglion cell complex (GCC), ICP is defined as the outer 20% of the GCC and inner 50% of the inner nuclear layer (INL); DCP is defined as the outer 50% of the inner nuclear layer (INL) and the outer plexiform layer (OPL); Outer retina is defined as the lower boundary of OPL to Bruch's membrane (BM); CC is defined as the region between BM and BM+$10um$. 17

3.2 Illustration of large vessel shadow compensation in structural optical coherence tomography (OCT). (A) Three-dimensional (3D) structural OCT; (B) Cross-section structural overlaid with a retinal region mask (red) made using a 3D adaptive thresholding algorithm; (C) Cross-sectional structural OCT overlaid with the region of interest (ROI) mask (green) covering the slab of ganglion cell complex (corresponding to a $120\mu m$ axial depth); (D) OCT angiogram generated in the superficial region using maximum projection; (E1) Enhanced vasculature; (E2) Denoised OCT angiogram generated by multiplying the enhanced vasculature (E1) with the original OCT angiogram (D); (F) Large vessel mask detected by using adaptive thresholding algorithm. (G1) Original cross-sectional OCT with shadowing artifacts under the large vessels; (G2) Shadowing artifacts compensated cross-sectional OCT. 20

3.3 Signal attenuation-compensated projection-resolved OCTA (sacPR-OCTA) in a healthy eye. (A) Superficial vascular complex (SVC). (B) Intermediate capillary plexus (ICP). (C) Deep capillary plexus (DCP). (D) Cross-sectional structural OCT overlaid with the sacPR-OCTA color coded according to anatomic location (violet: inner retina, yellow: outer retina red: choroid, position was highlighted by dotted line in A). The results recapitulate known features of retinal anatomy from histology[2]. 21

3.4 Algorithm comparison in a normal eye. The images include uncorrected optical coherence tomographic angiography (OCTA) (row 1), the initial projection-resolved OCTA (PR-OCTA) (row 2), reflectance-based projection-resolved OCTA (rbPR-OCTA) (row 3), and signal attenuation-compensated projection-resolved OCTA (sacPR-OCTA) algorithm (row 4). Column A-E: *En face* optical coherence tomography (OCT) angiogram of superficial vascular complex (SVC), intermediate capillary plexus (ICP), deep capillary plexus (DCP), outer retina and sub-macular choriocapillaris (CC). Column F: cross-sectional structural OCT overlaid with color coded flow signal (violet: inner retina, yellow: outer retina red: choroid) at the position indicated by the white dotted line A1. sacPR-OCTA removed more residual artifacts than the previous PR methods while maintaining vascular integrity (D), and the vessel tails (projection artifacts in uncorrected OCTA, F1) below the vessels in cross-section were replaced with the circles (F4). Large vessel artifacts are notable in the initial PR-OCTA method (E2), and flow magnitude are visually reduced in the rbPR-OCTA result. These over-processing artifacts are absent in the proposed sacPR-OCTA method (E4). 23

3.5 A comparison of projection-resolved OCTA (PR-OCTA) algorithms on a scan with shadow artifacts. Row 1-4: Uncorrected optical coherence tomographic angiography (OCTA), initial projection-resolved OCTA (PR-OCTA), reflectance-based projection-resolved OCTA (rbPR-OCTA), and signal attenuation-compensated projection-resolved OCTA (sacPR-OCTA). Column A-E are *en face* angiograms of the superficial vascular complex (SVC), intermediate capillary plexus (ICP), deep capillary plexus (DCP), outer retina, and sub-macular choriocapillaris (CC). Colum F are cross-sectional structural optical coherence tomography (OCT) overlaid with color coded flow signal (violet: inner retina, yellow: outer retina red: choroid). The proposed sacPR-OCTA algorithms preserved more *in-situ* flow signal in the shadowing area (highlighted by yellow dotted ellipses) and suppressed more projection artifacts (highlighted by white arrows). 27

3.6 A comparison of projection-resolved OCTA (PR-OCTA) algorithms on the neovascular age-related macular degeneration (AMD) with choroidal neovascularization (CNV). Row 1-4: Uncorrected, initial PR-OCTA, reflectance-based projection-resolved OCTA (rbPR-OCTA) and signal attenuation-compensated projection-resolved OCTA (sacPR-OCTA). Column A-E are *en face* angiograms of the superficial vascular complex (SVC), intermediate capillary plexus (ICP), deep capillary plexus (DCP), outer retina and sub-macular choriocapillaris (CC). The proposed sacPR-OCTA algorithms preserved more *in-situ* CNV signals (highlighted by white arrows). 28

3.7 Signal attenuation-compensated projection-resolved (sacPR-OCTA) on angioplex $3 \times 3 - mm$ scan. Row 1-2: Original uncorrected optical coherence tomographic angiography (OCTA) and sacPR-OCTA. Column A-C are *en face* angiograms of the superficial vascular complex (SVC), intermediate capillary plexus (ICP), deep capillary plexus (DCP). Colum D is cross-sectional structural optical coherence tomography (OCT) overlaid with color coded flow signals (violet: inner retina, yellow: outer retina red: choroid). The white arrow highlighted the dilated vessel in DCP 30

3.8 Signal attenuation-compensated projection-resolved optical coherence tomographic angiography (OCTA) (sacPR-OCTA) on Solix 9×9-mm scan. Row 1-2: Uncorrected optical coherence tomographic angiography (OCTA) and signal attenuation-compensated projection-resolved OCTA (sacPR-OCTA). Column A-C are *en face* angiograms of the superficial vascular complex (SVC), intermediate capillary plexus (ICP), deep capillary plexus (DCP). Colum D is cross-sectional structural optical coherence tomography (OCT) overlaid with color coded flow signals (gold: vitreous, violet: inner retina, yellow: outer retina red: choroid. The red arrow highlights the connection between the neovascularization (NV) and feeder vessel. sacPR-OCTA removed projection artifacts in this wide field of view showing the optic nerve head in a newly released commercial device. 31

4.1 Projection-resolved angiograms (bottom row) compared to original OCTA images (top row). (A), Cross-sectional structural optical coherence tomography (OCT) scans, with inner retinal flow signal overlaid in violet and choriocapillaris (CC) flow in red. Remaining columns are *en face* projections of (B), superficial vascular complex (SVC):inner 80% of the ganglion cell complex (GCC); (C), intermediate capillary plexus (ICP):outer 20% of the GCC and inner 50% of the inner nuclear layer (INL); (D), deep capillary plexus (DCP): outer 50% of the INL and outer plexiform layer (OPL). 35

4.2 Atrous kernels with rate = 1, 2 and 3. The red square is the center of kernel. 37

4.3 CNN architecture for NPA detection. The numbers below each convolution block is the number of kernels for each convolution layer, atrous dilation rate was demonstrated below 37

4.4 Ground truth generation. (A), In-house graphical user interface software; (B), manually graded NPA overlaid on the superficial vascular complex angiogram; (C), ground truth segmentation determined by majority vote from the three manually segmented images in (B). 39

4.5 Manufactured signal strength attenuation on inner retina angiograms. (A), Uninhibited scan; (B), scan captured with a 0.6 neutral density filter; (C), scan captured with 4 diopters of defocus. signal strength index (SSI). 40

4.6 Effects of signal attenuation for NPA detection. (A), Normalized SSI (see text) declines as optical density of the neutral density filter increases; algorithm performance in the superficial vascular complex (SVC) (B), intermediate capillary plexus (ICP) (C), and deep capillary plexus (DCP)(D) is unaffected by increasing optical density, as evidenced by the low regression values and slopes of the best fit lines to the normalized fovea avascular zone (FAZ) areas (see text). 40

4.7 Detected NPA (in blue) on optically filtered scans of a representative normal eye. The size and shape of the detected NPA (here, limited to the fovea avascular zone (FAZ)) did not appreciably change with increasing optical density (columns running left to right). 41

4.8 Effects of signal attenuation for NPA detection. (A), Normalized SSI (see text) declines as optical density of the neutral density filter increases; algorithm performance in the SVC (B), ICP (C), and DCP (D) is unaffected by increasing optical density, as evidenced by the low regression values and slopes of the best fit lines to normalized FAZ areas (see text). 42

4.9 Detected NPA (in blue) on defocused scans of a representative normal eye. The size and shape of the detected NPA (here, limited to the foveal avascular zone; FAZ) did not appreciably change with increasing defocus (columns running left to right). 42

4.10 Effects of SSI attenuation for NPA detection in three plexuses. NPA detection on the SVC(A), ICP (B) and DCP (C) were unaffected by SSI variation. 43

4.11 Detected NPA (in blue) on a low-quality scan of non-proliferative DR affected by shadow artifacts (white arrows). 44

4.12 Detected NPA (in blue) on a low-quality scan of proliferative DR eye affected by microsaccade artifacts. 44

4.13 Detected NPA (in blue) on a low-quality scan of proliferative DR affected by bulk motion artifacts. . . 45

4.14 NPA detection on a severe DR. (A), Angiograms in specific layers-superficial vascular complex (SVC), intermediate capillary plexus (ICP), and deep capillary plexus (DCP); (B), the ground truth delineated by an expert grader (green); (C), the output probabilities with brighter blue indicating a higher output probability; (D), the detected NPA (final results, with probability value > 0.5). 47

4.15 NPA detection on a healthy eye (in blue) affected by focal shadow artifacts (white arrows). 49

5.1 Choroidal neovascularization (CNV) segmentation on challenging scans using a saliency-based algorithm. Small residual projection artifacts are excluded in the saliency map (A1&B1, highlighted by white arrows). Strong residual artifacts in CNV and non-CNV scans were over-segmented in the saliency map, providing false positives (A2&B2, A4&B4, highlighted by red arrows), while large CNV was under-segmented in the saliency map, producing false negatives (A3&B3, highlighted by green arrows). 54

5.2 Comparison of non-choroidal neovascularization (CNV), including a healthy (column 1), diabetic retinopathy (DR)(column 2), and dry age-related macular degeneration (AMD) (column 3), and choroidal neovascularization (CNV) (wet AMD, column 4) scans with *en face* outer retinal angiograms (row A) and cross-sectional structural optical coherence tomography (OCT) overlaid with optical coherence tomographic angiography (OCTA) (row B) showing inner retinal (violet), choroidal (red), and pathological outer retinal flow (yellow). Slab segmentation lines are the inner limiting membrane (ILM) (violet), outer border of the outer plexiform layer (OPL) (yellow), and Bruch's membrane (BM) (green). White dotted lines in row A indicate the locations of the cross sections in row B. Red arrows indicate the pathologies in outer retina. 56

5.3 Input angiographic image set. (A) original (A1) and projection-resolved OCTA (PR-OCTA) (A2) with inner retinal (violet), choroidal (red), and outer retinal (yellow) flow overlaid on structural optical coherence tomography (OCT); (B) inner retinal angiogram, with white dotted line indicating the position of the B-scans in (A); (C) outer retinal angiogram generated from the original optical coherence tomographic angiography (OCTA) demonstrated in (A1); (D) outer retinal angiogram processed by slab -subtraction; (E) projection-resolved (PR) outer retinal angiogram. In (E) the entire choroidal neovascularization (CNV) is preserved but some residual projection artifacts persist. 56

5.4 Generation of outer retinal structural volume input. (A) Original structural optical coherence tomography (OCT) volume; (B) extracted outer retinal volume; (C) original cross-sectional OCT, with anatomic slab segmentation overlaid in violet (inner limiting membrane, ILM), yellow (outer plexiform layer, OPL), and green (Bruch's membrane, BM); (D) segmented outer retinal cross section, resampled so that the volume has a constant voxel depth. 57

5.5 Outline of the proposed automated choroidal neovascularization (CNV) identification and segmentation method. Input consists of the original inner retinal angiogram and original, slab-subtracted, and projection-resolved (PR) outer retinal angiograms, and volumetric structural data from the outer retina. We trained two separate CNNs in order to segment the CNV membrane and vessels, respectively. The first one (CNN-M) segments CNV membrane and outputs a mask corresponding to its location (if it is present). The second (CNN-V) segments CNV vascular pixels within the CNV membrane output by the first CNN. 58

5.6 Convolutional neural network (CNN) architecture for choroidal neovascularization (CNV) membrane segmentation (CNN-M). The atrous kernel sizes ($Rate = 1\ to\ 32$) are annotated below each encoder block. The number of kernels is annotated below each convolutional layer. Label I and $I/2$ indicate operations on the full ($304 \times 304 - pixel$) and half-sized ($152 \times 152 - pixel$) image, respectively. . 60

5.7 Encoder block architecture. The number of kernels are annotated below each convolutional layer. Dots at intersections along the lines indicate connections between layers. 60

5.8 Convolutional neural network architecture (CNN) for Choroidal neovascularization vessel segmentation (CNN-V). The atrous kernel sizes ($Rate = 1\ to\ 8$) are annotated below each encoder block. The number of kernels is annotated below the convolutional layer. Label beside the block is the image size; in this case, the network operates on the fully-sized($304 \times 304 - pixel$) image. 61

5.9 Ground truth generation. (A) outer retina angiogram generated from projection-resolved OCTA (PR-OCTA); (B) Choroidal neovascularization (CNV) membrane outline drawn by an expert grader; (C) CNV vessel mask verified by an expert grader. 63

5.10 Choroidal neovascularization (CNV) segmentation on scans with good image quality. (A) Projection-resolved (PR) outer retinal angiogram; (B) manually delineated CNV membrane (red outline) and vessel (white pixels) ground truths; (C) probability map output by the membrane segmentation convolutional neural network (CNN) (CNN-M); (D) probability map output by the vessel segmentation CNN (CNN-V); (E) segmented CNV membrane (white outline, with $probability > 0.5$) and vessels (with pixels of $probability > 0.5$). 65

5.11 Choroidal neovascularization (CNV) segmentation on challenging scans containing a wide range of flow rates. (A) Projection-resolved (PR) outer retinal angiogram; (B) manually delineated CNV membrane (red outline) and vessels (white pixels) ground truths; (C) probability map output by the membrane segmentation convolutional neural network (CNN) (CNN-M); (D) probability map output by the vessel segmentation CNN (CNN-V); (E) segmented CNV membrane (white outline, with $probability > 0.5$) and vessels (with pixels of $probability > 0.5$). Large inter capillary space, highlighted by stars, were correctly included in the membrane area by the proposed algorithm. 66

5.12 Choroidal neovascularization (CNV) segmentation on two cases with strong residual projection artifacts. Bottom row shows a special case with a retinal angiomatous proliferation lesion. (A) Projection-resolved (PR) outer retinal angiogram; (B) manually delineated CNV membrane (red outline) and vessel (white pixels) ground truths; (C) probability map output by the membrane segmentation convolutional neural network (CNN) (CNN-M); (D) probability map output by the vessel segmentation CNN (CNN-V); (E) segmented CNV membrane (white outline, with $probability > 0.5$) and vessels (with pixels of $probability > 0.5$). 67

5.13 Choroidal neovascularization (CNV) segmentation on scans with defocusing. (A) Projection-resolved (PR) outer retinal angiogram; (B) manually delineated ground truth of CNV membrane (red outline) and vessels (white pixels); (C) probability map output by the membrane segmentation convolutional neural network (CNN) (CNN-M); (D) probability map output by the vessel segmentation CNN (CNN-V); (E) segmented CNV membrane (white outline, with $probability > 0.5$) and vessels (with pixels of $probability > 0.5$). 68

5.14 The proposed method correctly classifies scans with no choroidal neovascularization (CNV) present. Shown are a case with dry age-related macular degeneration (AMD) (row 1) and diabetic retinopathy (DR) (row 2). No CNV is delineated in ground truths (column B). Despite strong motion artifacts (column A), the proposed method's probability map (column C&D) does not indicate any CNV, and so the algorithm correctly does not segment any membrane or vessels in the output (column E). 69

6.1 Proposed CNV diagnosis and segmentation method. (A) OCTA data is pre-processed by removing projection artifacts and segmenting retinal layers; OCTA scans were further graded as CNV/non-CNV scans and CNV membrane area was outlined in projection-resolved (PR) outer retinal angiogram. (B) Model inputs consist of an *en face* OCTA image-set, thickness maps, an *en face* structural OCT image-set, and outer retinal OCT&OCTA volumes. The OCTA image set consists of uncorrected inner and outer retinal angiograms, a slab subtracted outer retinal angiogram, and a PR outer retinal angiogram, all produced using maximum projection. The structural OCT image set includes *en face* mean projections of ten equal partitions of the entire data volume as well as a mean projection covering just the inner retina, and a mean projection of the entire volume. (C) The proposed hybrid multi-task CNN model combines 3D and 2D convolution; the feature extraction block is shared between the CNV diagnosis and membrane segmentation modules. F1-F8 are tensor connection tags. 80

6.2 Example choroidal neovascularization (CNV) membrane segmentation results. (Column A) Inner retinal angiogram; (B) projection-resolved outer retinal angiogram with CNV membrane ground truth (white outline); (C) output CNV membrane probability map; (D) structural OCT cross-section at the location of the white line in A, with flow signal overlaid (violet: inner retinal; yellow: pathological outer retinal; red: choroidal). Row 1: example in which the network achieved an accurate segmentation. Row 2: example of a under segmentation. The lesion in this scan extended beyond the optical coherence tomographic angiography (OCTA) scan's field of view, which may be difficult for the network to properly analyze due to the truncated nature of the information available at the edge of the image. Row 3: an example of over-segmentation and low prediction confidence in the CNV membrane area. Note that the pathologic flow signal in the outer retina was of similar magnitude to the background in this scan, making analysis difficult. Row 4: an example of a segmentation error in an extremely low-quality scan. This eye exhibits extreme defocus and a large number of residual artifacts. Note that the network did make a low confidence prediction of a CNV membrane in a region that overlapped with the ground truth. 83

6.3 Choroidal neovascularization (CNV) membrane segmentation on both $3\times3-mm$ and $6\times6-mm$ scans. (A) Inner retinal angiogram; (B) Projection-resolved outer retinal angiogram with CNV membrane ground truth (white outline); (C) CNV probability map; (D) Structural OCT cross-section at the location of the white line in (A), with flow signal overlaid (violet: inner retinal; yellow: pathological outer retinal; red: choroidal). Case 1 shows a large CNV lesion that cannot be fully imaged using a small scanning window. Case 2 shows a small CNV lesion in a defocused scan with strong residual artifacts. Both cases at both resolutions resulted in correct detections. SSI: Signal strength index. 85

6.4 Choroidal neovascularization (CNV) membrane segmentation results in several retinal diseases. (A) Inner retinal angiogram; (B) Projection-resolved outer retinal angiogram with CNV membrane ground truth (white outline); (C) CNV probability map; (D) Structural optical coherence tomography (OCT) cross-section at the location of the white line in (A), with flow signal overlaid (violet: inner retinal; yellow: pathological outer retinal; red: choroidal). Row 1: Example segmentation in neovascular age-related macular degeneration (AMD). Row 2: Example segmentation in angiomatous proliferation. The identity of the lesion is best appreciated in the cross sectional image (D2). Despite the small lesion size, this scan resulted in a correct prediction. Row 3: Example segmentation in polypoidal choroidal vasculopathy (PCV). Flow signal in PCV is often very weak, which makes it difficult to distinguish from background (B3). Row 4: Example segmentation in pathologic myopia. Eyes with pathologic myopia often suffer from extreme defocus in optical coherence tomographic angiography (OCTA) imaging (A4, B4). The residual artifacts in these scans probably account for the relatively low performance (C4). SSI: Signal strength index. 86

6.5 Choroidal neovascularization (CNV) growth dynamics illuminated by the proposed detection algorithm. CNV vessels were detected in the segmented CNV membrane area (white outline) using Otsu's algorithm. CNV vascular patterns changed dramatically after treatment. The scatter plot of CNV vessel area and membrane area shows the CNV dynamics following anti–vascular endothelial growth factor (anti-VEGF) treatments (red arrows) in longitudinal follow-ups. 88

7.1 Illustration of retinal layer segmentation and angiogram generation on superficial vascular complex (SVC) (inner 80% of the ganglion cell complex (GCC)), intermediate capillary plexus (ICP) (outer 20% of the GCC and inner 50% of the inner nuclear layer (INL)), deep capillary plexus (DCP) (outer 50% of the INL and outer plexiform layer (OPL)), and inner retina (between the inner limiting membrane (ILM) and the OPL). 95

7.2 Overview of the invariant features-based automated registration and montage algorithm. SURF – Speed-Up Robust Features. 96

7.3 Speed-up robust-features SURF detection on OCTA. (A) The green crosses are the locations of detected features on the angiogram. (B) Some of the SURF features in A were selected randomly for clear representation of orientation and scale. The scale of features is represented by the radius of the green circles. The direction of features and scale is represented by the green line highlighted with white arrows in C and D. (C-D) Magnified insets correspond to the regions indicated by black and blue boxes in B. 98

7.4 Invariant features matching. The paired points were connected using the cyan dashed lines. 99

7.5 Illustration of the scale and orientation of paired points. A1, A2 were correctly paired points of interest; their scale and direction were very similar. B1, B2 were mismatched points, for which both direction and scale were very different. C1, C2 were also mismatched points, where the scale is similar but the difference of direction was great. D is the illustration for the scale and direction restriction for feature matching. The scales of A, B C and D are $1.65 \times 1.65 - mm$, $1.3 \times 1.3 - mm$, $1.65 \times 1.65 - mm$ and $0.9 \times 0.9 - mm$, separately. 100

7.6 Illustration of the pairs reserved for the random sampling consensus (RANSAC) input after local area verification by imposition of the two restrictions described in section of angiograms registration and montage 101

7.7 Illustration of the pairs reserved after the last step of mismatch removal using random sampling consensus (RANSAC) algorithm. 101

7.8 Angiography montage with visible seams. 102

7.9 Illustration of the seamless blending routine. 104

7.10 The montaged seamless angiogram applying flow signal compensation and seamless blending. (B) and (C) represent the detail capillary network within the green and blue rectangles in (A). 105

7.11 Illustration of the algorithm evaluation. Green and cyan lines illustrated both sides of the seam between the target and moving images. 106

7.12 Grossly montaged wide-field angiogram before matching verification in local area, flow signal compensation and seamless blending. Five pixel mismatch was demonstrated. 107

7.13 Automated montaged angiogram on four slabs of projection-resolved OCTA (PR-OCTA) (2 scans). (A) Superficial vascular complex (SVC). (B) Intermediate capillary plexus (ICP). (C) Deep capillary plexus (DCP). (D) Choriocapillaris (CC). 108

7.14 Ultra wide-field optical coherence tomographic angiography (OCTA) ($15 \times 20 - mm$) of a healthy eye registered and montaged by sixteen $6 \times 6 - mm$ OCTA scans. 109

7.15 Montaged wide-field optical coherence tomographic angiography (OCTA) ($6 \times 15 - mm$, 3 scans) of a diabetic retinopathy (DR) case. Three scans centered on disc, fovea, and temporal were montaged using the algorithm described in the text. 109

7.16 Montaged optical coherence tomographic angiography (OCTA) ($10 \times 25 - mm$, 4 scans) of the nasal, disc, macula and temporal regions from an image of a diabetic retinopathy case acquired by a prototype OCTA system. The white arrow highlights the vitreous neovascularization. 110

List of Tables

3.1 Comparison among uncorrected optical coherence tomographic angiography (OCTA), initial projection-resolved OCTA (PR-OCTA), reflectance-based projection-resolved OCTA (rbPR-OCTA) and signal attenuation-compensated projection-resolved OCTA (sacPR-OCTA)on Pearson's correlation coefficient between the current and upper slabs. 23

3.2 Comparison among uncorrected optical coherence tomographic angiography (OCTA), initial projection-resolved OCTA (PR-OCTA), reflectance-based projection-resolved OCTA (rbPR-OCTA), and signal attenuation-compensated projection-resolved OCTA (sacPR-OCTA) on vascular integrity and continuity. 25

3.3 Comparison among uncorrected optical coherence tomographic angiography (OCTA),initial projection-resolved OCTA (PR-OCTA), reflectance-based projection-resolved OCTA (rbPR-OCTA) and signal attenuation-compensated projection-resolved OCTA (sacPR-OCTA) on residual projection artifacts in outer retina 26

3.4 Correlation and vessel density (VD) between flow underneath large vessels in the uncorrected optical coherence tomographic angiography (OCTA), initial projection-resolved OCTA (PR-OCTA), reflectance-based projection-resolved OCTA (rbPR-OCTA) and signal attenuation-compensated projection-resolved OCTA (sacPR-OCTA)on vessel density 26

4.1 Agreement between detected NPA and ground truth ($mean \pm standard\,deviation$) grouped by DR severity 46

4.2 Repeatability of NPA detection on healthy eyes 48

5.1 Dataset for training and testing 62

5.2 Choroidal neovascularization (CNV) diagnostic accuracy 64

5.3 Agreement between choroidal neovascularization (CNV) membrane outputs and ground truth ($mean \pm std$) 64

5.4 Comparison of repeatability among ground truth, saliency-based method and our proposed method . . 65

6.1 Dataset enrolled in the study 81

6.2 Choroidal neovascularization (CNV) data enrollment in retinal diseases 81

6.3 Overall performance of choroidal neovascularization (CNV) diagnosis and membrane segmentation . 82

6.4 Performance of choroidal neovascularization (CNV) diagnosis and membrane segmentation on different scan sizes 84

6.5 Performance of choroidal neovascularization (CNV) diagnosis and membrane segmentation on different diseases 87

7.1 Evaluation of the performance of the automated montage algorithm on 10 normal eyes by the correlation and mean square errors 107

List of Abbreviations

Symbols

2D two-dimensional. ix, 4, 5, 9, 59, 74, 78–80, 89, 94, 96, 103

3D three-dimensional. v, ix, 5, 20, 33, 52, 59, 74, 78–80, 82, 89, 94

A

AI artificial intelligence. 8, 53, 113

AMD age-related macular degeneration. iv, vi–ix, 3–5, 11, 28, 51, 53, 55, 56, 61, 63, 69, 71, 73, 75, 76, 81, 84, 86, 87, 92

anti-VEGF anti–vascular endothelial growth factor. ix, 5, 88

AROC area under receiver operating characteristic curve. 63, 69, 73, 81, 82, 84, 87

B

BM Bruch's membrane. iv, v, vii, 1, 3, 13, 17, 55–57, 71, 77, 90

BRAO branch retina arterial occlusion. 55, 61, 76

BRVO branch retina vein occlusion. 3, 55, 61, 76

C

CC choriocapillaris. v, vi, x, 13, 17, 22, 23, 27–29, 35, 107, 108

CNN convolutional neural network. vi, viii, ix, xiv, 8, 9, 33, 34, 36, 37, 39, 41, 48–51, 53–55, 57–63, 65–68, 70–73, 75, 78, 80, 87, 89, 90, 113, 114

CNV choroidal neovascularization. iv, vi–ix, xi, xiv, 3–5, 8, 9, 25, 28–30, 51–91, 114

CRAO central retina arterial occlusion. 3

CRVO central retina vein occlusion. 3, 76

CSC central serous chorioretinopathy. 55, 61, 76

CV coefficient of variation. 47, 50, 64, 65

D

DCP deep capillary plexus. iv–vii, ix, x, 2, 8, 10, 13, 17, 21–31, 33–35, 40, 42, 43, 46–48, 95, 107, 108

DME diabetic macular edema. iv, 5, 11

DR diabetic retinopathy. iv, vii, viii, x, xi, 3, 5, 11, 33, 38, 43–48, 50, 55, 56, 61, 69, 76, 92, 94, 108, 109

DVC deep vascular complex. iv, 2, 3

F

FA fluorescein angiograph. iv, xiv, 4–6, 51, 74

FAZ fovea avascular zone. vi, vii, 13, 40–43, 48, 94

FOV field of view. 93, 94, 110–112

G

GCC ganglion cell complex. v, vi, ix, 13, 17, 35, 95

GCL ganglion cell layer. 2, 17

GCLP ganglion cell layer plexus. iv, 2

H

HD high-definition. 108

I

ICGA indocyanine green angiograph. xiv, 4–6, 51, 74

ICP intermediate capillary plexus. iv–vii, ix, x, 2, 8, 10, 13, 17, 21–31, 33–35, 40, 42, 43, 46–48, 95, 107, 108

ILM inner limiting membrane. iv, v, vii, ix, 1, 2, 13, 17, 55–57, 71, 77, 90, 95

INL inner nuclear layer. v, vi, ix, 2, 13, 17, 35, 95

IOU intersection over union. 45–47, 64, 81, 82, 84, 87, 89, 90

IPL inner plexiform layer. 2, 17

ISOS inner/outer segments layer. 2

M

MCT motion correction technology. 68

N

NFL nerve fiber layer. 2

NFLP nerve fiber layer plexus. iv, 2

NPA non-perfusion area. vi, vii, xi, xiv, 9, 29, 33–50

NV neovascularization. vi, 29–31

O

OCT optical coherence tomography. iv–vii, ix, xiv, 5, 6, 11–15, 17, 20, 21, 23, 24, 27, 30, 31, 33, 35, 36, 48, 49, 52, 53, 56, 57, 70, 74–80, 83, 85, 86, 89, 92, 93, 102, 111

OCTA optical coherence tomographic angiography. iv–vii, ix–xi, xiv, 6–18, 21–27, 29–31, 33–36, 41, 43, 48, 49, 52, 54–56, 62, 69–71, 73–78, 80, 81, 83, 84, 86, 89, 90, 92–95, 97, 98, 105, 108–111, 113, 114

OMAG optical microangiography. 7, 16

ONL outer nuclear layer. iv, 2, 12, 17

OPL outer plexiform layer. iv–vii, ix, 1, 2, 12, 13, 17, 35, 55–57, 71, 77, 90, 95

P

PCV polypoidal choroidal vasculopathy. ix, 76, 81, 84, 86, 87

PR projection-resolved. vii–ix, 56, 58, 62, 65–68, 77–80, 95

PR-OCTA projection-resolved OCTA. v–viii, x, xi, 9, 13, 15, 22–29, 31–33, 35, 46, 51, 52, 55, 56, 61, 63, 65–67, 77–79, 107, 108, 113

R

RANSAC random sampling consensus. x, 96, 98, 100, 101, 106, 110–112

rbPR-OCTA reflectance-based projection-resolved OCTA. v, vi, xi, 22–29

ROI region of interest. v, 20

RPCP radial peripapillary capillaries. 2

RPE retinal pigment epithelium layer. 2, 52, 55, 56, 74, 75, 89

S

sacPR-OCTA signal attenuation-compensated projection-resolved OCTA. v, vi, xi, xiv, 9, 14–16, 21–32, 113, 114

SIFT scale-invariant feature transform. 97, 111

SSADA split-spectrum amplitude decorrelation angiography. 7, 16, 34, 55, 76, 94

SSD sum of squared differences. 97

SSI signal strength index. vi, vii, ix, 39–43, 49, 54, 68, 81, 85

SURF speed-up robust-features. x, 96–98, 100, 110, 111

SVC superficial vascular complex. iv–vii, ix, x, 2, 3, 8, 10, 13, 17, 21, 23, 26–28, 30, 31, 33–35, 40, 42, 43, 46–48, 95, 107, 108

V

VC vascular continuity. 24, 25

VD vessel density. xi, 24–26

ABSTRACT

Optical coherence tomographic angiography (OCTA) has been successfully used in ophthalmology, providing noninvasive, non-dye-based, high-speed, and depth-resolved imaging of retinal and choroidal circulatory networks in vivo at capillary-scale detail. OCTA is able to detect capillary dropout and nonexudative choroidal neovascularization (CNV), which may be missed by traditional imaging modalities such as fluorescein angiograph (FA) / indocyanine green angiograph (ICGA), and are risk factors for vision loss. However, conventional/commercial automated OCTA processing platforms are limited by (i) projection artifacts causing specious flow signal mimicking the morphology of superficial vasculature to appear in deeper anatomic layers and further leading to misinterpretation of retinal vascular disorders, (ii) automated rules-based retinal vascular disorders detection algorithms that fail on low quality scans, and (iii) a limited field of view that cannot image the entire retina. This dissertation presents technical achievements in plexus-specific micro-vascular disorder detection on OCTA, including (i) projection artifacts removal, (ii) macular ischemia detection in vascular layers in the inner retina, (iii) CNV detection in the outer retina, and (iv) wide-field OCTA generated by stitching miltiple small-field OCTA seamlessly. First, a novel signal attenuation-compensated projection-resolved OCTA method (sacPR-OCTA) was developed to remove the projection artifacts at voxel scale. Quantitative metrics and exemplar cases demonstrated that sacPR-OCTA improved the vascular integrity and signal-to-noise ratio compared to previous reported approaches, enabling better visualization and quantification of retinal vascular disorders. Second, a robust non-perfusion area (NPA) detection method was developed using a convolutional neural network (CNN) to segment macular ischemia. By merging information from OCTA angiograms and OCT structural images, the proposed CNN could exclude signal reduction and motion artifacts and detect the avascular features from local to global with resolution preserved. Across a wide range of signal strength indices, and on both healthy and DR eyes, the algorithm achieved high accuracy and repeatability. Third, a fully automated CNV diagnosis and segmentation algorithms based on a CNN were developed. The CNN models were trained and tested on real-world clinical datasets that included both scans with and without CNV, and scans of eyes with different pathologies and diseases. The quantitative metrics demonstrated reliable CNV diagnosis and segmentation which would offer benefits for CNV diagnosis, visualization monitoring in clinical services. Fourth, the field of view of OCTA images of the retina was increased by montaging consecutive scans acquired at different retinal regions. Invariant features were used to register the overlapping areas between adjacent scans by estimating the affine transformation matrix needed to accurately stitch them. Then, the flow signal was compensated to homogenize the angiograms with different brightness and the joints were blended to generate a seamless, montaged wide-field angiogram. In brief, the goal of this dissertation is to develop an fully automated OCTA processing platform.

Acknowledgments

I'm deeply grateful for the guidance provided by my mentor Dr. Yali Jia. I couldn't have completed this dissertation without her help. Dr. Jia is a diligent and responsible mentor. We often meet one-on-one to review and discuss the problems in my studies, and she can always provide me with valuable advice that helped me solve techinical issues. Dr. Jia cares deeply about my career developments, as she often shares experiences in her career, introduces me to collaborative studies to gain experience, and encourages me to ask collaborative clinicians questions to gain knowledge.

I would also like to express sincere appreciation to my dissertation advisory committee, Dr. Yong Hwang Chang, Dr. J. Peter Campbell, Dr. Meysam Asgari, and Dr. David Huang for taking time from their busy schedule to serve in this committee, and giving me valuable advice for my studies and future career development. Without their encouragement, this dissertation would not have been possible.

I am deeply indebted to Dr. Tristan T. Hormel's great help and advice on writing manuscripts. Dr. Hormel always gives me valuable and very detailed advice for improving my writing and oral presentation. I would like to thank Dr. Steven Bailey, Dr. Thomas S. Hwang, and Dr. Kotaro Tsuiboi for their great support with clinical knowledge, the research coordinator team Denzil Romfh, Humberto Martinez, Chinmay Deshpande, George Pacheco, and Kevin Lathrop for their efforts with data collection. I also would like to thank all the lab members of the Center for Ophthalmic Optics & Lasers at Casey Eye Institute for their help and friendship during my PhD studies.

I hope this dissertation is an unique and special gift for my family. Twenty years later, I still remember when my father bought an English workbook for enriching my summer break the first year of middle school, because I got the lowest grades in all my tests in this subject. Even I forget if I finished all the tasks it included, I would like to use this dissertation as a special gift to my parents to tell them that it seems the English workbook helped me. I met and fell in love with my beloved wife in high school seventeen years ago. We then studied at different universities in the same city, and have been married for seven years this winter and now have a lovely daughter. Half the effort in this dissertation was from my wife with her steadfast contributions to our family. After graduation,

we will take our daughter to try the places on the street we often ate at, walk on the trails we often took, and tell her our stories.

1 Introduction

1.1 Retina structural and vascular anatomical terminology

Hike onto the top of mountain and take a look around the surroundings; what do you see? Colorful wild flowers, cute squirrels, maybe a river and snowy mountains in the distance - the view is so nice and everything is just there. Have you ever thought about how we perceive the environments? Yes, it's human vision system what generates the vision and perception. Human eyes are wondrous sensory organs and a key component of our visual system. Visual acuity impacts our quality of life[3, 4, 5, 6], which is not surprisingly because vision is involved in almost everything we do.

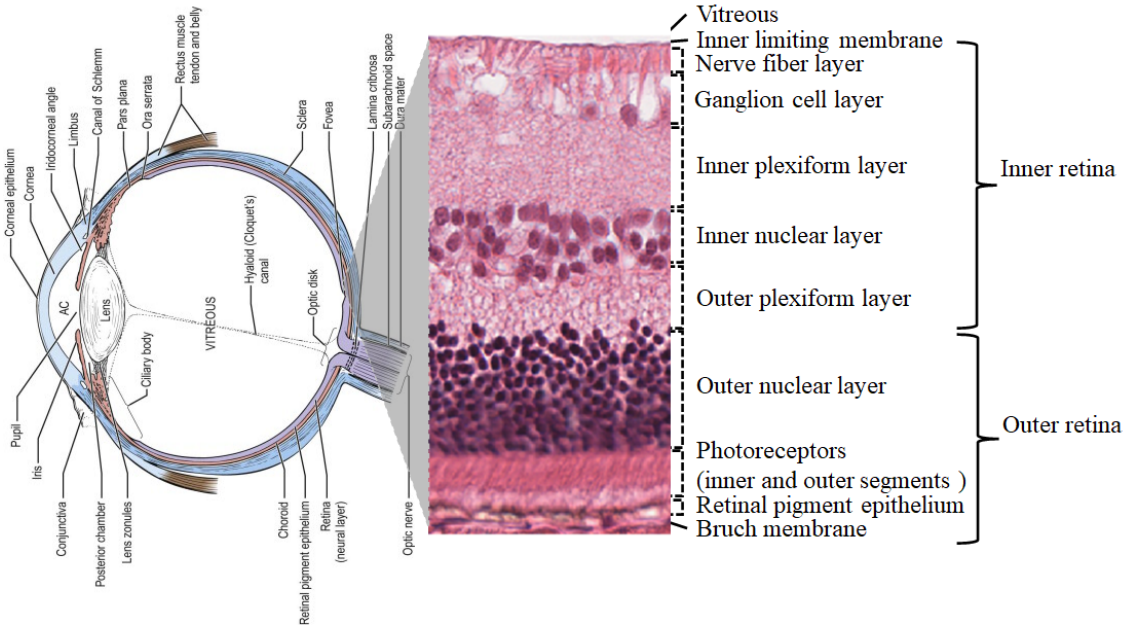


Figure 1.1: (A) Cross-section of a human eye and location of retina; (B) Retinal histology. The inner retina consists of the inner limiting membrane (ILM) through to the outer boundary of outer plexiform layer (OPL). The outer retina consists of outer boundary of OPL through to the Bruch's membrane (BM).

Our eyes contain several features which are essential for forming a sharp image. Some elements, including the tear film, cornea and lens, help focus light so that it can be detected to form an image (Fig. 1.1 A [7]). Light detection occurs in the retina, a structure that most of the algorithms in this dissertation target. Th retina is a thin, transparent and light-sensitive tissue located at the back of the eye; there, photoreceptors (Fig. 1.1 B[8]) convert the light into bioelectric

signal. The signal travels through the optical nerve and into brain to interpret what we are seeing. On a healthy eye, millions of nerves are well organized and displayed which constitutes the retina structural layers that can be visualize on the cross-sectional histological image (Fig. 1.1 B) including (1) inner limiting membrane (ILM), (2) nerve fiber layer (NFL), (3)ganglion cell layer (GCL), (4)inner plexiform layer (IPL), (5)inner nuclear layer (INL), (6)outer plexiform layer (OPL), (7)outer nuclear layer (ONL), (8)inner/outer segments layer (ISOS), and (9)retinal pigment epithelium layer (RPE). The most version is captured by the macula that is the small but important area in the center of retina (which has about a 5mm diameter centered on the fovea, Fig. 1.1 A).

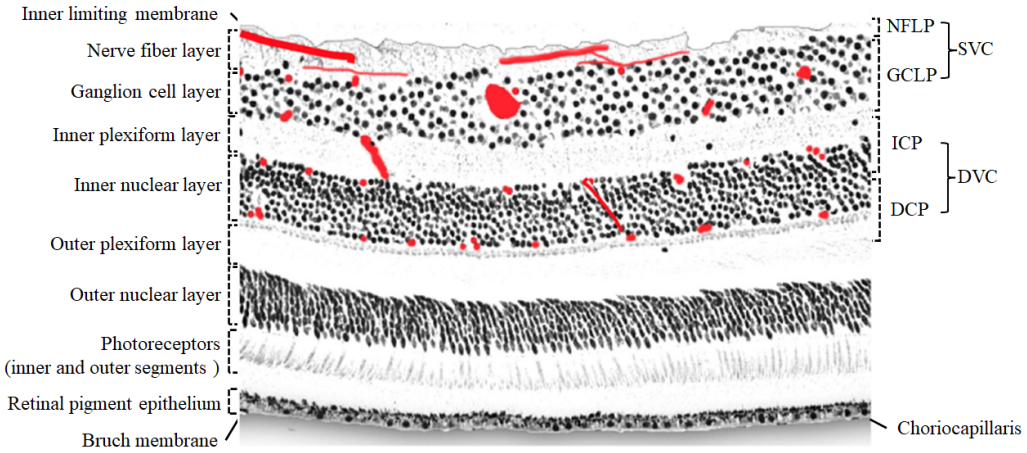


Figure 1.2: Anatomic cross-sectional retinal structure and location of the vascular plexuses in the human retina at the macula. The vessels are illustrated in red. Four vascular networks including the nerve fiber layer plexus (NFLP), ganglion cell layer plexus (GCLP), intermediate capillary plexus (ICP), and deep capillary plexus (DCP). superficial vascular complex (SVC) consists of NFLP and GCLP, and deep vascular complex (DVC) consists of ICP and DCP

The macula, one of the most metabolically active tissues in the human body, is supplied by two vascular systems: (1) the central artery supplies the inner retina and (2) the choriocapillaries supply the outer retina. From previous studies, we know that there are up to four retinal vascular networks in the macula (Fig. 1.2) [9],including (1) nerve fiber layer plexus (NFLP), also known as the radial peripapillary capillaries (RPCP) that are long, straight capillaries arising from peripapillary retinal arterioles, extending radially from the optic disc, and running in parallel with the NFL axons, furthest along the temporal arcades[10]; (2) ganglion cell layer plexus (GCLP) the vascular network that supplies the GCL; (3) intermediate capillary plexus (ICP), the capillary network that nourishes cells at the junction between the IPL and INL;and (4) deep capillary plexus (DCP), the capillary network that nourishes the junction between the INL and OPL. Four vascular

plexuses can be further group into superficial vascular complex (SVC) and deep vascular complex (DVC). High visual acuity is reliant on the efficient retinal and choroidal circulations that supply nutrition and oxygen and carry away metabolic waste.

1.2 Two critical vascular biomarkers in retinal vascular diseases

Macular ischemia[11, 12, 13, 14, 15] and choroidal neovascularization (CNV) [16, 17, 18] are important biomarkers of retinal diseases that canlead to vision loss and blindness, and symptoms of macular vascular diseases commonly found in the inner and outer retina, respectively. *Macular ischemia* is caused by insufficient blood supply, leading to irreversible optic nerve death and further disturbing visual perception. Macular ischemia is an important clinical feature in many retinal vascular disorders, such as diabetic retinopathy (DR), central retina vein occlusion (CRVO) / branch retina vein occlusion (BRVO)[19, 20], and central retina arterial occlusion (CRAO)/branch retina vein occlusion (BRVO)[21], as well as other more rare afflictions. *CNV* is pathological angiogenesis wherein abnormal vessels grow from the choroid and break through the BM into the normally avascular outer retina. CNV is an important biomarker in multiple macular diseases. Development of CNV is associated with a significantly higher chance of severe vision loss. CNV is found in many retinal vascular diseases such as neovascular age-related macular degeneration (AMD), pathologic myopia[22], angioid streaks[23], ocular histoplasmosis[24] and traumatic choroidal rupture[25].

Retinal vascular disorders, resulting in an unbalanced metabolic nutrient supply and demand, as well as disrupted optic nerve function, have deleterious effects on normal vision. Early detection of macular ischemia and CNV is essential to monitoring disease progression and preventing irreversible vision loss, and performing timely antiangiogenic or leaser therapy to prevent vision loss.

1.3 Currently available imaging modalities

With its transparent structure, the retina can be visualized using ophthalmic and fundus imaging techniques. Imaging the retina is essential for documenting and diagnosing retinal vascular

disease by allowing clinicians to identify symptoms. Fundus photography and invasive dye-based fluorescein angiograph (FA) / indocyanine green angiograph (ICGA) imaging modalities are traditionally used as the gold standard for diagnosis of retinal vascular diseases.

(1) *Color fundus photography* images the retina using a fundus camera and white light illumination. Because A large amount of retinal disease symptoms can be visualized in color fundus photographs (Fig. 1.3 B), and because taking color fundus photographs is easy,low-cost and non-invasive, this image modality has been widely used in retinal disease screening, documentation and diagnosis.

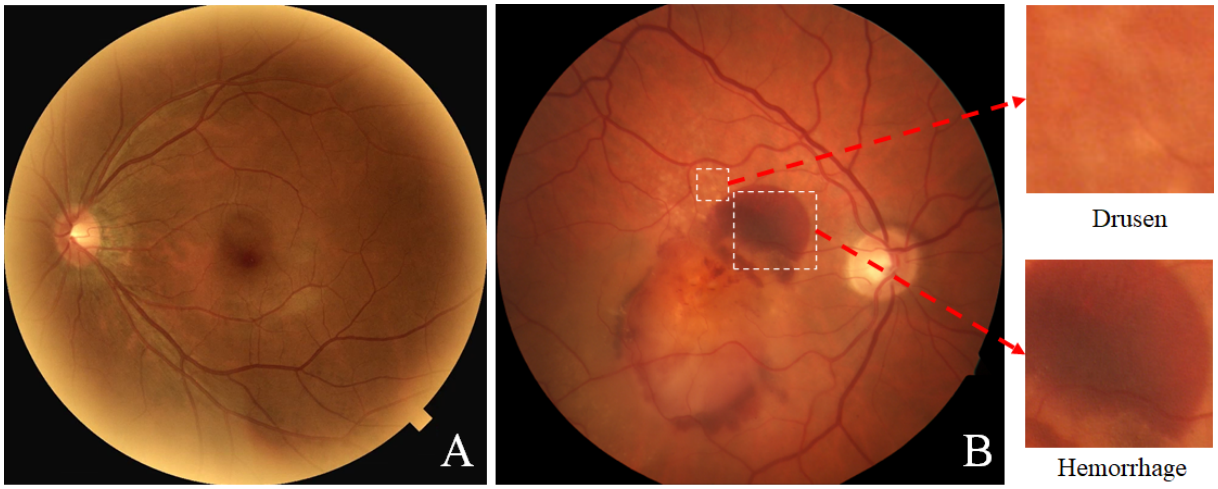


Figure 1.3: Color fundus photograph of a healthy eye (A) and an eye diagnosed with neovascular age-related macular degeneration (AMD) (B). Retinal pathologies, e.g. hemorrhages, drusen, can be visualized with color fundus photography (B)

(2) *Invasive dye-based FA / ICGA* is traditionally used as the gold standard for diagnosis of macular ischemia (Fig. 1.4 A) and CNV(Fig. 1.4 B). However, the drawbacks to FA / ICGA include that it acquires only two-dimensional (2D) and low-resolution images of vascular networks and is therefore incapable of visualizing the detailed microvascular changes associated with developing pathology. It also requires invasive intravenous contrast dye that can lead to nausea and anaphylaxis, and needs long acquisition times (around 10-15 minutes). As an invasive imaging modalities neither FA or ICGA is suitable for retinal vascular disease screening.

The drawbacks to traditional imaging modalities of color fundus photography and invasive dye-based FA / ICGA include that they acquire only 2D and low-resolution images of vascular

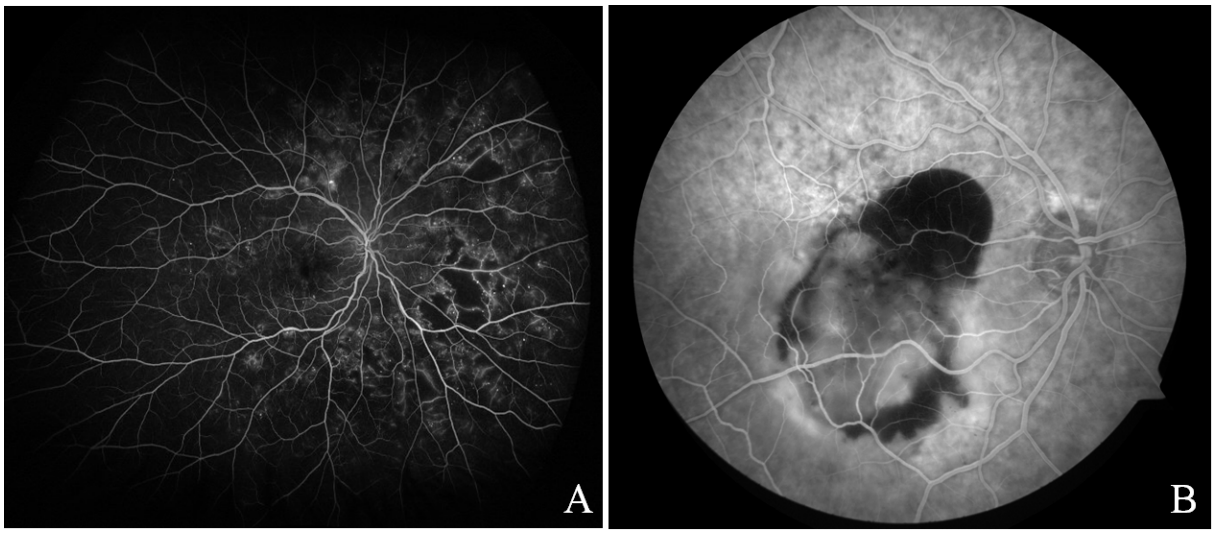


Figure 1.4: fluorescein angiograph (FA) of an eye diagnosied with diabetic retinopathy (DR)(A), and an eye diagnosed with neovascular age-related macular degeneration (AMD) (B). The profile of retinal pathologies of macular ischemia (A) and choroidal neovascularization (CNV) (B) can be imaged with FA, but the visualization of pathological details is limited due to the low image resolution

networks and are therefore incapable of visualizing the detailed micro-vascular changes associated with developing pathologies. The three-dimensional (3D) pathology is projected onto 2D plane which lacks the capability to locate vascular pathology within specific anatomic slabs.

(3) Since the first time-domain *optical coherence tomography (OCT)* article was published in 1991[26], OCT technology developed rapidly and is now an indispensable ophthalmic imaging tool. With the invention of spectral-domain and swept-source imaging modalities[27, 28, 29], current OCT devices allow acquisition of 3D retinal volume (Fig. 1.5 A) sufficient to resolve separate anatomic layers (Fig. 1.5 B) and structural pathologies (e.g. diabetic macular edema (DME) shown on Fig. 1.5 C). Approximately 30 million examinations were performed per year worldwide for the diagnosis of several retina diseases[30, 31, 32], due primarily to the merits of visualization and measurement of retinal structural disorders in micro-scale. OCT has been estimated to have provided $\$11$ billion healthcare savings from 2008 to 2015 for guiding the usage of anti-vascular endothelial growth factor (anti–vascular endothelial growth factor (anti-VEGF)) treatment [33]. structural OCT is also the commonly used tool for detecting retinal vascular diseases. OCT only provides depth-resolved retinal structural imaging which is a dramatic improvement for visualizing and diagnosing retinal diseases and greatly reduced the usage of invasive FAindocyanine green

angiograph (ICGA). While OCT is incapable of presenting retinal vascular networks at capillary scale resolution. The invasive dye-based FA / ICGA is still needed for conforming retinal vascular disorders.

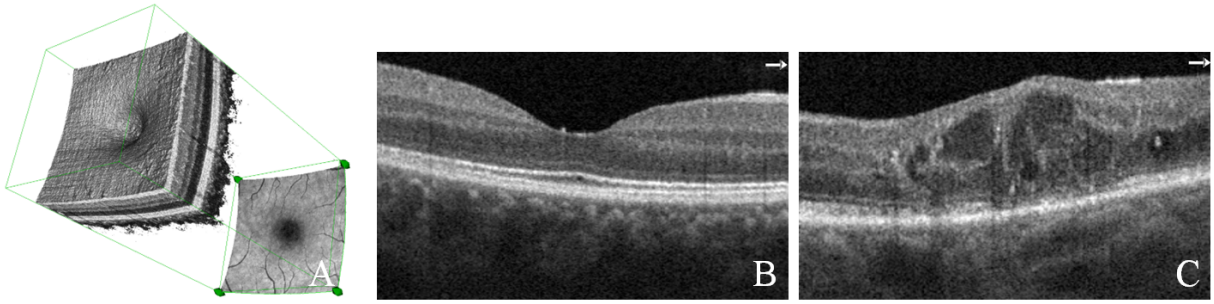


Figure 1.5: Optical coherence tomography captured 3D retinal structure (A) showing well arranged anatomic retinal nerve layers in a healthy eye and depth-resolved retinal structural pathologies, e.g. diabetic macular edema (C), in an eye diagnosed with diabetic retinopathy

It is natural to wonder if the OCT technique could be extended to image retinal vessels to enable the precision diagnosis and measurements of vascular disorders, similar to its use for analyzing retinal structure.

1.4 Optical coherence tomographic angiography and its major artifacts

Optical coherence tomographic angiography (OCTA) is a successful functional extension of the OCT technique. The retinal vessels are imaged by measuring the variation in the OCT signal caused by moving blood cells on continuous B-scans acquired at the same location. The signal back-scatted from static retinal tissue won't produce much variation, while the signal from blood cells will be changed dramatically. The principle of OCTA can be illustrated by analogy with moving tennis balls (Fig. 1.6[34, 35]). The moving balls can be detected by measuring the differences among the consecutive video frames, while static background is ignored. unfortunately, besides the moving balls, the shadow of moving balls projected onto the wall are also mistakenly detected, which is one of the major limitations of OCTA (see Section 3).

The OCT signal is described by complex numbers with both magnitude (amplitude) and phase components; the variation in the detected OCT amplitude and phase signal due to moving blood cells is much greater than the surrounding static tissues [36]. Thus, flow signal could be detected by

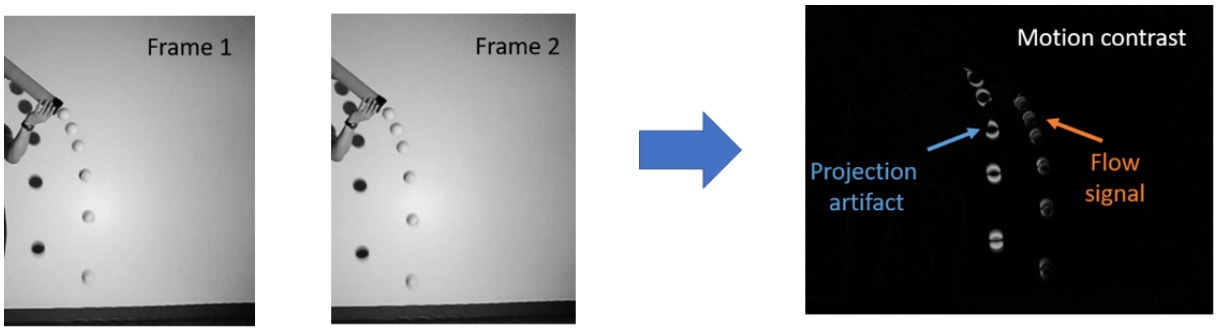


Figure 1.6: The principle of motion contrast in optical coherence tomographic angiography (OCTA) is explained using video frames. In frames 1 and 2, tennis balls falling out of a tube represent red blood cells. Motion contrast is generated by subtracting the two frames from each other, which accentuates the moving parts in the image while removing the stationary parts (right). Note both the tennis balls (representing flowing blood) and the shadows they cast on the wall (representing projection artifacts) are highlighted.

evaluating the variation of either the magnitude, phase, or both. OCTA algorithms could therefore be classified into three types: (1) *Phase-based methods* where the flow signal was obtained only from the phase component[37, 38, 39, 40], (2) *Amplitude-based methods* where the flow signal was obtained only from the magnitude component[41, 42, 43, 44], and (3) *Complex-signal-based methods* where the flow signal is measured utilizing both amplitude and phase components[45, 46, 47]. In current practical implementations, the most common approaches are amplitude-based and complex-signal-based methods. Split-spectrum amplitude-decorrelation angiography split-spectrum amplitude decorrelation angiography (SSADA) [43, 44] is a representative amplitude-based method that has been applied on commercial OCTA system (OptoVue, Avanti) and used in clinical trials worldwide. SSADA detects the flow signal using only two repeat B-scans. One of the most widely used complex-signal-basd methods is opticl microangiography (optical microangiography (OMAG)) [45, 46, 47]. The OMAG algorithm has been applied on a commercial OCTA system (Zeiss, Angioplex) and also widely used for clinical researches.

OCTA has been successfully used in ophthalmology, providing noninvasive, non-dye-based, high-speed, and depth-resolved imaging of retinal and choroidal circulatory networks in vivo at capillary-scale detail, which enables the potential to explore valuable biomarkers for early diagnosis and the precise measurement of retinal vascular diseases. By applying the anatomic structural layer segmentation to the OCTA volume we are able to visualize the retinal vasculature

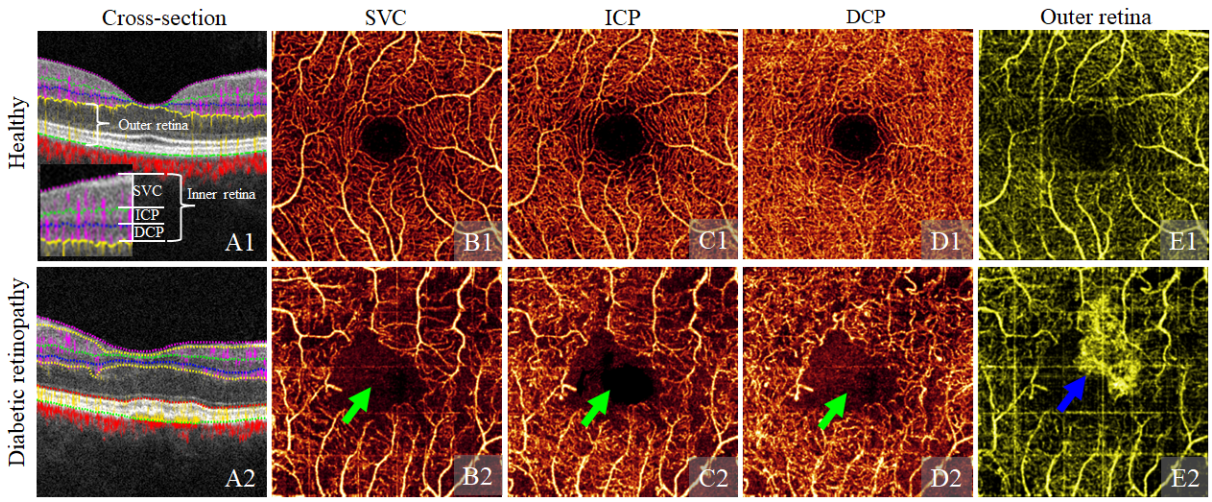


Figure 1.7: optical coherence tomographic angiography (OCTA) from an healthy eye (row 1) and an eye diagnosed with diabetic retinopathy shows macular ischemia in slab-specific *en face* angiograms of the superficial vascular complex (SVC), intermediate capillary plexus (ICP), deep capillary plexus (DCP) in the inner retina, and choroidal neovascularization (CNV) in the outer retina. Macular ischemia is highlighted by the green arrows, and CNV is highlighted by the blue arrow.

and vascular pathologies in the SVC(Fig. 1.7 B), ICP(Fig. 1.7 C), DCP(Fig. 1.7 D), and CNV in outer retina (Fig. 1.7 E2).

However, major limitations of OCTA as originally proposed are shadow, motion, and projection artifacts[34]. Each of these are due to the way that OCTA data is acquired and processed, and manifest differently in the images[34, 48]. Shadow artifacts are due to the insufficient signal quality that media opacities, vitreous floaters or vignetting of a corner blocks the light path and causes reflectance magnitude reduction. Motion artifacts are due to the eye motion that causes significant signal variation among consecutive B-scans. Projection artifacts are particularly challenging because they cause specious flow signal mimicking the morphology of superficial vasculature to appear in deeper anatomic layers (Fig. 1.7), which can cause the misinterpertation of vascular pathologies in deep vascular plexus (Fig. 1.7 B2-D2) and CNV in the outer retina. More details of projection artifacts are described in section 3.

1.5 Artificial intelligence for aiding optical coherence tomographic angiography-based vascular biomarker detection and quantification

Convolutional neural network CNN, one of the outstanding artificial intelligence (AI) techniques, is the state-of-the-art approach of accomplishing the goals in this study. Published

results indicate the superior performance of CNNs adapted to complex tasks such as object classification and semantic segmentation[49, 50, 51] when compared to traditional image processing techniques that rely on handcrafted features. CNNs have also been successfully used for age-related macular degeneration diagnosis on 2D fundus photographs[52], to segment non-perfusion area (NPA)[53, 54, 55] and to perform retinal layer segmentation[56, 57]. However, an end-to-end NPA and CNV diagnosis and quantification system for OCTA has never been developed. As CNV and NPA represent the most important pathological development in age-related macular degeneration and diabetic retinopathy, this is a major limitation in current clinical practice.

1.6 Outline

A complete procedure for OCTA analysis of plexus-specific micro-vascular pathology detection is presented in this dissertation. My research work was implemented on a customer-designed OCTA reading tool kit with 5 key modules including (i) retinal layers segmentation and image denoising, (ii) an advanced sacPR-OCTA algorithm, (iii) robust NPA detection using a CNN, (iv) automated CNV diagnosis and segmentation algorithms using deep learning, and (v) invariant features-based automated registration and montage for wide-field OCTA. The work described in this dissertation will help in disease diagnosis, and enable new insights into disease pathophysiology.

The following chapters of this dissertation are organized as follows: section 2 presents a fully automated OCTA analysis platform, section 3 presents signal attenuation compensated PR-OCTA algorithm; section 4 presents the robust NPA detection in three retinal plexuses using a CNN in OCTA, section 5 and 6 present automated diagnosis and segmentation of CNV in OCTA using deep learning, and section 7 presents invariant features-based automated registration and montage for wide-field OCTA, and section 8 discussed the future works and conclusion of this dissertation.

2 Optical coherence tomographic angiography reading toolkit

An entire procedure to detect slab-specific retinal vascular pathology with optical coherence tomographic angiography (OCTA) consists of three key steps, including (1) retinal layers segmentation for localizing the specific anatomic slabs, (2) projection artifact removal for precise interpretation of micro-vascular pathologies in deeper anatomic slabs, and (3) detection of micro-vascular pathologies within a specific plexus.

This sections discusses task (1); tasks (2) and (3) will be addressed in subsequent sections.

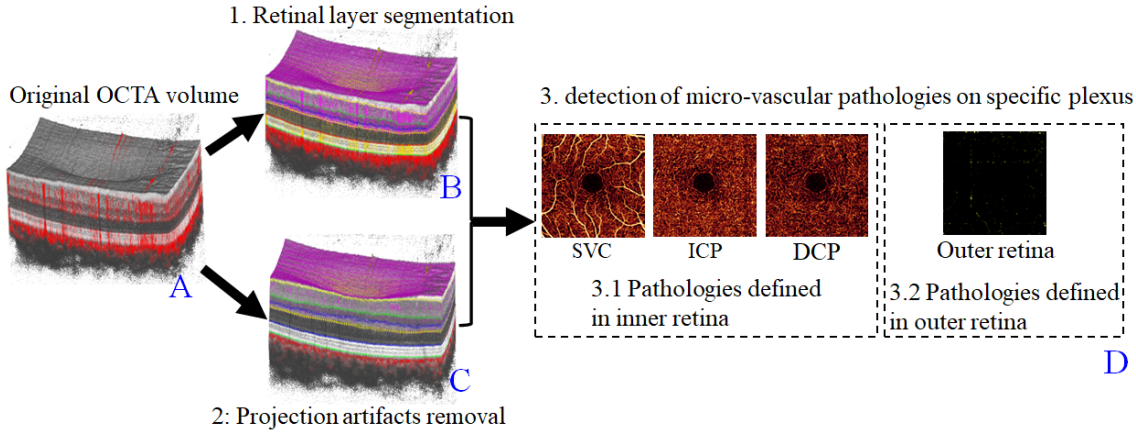


Figure 2.1: Procedure for detecting plexus-specific micro-vascular pathologies defined by optical coherence tomographic angiography. (A) Color coded uncorrected flow signal volume overlaid on the structural volume, (B) Color coded uncorrected flow signal volume overlaid on the structural volume and illustration of retinal layers segmentation, (C) Color coded projection-resolved flow signal volume overlaid on the structural volume and illustration of retinal layer segmentation, (D) plexus-specific optical coherence tomographic angiography (OCTA) angiograms of the superficial vascular complex (SVC), intermediate capillary plexus (ICP), deep capillary plexus (DCP), and outer retina.

2.1 Retinal layers segmentation and intelligent manual correction

To generate slab-specific angiograms, retinal layer boundaries are needed to localize specific retinal tissue slabs. In a previously reported directional graph search-based algorithm[1] retinal tissue boundaries were tracked by finding the weighted shortest path from one side to the other. Vertical gradients are the most significant features for tracking retinal layer boundaries (Fig. 2.2 B1-3). Retinal layer boundaries displayed on OCT have two types of intensity transitions, which are light-to-dark and dark-to-light. The vertical gradient can also be inverted to redefine the dark-to-light retinal intensity transition. The directional graph search tracks the retinal boundaries by searching for the shortest path with the lowest total cost. In healthy eyes (Fig. 2.2 A1), gradients at retinal

tissue boundaries are large (Fig. 2.2 B1), and the graph search-based algorithm is able to segment retinal layers accurately (Fig. 2.2 C1). However, gradients can be reduced or vanish in pathological regions (Fig. 2.2 B2&3), which can cause segmentation errors (Fig. 2.2 C2&3).

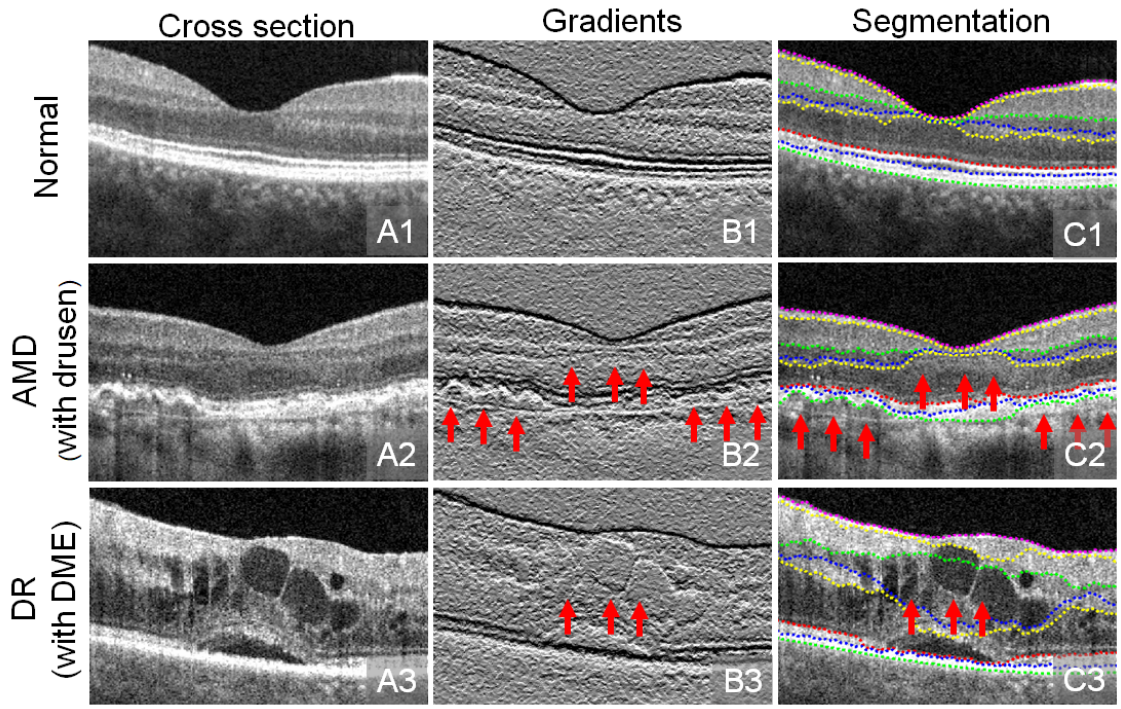


Figure 2.2: Anatomic slab segmentation in a healthy eye (row 1, age matched with A2), an eye with age-related macular degeneration (AMD)(row 2), and a diabetic retinopathy (DR) eye with diabetic macular edema (DME). Column A: cross-sectional structural optical coherence tomography (OCT). Column B: gradient images of column A. Gradients vanish in some pathological areas in the AMD eye (B2). Column C: cross-sectional structural OCT with boundaries detected through a graph search algorithm[1] (colored dotted lines). Red arrows in C2 indicate mis-segmented regions. Such processing failures can lead to difficulty in interpreting images and generate errors in structural OCT and optical coherence tomographic angiography (OCTA).

Manual correction of erroneous segmentation is required on the challenging scans, especially in areas with severe pathological changes (Fig. 2.3 A1). The semi-automated intelligent manual correction module allows the users to move the cursor to set up the anchor points and the directional graph search algorithm is further applied to track the path between adjacent anchors.

In practical applications, users are often unable to set an ideal anchor that has the highest gradient on the dark-to-light boundary or the lowest gradient on the light-to-dark boundary. We devised an automated anchor search function that is able to set the anchor automatically, by (1) dark-to-light boundary: searching the position with the highest gradient in the cursor's neighborhood (equation 2.1); (2) light-to-dark boundary: inverting gradients, and then searching for the anchor the

same approach:

$$(k_0, n_0) = \{(x_0 - r_x) \leq k \leq (x_0 + r_x), (y_0 - r_y) \leq n \leq (y_0 + r_y)\}_{\text{Max}[G(k,n)]} \quad (2.1)$$

where (k_0, n_0) is the anchor with the highest gradient, (k, n) is the pixel position, (x_0, y_0) is the cursor position, and (r_x, r_y) are horizontal and vertical radii of rectangle searching area radius, respectively.

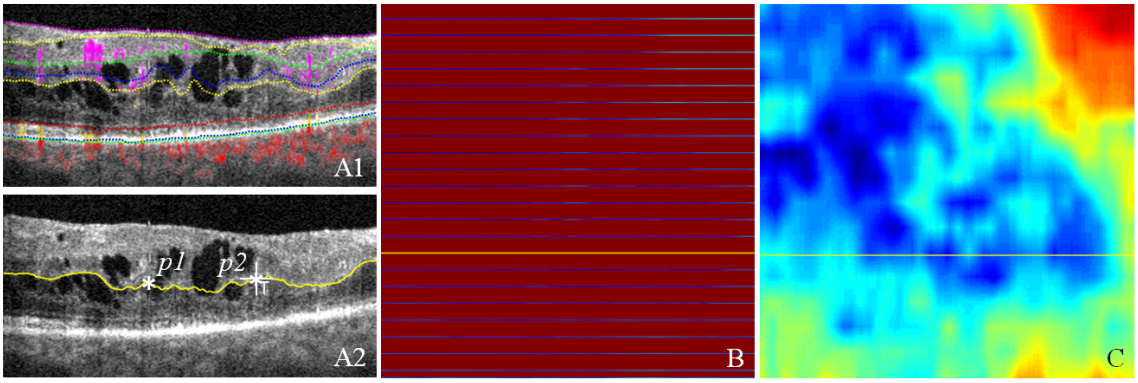


Figure 2.3: Demonstration of semi-automated layer correction. (A1) Uncorrected layer segmentation, (A2) Manual correction of outer plexiform layer (OPL) / outer nuclear layer (ONL) segmentation, two stars are anchors used for segmentation correction; (B) Enface segmentation map on key frames;(C) *En face* segmentation map after manual correction propagation. The yellow line in B and C indicate the B-scan position of A.

Erroneous segmentation generally occurs only along partial segments of the boundary. Semi-automated intelligent manual correction is only activated in the partial region that is set with anchors, and original segmentation will be preserved on both sides of the anchored region. For instance, if p_1 and p_2 are two anchors (Fig. 2.3 A2), and the directional graph search algorithm is applied to track the boundary between p_1 and p_2, and the right segmentation (left side of p_1, and the right side of p_2) will be conserved. Users only need to correct the segmentation on a few key B-scans (Fig. 2.3 8 B), and the correction will be propagated onto adjacent B-scans (Fig. 2.3 8 C).

2.2 User interface and case report

The user interface of OCTA reading toolkit software was shown in Figure 2.4. OCTA reading toolkit software can show cross-sectional images, layer segmentation, thickness maps, and *en face* images of OCT/OCTA in customer-defined slabs.

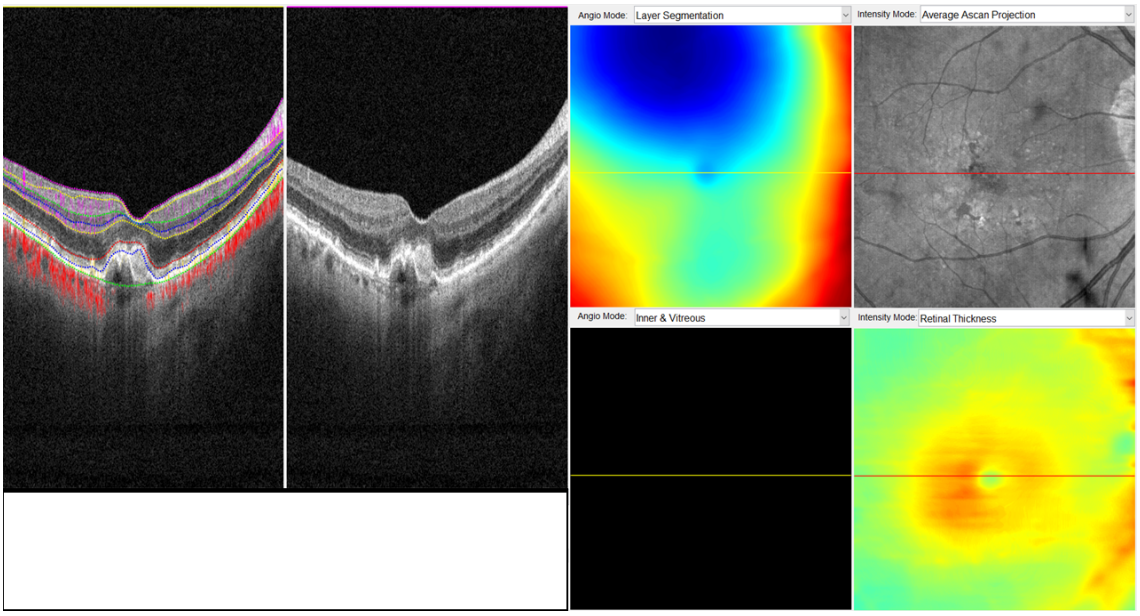


Figure 2.4: The user interface of optical coherence tomographic angiography (OCTA) reading toolkit software

This customer-designed OCTA reading toolkit can generate a scan report including projection-resolved *en face* angiograms in multiple slabs (Fig. 2.5 A-F), *en face* structural OCT image (Fig. 2.5 G), and the cross-sectional OCT overlaid with a color-coded PR-OCTA signal (Fig. 2.5 H). Users can add notes in the report and mark the position of interesting cross-sectional frame. Users can also use the cursor to mark the FAZ/Disc center on the user interface.

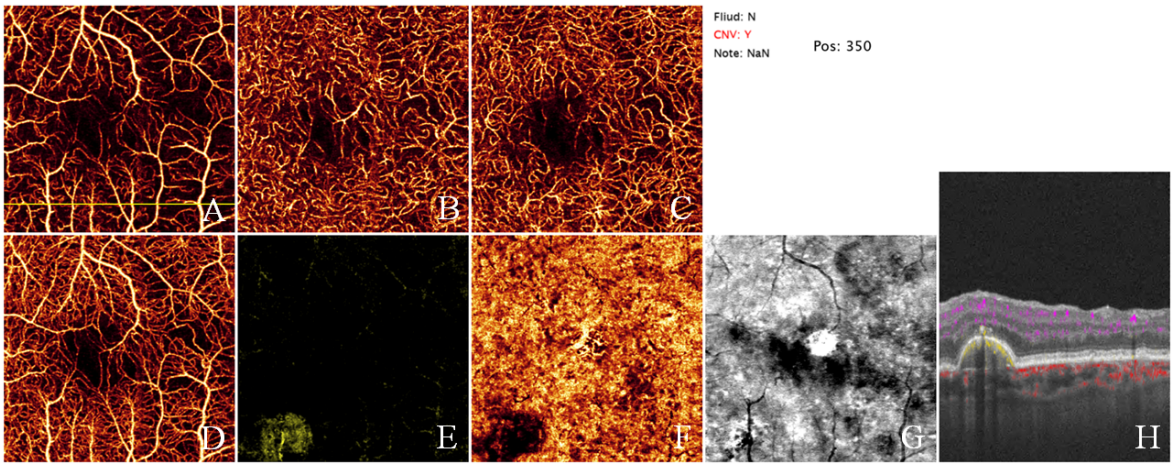


Figure 2.5: Case report. (A) superficial vascular complex (SVC) defined as the anterior 80% of the ganglion cell complex (GCC); (B)intermediate capillary plexus (ICP) defined as the outer 20% of the GCC and inner 50% of the inner nuclear layer (INL); (C) deep capillary plexus (DCP) defined as the outer 50% of the INL and the outer plexiform layer (OPL); (D) Inner retina: defined as the boundary of vitreous inner limiting membrane (ILM) to the low boundary of OPL; (E) The outer retina is defined as the lower boundary of OPL to Bruch's membrane (BM); (F) choriocapillaris (CC) is defined as the region between BM and BM+$10um$; (G) Mean projection of OCT volume; (H) cross-sectional OCT overlaid with color-coded PR-OCTA signal (violet: inner retinal; yellow: pathological outer retinal; red: choroidal) at the position indicated by the yellow line in (A).

3 Signal attenuation-compensated projection-resolved optical coherence tomographic angiography

3.1 Abstract

Projection artifacts are one of the major limitations of optical coherence tomographic angiography (OCTA). Existing techniques to suppress these artifacts exhibit sensitivity to image quality, and may become unreliable on low quality images. In this study, we propose a novel signal attenuation-compensated projection-resolved OCTA (sacPR-OCTA) algorithm. In addition to removing projection artifacts, our method also compensates shadows beneath large vessels shadow. We show that the proposed sacPR-OCTA algorithm improves vascular continuity, reduces the similarity of vascular patterns in different plexuses, and removes more residual artifacts compared to existing methods. We also show that the sacPR-OCTA algorithm better preserved flow signal in choroidal neovascular lesions and in shadow affected areas. Because sacPR-OCTA processes the data along normalized A-lines, it is agnostic to platform and OCTA processing choices and provides a general solution for removing projection artifacts.

3.2 Introduction

Optical coherence tomographic angiography (OCTA) provides powerful means to image retinal vasculature down to the capillary scale[43, 46]. Because it is based on an alternative means of processing optical coherence tomography (OCT) data, OCTA inherits many of the advantages of OCT data imaging: it is non-invasive, depth-resolved, and high-resolution. These qualities offer hope that OCTA could improve management of retinal vascular disorders by providing plausible screening (in addition to being non-invasive, OCTA procedures are rapid and inexpensive) and precise quantification of vascular biomarkers and other pathologic vascular features. Indeed, OCTA-based metrics such as retinal vessel density and non-perfusion area are correlated with disease severity in multiple prevalent blinding diseases[58, 59, 60, 61, 62, 63, 64], and OCTA can detect other key pathologies, such as choroidal neovascularization[65] or polypoidal choroidal vasculopathy[66], that could prove to be viable targets for therapeutic intervention.

Feature detection and quantification in OCTA benefit especially from depth resolution. The ability to locate vascular disorders within a specific plexus improves diagnostic utility[67] and can inform our understanding of disease pathophysiology[13, 68, 69]. Furthermore, because OCTA achieves capillary scale resolution alongside volumetric imaging, it could provide a complete description of retinal and choroidal vascular morphology, in principle. In practice, it falls short. The most obvious reason for this shortcoming is the need to correctly remove projection artifacts in posterior anatomic slabs. The first attempts at projection artifact removal merely scaled and subtracted vascular patterns in superficial *en face* angiograms from posterior angiograms[70, 71], which only works for *en face* images. Precision projection artifact removal should instead be performed on a voxel-by-voxel basis so that any region of the scan volume could still be viewed in either cross-section or en face orientation. This is a more difficult task because projection artifact magnitude within a voxel is not measurable; instead, artifact magnitude must be estimated data statistics or optical principles. Projection-resolved OCTA (PR-OCTA) approaches attempt this by considering flow signal statistics alone[72] or in conjunction with the OCT reflectance signal[73]. However, neither of these approaches account for signal attenuation along the optical length (axial depth), which is also problematic for imaging posterior vascular layers. In our studies, we observed that flow signal strength is associated with the reflectance signal strength[72, 73, 74, 75]. In addition to the inherent reflectivity of different anatomic layers, the reflectance signal is modulated by attenuation due to light scattering and absorption. Thus, projection artifact magnitude is dependent not just on the reflectivity of the tissue in which the projection artifact is located, but also on the depth of the projection artifact within the retina. This can be visualized in uncorrected OCTA cross-sections, where the artifactual tails extending beneath real vessels gradually diminish and then disappear.

Here, we report a new projection artifact removal approach, signal attenuation-compensated projection-resolved OCTA (sacPR-OCTA), that estimates projection artifact magnitude while modeling signal attenuation. This method both removes projection artifacts and can enhance *in situ* flow signal underneath large vessels- a location that is under/over processed by alternative approaches[72, 73]. We assessed the algorithm's performance by quantifying vascular similarity

between en face projections at different depths, vessel continuity, and the magnitude of residual artifacts. Together, these metrics provide a description of the degree to which artifacts are removed while *in situ* flow is preserved. We also assessed algorithm performance on challenging scans with shadows artifacts caused by anterior blockage (pupil, vitreous floaters), scans from multiple devices, and scans exhibiting pathology. Our results indicate that the sacPR-OCTA approach achieves state of the art projection artifact removal.

3.3 Data acquisition and pre-processing

Participants were scanned using three commercial spectral-domain OCTA systems: (1) RTVue-XR (Visionix Inc., Fremont, CA) with a center wavelength of $840nm$ and $70kHz$ axial scan rate, (2) Solix (Visionix Inc., Fremont, CA) with a center wavelength of $840nm$ and $130kHz$ axial scan rate, and (3) Angioplex (Carl Zeiss, Inc., Dublin, California) with a center wavelength of $840nm$ and $68kHz$ axial scan rate. In both RTVue-XR and Solix systems, flow signal was detected using the commercial version of split-spectrum amplitude decorrelation angiography (SSADA) algorithm which evaluates the reflectance variation between two consecutive B-scans acquired at the same position[43]; one X-fast and one Y-fast volume were obtained and registered to suppress motion artifacts[76]. The $3 \times 3 - mm$ and $6 \times 6 - mm$ scans were acquired using RTVue-XR system, and $3 \times 3 - mm$, $6 \times 6 - mm$, $9 \times 9 - mm$ and $12 \times 12 - mm$ scans were acquired using the Solix system. On the RTVue-XR system, a $3 \times 3 - mm$ volume consists of 304 B-scans and each B-scan consists of 304 A-lines, and a $6 \times 6 - mm$ volume consists of 400 B-scans and each B-scan consists of 400 A-lines. With faster scanning rate, Solix system was able to perform higher scanning density that $3 \times 3 - mm$ volume consists of 400 B-scans and each B-scan consists of 400 A-lines, a $6 \times 6 - mm$ volume consists of 512 B-scans and each B-scan consists of 512 A-lines, a $9 \times 9 - mm$ volume consists of 600 B-scans and each B-scan consists of 600 A-lines. The Angioplex system detected the flows using optical microangiography (OMAG) algorithm[46]. A $3 \times 3 - mm$ Angioplex scan consists of 245 B-scans and each B-scan consists of 245 A-lines. This study was conducted in compliance with Declaration of Helsinki.

Retinal neural layers were segmented using a graph search-based algorithm that tracks the boundaries between adjacent tissue slabs on structural OCT volume[1]. Boundaries between the vitreous / inner limiting membrane (ILM), ganglion cell layer (GCL) / inner plexiform layer (IPL), IPL / outer plexiform layer (OPL), OPL / outer nuclear layer (ONL) and Bruch's membrane (BM) were all segmented. Segmentation errors were manually corrected using our custom-designed COOL-ART software implemented with intelligent manual correction function. Applying retinal layers segmentation of structural OCT to OCTA volume, *en face* OCTA angiograms were generated using maximum projection in multiple slabs including the superficial vascular complex (SVC) comprising the inner 80% of the ganglion cell complex (GCC), the intermediate capillary plexus (ICP) comprising the outer 20% of the GCC and inner 50% of the INL, the deep capillary plexus (DCP), comprising the outer 50% of the INL and OPL, the outer retina comprising the slab between the outer boundary of OPL and BM, and the choriocapillaris (CC), comprising the slab between the BM and BM+$10um$.

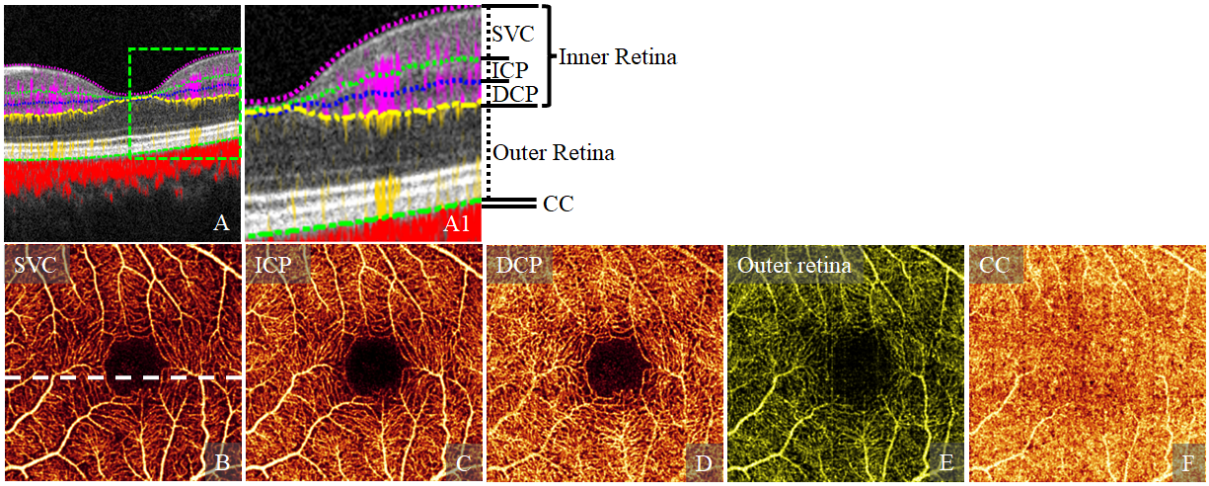


Figure 3.1: Uncorrected optical coherence tomographic angiography (OCTA) exhibiting projection artifacts. (A) Cross-sectional structural optical coherence tomography (OCT) overlaid with color coded OCTA flow in the inner retina (violet), outer retina (yellow), and choroid (red). (A1) Magnification of the region within the green box in A. *En face* images are produced by maximum projection over the relevant regions to show the superficial vascular complex (SVC) (B), intermediate capillary plexus (ICP) (C), deep capillary plexus (DCP) (D), outer retina (E), and choriocapillaris (CC) (F). Vascular patterns from the SVC are clearly duplicated in each of the deeper regions. SVC is defined as the anterior 80% of the ganglion cell complex (GCC), ICP is defined as the outer 20% of the GCC and inner 50% of the inner nuclear layer (INL); DCP is defined as the outer 50% of the inner nuclear layer (INL) and the outer plexiform layer (OPL); Outer retina is defined as the lower boundary of OPL to Bruch's membrane (BM); CC is defined as the region between BM and BM+$10um$.

3.4 Method

3.4.1 Optical coherence tomogeaphic angiography signal attenuation compensation

As an interferometric measurement, OCTA signal can be generated by measuring motion contrast using the amplitude (the magnitude of real and imaginary components), phase (the angle between the real and imaginary components), or complex signal (combining both amplitude and phase) from repeated structural B-scans acquired at the same location. Fluctuating shadows and multiple scattering of photons caused by the anterior moving blood cells can be detected by OCTA algorithms and manifest as motion contrast. This is the mechanism that produces projection artifacts, which can be identified in cross-section as "tails" (Fig. 3.1 A) and in *en face* images as the duplication of superficial vascular patterns in deeper anatomic slabs (Fig. 3.1 B-F).

In this work, we model the observed flow signal $S(z)$ within an A-line at depth z as the sum of contributions from in situ flow $S_i(z)$, anatomically spurious flow signal from projection artifacts $S_a(z)$, and noise σ according to

$$S(z) = S_i(z) + S_a(z) + \sigma \tag{3.1}$$

We seek to recover the *in situ* flow $S_i(z)$ (which is the anatomically relevant signal) from the observed signal $S(z)$, however we lack the ability to directly measure any of the terms in (3.1). We define proportion coefficient $p(z)$ such that

$$S_i(z) = p(z)S(z) \tag{3.2}$$

Ignoring the noise contribution since it will in general be small relative to *in situ* flow, and further applying the equation (2) to the (1), observed flow signal S(z) can be rewritten by

$$S(z) = p(z)S(z) + (1 - p(z))S(z) \tag{3.3}$$

The task for projection artifact removal can therefore be equated to estimating $p(z)$, for which we require an estimate of $S_a(z)$. To obtain this we begin by observing that projection artifact

magnitude at depth z depends on both the inherent reflectivity $R_{\text{OCT}}(z)$ of the tissue at that location and attenuation as the distance from the generating in situ flow $d(z) = z - z_0$. This yields

$$\begin{cases} A(z) = g[R_{\text{OCT(z)}}, d(z)] \\ S_a(z) = A(z) S_i(z_0) \end{cases} \tag{3.4}$$

where $g(\cdot)$, which we cannot access, describes the functional dependence of the scaling coefficient for artifactual signal relative to the *in situ* flow that produced it. To simplify, we assume that artifact strength scales linearly with the in situ flow strength. To proceed we approximate (3.4) according to

$$\widehat{S}_a(z) = \begin{cases} \left[\alpha R_{\text{OCT}}(z) + \beta\left(1 - \dfrac{d(z)}{d_{\max}}\right)\right] S_i(z_0), & \text{if } (z - z_0) \le d_{\max} \\ \alpha R_{\text{OCT}}(z)\, S_i(z_0), & \text{if } (z - z_0) > d_{\max} \end{cases} \tag{3.5}$$

where $\widehat{S}_a(z)$ is the estimated projection artifacts strength at depth z, α and β are coefficients describing contributions from tissue reflectivity and artifact attenuation with depth, respectively, and $d_{\max}$ restricts attenuation to the optical path length. A soft process to enhance real flows was applied by

$$p(z) = \text{Nor}\left(p(z) - \widehat{S}_a(z)\right) \tag{3.6}$$

where $\text{Nor}(\cdot)$ is the normalization operator. Applying the equation (3.6) to the (3.2), the *in situ* flow $S_i(z)$ can be restored by

$$\widehat{S}_i(z) = \begin{cases} \left\{\text{Nor}\left\{s(z) - \left[\alpha R_{\text{OCT}}(z) + \beta\left(1 - \dfrac{d(z)}{d_{\max}}\right)\right]\right\}\right\}, & \text{if } (z - z_0) \le d_{\max} \\ \left\{\text{Nor}\left\{S(z) - \alpha R_{\text{OCT}}(z)\, S_i(z_0)\right\}\right\} S(z), & \text{if } (z - z_0) > d_{\max} \end{cases} \tag{3.7}$$

In implementation, the structural OCT intensity was normalized to $[0, 1]$ according to the signal strength variation.

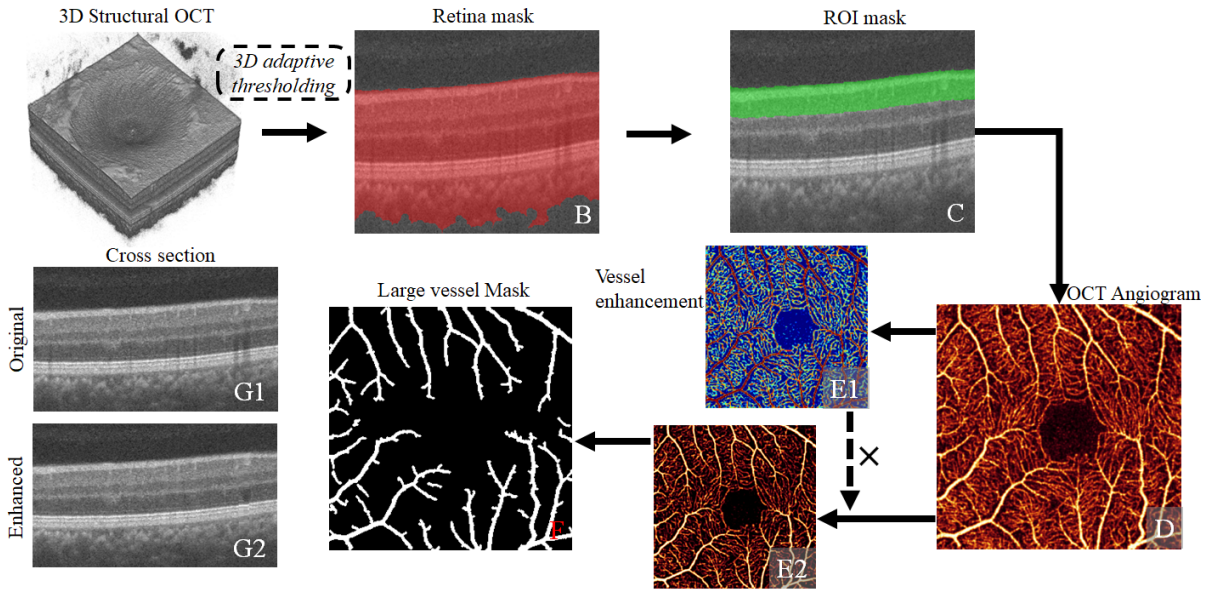


Figure 3.2: Illustration of large vessel shadow compensation in structural optical coherence tomography (OCT). (A) Three-dimensional (3D) structural OCT; (B) Cross-section structural overlaid with a retinal region mask (red) made using a 3D adaptive thresholding algorithm; (C) Cross-sectional structural OCT overlaid with the region of interest (ROI) mask (green) covering the slab of ganglion cell complex (corresponding to a $120\mu m$ axial depth); (D) OCT angiogram generated in the superficial region using maximum projection; (E1) Enhanced vasculature; (E2) Denoised OCT angiogram generated by multiplying the enhanced vasculature (E1) with the original OCT angiogram (D); (F) Large vessel mask detected by using adaptive thresholding algorithm. (G1) Original cross-sectional OCT with shadowing artifacts under the large vessels; (G2) Shadowing artifacts compensated cross-sectional OCT.

3.4.2 Large vessel shadow compensation

Due to the light attenuation, large anterior vessels can produce shadow artifacts in posterior slabs. This complicates projection artifact removal since the shadow artifacts reduce image intensity. We therefore include extra processing in regions near such vessels. First, retinal region (Fig. 3.2 B red) is detected in the structural OCT channel using adaptive thresholding[77, 78]. We next generate an angiogram (Fig. 3.2 D) covering the slab of ganglion cell complex (Fig. 3.2 C) (corresponding to a $120\mu m$ axial depth, the average thickness of the ganglion cell complex[79]). Retinal vasculature is then enhanced using a vesselness filter [80] (Fig. 3.2 E1). The vessel enhanced image is then used to scale the original angiogram (Fig. 3.2 E2). We obtain the large vessel mask by binarizing the scaled image using Otsu's method [81] and morphological operations (Fig. 3.2 F). Voxel values in this large vessel mask are compensated by scaling according to the ratio of the surrounding tissue reflectivity to the area in the vessel mask, but only when signal attenuation occurs (i.e., when the voxels in the vessel area have lower reflectivity than the surrounding voxels). Compared to the

uncorrected cross-sectional OCT (Fig. 3.2 G1), large vessel shadows were reduced (Fig. 3.2 G2), allowing us to apply the proposed flow signal attenuation-compensated method (described in section 3.1) throughout the entire volume.

3.4.3 Implementation

The proposed sacPR-OCTA algorithm was implemented using C++ and multithreading programing on the computer with Intel(R) $i9-10980XE$ CPU @ $3.00GHz$. An OCTA scan with standard resolution ($640 \times 340 \times 304 - (pixel)$) was able to be processed in 0.5 second.

3.5 Results

Visual inspection indicates that compared to the uncorrected original optical coherence tomographic angiography (OCTA) (Fig. 3.1), sacPR-OCTA removed projection artifacts volumetrically, flow "tails" were removed in the inner retinal (Fig. 3.3 D), vessel patterns from upper slab (Fig. 3.3 A) were removed in intermediate (Fig. 3.3 B) and deep (Fig. 3.3 C) slabs, and projection artifacts were suppressed in the outer retina (Fig. 3.3 D).

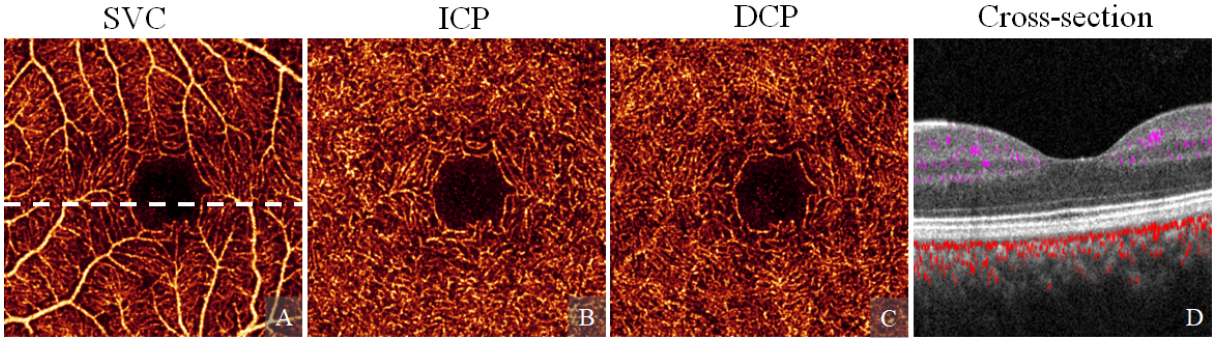


Figure 3.3: Signal attenuation-compensated projection-resolved OCTA (sacPR-OCTA) in a healthy eye. (A) Superficial vascular complex (SVC). (B) Intermediate capillary plexus (ICP). (C) Deep capillary plexus (DCP). (D) Cross-sectional structural OCT overlaid with the sacPR-OCTA color coded according to anatomic location (violet: inner retina, yellow: outer retina red: choroid, position was highlighted by dotted line in A). The results recapitulate known features of retinal anatomy from histology[2].

3.5.1 Evaluation on healthy eyes

In uncorrected original OCTA, projection artifacts appear as "tails" descending from vessels in cross-section (Fig. 3.4 F1), while vascular patterns in the SVC (Fig. 3.4 A1) are also visibly transposed to the ICP (Fig. 3.4 B1), DCP (Fig. 3.4 C1), outer retina (which is normally avascular;

Fig. 3.4 D1), and choriocapillaris (CC) (Fig. 3.4 E1). Comparing with the previous generation PR-OCTA algorithms (Fig. 3.4 A2-F2, A3-F3), the described sacPR-OCTA algorithm (Fig. 3.4 A4-F4) preserved more flow signal and shows more complete microvascular patterns in deeper slabs including the ICP(Fig. 3.4 B4), DCP(Fig. 3.4 C4) and CC(Fig. 3.4 E4), especially in the large vessel shadow graphic area, and also suppressed more projection artifacts showing a much cleaner outer retina angiogram(Fig. 3.4 D4). Moreover, the CC(Fig. 3.4 E4) is more even using sacPR-OCTA than original uncorrected OCTA(Fig. 3.4 E1),initial PR-OCTA(Fig. 3.4 E2)[72], and reflectance-based projection-resolved OCTA (rbPR-OCTA)(Fig. 3.4 E3)[73], which would benefit analysis exploring biomarkers in diseases associated with the CC.

A better algorithm should remove more projection artifacts and preserve more real flow signal. In uncorrected OCTA, projection artifacts are vascular patterns duplicated from anterior slabs. To evaluate the improvements quantitatively, we assessed 296 OCTA scans from 296 healthy eyes using the initial PR-OCTA[72], rbPR-OCTA[73] and sacPR-OCTA processing according to metrics: the vascular similarity between superficial and deeper slabs, vascular continuity, and residual artifacts strength (S_{RA}) in the outer retina.

(1) *Vascular similarity as a measurement of projection artifacts removal*

Vascular similarity was measured using the Pearson's correlation coefficient (r)[82] according to

$$r\left(I_{\mathrm{A}}, I_{\mathrm{B}}\right)=\frac{1}{N-1} \sum_{i=1}^{N}\left(\frac{I_A(i)-u_A}{\sigma_A}\right)\left(\frac{I_B(i)-u_B}{\sigma_B}\right) \tag{3.8}$$

where, i is the index of pixel, N is the total number of pixels, u_A and u_B are intensity average of objects A and B, respectively; σ_A and σ_B are standard deviation of objects A and B, respectively. Pearson correlation coefficient is bounded between -1 and 1, with a r value of -1 indicating perfect negative correlation, a r value of 0 indicating no correlation, and a r value of 1 indicating perfect correlation.

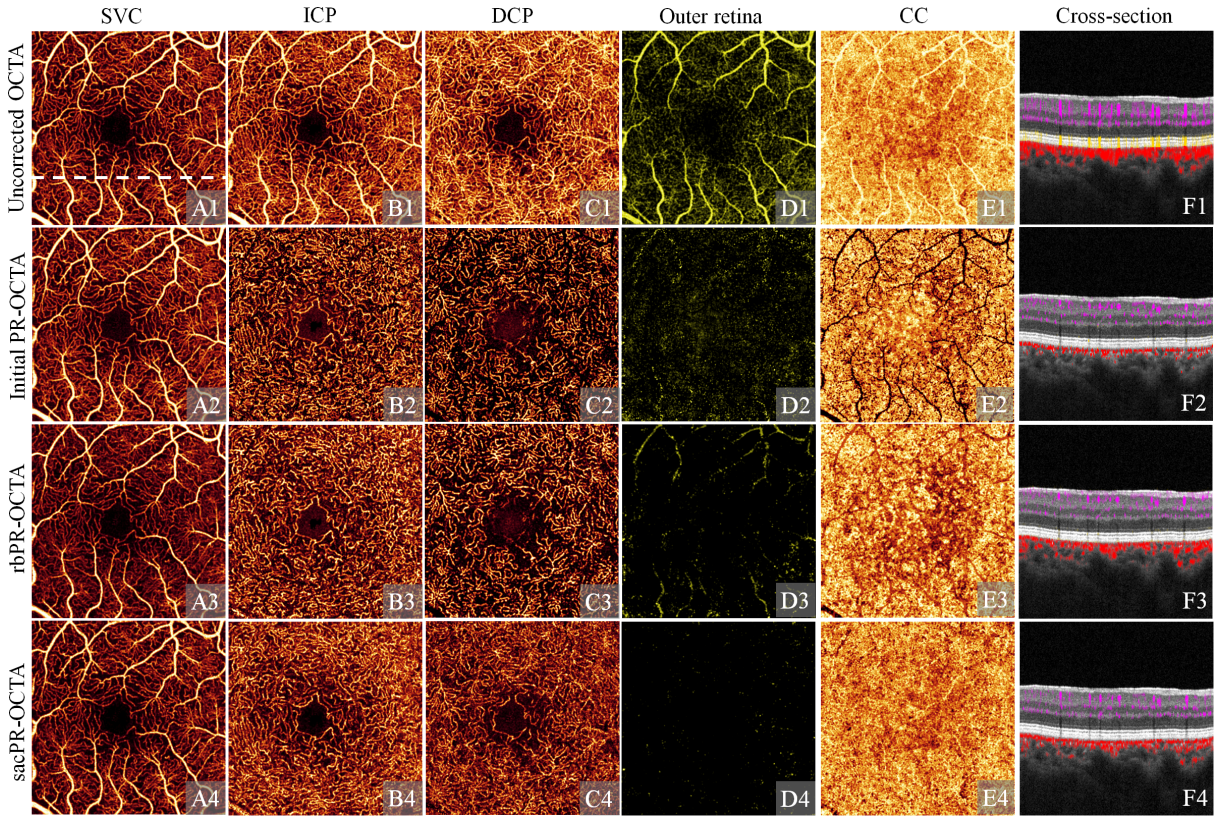


Figure 3.4: Algorithm comparison in a normal eye. The images include uncorrected optical coherence tomographic angiography (OCTA) (row 1), the initial projection-resolved OCTA (PR-OCTA) (row 2), reflectance-based projection-resolved OCTA (rbPR-OCTA) (row 3), and signal attenuation-compensated projection-resolved OCTA (sacPR-OCTA) algorithm (row 4). Column A-E: *En face* optical coherence tomography (OCT) angiogram of superficial vascular complex (SVC), intermediate capillary plexus (ICP), deep capillary plexus (DCP), outer retina and sub-macular choriocapillaris (CC). Column F: cross-sectional structural OCT overlaid with color coded flow signal (violet: inner retina, yellow: outer retina red: choroid) at the position indicated by the white dotted line A1. sacPR-OCTA removed more residual artifacts than the previous PR methods while maintaining vascular integrity (D), and the vessel tails (projection artifacts in uncorrected OCTA, F1) below the vessels in cross-section were replaced with the circles (F4). Large vessel artifacts are notable in the initial PR-OCTA method (E2), and flow magnitude are visually reduced in the rbPR-OCTA result. These over-processing artifacts are absent in the proposed sacPR-OCTA method (E4).

Table 3.1: Comparison among uncorrected optical coherence tomographic angiography (OCTA), initial projection-resolved OCTA (PR-OCTA), reflectance-based projection-resolved OCTA (rbPR-OCTA) and signal attenuation-compensated projection-resolved OCTA (sacPR-OCTA)on Pearson's correlation coefficient between the current and upper slabs.

	Uncorrected OCTA	Initial PR-OCTA	rbPR-OCTA	sacPR OCTA
ICP	0.70 ± 0.03	0.04 ± 0.09	0.21 ± 0.07	0.15 ± 0.06
DCP	0.53 ± 0.08	-0.11 ± 0.02	0.07 ± 0.08	0.16 ± 0.07

ICP:Intermediate capillary plexus, deep capillary plexus (DCP):Deep capillary plexus.

Pearson's correlation coefficient r measures the removal of duplicated vascular patterns in the deeper slabs. A r value close to 0 demonstrates better performance for removing the projection artifacts, a negative r which means bright voxels were replaced with 0, which is also artifactual

causing disrupted vascular integrity. Projection artifacts in the uncorrected OCTA produce a high r in the ICP and DCP (Table 3.1). Compared to the uncorrected OCTA, vascular correlation was significantly reduced (p<0.01, t-test) using the initial PR-OCTA, rbPR-OCTA, or sacPR-OCTA algorithm (Table 3.1). The initial PR-OCTA method produced low ICP and DCP correlations; however, the negative r in the DCP ($r = -0.11$) indicates that the *in-situ* flows were over processed and produced shadows in deeper slabs[72]. This effect was reduced in the rbPR-OCTA method. Compared to rbPR-OCTA, the sacPR-OCTA showed significant improvements in the ICP ($p < 0.01$, t-test). While the r of sacPR-OCTA was slightly higher than rbPR-OCTA in the DCP ($p < 0.01$, t-test), the duplicated vascular patterns were also largely removed ($r = 0.16$). While the rbPR-OCTA result obtained a lower similarity in the DCP, this does not necessarily indicate that the sacPR-OCTA method removed fewer projection artifacts. In fact, we expect some similarity between anterior and posterior retinal layers because some flow values will be similar. The very low similarity in rbPR-OCTA might indicate that this region was overprocessed, with *in-situ* as well as artifactual flow removed. Indeed, visual inspection indicates that the sacPR-OCTA approach did not yield more residual artifacts, while fragmented vessels can be seen in the initial PR-OCTA and rbPR-OCTA solutions (Fig. 3.4).

(2) *Vascular integrity and continuity as measurements of in situ flows preservation*

We measured vascular integrity by calculating the vessel density (VD) defined by the ratio of the vascular to avascular pixels. Vascular continuity (VC) was measured by vascular skeleton connectivity that was defined as the ratio of the number of connected skeletonized pixels (more than 5 pixels connected if their edges or corners touch) to the total number of skeletonized pixels. The vascular binary mask was generated after application of the Frangi vesselness filter[80] which has been frequently used for the vessel density quantification on OCTA. This filter is able to enhance the vasculature and suppress the background noise according to the local contrast measured by using Hessian matrix (Fig. 3.2 E1). And then the vascular skeleton mask was obtained using the thinning methodology algorithm[83, 84]. For fair comparison, the dynamic range of the OCT angiograms was truncated and normalized to the interval $[0, 1]$ before applying the vesselness filter according to

$$I_{\text{nor}} = \begin{cases} 0, & I \leq I_{\text{min}} \\ \dfrac{I - I \leq I_{\text{min}}}{I_{\text{max}} - I_{\text{min}}}, & I_{\text{min}} < I < I_{\text{max}} \\ 1, & I \geq I_{\text{max}} \end{cases} \tag{3.9}$$

where, I_{min} and I_{max} are the 2.5 and 97.5 percentiles of elements in input I, respectively.

The described sacPR-OCTA algorithm showed significant improvements (Table 3.2) in VD in deeper slabs ($p < 0.01$, t-test), which indicated the sacPR-OCTA preserved more *in situ* flow. Of course, residual projection artifacts would also increase VD. However, both visual inspection and the low Pearson correlation coefficient (Table 3.1) in the sacPR-OCTA method indicate that this was not the case; the difference in VD between rbPR-OCTA and sacPR-OCTA appears to be caused by the improved preservation of *in-situ* flow with the sacPR-OCTA approach. The higher VC indicates better performance of the sacPR-OCTA approach for preserving the vascular integrity (Table 3.2).

Table 3.2: Comparison among uncorrected optical coherence tomographic angiography (OCTA), initial projection-resolved OCTA (PR-OCTA), reflectance-based projection-resolved OCTA (rbPR-OCTA), and signal attenuation-compensated projection-resolved OCTA (sacPR-OCTA) on vascular integrity and continuity.

	ICP		DCP	
	VD	VC	VD	VC
Uncorrected OCTA	0.55 ± 0.04	0.99 ± 0.00	0.57 ± 0.03	0.99 ± 0.00
Initial PR-OCTA	0.39 ± 0.03	0.95 ± 0.01	0.37 ± 0.04	0.94 ± 0.02
rbPR-OCTA	0.43 ± 0.08	0.98 ± 0.01	0.45 ± 0.06	0.97 ± 0.00
sacPR-OCTA	0.55 ± 0.02	0.98 ± 0.00	0.56 ± 0.02	0.98 ± 0.01

ICP:Intermediate capillary plexus,DCP:Deep capillary plexus, VD:Vessel density, VC:Vessel continuity.

(3) *Remaining projection artifacts strength in the outer retina*

Remaining projection artifact strength (S_{RA}) in the outer retina, which is important for the accurate detection and quantification of choroidal neovascularization (CNV) in normal avascular outer retina, was evaluated by

$$S_{\text{RA}} = \frac{M_{\text{outer}} + 3 \times \sigma_{\text{outer}}}{M_{\text{inner}} + 3 \times \sigma_{\text{inner}}} \tag{3.10}$$

where M_{outer} and M_{outer} are the mean and σ_{outer} and σ_{inner} are standard deviation in outer and inner retina, respectively.

The low S_{RA} demonstrated that both the rbPR-OCTA and sacPR-OCTA was able to remove the projection artifacts on healthy eyes (Table 3.3).

Table 3.3: Comparison among uncorrected optical coherence tomographic angiography (OCTA),initial projection-resolved OCTA (PR-OCTA), reflectance-based projection-resolved OCTA (rbPR-OCTA) and signal attenuation-compensated projection-resolved OCTA (sacPR-OCTA) on residual projection artifacts in outer retina

Uncorrected OCTA	Initital PR-OCTA	rbPR-OCTA	sacPR-OCTA
0.94 ± 0.11	0.62 ± 0.19	0.32 ± 0.08	0.31 ± 0.07

(3) *Evaluation of projection artifacts removal beneath large vessels*

Large vessels' projection artifacts are more visually obvious due to the co-occurring shadow artifacts caused by the same vessels. These features make projection artifact removal more challenging under large vessels. To evaluate the performance, Pearson's correlation coefficient r and VD were used to evaluate the performance beneath large vessels.

Table 3.4: Correlation and vessel density (VD) between flow underneath large vessels in the uncorrected optical coherence tomographic angiography (OCTA), initial projection-resolved OCTA (PR-OCTA), reflectance-based projection-resolved OCTA (rbPR-OCTA) and signal attenuation-compensated projection-resolved OCTA (sacPR-OCTA)on vessel density

	ICP		DCP	
	r^+	VD$^+$	r^+	VD$^+$
Uncorrected OCTA	0.75 ± 0.04	0.80 ± 0.02	0.36 ± 0.12	0.76 ± 0.04
Initial PR-OCTA	-0.12 ± 0.09	0.44 ± 0.08	-0.33 ± 0.05	0.28 ± 0.06
rbPR-OCTA	-0.02 ± 0.11	0.63 ± 0.09	-0.04 ± 0.10	0.48 ± 0.09
sacPR-OCTA	0.00 ± 0.07	0.65 ± 0.03	0.03 ± 0.09	0.62 ± 0.05

ICP:Intermediate capillary plexus,deep capillary plexus (DCP):Deep capillary plexus, $+$: Metrics were measured in the area under the larger vessels.

In the uncorrected OCTA with projection artifacts correlation r is larger in both the ICP and DCP (Table 3.4). The higher correlation between the ICP and the SVC also indicates projection artifacts are stronger in the ICP (Fig. 3.4 B1) than the DCP (Fig. 3.4 C1). The negative correlation of the initial PR-OCTA indicates that the *in situ* flow is overprocessed. Both the rbPR-OCTA and sacPR-OCTA algorithm produced low correlation, which indicates that projection artifacts have mostly been removed in the deep slabs (Table 3.4). However, the correlation is much lower and VD

is much higher with sacPR-OCTA ($p < 0.01$), which is due to the fact that sacPR-OCTA preserved more *in situ* flow signals.

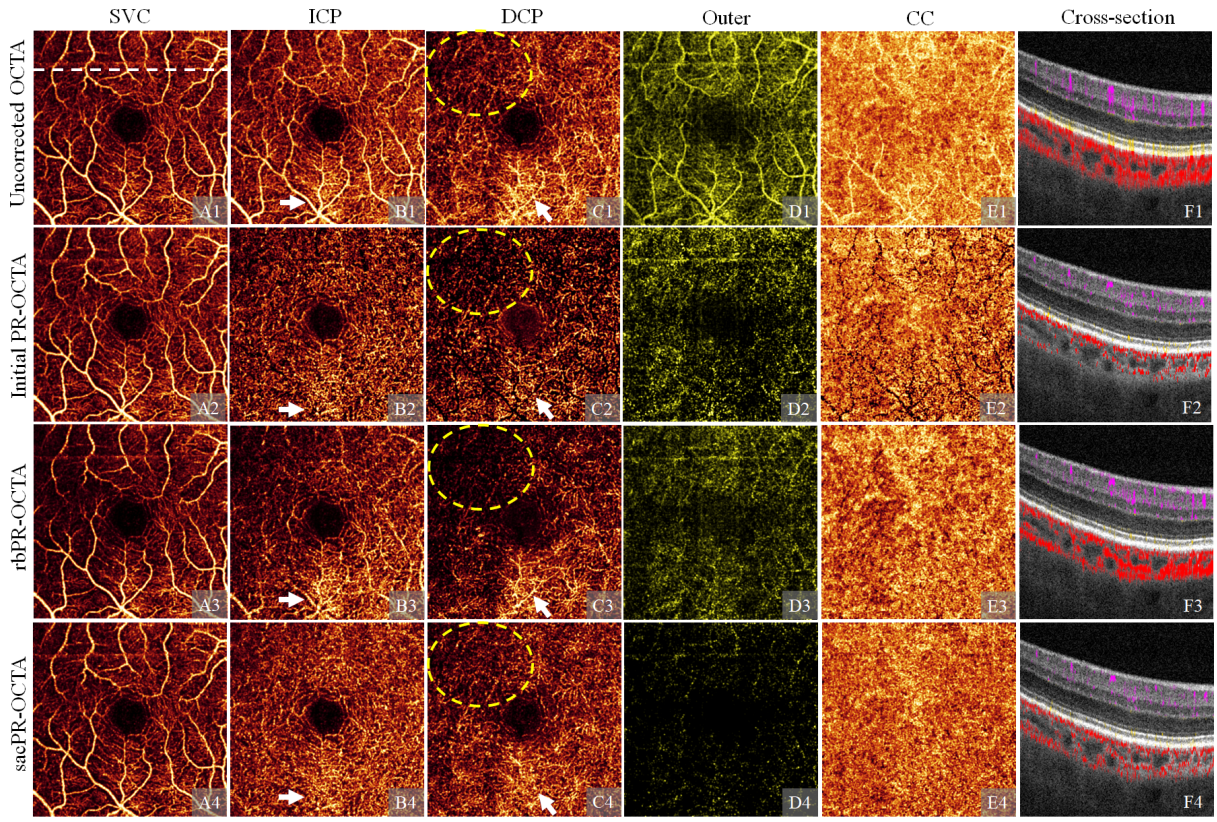


Figure 3.5: A comparison of projection-resolved OCTA (PR-OCTA) algorithms on a scan with shadow artifacts. Row 1-4: Uncorrected optical coherence tomographic angiography (OCTA), initial projection-resolved OCTA (PR-OCTA), reflectance-based projection-resolved OCTA (rbPR-OCTA), and signal attenuation-compensated projection-resolved OCTA (sacPR-OCTA). Column A-E are *en face* angiograms of the superficial vascular complex (SVC), intermediate capillary plexus (ICP), deep capillary plexus (DCP), outer retina, and sub-macular choriocapillaris (CC). Colum F are cross-sectional structural optical coherence tomography (OCT) overlaid with color coded flow signal (violet: inner retina, yellow: outer retina red: choroid). The proposed sacPR-OCTA algorithms preserved more *in-situ* flow signal in the shadowing area (highlighted by yellow dotted ellipses) and suppressed more projection artifacts (highlighted by white arrows).

3.5.2 Preservation on challenging scan affected by shadow artifacts

Shadow artifacts are very common in real-world clinical data. The *in situ* flow signal is also attenuated in shadowed areas (Fig. 3.5 C1), which makes it more difficult to remove projection artifacts in deeper slabs. The initial PR-OCTA method over-processed the real slow signal and generated large vessel shadows in ICP (Fig. 3.5 B2) and DCP (Fig. 3.5 C2). Since the rbPR-OCTA algorithm relies on vascular contrast in structural OCT, which can disappear in shadow affected regions, it can over-process both the projection artifacts and real flow signal in these regions (Fig. 3.5

C3). The sacPR-OCTA algorithm does not suffer from this limitation, as the flows were processed by A-line instead of by region, and so more capillaries in both ICP (Fig. 3.5 B4) and DCP (Fig. 3.5 C4) are preserved. Moreover, sacPR-OCTA showed better performance for removing projection artifacts (Fig. 3.5 C4) that were not removed in rbPR-OCTA (Fig. 3.5 C3), as well as producing a clearer outer retina (Fig. 3.5 D4). sacPR-OCTA also generated more even appearing CC in which more flow signals under large vessels were preserved (Fig. 3.5 E4). These same regions were over-processed by initial PR-OCTA (Fig. 3.5 E2) and rbPR-OCTA (Fig. 3.5 E3).

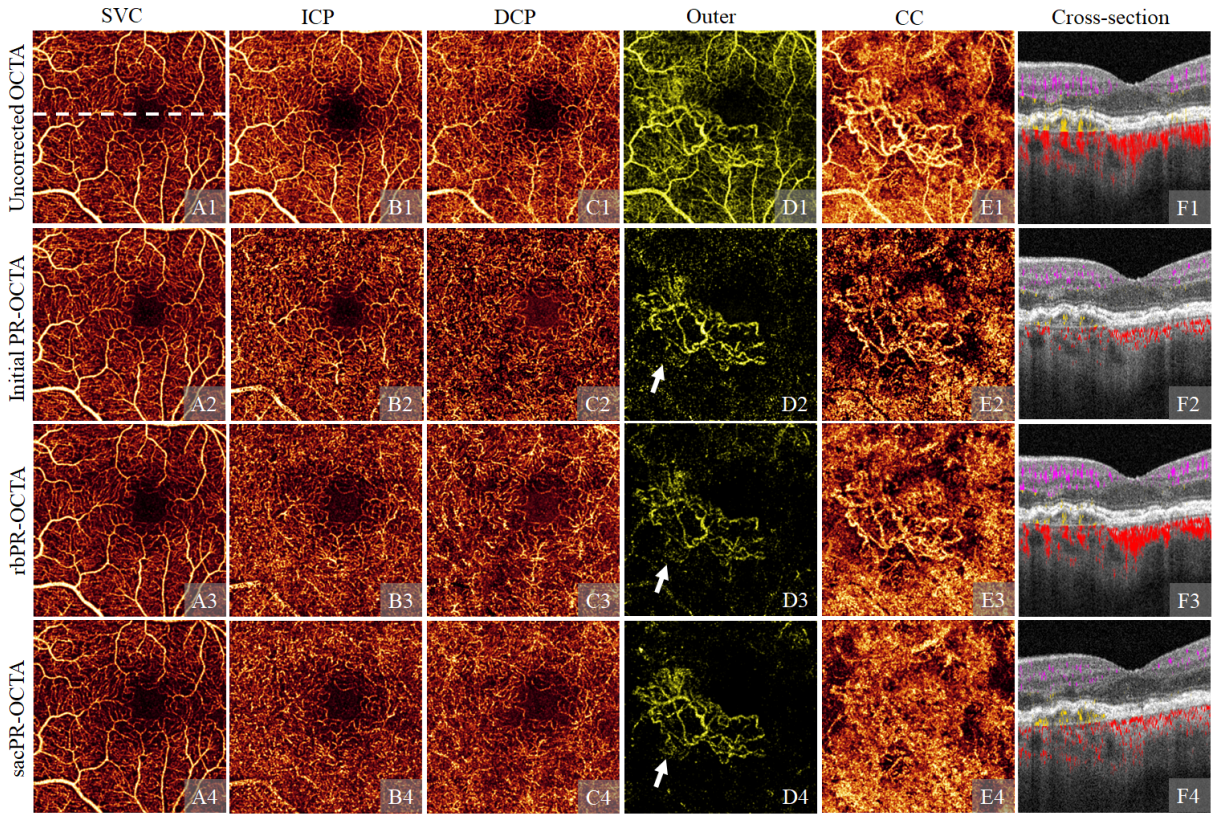


Figure 3.6: A comparison of projection-resolved OCTA (PR-OCTA) algorithms on the neovascular age-related macular degeneration (AMD) with choroidal neovascularization (CNV). Row 1-4: Uncorrected, initial PR-OCTA, reflectance-based projection-resolved OCTA (rbPR-OCTA) and signal attenuation-compensated projection-resolved OCTA (sacPR-OCTA). Column A-E are *en face* angiograms of the superficial vascular complex (SVC), intermediate capillary plexus (ICP), deep capillary plexus (DCP), outer retina and sub-macular choriocapillaris (CC). The proposed sacPR-OCTA algorithms preserved more *in-situ* CNV signals (highlighted by white arrows).

3.5.3 Preservation on choroidal neovascularization

Choroidal neovascularization (CNV) consists of abnormal vessels in the outer retina. It results in exudation, hemorrhage, and fibrosis formation, each of which constitute a major threat of serious

vision loss[85, 86]. OCTA as originally proposed was capable of detecting CNV, but doing so was difficult due to the presence of the strongly reflecting retinal pigment epithelium nearby, which produces strong projection artifacts (Fig. 3.6 D1)[70]. These artifacts are strong enough that it is simple to misinterpret some as CNV, and they can further cloak the real CNV vessels in spurious signal. Quantification of the lesion is virtually impossible under these conditions, but accurate quantification and monitoring of CNV dynamics is a clinical priority. The initial PR-OCTA method (Fig. 3.6 D2) and rbPR-OCTA (Fig. 3.6 D3) algorithms removed the strong projection artifacts, but remaining background can still interfere with CNV quantification. Moreover, the projection artifacts from the CNV itself are visible in the CC (Fig. 3.6 E1) in the uncorrected , initial PR-OCTA (Fig.6 E2) and rbPR-OCTA results (Fig. 3.6 E3). The proposed sacPR-OCTA algorithm removed the projection in inner retinal slabs (Fig. 3.6 A4-C4) and suppressed more background noise in the outer retina (Fig. 3.6 D4), as well as preserved more real CNV signals (Fig. 3.6 D4). The projected CNV vascular patterns were also removed in CC (Fig. 3.6 E4) and large vessel shadows cleaned (Fig. 3.6 E2).

3.5.4 Platform independence

The generalizability of the algorithm is important for applying to different OCTA system. Since the proposed algorithm processed the flow signals on each A-line, it is theoretically independent of OCTA devices specifics and the image resolution. We tested platform and image resolution independence on the Zeiss angioplex OCTA, the latest Optovue Solix OCTA, and our customer designed OCTA devices by simply adjusting three parameters: α, β, and d_{max} in equation (3.7).

The proposed model could remove the projections showing clear vasculature in deeper slabs (ICP&DCP, Fig. 3.7 B&C), and the tailed projection artifacts (Fig. 3.7 D1) were suppressed in voxel (Fig. 3.7 D2). Pathological non-perfusion area (NPA) and dilated vessel were also preserved (Fig. 3.7 B2&C2).

The faster imaging speed on Optovue Solix device allows to acquire the image in a wider area with dense A-lines. The Solix macular $9 \times 9 - mm$ has 600 A-lines in each B-scan and 600 B-scans in each volume. A wider imaging area was able to detect neovascularization (NV) in the vitreous in

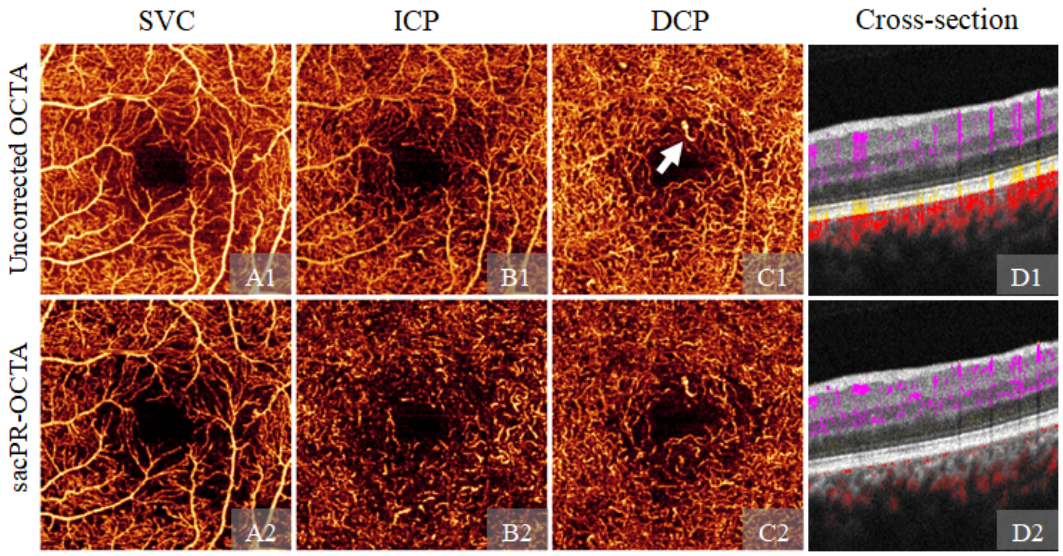


Figure 3.7: Signal attenuation-compensated projection-resolved (sacPR-OCTA) on angioplex $3 \times 3 - mm$ scan. Row 1-2: Original uncorrected optical coherence tomographic angiography (OCTA) and sacPR-OCTA. Column A-C are *en face* angiograms of the superficial vascular complex (SVC), intermediate capillary plexus (ICP), deep capillary plexus (DCP). Colum D is cross-sectional structural optical coherence tomography (OCT) overlaid with color coded flow signals (violet: inner retina, yellow: outer retina red: choroid). The white arrow highlighted the dilated vessel in DCP

the superior disc that cannot be caught in often-used $6 \times 6 - mm$ scans. The dense A-lines showed distinct NV vessels (Fig. 3.8 A1); however, the projection artifacts blocked capillary dropout in the SVC (Fig. 3.8 B1). The proposed algorithm was able to preserve the real NV flow and suppress the projection artifacts, revealing distinct twisted vessels in the SVC (Fig. 3.8 B2), as well as the connection of NV to feeder vessels in cross-section (Fig. 3.8 E2).

3.6 Discussion and conclusion

In this study, we developed a novel sacPR-OCTA algorithm that removes flow projection artifacts and preserves *in situ* flow signals in OCTA. The sacPR-OCTA algorithm suppressed projection artifacts at the voxel-level, preserved more flow signal, and could benefit automatic vascular disease-related quantifications such as vessel density, non-perfusion area and CNV detection.

Several innovative features contributed to our approach's reliable performance. *First*, the theoretical foundation was improved by considering not just the reflectivity of the tissue in which the artifacts originate but also attenuation with increasing distance from the signal-producing *in situ* flow. *Second*, by using the theoretical form to fit the flow signal across the whole volume, our

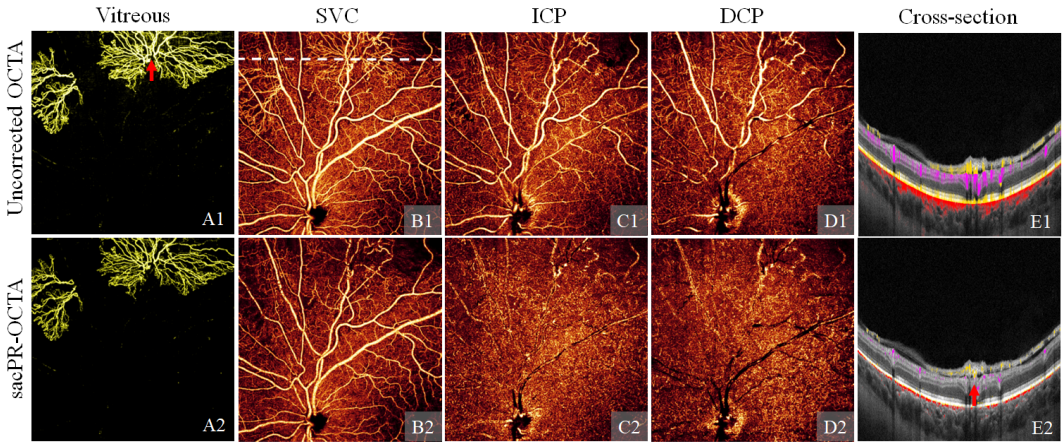


Figure 3.8: Signal attenuation-compensated projection-resolved optical coherence tomographic angiography (OCTA) (sacPR-OCTA) on Solix 9×9-mm scan. Row 1-2: Uncorrected optical coherence tomographic angiography (OCTA) and signal attenuation-compensated projection-resolved OCTA (sacPR-OCTA). Column A-C are *en face* angiograms of the superficial vascular complex (SVC), intermediate capillary plexus (ICP), deep capillary plexus (DCP). Colum D is cross-sectional structural optical coherence tomography (OCT) overlaid with color coded flow signals (gold: vitreous, violet: inner retina, yellow: outer retina red: choroid. The red arrow highlights the connection between the neovascularization (NV) and feeder vessel. sacPR-OCTA removed projection artifacts in this wide field of view showing the optic nerve head in a newly released commercial device.

algorithm has the added advantage of enhancing flow signal in regions beneath large vessels which are under/over-processed in other projection resolved algorithms. For the same reason our algorithm also better preserved *in situ* flow in regions affected by shadow artifacts. *Third*, device and scan size independence imply that our method is generalizable.

A reliable PR-OCTA algorithm is expected to have the capability to remove projection artifacts and preserve *in situ* flow. Four metrics, including Pearson's correlation coefficient, vessel density, vessel continuity, and remaining artifacts were used to evaluate the performance of the sacPR-OCTA algorithm, since any one of them could not thoroughly describe performance. Overprocessing can decrease correlation, while projection artifacts can increase vessel density, continuity in the inner retina. There is not a straightforward answer as to whether one of these metrics should be independently optimized. For example, deeper slabs could be made to correlate less with anterior by removing more *in situ* flow, so less correlated slabs cannot be a direct indicator of performance. Instead, only by combining these three metrics (correlation, vessel density, vessel continuity, remaining artifacts) can we obtain a complete picture of performance: the sacPR-OCTA algorithm removed more projection artifacts (lower correlation and remaining artifact magnitude) while preserving more *in situ* flow (higher vessel density and connectivity).

Moreover, sacPR-OCTA demonstrated cleaner backgrounds in outer retina on scans affected by projection artifacts and pathological changes that were frequently observed in the clinic, which demonstrates that sacPR-OCTA was more reliable to visualize and provide precise quantitative measurements of biomarkers for clinical application. For example, the sacPR-OCTA enables us to visualize macular ischemia and quantify non-perfusion area in the multiple specific anatomic slabs[53, 58, 67] and highly sensitive *in situ* flow preservation can provide more accurate quantification of CNV lesions[65, 70].

The relationship between signal attenuation and reflectance and optical distance is complex. In our implementation, the complex dynamics were simplified using a linear model, which is a limitation of the proposed sacPR-OCTA. In the current case, the linear parameters can be adjusted individually to acquire the best PR-OCTA data. A non-linear model may be able to further improve PR-OCTA.

4 Robust non-perfusion area Detection in three retinal plexuses using convolutional neural network in optical coherence tomographic angiography

4.1 Abstract

Non-perfusion area (NPA) is a quantitative biomarker useful for characterizing ischemia in diabetic retinopathy (DR). Projection-resolved optical coherence tomographic angiography (PR-OCTA) allows visualization of retinal capillaries and quantify NPA in individual plexuses. However, poor scan quality can make current NPA detection algorithms unreliable and inaccurate. In this work, we present a robust NPA detection algorithm using convolutional neural network (CNN). By merging information from optical coherence tomography (OCT) angiograms and OCT reflectance images, the CNN could exclude signal reduction and motion artifacts and detect the avascular features from local to global with the resolution preserved. Across a wide range of signal strength indices, and on both healthy and DR eyes, the algorithm achieved high accuracy and repeatability.

4.2 Introduction

Diabetic retinopathy (DR) is a major cause of vision loss worldwide[87, 88, 89, 90, 91]. Diabetic macular ischemia is an important clinical feature in DR [67, 92, 93, 94], with prognostic value in DR[95, 96, 97]. An objective evaluation of macular ischemia has become more practical with optical coherence tomographic angiography (OCTA)[58, 67, 98], which captures capillary level-detail of macular vasculature in three-dimensional (3D) non-invasively.

More recently, we developed a projection-resolved OCTA (PR-OCTA) algorithm[72, 73, 99] that suppresses projection artifacts on both *en face* and cross-sectional angiograms and enhances depth resolution of vascular networks[67, 94]. By using PR-OCTA, it is possible to acquire accurate, detailed images not only of the superficial vascular complex (SVC) but also the intermediate capillary plexus (ICP) and deep capillary plexus (DCP). Recent work indicates that an evaluation of the individual plexuses provides a superior diagnostic accuracy in DR[59, 67, 94, 100].

This work has been published in Biomedical Optics Express: Jie Wang, Tristan T. Hormel, Qisheng You, Yukun Guo, Xiaogang Wang, Liu Chen, Thomas S. Hwang, and Yali Jia, "Robust non-perfusion area detection in three retinal plexuses using convolutional neural network in OCT angiography," Biomed. Opt. Express 11, 330-345 (2020).

However, automated image analysis can yield incorrect estimations of NPA when the images are compromised by poor scan quality, motion, or signal reduction artifacts. Our recent progress on detecting NPA on $6 \times 6mm^2$ SVC angiograms using a customized network[54, 101]. Despite this preliminary promise, it is more challenging to detect NPA in the ICP and DCP since these angiograms are more susceptible to signal reduction and motion artifacts. With light propagating deeper, the signal strength would be attenuated, the signal to noise ratio might be decreased. Although projection artifacts were suppressed by our prior work, the discontinuity of vasculature caused by superficial vascular shadow is still very obvious, which makes the NPA detection more challenging. Therefore, a robust NPA detection platform is essential to investigate the pathological effects on ICP and DCP.

In this work we present a robust NPA detection algorithm using a CNN that, regardless of image quality, is able to detect NPA in three retinal plexuses by accurately distinguishing decreased flow signal from nonperfusion from artifacts caused by signal reduction and motion artifacts.

4.3 Dataset

OCTA scans were collected in Casey Eye Institute, Oregon Health & Science University, Portland, OR, USA and Shanxi Eye Hospital, Taiyuan, Shanxi, PR China. The study was conducted in compliance with the Declaration of Helsinki.

Participants with healthy eyes and patients diagnosed with DR were scanned using a $70kHz$ commercial OCTA system (RTVue-XR; Optovue, Fremont, CA) with a central wavelength of 840nm. The eyes were scanned using a $3 \times 3mm^2$ macular scan pattern. There were 304 A-lines in each B-scan and 304 B-scans in each volumetric scan. B-scans were repeated two times at the same location to produce an OCTA volume, and retinal blood flows were detected using the commercial split-spectrum amplitude decorrelation angiography (SSADA) algorithm[43]. One X-fast and one Y-fast scan were obtained and registered to suppress motion artifacts[76].

For data preprocessing, retinal layers were segmented by a directional graph search algorithm incorporated in our in-house COOL-ART software for OCTA image processing, and segmenta-

tion errors were corrected manually on challenging scans (Fig. 4.1A)[1, 55]. The PR-OCTA algorithm[73] removed projection artifacts and visualized retinal capillary plexuses in three distinct slabs located at different depths (Fig. 4.1B-E)[9].

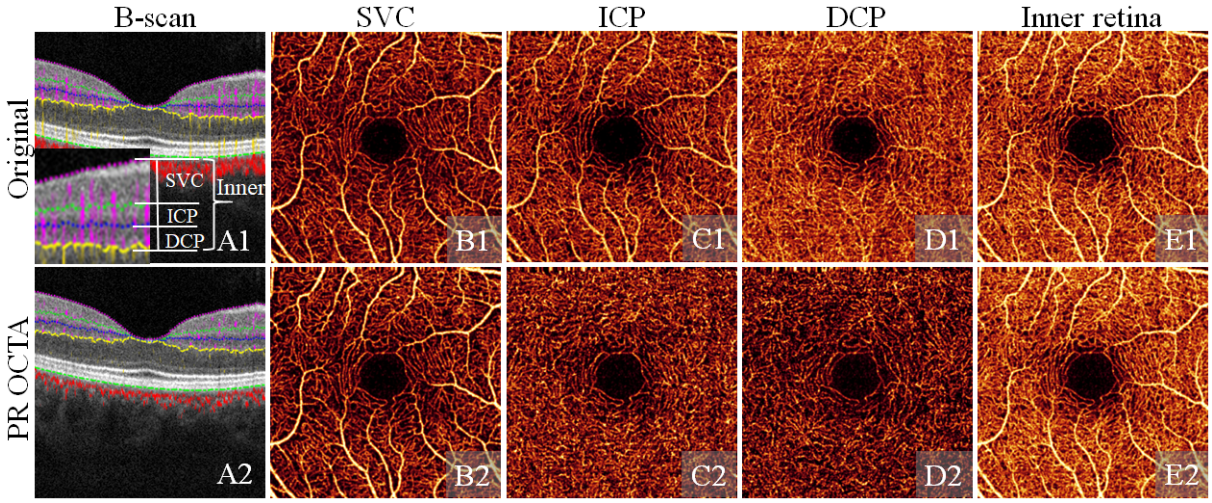


Figure 4.1: Projection-resolved angiograms (bottom row) compared to original OCTA images (top row). (A), Cross-sectional structural optical coherence tomography (OCT) scans, with inner retinal flow signal overlaid in violet and choriocapillaris (CC) flow in red. Remaining columns are *en face* projections of (B), superficial vascular complex (SVC):inner 80% of the ganglion cell complex (GCC); (C), intermediate capillary plexus (ICP):outer 20% of the GCC and inner 50% of the inner nuclear layer (INL); (D), deep capillary plexus (DCP): outer 50% of the INL and outer plexiform layer (OPL).

4.4 Non-perfusion area Detection using a convolutional neural network

4.4.1 Artifact included challenges in detecting non-perfusion area

Signal reduction is one of the major challenges for NPA detection. It is mainly caused by two factors: 1. shadow artifacts caused by vitreous opacity or vignetting; and 2. Defocus artifacts caused by the quality of focusing, astigmatism, and aberrations. In the view of optics, shadow artifacts can be explained by signal attenuation below strongly absorbing or scattering obstructions, and present similar visual characteristics as NPA in that no vessels or capillaries appear in the affected area. This poses a challenge for machine learning methods. On defocused scans, not only is flow signal reduced, but NPA boundaries are blurred, which increases the difficulty of identifying small NPA.

Eye motion artifacts are the other major challenge. They include microsaccadic and bulk motion artifacts. Miscrosaccadic artifacts manifest as bright stripes with high flow value on angiograms, and can cause under-segmentation when they happen to fall on NPA. Bulk motion artifacts have

similar signal strength to capillaries, and can entail minimal contrast between NPA and vascular areas. In particular, they make calculating a self-adapted thresholding map to detect the NPA area challenging.

4.4.2 Detecting non-perfusion area using convolutional neural network

Regardless of the causes, a key challenge for accurate NPA detection is differentiating signal loss due to artifacts from true NPA. We hypothesize that the *en face* mean projection of OCT reflectance, along with the corresponding OCTA angiograms, can be used for this purpose. The key insight is that true NPA should manifest in only the OCTA signal, while signal loss due to artifacts will affect both the structural and angiographic signal simultaneously. In this study, the goal was to reliably segment NPA in three retinal plexuses. Input to the CNN then consisted of the slab-specific mean projection of angiographic and structural images. The mean projection of the OCT reflectance of the entire inner retina is also included because it could help distinguish reduced tissue reflectivity (e.g. due to fluid accumulation) from shadow.

In common CNN architecture, pooling layers are repeated with convolution layers. The replicated pooling layers compress features, enabling detection across multiple scales. However, with capillary widths of only 1-5 pixels, the feature resolution reduction caused by replicated pooling layers is unacceptable since it may completely eliminate capillaries from being considered. Hence, we replaced most pooling layers with atrous kernels, which detect and extract multi-scale features while maintaining feature resolution.

Atrous kernels are generated by dilating the kernel with zeros. The dilation size refers to the distance between the kernel elements. A dilation rate of one is the original 3×3 size; while a dilation rate of two adds one zero among the kernel elements, and a dilation rate of three is adding two zeros among the kernel elements (Fig. 4.2). The overall kernel size increases with the number of zeros included, as does the distance between the kernel elements. As illustrated in Fig. 4.2, the result is that as kernel size increases the field of view for feature extraction grows, but critically the computational cost is equivalent across each atrous dilation rate.

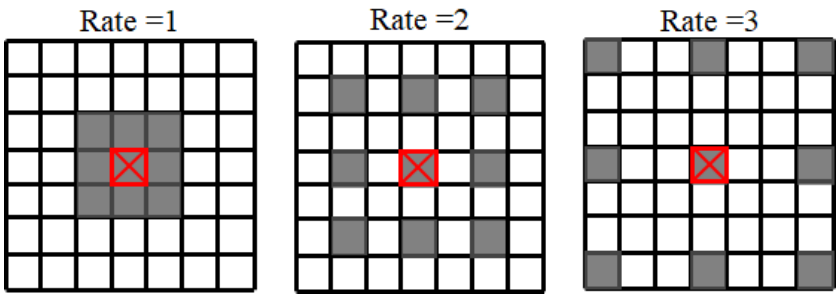


Figure 4.2: Atrous kernels with rate = 1, 2 and 3. The red square is the center of kernel.

The CNN architecture designed by this study is shown in Fig. 4.3. During encoding, atrous kernels were applied in convolution layers. In deeper layers of the network the feature dimension increases. During decoding, the U-net-like architecture concatenated raw features from the encoding. To detect variously sized NPAs, atrous kernels were also used to parallelize feature decoding and extract the multi-scale features for decision-making. The softmax activation function generated the NPA probability maps as output. Pixels with probability greater than 0.5 were labeled as NPA.

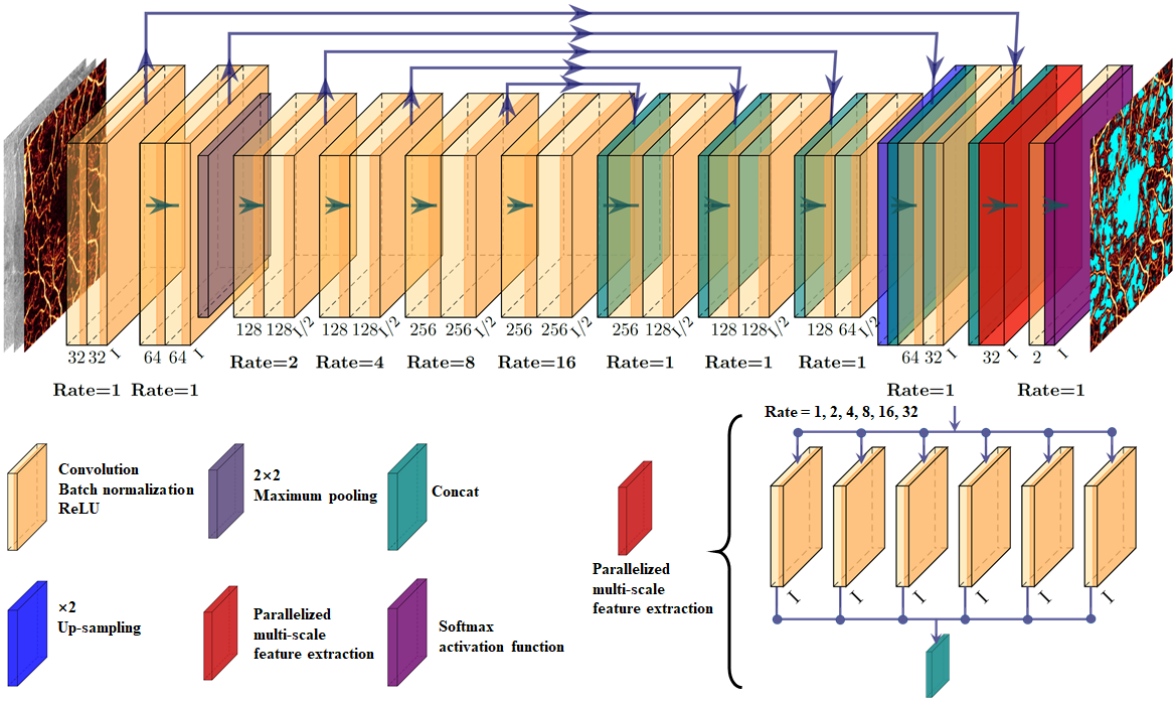


Figure 4.3: CNN architecture for NPA detection. The numbers below each convolution block is the number of kernels for each convolution layer, atrous dilation rate was demonstrated below

4.4.3 Training

(1)*Subjects and ground truth generation*

The data used in this study consisted of a total 1428 scans acquired from both eyes of 428 participants, including 122 normal controls, 56 diabetics without retinopathy, 118 with mild to moderate DR, and 132 with severe DR. DR scans included 2 repeat scans within each visit and $2-3$ follow-up visits per patient. We reserved 110 cases for testing, and used the remainder for training. 10 healthy eyes were also scanned to generate scans with manufactured reduced signal strength artifacts for training and testing the robustness of the proposed algorithm in low-quality images. We manufactured scan quality reduction by placing neutral density filters in the beam path to simulate shadow artifacts and adjusted the defocus parameter on the AngioVue software manually to simulate defocus artifacts. The optical density filters ranged from 0.1 to 0.6, and the defocus ranged from -0.5 to -4.5 diopters related to the baseline which was scanned without neutral density filters and with optimal focus. Five of ten manufactured signal reduction scan sets were reserved for validation.

Certified graders manually delineated the ground truth NPA and a retinal specialist reviewed the results on our in-house software which was equipped with a semi-automated NPA detection algorithm (Fig. 4.4). Shadow graphics were identified on the both inner retinal slab (Fig. 4.4 bottom left) and plexus-specific *en face* reflectance images (Fig. 4.4 bottom right). The manual correction function allowed graders to remove the over-detected NPA in shadow area, and delineate the under-detected NPA area with a stylus or mouse, which a region growing software then would fill this area automatically. To generate reliable ground truth, three graders were manually defined the NPA, and a majority-vote scheme was applied that the NPA was graded by two more graders in pixel-level(Fig. 4.4B1-B3).

(2) *Implementation* The training loss was calculated by the cross-entropy function with $L2$ regularization to prevent overfitting:

$$J_{L2} = -\sum_{i=1}^{N} y_i \cdot log(p_i) + \alpha \sum w^T w \tag{4.1}$$

where y_i is the label, p_i is the output from a softmax activation function, N is the number of classes, w is vector containing the weights of the convolution kernels, and α is the $L2$ regularization weight.

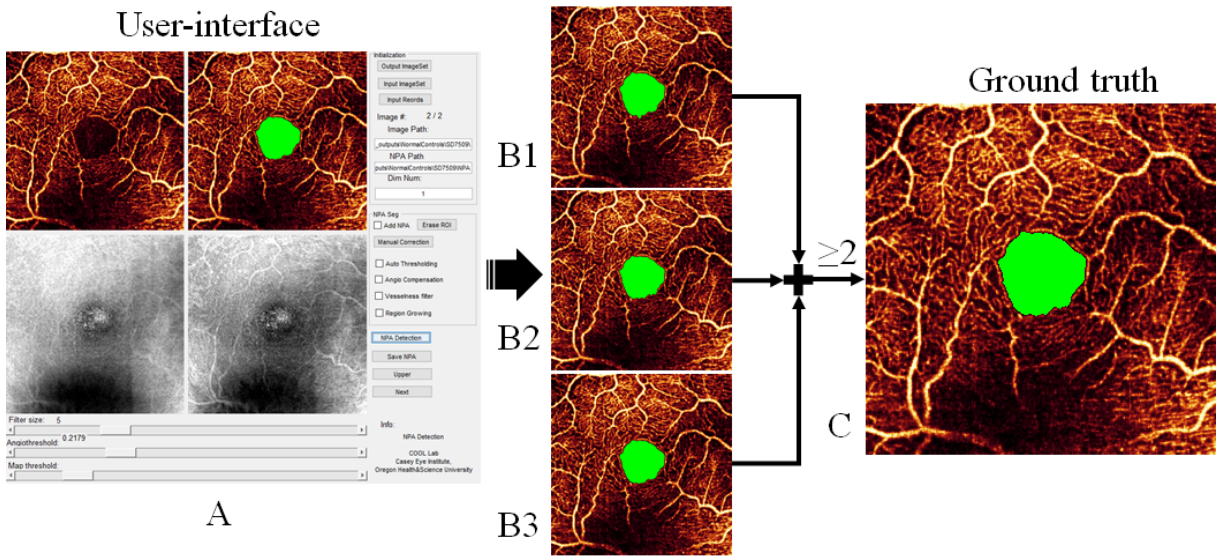


Figure 4.4: Ground truth generation. (A), In-house graphical user interface software; (B), manually graded NPA overlaid on the superficial vascular complex angiogram; (C), ground truth segmentation determined by majority vote from the three manually segmented images in (B).

During the training, the Adam optimizer was used to accelerate convergence. Batch normalization was also applied to help prevent over-fitting and improve generalization capability. The learning rate was getting smaller with training to achieve the optimal parameters.

The designed CNN was implemented using Tensor Flow with an intel $i7-6800K@3.40GHZ$, DDR4 $128GB$ RAM, and Nvidia $2080Ti$ graphics card (4352 CUDA cores, $1635MHZ$ Boost clock, $11GB$ GDDR6 memory).

4.5 Results

4.5.1 Effect of signal attenuation

As illustrated by Fig. 4.5, neutral density filters attenuated the brightness of OCT angiograms, but the vasculature was sharply defined because the laser beam was still focused on the retina (Fig. 4.5B). This can be qualified by the signal strength index (SSI), a proprietary measurement provided by averaging the logarithmic reflectance of tissue volume and normalizing the value in $[0,\ 100]$[102]. SSI relates to overall image brightness, a proxy for image quality. Defocus, however, not only reduces SSI but blurs the entire angiogram (Fig. 4.5C). As demonstrated in Fig. 4.5, the

effects of the neutral density filter and defocus are different, however in neither case are additional imaging artifacts introduced by the manufactured signal attenuation.

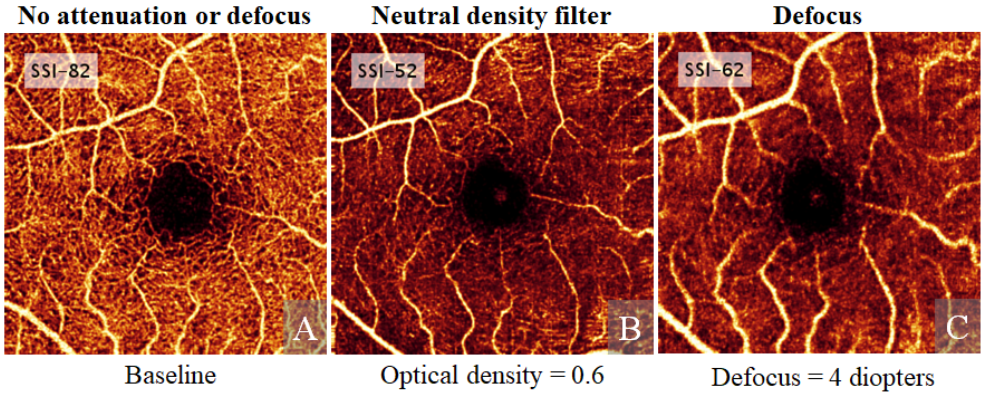


Figure 4.5: Manufactured signal strength attenuation on inner retina angiograms. (A), Uninhibited scan; (B), scan captured with a 0.6 neutral density filter; (C), scan captured with 4 diopters of defocus. signal strength index (SSI).

To better explore effect of these artifacts, we normalized SSI by its highest value in the complete manufactured artifact data set. This normalization in this manner indicates that neutral density filters effectively lowered SSI (Fig. 4.6A).

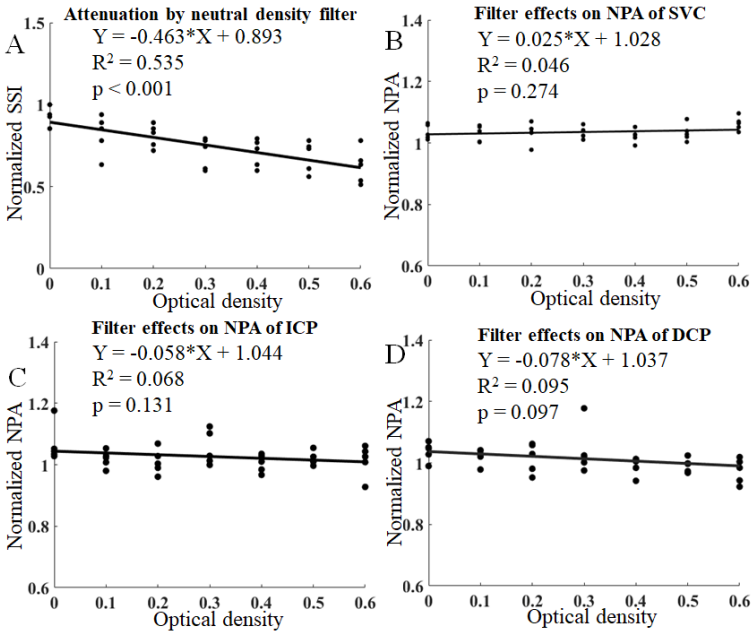


Figure 4.6: Effects of signal attenuation for NPA detection. (A), Normalized SSI (see text) declines as optical density of the neutral density filter increases; algorithm performance in the superficial vascular complex (SVC) (B), intermediate capillary plexus (ICP) (C), and deep capillary plexus (DCP)(D) is unaffected by increasing optical density, as evidenced by the low regression values and slopes of the best fit lines to the normalized fovea avascular zone (FAZ) areas (see text).

In healthy eyes, only the fovea avascular zone (FAZ) is avascular. We determined an FAZ baseline from the inner retinal maximum projection *en face* angiogram, since the FAZ has the best contrast (Fig. 4.7A). Even in neutral density filter signal-attenuated OCTA scans, the detected NPAs were quite similar to the unaltered scans (Fig. 4.7B-D). In order to directly quantify these results, we normalized the detected FAZ areas to the manually delineated baseline case. Ideally the normalized FAZ area would have a value of 1, indicating that signal reduction did not affect the CNN's performance. As can be seen by the essentially similar shape and size of the segmented NPA even as SSI declines from left to right in the figure, the algorithm's performance was not affected detrimentally by SSI decline. Indeed, in all of our measurements normalized FAZ area was close to unity, and showed no significant trend with SSI reduction (Fig. 4.6B-D).

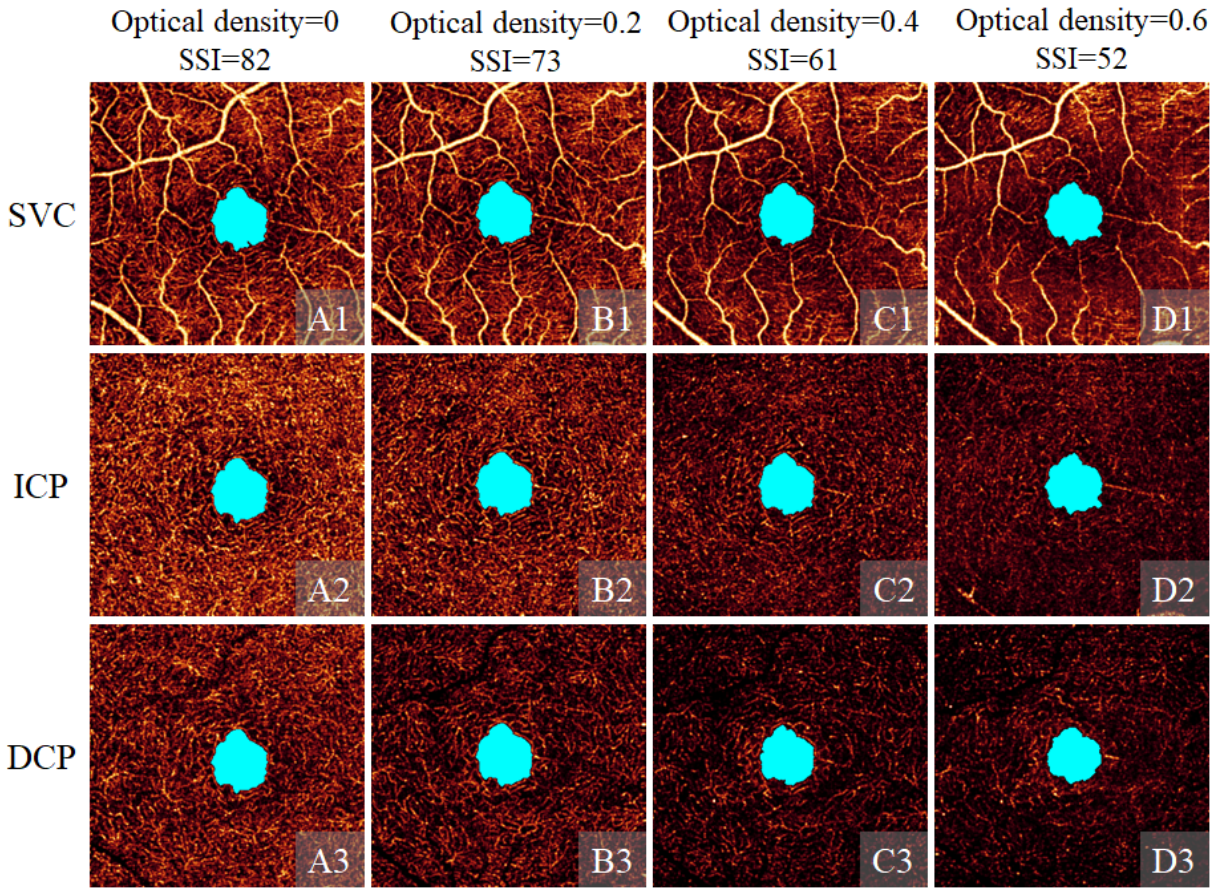


Figure 4.7: Detected NPA (in blue) on optically filtered scans of a representative normal eye. The size and shape of the detected NPA (here, limited to the fovea avascular zone (FAZ)) did not appreciably change with increasing optical density (columns running left to right).

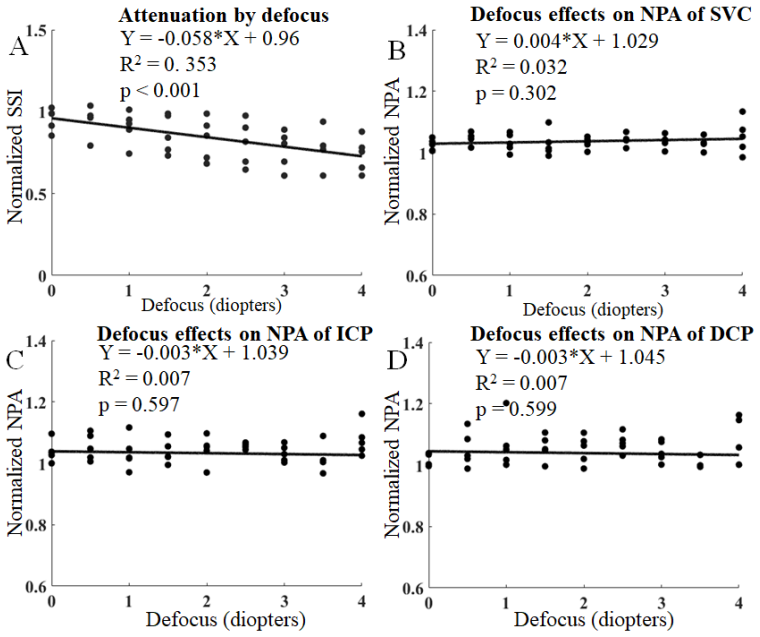


Figure 4.8: Effects of signal attenuation for NPA detection. (A), Normalized SSI (see text) declines as optical density of the neutral density filter increases; algorithm performance in the SVC (B), ICP (C), and DCP (D) is unaffected by increasing optical density, as evidenced by the low regression values and slopes of the best fit lines to normalized FAZ areas (see text).

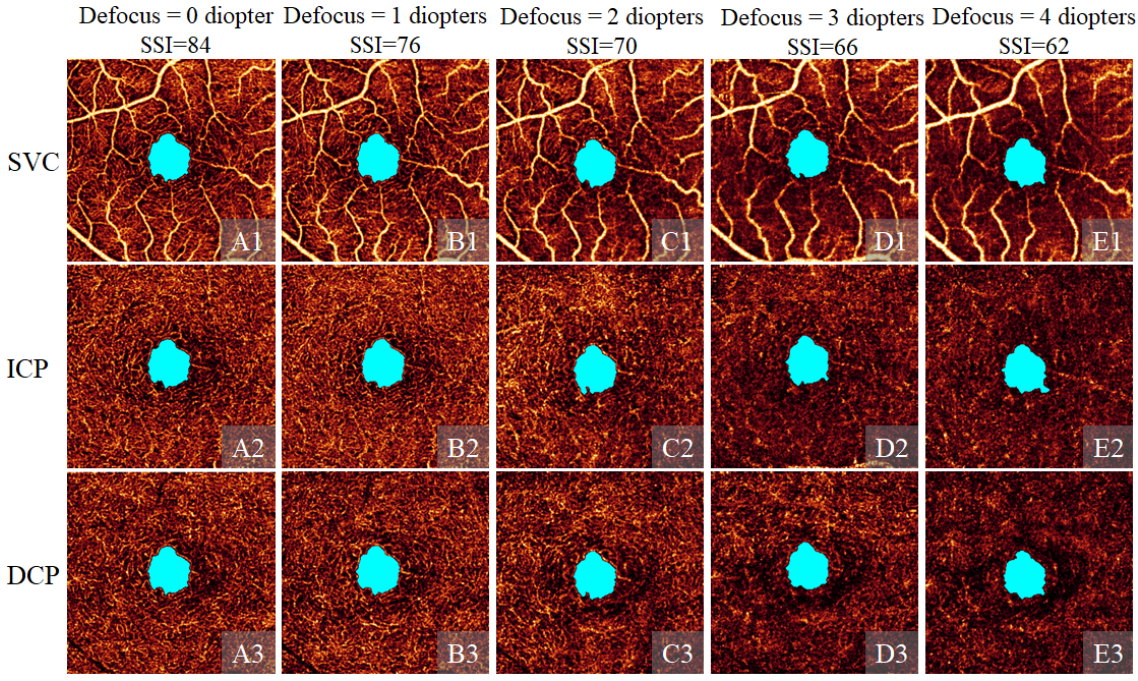


Figure 4.9: Detected NPA (in blue) on defocused scans of a representative normal eye. The size and shape of the detected NPA (here, limited to the foveal avascular zone; FAZ) did not appreciably change with increasing defocus (columns running left to right).

Next, we tested the performance of the proposed algorithm on manufactured defocus scans. The beam defocus was calibrated by diopters. By again normalizing SSI and FAZ area to the highest

measured SSI value in the defocus data set, we found that defocus successfully produces signal attenuation but did not adversely affect our algorithm's performance (Fig. 4.8). Visual inspection confirms this conclusion, as the shape and area of the detected FAZ area did not obviously change with increasing defocus (Fig. 4.9).

In order to quantify the effect of SSI reduction directly, we compared normalized FAZ area in our manufactured artifact data set directly, again found no significant trend (Fig. 4.10).

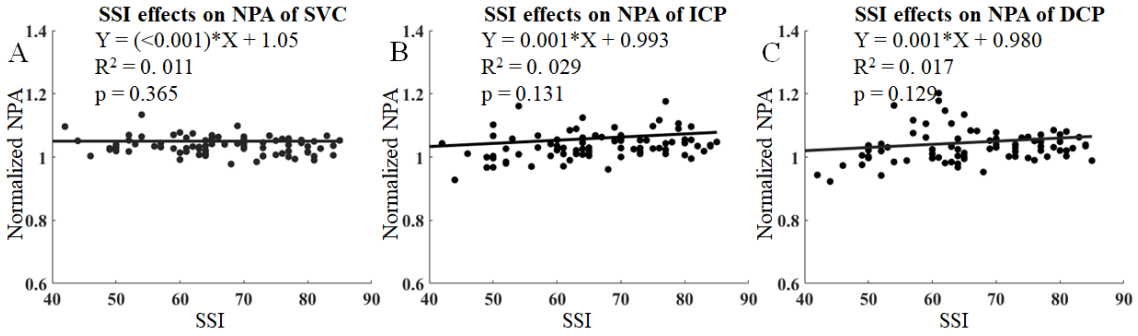


Figure 4.10: Effects of SSI attenuation for NPA detection in three plexuses. NPA detection on the SVC(A), ICP (B) and DCP (C) were unaffected by SSI variation.

4.5.2 Effect of artifacts in clinical dataset

While it is not possible to manufacture other artifacts in a similar manner to signal strength reduction, it is still possible to assess our algorithm's performance on representative scans qualitatively. As noted, shadow artifacts are especially detrimental for NPA detection, since they mimic the appearance of avascular regions. As indicated in a representative scan (from non-proliferative DR eye, Fig. 4.11), our algorithm was able to correctly exclude shadow area from being detected as NPA.

In our previous algorithms, microsaccadic artifacts can also disrupt NPA detection and quantification. The algorithm we propose here also correctly classified regions affected by microsaccadic artifacts as NPA (Fig. 4.12).

Finally, bulk motion artifacts can increase the background level in OCTA scans, potentially diminishing contrast between vasculature and static tissue. This artifact also did not obviously affect our algorithm's performance (Fig. 4.13).

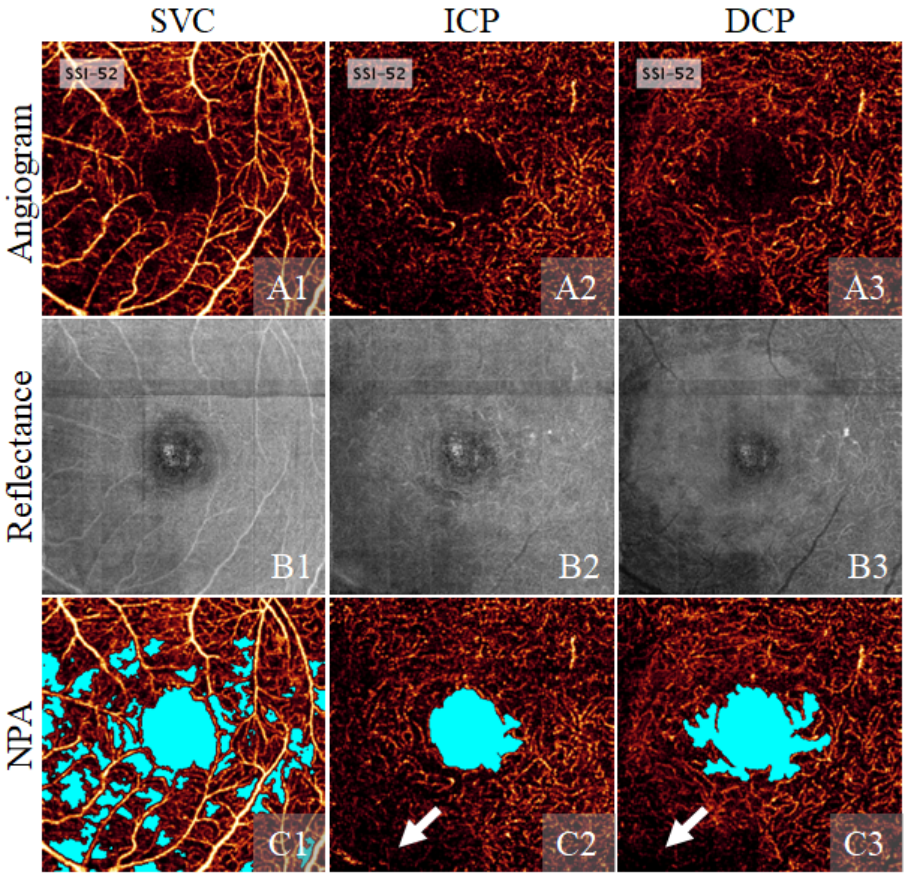


Figure 4.11: Detected NPA (in blue) on a low-quality scan of non-proliferative DR affected by shadow artifacts (white arrows).

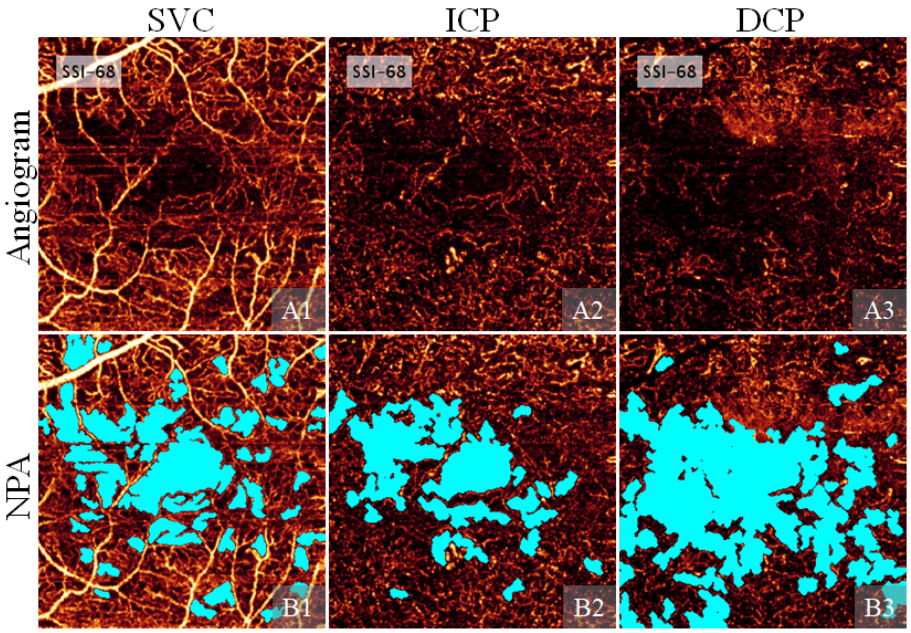


Figure 4.12: Detected NPA (in blue) on a low-quality scan of proliferative DR eye affected by microsaccade artifacts.

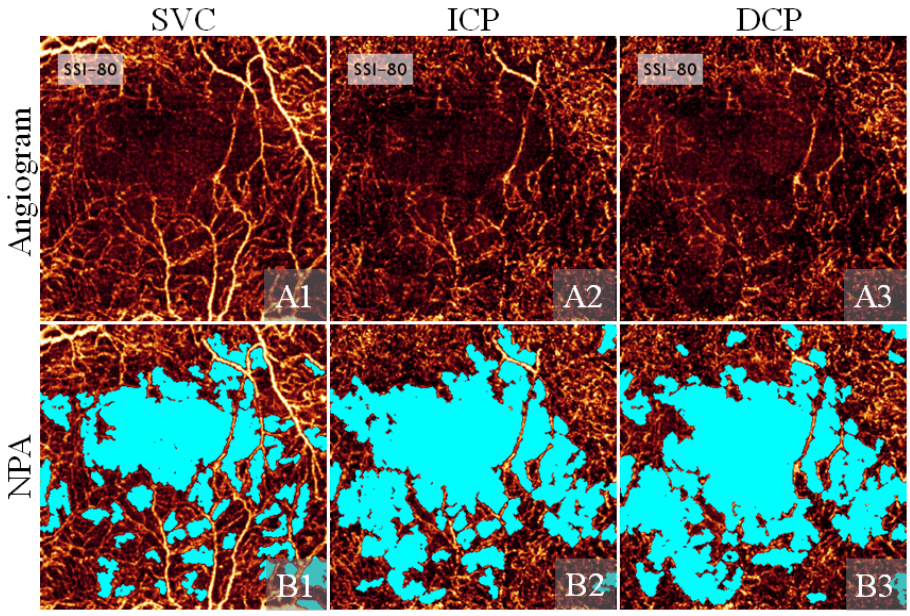


Figure 4.13: Detected NPA (in blue) on a low-quality scan of proliferative DR affected by bulk motion artifacts.

4.5.3 Performance on clinical DR scans

To further assess performance of the algorithm, we evaluated its segmentation accuracy on DR scans, since DR is a key application for NPA detection. We assessed the agreement between the outputs of the algorithm and the ground truth using four metrics: intersection over union (IOU), precision, recall, and F1 score. They are defined as:

$$IOU = \frac{GT \bigcup Out}{GT \bigcap Out} \tag{4.2}$$

$$precision = \frac{TP}{TP + FP} \tag{4.3}$$

$$recall = \frac{TP}{TP + FN} \tag{4.4}$$

$$F1 = 2 \times \frac{precision \times recall}{precision + recall} \tag{4.5}$$

where GT is the manually graded NPA and Out is the NPA detected by the proposed algorithm, TP is true positive, FP is the false positive, and FN is false negative.

Table 4.1: Agreement between detected NPA and ground truth ($mean \pm standard\,deviation$) grouped by DR severity

	DR severity	Inner retina	SVC	ICP	DCP
IOU	Controls	0.94 ± 0.04	0.86 ± 0.09	0.92 ± 0.08	0.88 ± 0.07
	Diabetics without retinopathy	0.90 ± 0.09	0.82 ± 0.12	0.81 ± 0.18	0.80 ± 0.07
	Mild to moderate DR	0.87 ± 0.07	0.80 ± 0.07	0.71 ± 0.12	0.71 ± 0.12
	Severe DR	0.84 ± 0.06	0.79 ± 0.07	0.66 ± 0.09	0.66 ± 0.09
Precision	Controls	0.96 ± 0.03	0.96 ± 0.04	0.98 ± 0.03	0.94 ± 0.08
	Diabetics without retinopathy	0.96 ± 0.08	0.93 ± 0.09	0.92 ± 0.12	0.90 ± 0.11
	Mild to moderate DR	0.95 ± 0.04	0.95 ± 0.09	0.93 ± 0.09	0.88 ± 0.14
	Severe DR	0.95 ± 0.04	0.96 ± 0.03	0.89 ± 0.11	0.94 ± 0.07
Recall	Controls	0.97 ± 0.03	0.89 ± 0.11	0.86 ± 0.15	0.88 ± 0.10
	Diabetics without retinopathy	0.94 ± 0.08	0.94 ± 0.08	0.94 ± 0.04	0.94 ± 0.04
	Mild to moderate DR	0.92 ± 0.07	0.82 ± 0.08	0.74 ± 0.14	0.70 ± 0.13
	Severe DR	0.88 ± 0.08	0.94 ± 0.08	0.94 ± 0.04	0.94 ± 0.04
F1 Score	Controls	0.97 ± 0.02	0.93 ± 0.05	0.96 ± 0.05	0.94 ± 0.05
	Diabetics without retinopathy	0.94 ± 0.07	0.90 ± 0.07	0.88 ± 0.12	0.89 ± 0.08
	Mild to moderate DR	0.93 ± 0.04	0.89 ± 0.09	0.83 ± 0.09	0.82 ± 0.09
	Severe DR	0.91 ± 0.04	0.88 ± 0.04	0.79 ± 0.06	0.78 ± 0.07
NPA(mm^2)	Controls	0.23 ± 0.08	0.24 ± 0.08	0.24 ± 0.08	0.26 ± 0.07
	Diabetics without retinopathy	0.29 ± 0.07	0.34 ± 0.11	0.37 ± 0.15	0.50 ± 0.28
	Mild to moderate DR	0.49 ± 0.43	0.96 ± 0.66	0.68 ± 0.87	1.35 ± 0.96
	Severe DR	1.02 ± 0.55	1.88 ± 0.66	1.43 ± 0.79	2.29 ± 1.14

DR–diabetic retinopathy; SVC–Superficial vascular complex; ICP–Intermediate capillary plexus; DCP–Deep capillary plexus; IOU–Intersection over union; NPA–Non-perfusion area.

Using these metrics, we explored the effect of DR severity on NPA detection (Table 4.1). Across all DR severities and in each plexus, the algorithm achieved high IOU, precision, recall, and F1 score. As expected, the extent of NPA increases with DR severity. Importantly, NPA on diabetics without retinopathy was larger than that in normal controls, indicating that NPA could serve as a biomarker for detecting DR at an early stage. However, the mean IOU deteriorated in more severe DR in the ICP and DCP. Despite the PR-OCTA algorithm, some projection artifacts remain in these plexuses. Scattering and absorption of light also attenuates flow signal in the deeper layers, reducing the NPA contrast with the surrounding vasculature. The decline in performance, however, partially due to the difficulty of establishing an adequate ground truth. In eyes with large NPA and significant signal attenuation, human graders may find it difficult to clearly delineate the true NPA.

NPA detection on a representative severe DR case ($SSI = 54$) is demonstrated (Fig. 4.14). The detected NPA well matches the ground truth in the SVC (Fig. 4.14A1-D1), where NPA contrasts

most with perfused regions. In the ICP (Fig. 4.14A2-D2), the primary detected regions still match the ground truth; and even in the DCP with least contrast (Fig. 4.14A3-D3) the detection was accurate. After close visual inspection, we found that small capillaries with low flow strength and isolated area were excluded on the manually graded ground truth; the algorithm-labeled regions appear more "realistic" than the human-labeled. This explains why mean IOU is low in severer cases.

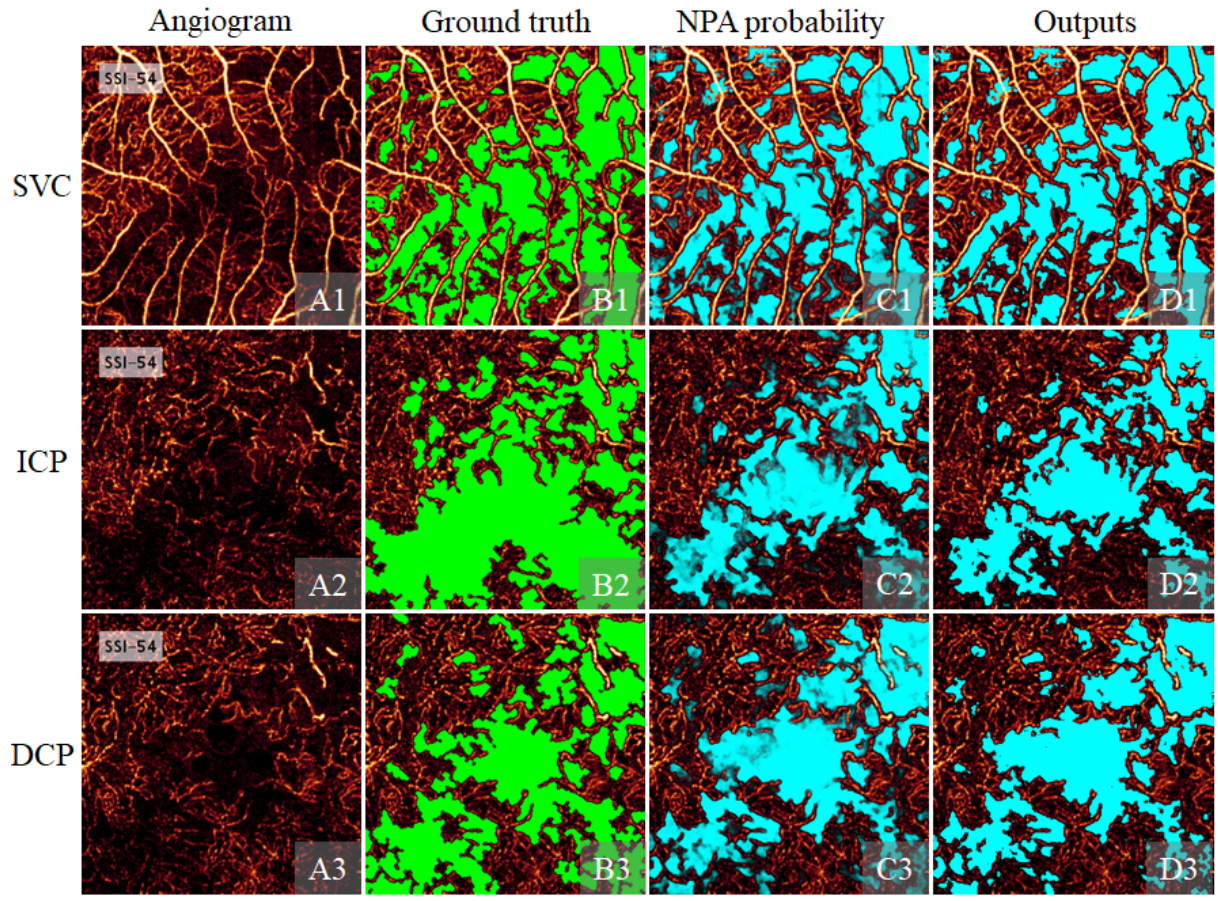


Figure 4.14: NPA detection on a severe DR. (A), Angiograms in specific layers-superficial vascular complex (SVC), intermediate capillary plexus (ICP), and deep capillary plexus (DCP); (B), the ground truth delineated by an expert grader (green); (C), the output probabilities with brighter blue indicating a higher output probability; (D), the detected NPA (final results, with probability value > 0.5).

4.5.4 Repeatability Assessment

50 healthy eyes enrolled in our clinical studies were scanned twice to test repeatability by calculating the coefficient of variation (CV) in NPA segmentation. Scans affected by shadow and motion artifacts were also included in this dataset. Our study shows the intra-visit repeatability is

very high (Table 4.2). In a healthy eye, detected NPA should be identical in the whole inner retinal slab, SVC, ICP and DCP. This was demonstrated by the nearly consistent NPA area in (Table 4.1). Moreover, the size of detected FAZ is also highly matched with our previous outcome[67], which indicated that the performance of the algorithm is robust in all layers and reliable in clinical studies. Fig. 4.15 demonstrated a test scan with focal shadow artifacts. The designed CNN was capable of differentiating shadow artifacts from NPA. The majority of shadow artifacts was excluded in outputs, and only a few small areas were mis-detected (Fig. 4.15C1). Despite these occasional mis-segmentations, our algorithm performs favorably against other algorithms that have either ignored the effect on shadow artifacts, as in[60, 103] or required manual corrections[61].

Table 4.2: Repeatability of NPA detection on healthy eyes

	Inner retina	SVC	ICP	DCP
NPA (mm^2, $mean \pm std$)	0.23 ± 0.12	0.24 ± 0.18	0.23 ± 0.10	0.25 ± 0.12
Repeatability (Coefficient of variation)	0.06	0.07	0.07	0.07

SVC–Superficial vascular complex; ICP–Intermediate capillary plexus;
DCP–Deep capillary plexus; NPA–Non-perfusion area.

4.6 Discussion and conclusion

While NPA is as an important biomarker for DR[58, 59, 67, 94], accurately quantifying NPA from OCTA scans can be challenging. Particularly, artifacts that reduce signal have confounded previous automated approaches to identify NPA, resulting in misclassification [60, 103, 104], that require manual correction [61]. While our previous work also used the OCT reflectance image to account for shadow artifacts, our results were limited to the SVC[54, 101], requiring manual correction in the ICP or DCP. This is not an insignificant task, since it would require an expert to examine $2/3$ of plexus *en face* images. Because the NPA in ICP and DCP can provide information about DR progression distinct from SVC, an accurate assessment of the these plexuses is critical[69].

However, automated NPA detection in the deeper plexuses poses a significant challenge. First, it requires an accurate means of removing flow projection artifacts. Previous methods such as slab subtraction could not remove the projection artifacts without introducing disruption in the vasculature that led to false identification of NPA[105]. Secondly, signal strength diminishes in deeper anatomic slabs, making algorithms more vulnerable to error from signal reducing artifacts,

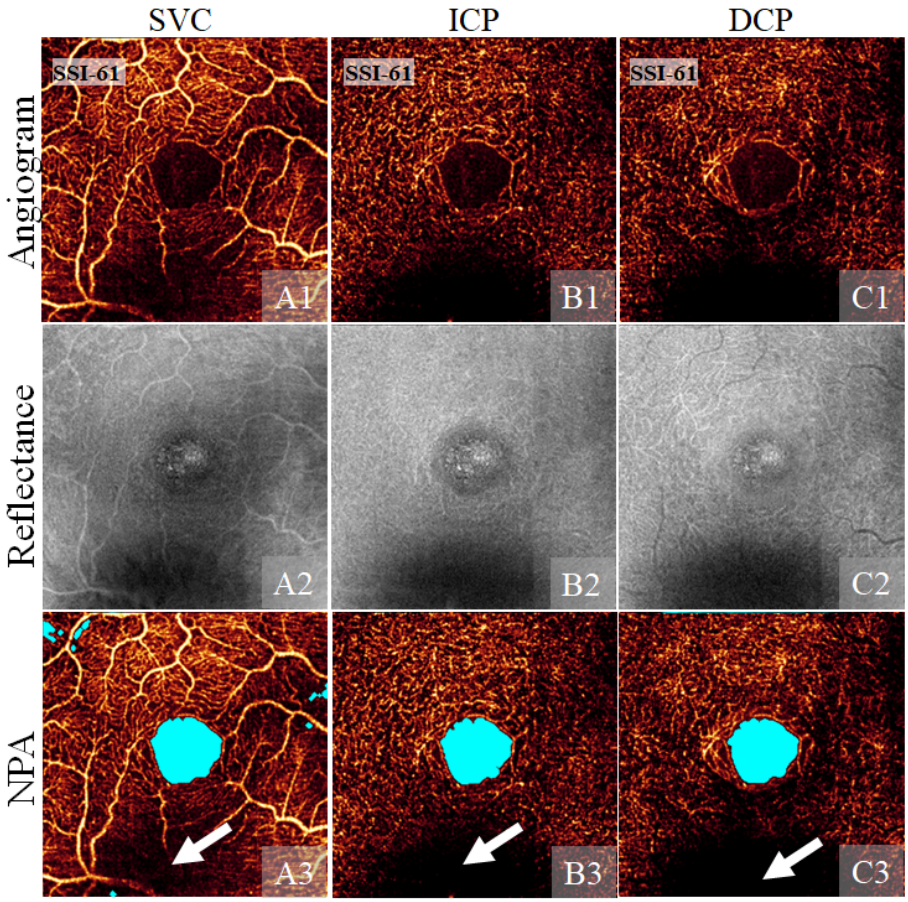


Figure 4.15: NPA detection on a healthy eye (in blue) affected by focal shadow artifacts (white arrows).

necessitating an algorithm that can demonstrate insensitivity to such variation (section 4.1). The ability to mitigate the effect of inherent signal variation between different images is especially important because diseased eyes often have lower SSI due to complications such as the presence of edema, cataract, floaters and poor tear film quality. Algorithm dependence on SSI could therefore compound the effect of diseases if it were dependent on SSI, since SSI-biased NPA detection is also potentially pathology-biased.

We have presented a method that accurately detects NPA on three retinal plexuses. The test set used to evaluate performance did not exclude any OCTA scans due to image quality regardless of artifacts or high noise levels, indicating that the CNN could be effective on clinical data sets.

Several design choices contributed to the CNN's performance. By including both plexus-specific angiograms and *en face* OCT reflectance maps in the CNN input, it was able to differentiate

NPA from shadow artifacts from NPA. The CNN also incorporated atrous kernels, which enabled it to detect NPA at multiple scales while maintaining the resolution of the detected regions. The low CV indicated the high repeatability of healthy controls collected on clinic. This proposed method contributed to a more repeatable results compared to manual grading, which might be affected by subjective judgements, thresholding and other image processing based methods[59, 104, 106]. Finally, the CNN trained on a diverse data set, which allowed it to learn a large variety of features relevant to the NPA detection task and facilitated accurate performance even on images with severe disease or low quality. One possible deficiency in the proposed solution is that its segmentation accuracy apparently diminished as DR severity increased. While disagreement with the ground truth is obviously not preferred, NPA segmentation in severe DR cases is difficult not just for automated procedures but for human graders as well. Thus, a reduced disagreement between the algorithm and human grader may not necessarily indicate a worse performance.

5 Automated diagnosis and segmentation of choroidal neovascularization in optical coherence tomographic angiography using deep learning

5.1 Abstract

Accurate identification and segmentation of choroidal neovascularization (CNV) is essential for the diagnosis and management of exudative age-related macular degeneration (AMD). Projection-resolved optical coherence tomographic angiography (PR-OCTA) enables both cross-sectional and *en face* visualization of CNV. However, CNV identification and segmentation remains difficult even with PR-OCTA due to the presence of residual artifacts. In this paper, a fully automated CNV diagnosis and segmentation algorithm using convolutional neural network (CNN) is described. This study used a clinical dataset, including both scans with and without CNV, and scans of eyes with different pathologies. Furthermore, no scans were excluded due to image quality. In testing, all CNV cases were diagnosed from non-CNV controls with 100% sensitivity and 95% specificity. The mean intersection over union of CNV membrane segmentation was as high as 0.88. By enabling fully automated categorization and segmentation, the proposed algorithm should offer benefits for CNV diagnosis, visualization monitoring.

5.2 Introduction

Age related macular degeneration (AMD) is a leading cause of vision loss and irreversible blindness [107, 108, 109]. AMD is characterized as neovascular based on the presence of choroidal neovascularization (CNV), a pathological condition in which new vessels grow from the choroid into the outer retina [16, 109, 110, 111]. CNV often results in vision loss because it can result in subretinal hemorrhage, lipid exudation, subretinal fluid, intraretinal fluid, or formation of fibrotic scars[85, 86]. Fluorescein (FA) and indocyanine green angiography (ICGA) are traditionally used for CNV identification and visualization, but drawbacks to dye based angiography include that it provides only two-dimensional visualization of vascular networks, that invasive intravenous contrast dye can lead to nausea and anaphylaxis [112], and that long acquisition times makes high

This work has been published in Biomedical Optics Express: Jie Wang, Tristan T. Hormel, Liqin Gao, Pengxiao Zang, Yukun Guo, Xiaogang Wang, Steven T. Bailey, and Yali Jia, "Automated diagnosis and segmentation of choroidal neovascularization in OCT angiography using deep learning," Biomed. Opt. Express 11, 927-944 (2020).

volume and multiple follow-up angiograms impractical. A promising alternative approach is optical coherence tomographic angiography (OCTA), which measures flow signal *in-vivo* by evaluating motion contrast between subsequent optical coherence tomography (OCT) B-scans at the same location [43, 48]. As opposed to conventional dye-based imaging modalities, OCTA is non-invasive, has rapid acquisition, is high-resolution, and generates three-dimensional (3D) datasets. However, OCTA is susceptible to several imaging artifacts [48, 75, 113]. Projection artifacts cause specious flow signal in deeper anatomical layers. CNV assessment in particular suffers, since its proper visualization requires images of the outer retina, where projection artifacts are especially prominent due to proximity to the highly reflective retinal pigment epithelium layer (RPE). Recently, PR-OCTA [72, 73, 99] has proven adept at removing projection artifacts, and consequently shown diagnostic potential and enabled detailed quantification of CNV [114, 115, 116].

Because it is non-invasive and images are acquired easily and rapidly in the clinical setting, PR-OCTA provides the opportunity to develop routine imaging for CNV detection and monitoring. Such monitoring has major clinical potential, since early detection of CNV and conversion to exudative CNV is crucial for successful intervention. Furthermore, improved quantification of CNV features may provide vital indicators for disease progression [117]. However, the presence of artifacts in OCTA images require careful interpretation. In such an environment, even evaluating images for the presence of CNV can be time consuming for clinicians. Furthermore, CNV metrics such as vessel density or morphology require membrane and vessel segmentation as a first step, but feature extraction may go awry when artifacts interfere with image analysis. These concerns argue for robust software automation solutions that will be capable of accurate identification of CNV and its precise segmentation in real-world datasets that may include poor quality scans or highly pathological scans in which CNV is not present.

A previous attempt at automated CNV segmentation was saliency-based [105]. This algorithm uses a saliency map to highlight the dominant objects that have strong distinctiveness defined by brightness, orientation contrast and position distance. The crux of this method is that CNV flow signal is higher than artifacts or background noise. However, even with PR-OCTA, large persistent

artifacts in outer retina can sometimes remain. The saliency-based approach will segment such artifacts as CNV, and furthermore large CNV membranes filling most of the angiogram cannot be fully segmented with such an approach. Finally, the saliency-based algorithm *always* segments CNV, regardless of whether it actually exists in an input scan. An important first step for a completely automated approach, then, is the ability to classify scans based on the presence or absence of CNV. However, CNV segmentation using *en face* outer retinal angiogram is compromised by a variety of image features, including residual projection and motion artifacts, as well as background noise. On scans where artifacts are small and have lower signal than the CNV, our previous saliency-based algorithm could segment the CNV properly (Fig. 5.1, case1). However, on scans where the area and signal of residual artifacts are similar to the CNVs, the algorithm readily kept false positives on the saliency map (Fig. 5.1, case2). Since saliency algorithm segments CNV based on the degree of saliency, larger CNV vessels with strong signal are easier to separate from artifacts than smaller CNV vessels. In cases with very large CNV, the large thick CNV vessels have a much higher flow signal than the smaller CNV capillaries and the saliency algorithm may mistakenly segment these smaller vessels as background (Fig. 5.1, case3). In a non-CNV control cases, it is important for an automated CNV segmentation algorithm to clean up the background noise instead of segmenting false positives. The saliency algorithm also fails in this case (Fig. 5.1, case4), therefore, an algorithm using CNNs was proposed in this study to overcome each of these limitations.

Convolution neural network (CNN), one of the outstanding artificial intelligence (AI) techniques, provide a feasible way to accomplish the goals in this study. Published results indicate the high performance of CNN adapted to complex tasks such as object classification and segmentation[118]. In the context of structural and angiographic OCT, CNNs have been used to identify glaucoma[119], segment non-perfusion area[54, 101] and perform retinal layer segmentation[56, 57]. However, an automated CNV diagnosis and quantification system has never been developed. As CNV represents the most important pathological development in AMD, this is a major limitation in current clinical practice.

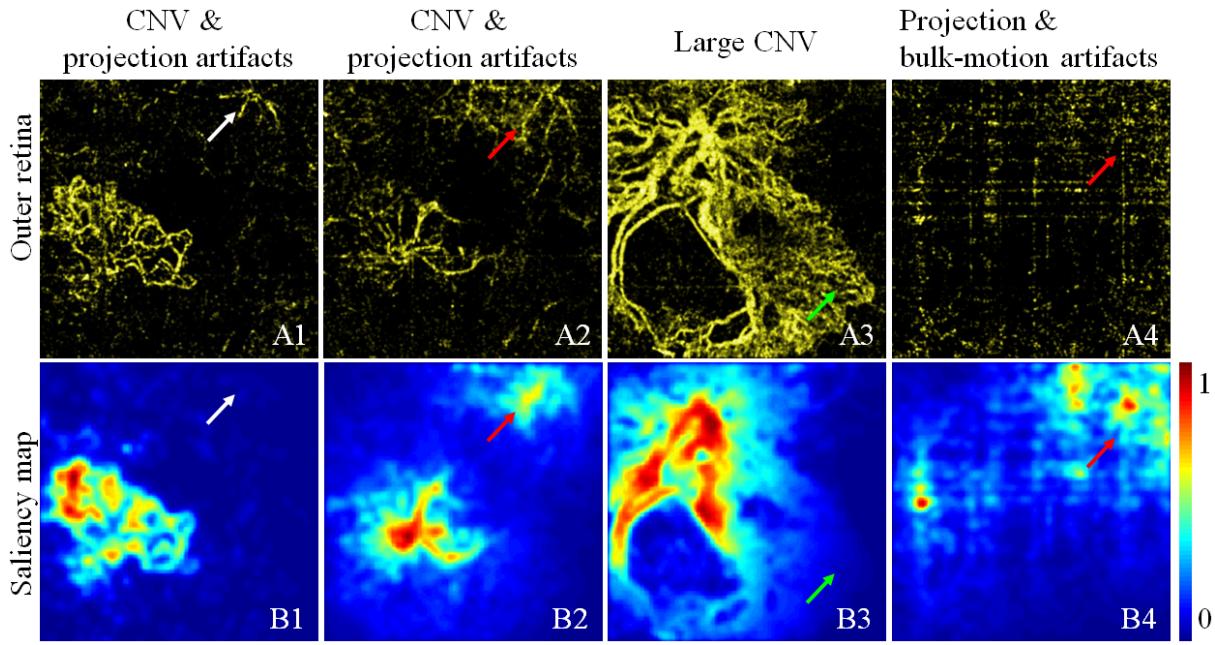


Figure 5.1: Choroidal neovascularization (CNV) segmentation on challenging scans using a saliency-based algorithm. Small residual projection artifacts are excluded in the saliency map (A1&B1, highlighted by white arrows). Strong residual artifacts in CNV and non-CNV scans were over-segmented in the saliency map, providing false positives (A2&B2, A4&B4, highlighted by red arrows), while large CNV was under-segmented in the saliency map, producing false negatives (A3&B3, highlighted by green arrows).

In this study, we developed an algorithm based on two CNNs. The algorithm classifies input scans based on the presence or absence of segmented CNV membrane, and then, if CNV is present, segments the CNV vasculature it encloses. In order to accomplish these tasks, we trained two separate CNNs, as detailed below. These networks perform complimentary tasks, and together comprise a robust system for CNV characterization.

5.3 Data acquisition and preprocessing

OCTA datasets with a large range of SSI were collected from the retina clinics at the Casey Eye Institute, Oregon Health & Science University, Portland, OR, USA and Shanxi Eye Hospital, Taiyuan, Shanxi, PR China. The study was conducted in compliance with the Declaration of Helsinki.

Participants were scanned using a $70kHz$ commercial OCTA system (RTVue-XR; Optovue, Fremont, CA) with a central wavelength of $840nm$. The scan area was $3 \times 3mm$ and centered on the fovea. Two repeat B-scans were collected at the same position, and retinal flows were detected

using the commercial split-spectrum amplitude decorrelation angiography (SSADA) algorithm [10]. One X-fast and one Y-fast scan were obtained and registered to suppress motion artifacts. Patients with CNV secondary to neovascular AMD were enrolled. Control eyes without CNV included eyes with non-neovascular AMD, diabetic retinopathy (DR), branch retina vein occlusion (BRVO) / branch retina arterial occlusion (BRAO), central serous chorioretinopathy (CSC), and healthy eyes. No scans were excluded due to low image quality.

Input to the CNN consisted of several *en face* images, each of which was useful for CNV identification or segmentation in some capacity. To generate the *en face* retinal angiograms used in this study requires anatomic slab segmentation; this was accomplished using a semi-automatic approach based on graph search [1, 55] and implemented in our in-house OCTA processing toolkit. Regarding our study aims, segmentation of the inner limiting membrane (ILM), outer plexiform layer (OPL), and Bruch's membrane (BM) was pertinent, and used to construct inner and outer retinal images (Fig. 5.2). The input images consisted of the uncorrected original inner and outer retinal *en face* angiograms, as well as slab-subtracted[70, 98, 105] and projection-resolved outer retinal angiograms [73] (Fig. 5.3). Most of these images are useful for artifact removal. PR-OCTA achieves the clearest angiograms in the outer retina, but some residual projection artifacts remain that could be confused for CNV. Slab-subtraction is a faster and simpler method for projection artifact removal wherein flow signal from superficial slabs is subtracted from deeper; compared to PR-OCTA it retains fewer regions with spurious signal, but true vessels are often interrupted or erased, severely disrupting vascular morphology. Original uncorrected angiograms of the outer retina have the opposite problem, as they are projection artifact-rich, with many false flow pixels mimicking superficial vasculature. Including all four of these angiograms (original inner and outer angiograms, slab-subtracted outer retina, and projection-resolved outer retina) allowed the CNN to efficiently differentiate artifacts from true signal, since the original angiograms could be used to corroborate the location of false flow, the slab-subtracted angiograms could be used to identify regions with a high probability of including CNV, and the PR-OCTA angiograms provides excellent image quality in the region containing CNV. Finally, an outer retinal structural volume was also included in the CNN input; since CNV appears along with the elevation of RPE, the slab can

facilitate artifact removal in regions where the RPE is in normal (Fig. 5.2B1), detached (Fig. 5.2B2) or lost (Fig. 5.2B3) states. To generate tidy outer volumes with the same size, all A-lines in the outer slab were resampled to same voxel depth for data alignment (Fig. 5.4).

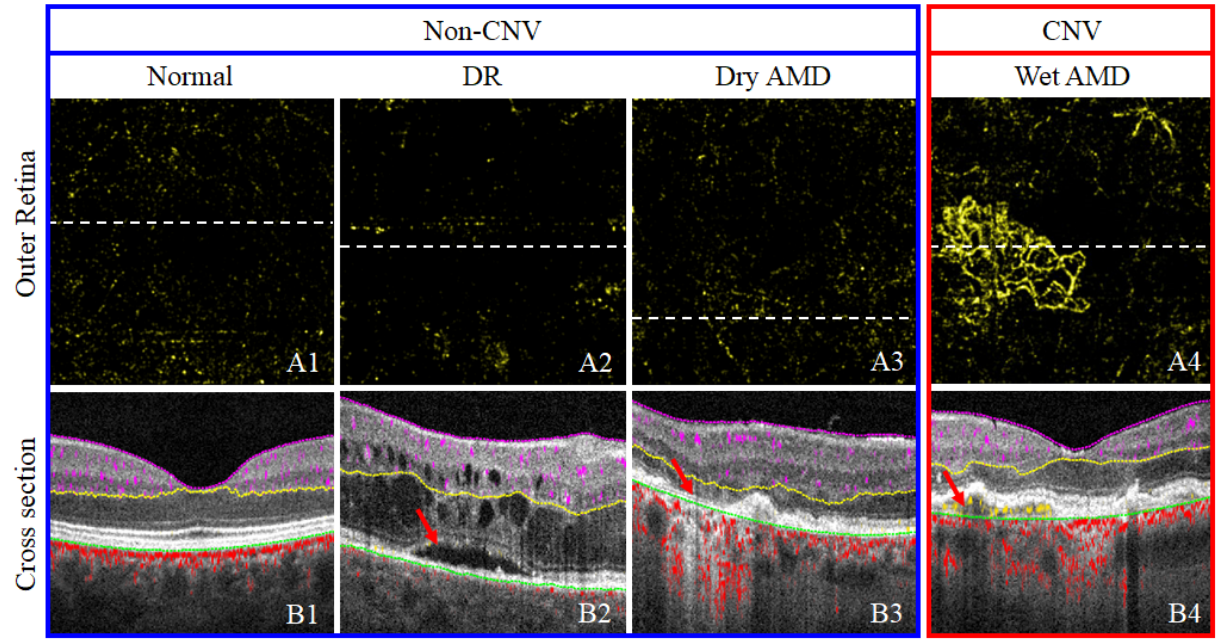


Figure 5.2: Comparison of non-choroidal neovascularization (CNV), including a healthy (column 1), diabetic retinopathy (DR)(column 2), and dry age-related macular degeneration (AMD) (column 3), and choroidal neovascularization (CNV) (wet AMD, column 4) scans with *en face* outer retinal angiograms (row A) and cross-sectional structural optical coherence tomography (OCT) overlaid with optical coherence tomographic angiography (OCTA) (row B) showing inner retinal (violet), choroidal (red), and pathological outer retinal flow (yellow). Slab segmentation lines are the inner limiting membrane (ILM) (violet), outer border of the outer plexiform layer (OPL) (yellow), and Bruch's membrane (BM) (green). White dotted lines in row A indicate the locations of the cross sections in row B. Red arrows indicate the pathologies in outer retina.

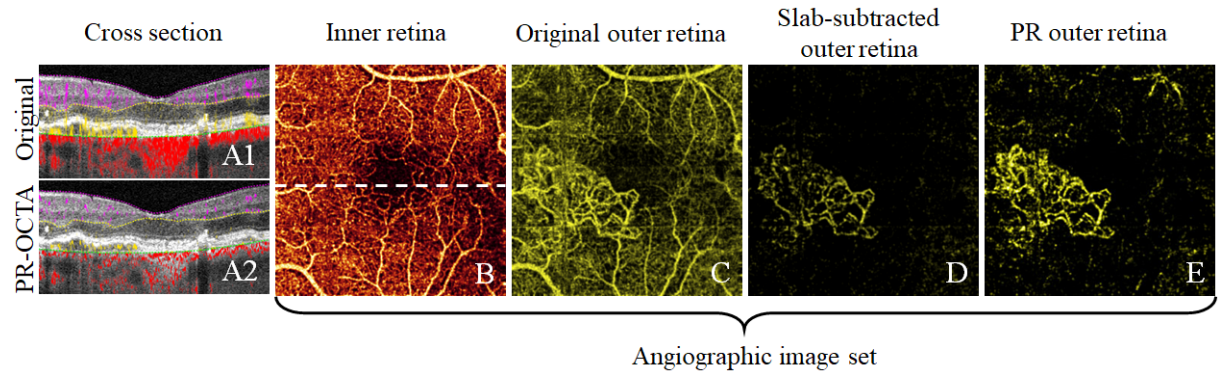


Figure 5.3: Input angiographic image set. (A) original (A1) and projection-resolved OCTA (PR-OCTA) (A2) with inner retinal (violet), choroidal (red), and outer retinal (yellow) flow overlaid on structural optical coherence tomography (OCT); (B) inner retinal angiogram, with white dotted line indicating the position of the B-scans in (A); (C) outer retinal angiogram generated from the original optical coherence tomographic angiography (OCTA) demonstrated in (A1); (D) outer retinal angiogram processed by slab -subtraction; (E) projection-resolved (PR) outer retinal angiogram. In (E) the entire choroidal neovascularization (CNV) is preserved but some residual projection artifacts persist.

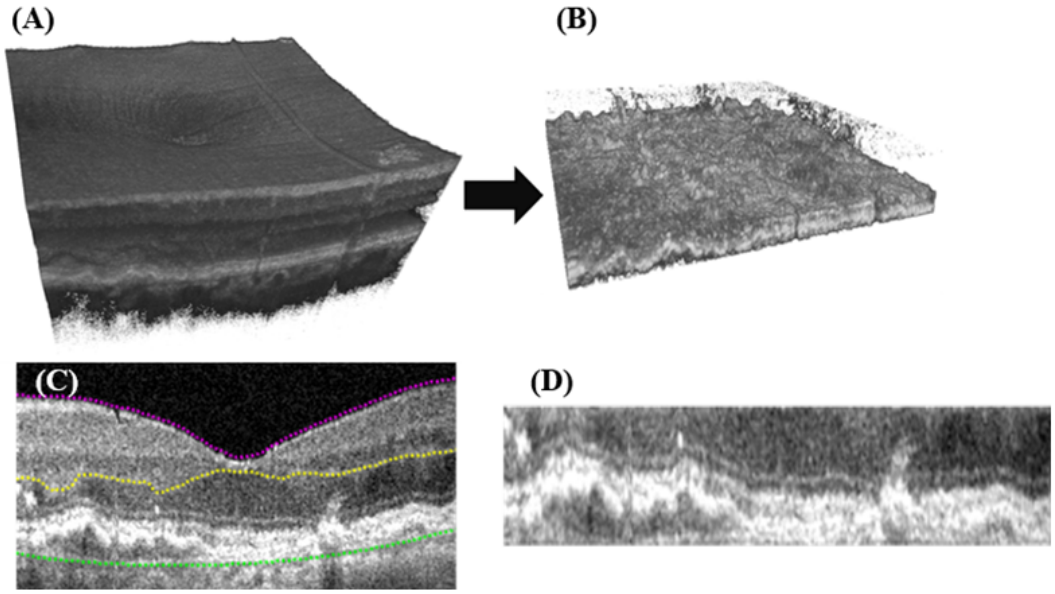


Figure 5.4: Generation of outer retinal structural volume input. (A) Original structural optical coherence tomography (OCT) volume; (B) extracted outer retinal volume; (C) original cross-sectional OCT, with anatomic slab segmentation overlaid in violet (inner limiting membrane, ILM), yellow (outer plexiform layer, OPL), and green (Bruch's membrane, BM); (D) segmented outer retinal cross section, resampled so that the volume has a constant voxel depth.

5.4 Choroidal neovascularization identification and segmentation using convolutional neural networks

Using the proposed algorithm, CNV scans could be identified based on the presence of a CNV membrane which is the damaged tissue mass within outer retina where CNVs grow into. Then, CNV vessels were further segmented on identified CNV scans.

5.4.1 Algorithm outline

The proposed algorithm incorporates two CNNs, one for CNV membrane identification and segmentation (CNN-M) and the other for pixel-wise vessel segmentation (CNN-V) (Fig. 5.5). The data pipeline is as follows. First of all, both the structural and angiographic image sets are fed into the CNN for CNV membrane segmentation. The CNV is diagnosed based on the presence of a detected CNV membrane. Without CNV present, the algorithm will classify the scan as CNV-free; however, even in some scans without CNV present, the CNN-M will be fooled into classifying a residual artifact as CNV. Since the interference of residuals is inevitable, a size cutoff threshold, which was estimated by maximizing the identification sensitivity in the training dataset, was applied. If a membrane (above the size cutoff) was segmented, then the input was diagnosed as CNV, and

the PR outer retinal angiogram is multiplied by the segmented CNV membrane probability map to suppress interference from the background. Last, the structural volume, angiographic image set and CNV membrane probability weighted PR outer retinal angiogram are fed into the CNN-V for CNV vessel segmentation.

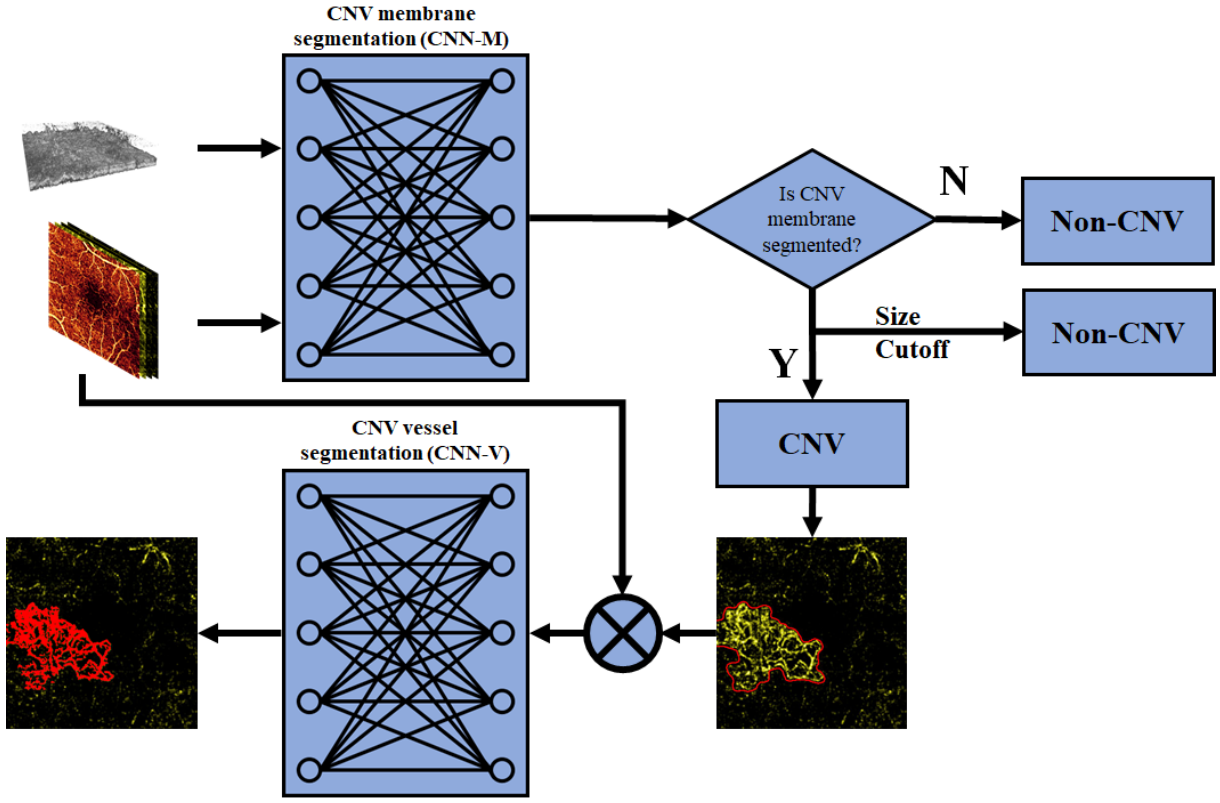


Figure 5.5: Outline of the proposed automated choroidal neovascularization (CNV) identification and segmentation method. Input consists of the original inner retinal angiogram and original, slab-subtracted, and projection-resolved (PR) outer retinal angiograms, and volumetric structural data from the outer retina. We trained two separate CNNs in order to segment the CNV membrane and vessels, respectively. The first one (CNN-M) segments CNV membrane and outputs a mask corresponding to its location (if it is present). The second (CNN-V) segments CNV vascular pixels within the CNV membrane output by the first CNN.

5.4.2 Choroidal neovascularization membrane segmentation using convolutional neural network

Repeated pooling layers are used in many image processing networks. They are beneficial to image classification in order to compress the key information for decision-making and extract features across different scales. However, the width of CNV vessels can be as small as just a single pixel. Repeated pooling layers may be problematic because they decrease feature resolution and therefore may remove thin vessels. To preserve feature resolution while maintaining segmentation across multiple scales, one alternative is using larger kernels. With this approach, however, the

memory and computational cost would be overly burdensome. Instead, our network design replaced most pooling layers with atrous kernels, which do not reduce feature resolution, in the convolutional layers [49, 120]. Atrous kernels dilate 3×3 kernels by inserting zeros between the kernel elements. The atrous kernel with size 1 is the original 3×3 kernel, while inserting one zero between the elements creates an atrous kernel of size two, and the atrous kernel with size 3 is created by inserting two zeros (etc.). As the size of the atrous kernel increases, the field of view is enlarged, but the memory and computational cost is nonetheless equivalent to the original 3×3 kernel.

The CNN architecture used for each part of the designed algorithm (membrane, CNN-M, and vessel, CNN-V, segmentation, respectively) have different designs. For CNN-M (Fig. 5.6), features in the structural volume, angiographic image set were first extracted, respectively. To feed three-dimensional (3D) outer retinal volumes into two-dimensional (2D) CNN, each separate depth in the original 3D volume was input as a separate channel. The following concatenation and convolutional layers merged the structural and angiographic features, and then fed them into the encoder blocks for feature extraction. A single pooling layer was added after feature merging. The encoder block was designed using atrous kernels, and the dilation rate increased in deeper layers. To make the best of low-level features and to transmit the loss from deeper to shallower layers, a U-net like architecture was applied in the decoder section. Moreover, the decision-making layer was parallelized using atrous kernels to refer features in multi-scales, with the atrous kernel dilation rates varying from 1 to 32, increasing by multiples of 2. A softmax activation was able to output the CNV membrane probability map.

Complex tasks often call for the addition of more convolutional layers and kernels, but memory considerations induce a limit on the number the network could use. The number of kernels in encoder and decoder layers was therefore fixed at 32. A densely connected CNN [121] structure (modified to include atrous kernels) was applied in the encoder blocks, and features at low levels were concatenated to deeper levels (Fig. 5.7). The dilation rate of each encoder block varied as demonstrated in (Fig. 5.6).

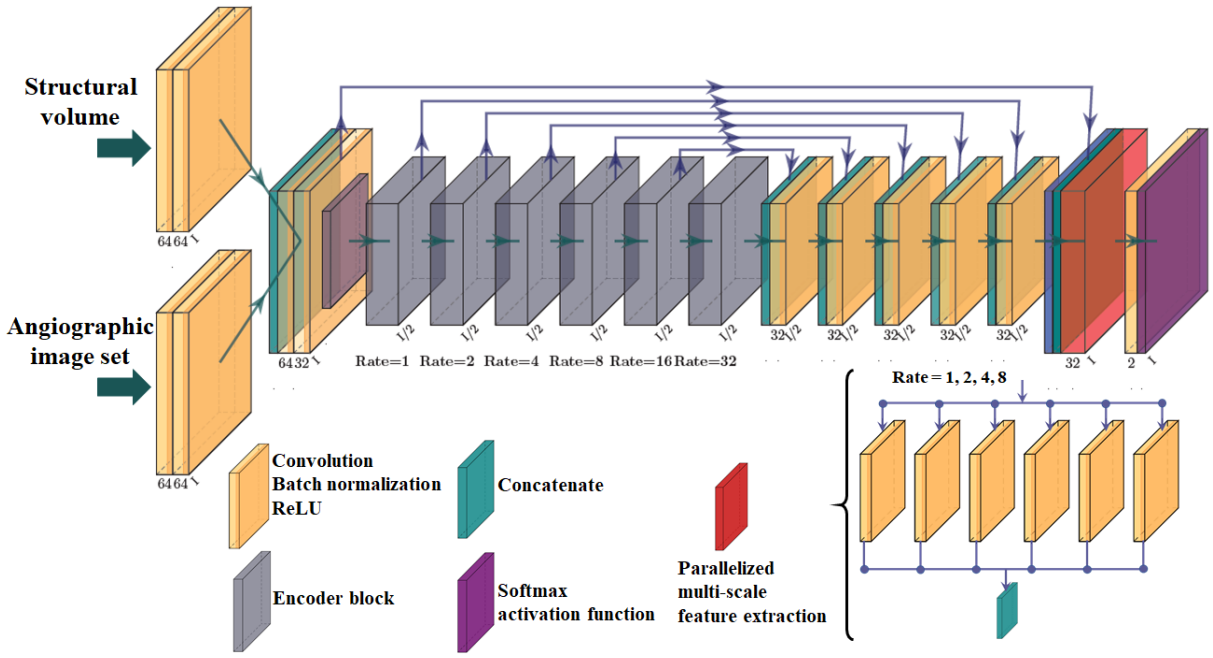


Figure 5.6: Convolutional neural network (CNN) architecture for choroidal neovascularization (CNV) membrane segmentation (CNN-M). The atrous kernel sizes ($Rate = 1\ to\ 32$) are annotated below each encoder block. The number of kernels is annotated below each convolutional layer. Label I and $I/2$ indicate operations on the full ($304 \times 304 - pixel$) and half-sized ($152 \times 152 - pixel$) image, respectively.

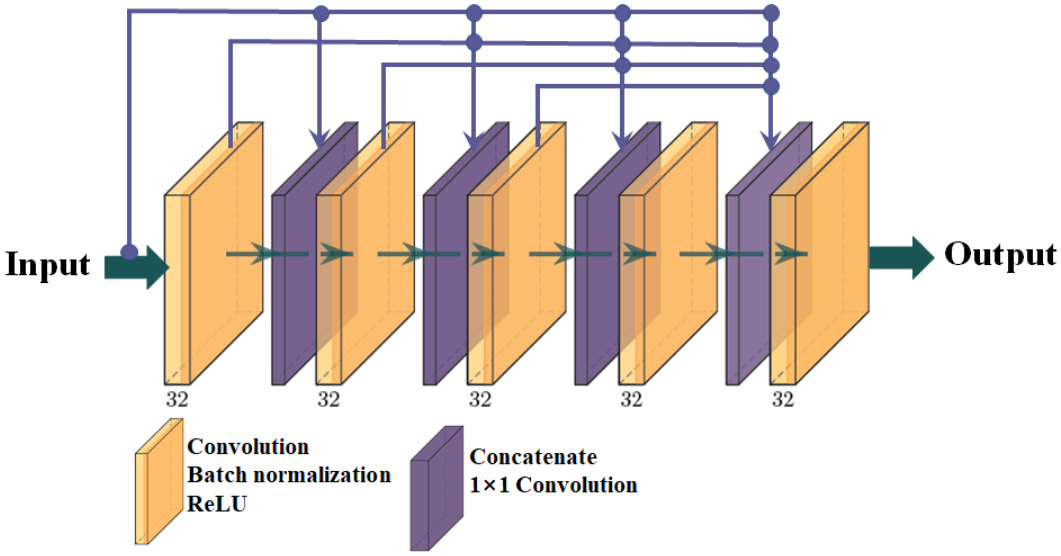


Figure 5.7: Encoder block architecture. The number of kernels are annotated below each convolutional layer. Dots at intersections along the lines indicate connections between layers.

5.4.3 Choroidal neovascularization vessel segmentation using convolutional neural network

The CNN-M output is a membrane probability map. Pixels with probabilities higher than 0.5 were identified as belong to the CNV membrane area. Here, the primary task (locating the mask) is reliant on detection across multiple scales, a challenge distinct from vessel segmentation (since

vessels mostly vary between 1 and 5 pixels in width). The CNN architecture used for membrane segmentation was simplified for CNV vessel segmentation (Fig. 5.8). The pooling layers in the feature merging section were removed to keep the resolution sufficient to segment any CNV vessel. The dilation rate of the atrous kernels were also reduced to $rate = 1,\ 2,\ 4,\ 8$ in the encoder and decision-making blocks.

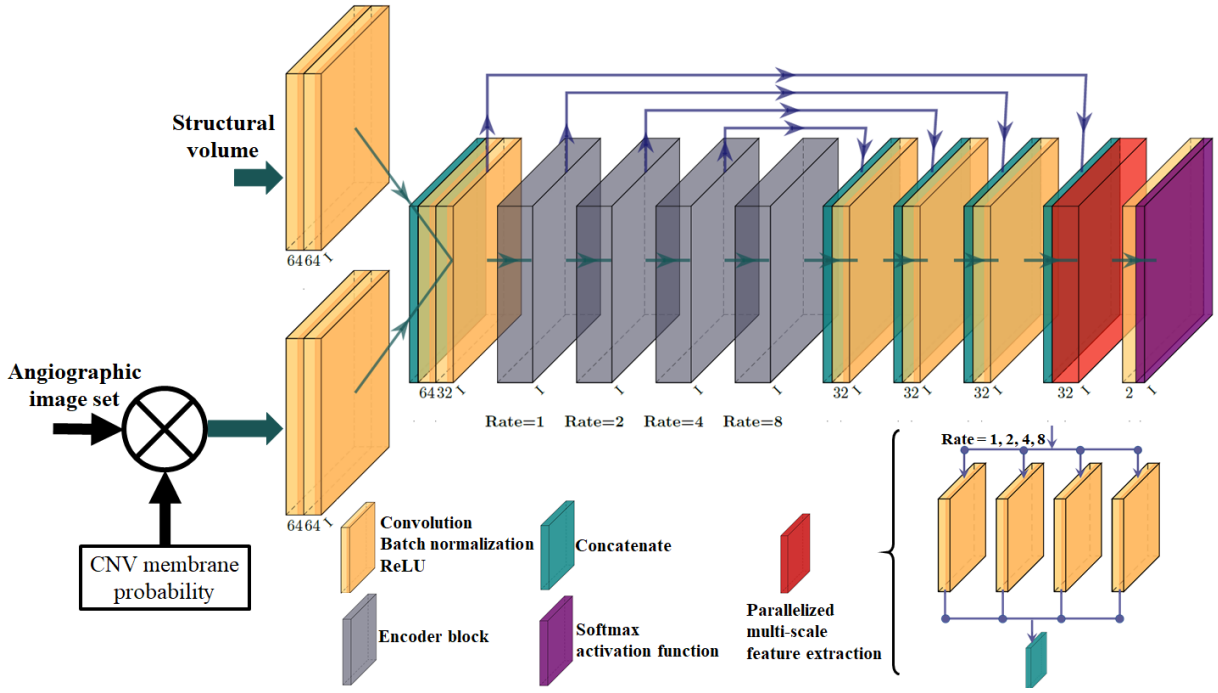


Figure 5.8: Convolutional neural network architecture (CNN) for Choroidal neovascularization vessel segmentation (CNN-V). The atrous kernel sizes ($Rate = 1\ to\ 8$) are annotated below each encoder block. The number of kernels is annotated below the convolutional layer. Label beside the block is the image size; in this case, the network operates on the fully-sized($304 \times 304 - pixel$) image.

5.4.4 Training

(1) *Training dataset*

The training dataset included both CNV and non-CNV control cases. The CNV patients were diagnosed by retinal specialists, with CNV due to AMD visible using PR-OCTA. The non-CNV control cases consist of healthy eyes and other retinal diseases including non-neovascular AMD, DR, BRVO / BRAO, and CSC. A total of 1676 scans including repeat and follow-up scans were collected from same macular area centered on the fovea. We treated the scans obtained from follow up appointments as unique cases as the CNV patterns changed significantly between imaging

sessions. No scan was excluded due to low image quality. The datasets used for training and testing are from completely different eyes (i.e., no single eye was included in both training and testing) and are listed in (Table 5.1). In order to prevent bias, the datasets used for training and testing were randomly selected from the entire dataset. Additionally, while the number of scans used in the test set was smaller, the number of eyes was comparable to the training set. The CNN's good performance on such a unique dataset indicates that the algorithm should be generalizable to other scans and that our results are not artificially inflated due to overfitting. Finally, we also examined the algorithm's performance on individual scans from the testing dataset that exhibit particular features that often confound OCTA data analysis; the algorithm's performance on these representative scans is discussed below.

(2) *Ground truth*

A certified grader, who is an experienced clinician, manually segmented the ground truth CNV membrane used in training. For this purpose, we used PR outer retinal angiograms since these include the fewest projection artifacts. To exclude any remaining artifacts, the grader also referred to the uncorrected original angiograms of the inner and outer retina. For small CNV in low quality scans, B-scans were also reviewed to confirm the CNV position. The CNV membrane area was manually delineated (Fig. 5.9B). The Otsu algorithm with manual correction was applied in the graded CNV membrane area to generate the ground truth of CNV vasculature. To avoid observer bias, the segmentation was reviewed by a second certified grader. If there was any disagreement, the second grader would correct the ground truth and send it back to the first grader for confirmation.

Table 5.1: Dataset for training and testing

	Training		Testing	
	CNV	Non-CNV	CNV	Non-CNV
Eyes/Scans	67/764	430/802	50/50	60/60

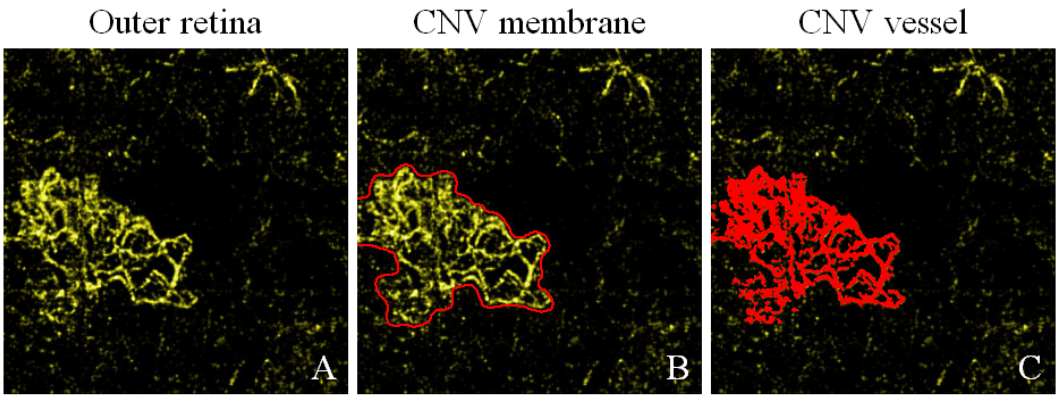


Figure 5.9: Ground truth generation. (A) outer retina angiogram generated from projection-resolved OCTA (PR-OCTA); (B) Choroidal neovascularization (CNV) membrane outline drawn by an expert grader; (C) CNV vessel mask verified by an expert grader.

5.5 Results

5.5.1 Choroidal neovascularization diagnostic accuracy

A highly sensitive algorithm for CNV identification is desirable because missed CNV may result in vision loss that is otherwise treatable. Likewise, high specificity is also desirable for not mistakenly identifying CNV in non-CNV eyes. However, some residual artifacts are inevitable, and may mimic the appearance of CNV and so be erroneously segmented. Because the network used in this study sometimes misidentifies small residual artifacts as CNV, we incorporated a cutoff value for CNV membrane area. Any regions the CNN identified as CNV membranes that were smaller than this cutoff were re-classified as background. This step removed many false positive identifications from our results. We chose the size cutoff value to maximize the detection sensitivity in order to guarantee the fewest number for false negative diagnoses, since conversion to wet AMD is a priority in AMD monitoring. Scans with CNV membrane areas smaller than $0.004mm^2$, which is equivalent to $49 - pixel$ area in image, were not considered to contain CNV. The sensitivity and specificity on our test data were 100% and 95%, respectively (Table 5.2), indicating we successfully achieved the goal of no missed diagnoses on this dataset. The area under receiver operating characteristic curve (AROC) is 0.997, which demonstrates reliable diagnostic performance.

Table 5.2: Choroidal neovascularization (CNV) diagnostic accuracy

CNV membrane area (cutoff value)	Sensitivity	Specificity
$0.004mm^2$	100%	95%

5.5.2 Choroidal neovascularization segmentation accuracy

The CNV membrane segmentation accuracy was evaluated by intersection over union (IOU), precision, recall, and F1 score, which are defined by:

$$IOU = \frac{GT \bigcup Out}{GT \bigcap Out} \tag{5.1}$$

$$precision = \frac{TP}{TP + FP} \tag{5.2}$$

$$recall = \frac{TP}{TP + FN} \tag{5.3}$$

$$F1 = 2 \times \frac{precision \times recall}{precision + recall} \tag{5.4}$$

where, GT is the manually graded CNV membrane and Out is the CNV membrane segmented by the proposed algorithm, TP is true positive, FP is the false positive, and FN is false negative.Overall, the algorithm achieved high scores in each of these metrics (Table 5.3). Comparing with the saliency-based CNV detection method[105], the segmentation accuracy was significantly improved using our proposed method.

Table 5.3: Agreement between choroidal neovascularization (CNV) membrane outputs and ground truth ($mean \pm std$)

	Mean intersection over union(mIOU)	Precision	Recall	F1 score
Proposed method	0.88 ± 0.10	0.95 ± 0.03	0.93 ± 0.11	0.93 ± 0.08
Saliency-based method	0.61 ± 0.23	0.65 ± 0.26	0.94 ± 0.09	0.72 ± 0.24

Repeatability of CNV membrane segmentation performed manually, using the saliency-based method and our proposed method was measured by coefficient of variation (CV) from 28 participants with repeated scans in the testing data and compared in (Table 5.4). Both the ground truth and

proposed method had low CV, which indicated the good performance and repeatability of our proposed method and the reliable ground truth for training.

Table 5.4: Comparison of repeatability among ground truth, saliency-based method and our proposed method

	Ground truth	Saliency-based method	Our proposed method
Coefficient of variation	0.047	0.269	0.069

Data was from 28 participants with repeated scans in the testing data.

In order to better elucidate these results, we also report the proposed algorithm's performance on several exemplar scans exhibiting a variety of features. In the scans with clear CNV vasculature and minor artifacts (Fig. 5.10A), the CNV membrane outline and vascular patterns are prominent. In the CNV membrane probability map obtained from CNN-M, the region with high probability matched well with the CNV membrane area. Multiplying the PR-OCTA outer retinal angiogram with the CNV membrane probability map suppresses residual artifacts outside the membrane area, which improved the reliability of CNV vessel segmentation. It is also apparent that CNN-V was able to remove the noise in the CNV inter-capillary space (Fig. 5.10E1). The proposed method not only demonstrated clear CNV vasculature (Fig. 5.10E1), but also excluded the artifacts surrounding the CNV that might be mis-segmented (Fig. 5.10E2).

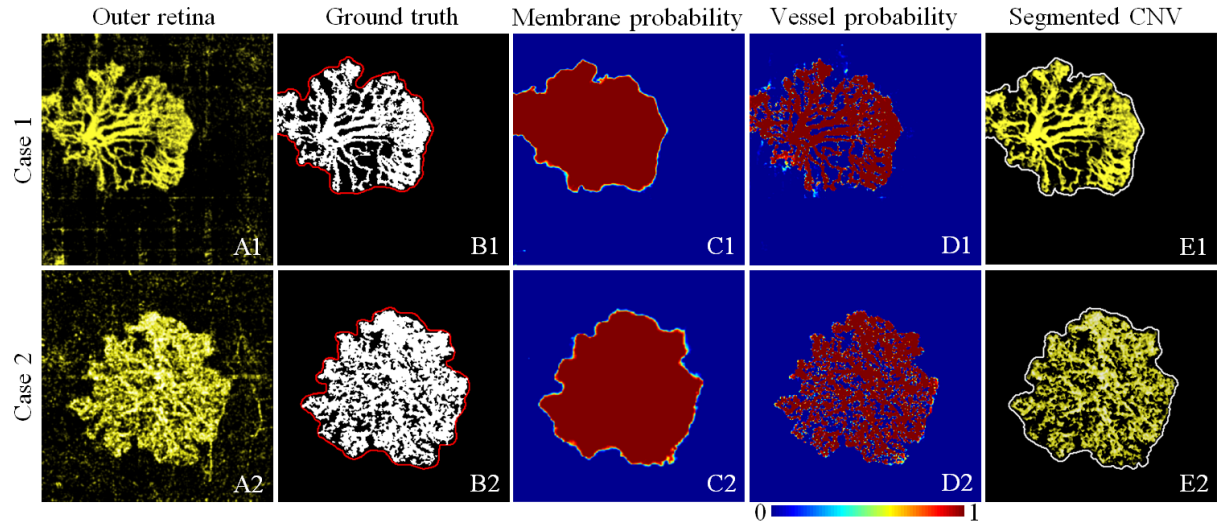


Figure 5.10: Choroidal neovascularization (CNV) segmentation on scans with good image quality. (A) Projection-resolved (PR) outer retinal angiogram; (B) manually delineated CNV membrane (red outline) and vessel (white pixels) ground truths; (C) probability map output by the membrane segmentation convolutional neural network (CNN) (CNN-M); (D) probability map output by the vessel segmentation CNN (CNN-V); (E) segmented CNV membrane (white outline, with $probability > 0.5$) and vessels (with pixels of $probability > 0.5$).

The dataset used in this study also contained challenging scans that our previous saliency-based algorithm had difficulty correctly analyzing. One type of challenge is large CNV membrane area with wide range of flow rates (Fig. 5.11A). Especially in the membrane periphery, where vessels are generally smaller and have only low flow signal, the CNV area is difficult to distinguish. The saliency-based algorithm would both reject such peripheral CNV vessels (creating false negatives), and under-segment gaps in the CNV vasculature (Fig. 5.11A1, highlighted by white star). Using our proposed method, the entire CNV membrane region showed high probability despite the influence of slow flow and large inter-capillary space (Fig. 5.11C1), and the residual projection artifacts were also excluded in the probability map (Fig. 5.11C2). To accomplish this, it was important to include all of the inner and outer retinal (original, slab-subtracted, and PR-OCTA) angiograms in the CNN inputs, since in tandem they could indicate the location of low-flow CNV vessels that might otherwise be mistaken for projection artifacts. After excluding the residual artifacts in the PR outer retinal angiogram, the CNV vessels were further segmented with high probabilities by CNN-V.

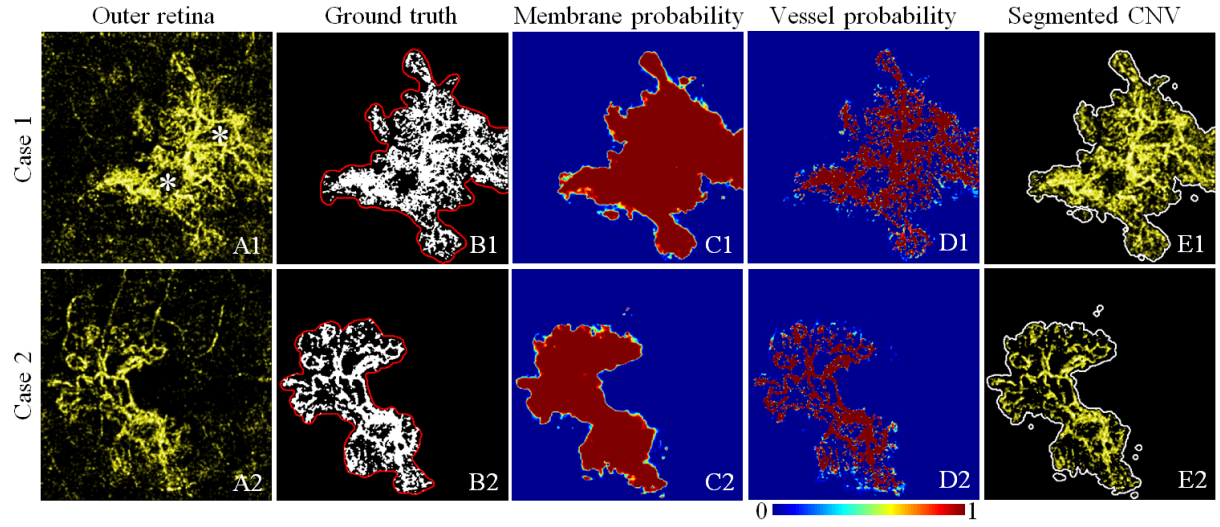


Figure 5.11: Choroidal neovascularization (CNV) segmentation on challenging scans containing a wide range of flow rates. (A) Projection-resolved (PR) outer retinal angiogram; (B) manually delineated CNV membrane (red outline) and vessels (white pixels) ground truths; (C) probability map output by the membrane segmentation convolutional neural network (CNN) (CNN-M); (D) probability map output by the vessel segmentation CNN (CNN-V); (E) segmented CNV membrane (white outline, with $probability > 0.5$) and vessels (with pixels of $probability > 0.5$). Large inter capillary space, highlighted by stars, were correctly included in the membrane area by the proposed algorithm.

Vessels in the CNV membrane with low flow may be faint enough to appear as projection artifacts, but in other cases projection artifacts are obtrusive enough that they appear as prominent as

any vessels in the CNV membrane (Fig. 5.12A). The saliency-based algorithm would mis-segment such artifacts as true CNV (Fig. 5.1A2&B2).Our proposed method can successfully distinguish real CNV from strong residual projection artifacts in CNV cases (Fig. 5.12A1) and a case diagnosed with retinal angiomatous proliferation (Fig. 5.12A2), in which the neovascularization lesion lies on top of these intense residual projection artifacts since it is growing from inner retina down to the outer retina. As in previous example with a large CNV membrane area, including each of the differently processed outer retinal angiograms enabled the trained network to distinguish true CNV from artifacts, since the angiographic image set and outer retinal structural volume yield features that can uniquely identify an artifact and true signal.

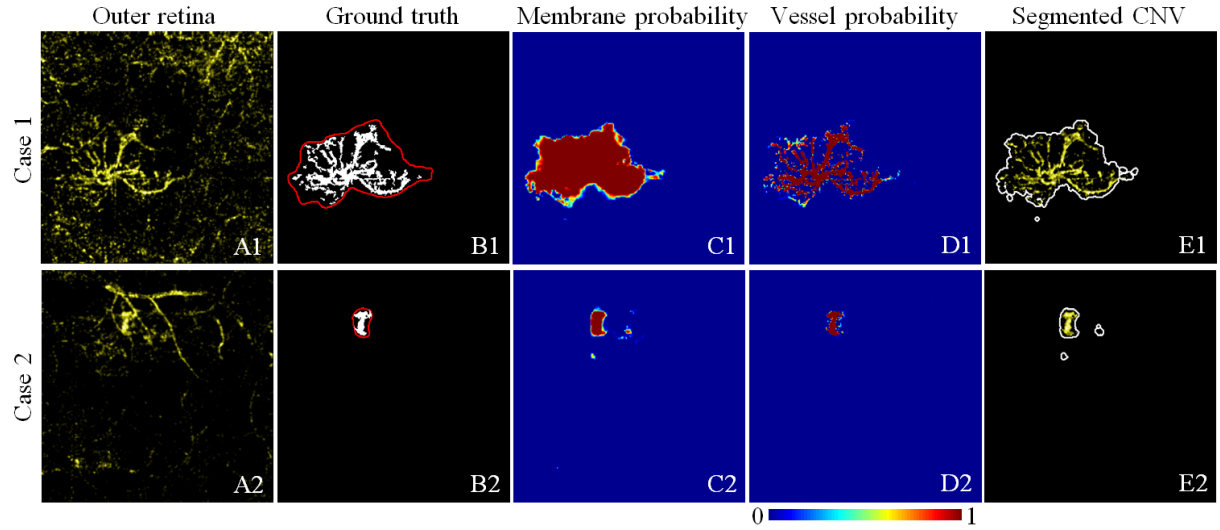


Figure 5.12: Choroidal neovascularization (CNV) segmentation on two cases with strong residual projection artifacts. Bottom row shows a special case with a retinal angiomatous proliferation lesion. (A) Projection-resolved (PR) outer retinal angiogram; (B) manually delineated CNV membrane (red outline) and vessel (white pixels) ground truths; (C) probability map output by the membrane segmentation convolutional neural network (CNN) (CNN-M); (D) probability map output by the vessel segmentation CNN (CNN-V); (E) segmented CNV membrane (white outline, with $probability > 0.5$) and vessels (with pixels of $probability > 0.5$).

Another source of difficulty for CNV analysis is low scan quality (Fig. 5.13A). Two common sources of low scan quality are low signal strength and defocus. Defocus not only causes a reduction in signal strength, but also causes broadening of capillaries and generally makes images less clear (Fig. 5.13A). In defocused scans, the membrane outline is consequently blurred and indistinct. Simultaneously, such low quality scans are problematic for PR-OCTA correction, leading to more prevalent residual projection artifacts. As in the previous examples, the full angiographic image

set was essential for correct exclusion of these artifacts, but as can be seen (Fig. 5.13case2) CNN-M still incorrectly segmented some projection artifacts. However, CNN-V further shrank the artifacts in determining the vessel probability (Fig. 5.13D2), yielding a vessel segmentation that was correct despite the false positive membrane segmentions. With the benefits of CNV membrane and vessel segmentation, the visualization of the CNV on defocused scans was dramatically improved, providing an image with clear boundaries and vasculature.

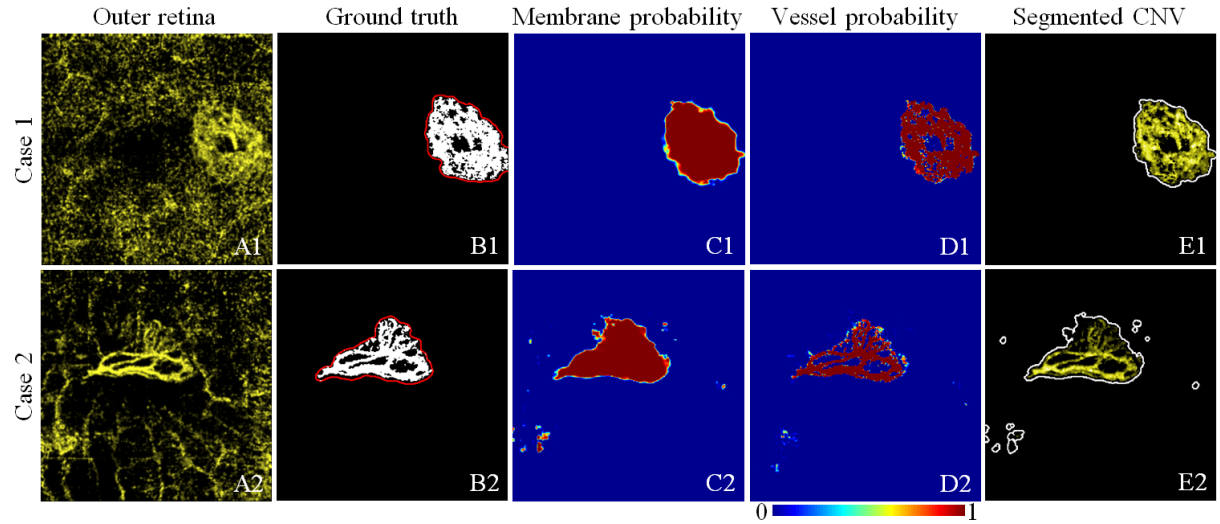


Figure 5.13: Choroidal neovascularization (CNV) segmentation on scans with defocusing. (A) Projection-resolved (PR) outer retinal angiogram; (B) manually delineated ground truth of CNV membrane (red outline) and vessels (white pixels); (C) probability map output by the membrane segmentation convolutional neural network (CNN) (CNN-M); (D) probability map output by the vessel segmentation CNN (CNN-V); (E) segmented CNV membrane (white outline, with $probability > 0.5$) and vessels (with pixels of $probability > 0.5$).

One more important advantage of the proposed algorithm over the saliency-based approach is its ability to correctly omit CNV from scans in which it is not present. These scans are challenging because even in the absence of CNV many scans contain spurious artifactual signal. In particular, in the scans with low SSI, proprietary motion correction technology (MCT) software may fail to suppress motion artifacts after merging one X-fast and one Y-fast scan. In the saliency-based approach these artifacts would be identified as CNV (Fig. 5.1A4&B4), since they appear as bright as real CNV. They also pose problems for differentiating artifact from signal using the angiographic image set used in this study, since they do not share the same relationships between the images as projection artifacts. The inclusion of the outer retinal reflectance image is useful in such cases, since CNV development induces structural changes in the retina that can be used to differentiate afflicted

eyes from either healthy eyes or eyes that have developed different pathology in outer retina. By including the reflectance information as well, the proposed method was able to correctly classify eyes as CNV-free, as shown for a dry-AMD and DR case in Fig. 5.14. These cases are indicative of the proposed algorithm's robust performance, since CNV was not detected in either.

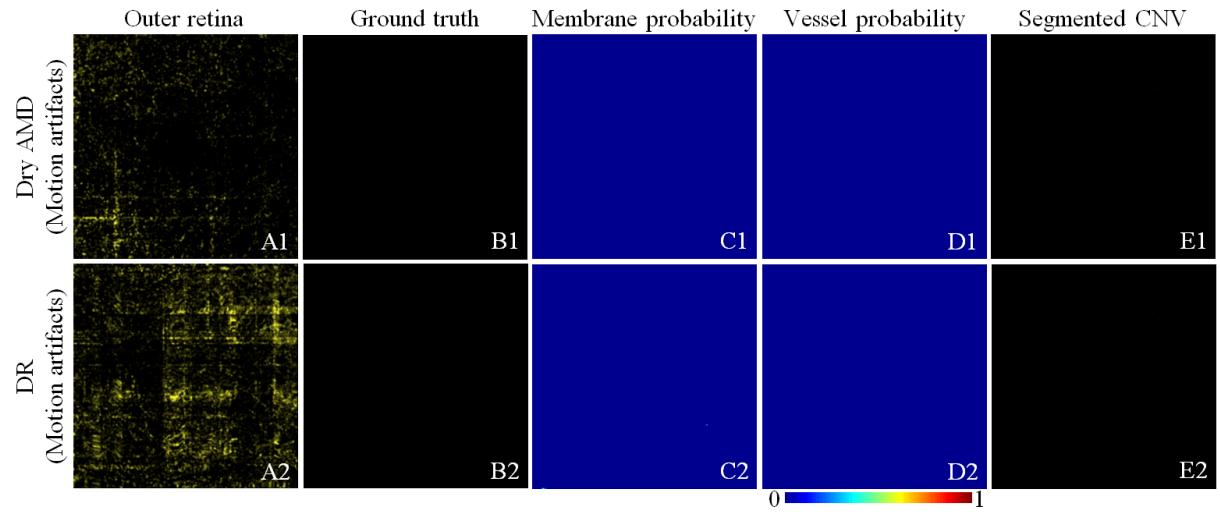


Figure 5.14: The proposed method correctly classifies scans with no choroidal neovascularization (CNV) present. Shown are a case with dry age-related macular degeneration (AMD) (row 1) and diabetic retinopathy (DR) (row 2). No CNV is delineated in ground truths (column B). Despite strong motion artifacts (column A), the proposed method's probability map (column C&D) does not indicate any CNV, and so the algorithm correctly does not segment any membrane or vessels in the output (column E).

5.6 Discussion and conclusion

In this study, we demonstrated a new CNV identification and segmentation algorithm using deep learning. Two tasks were achieved in this work: first, the algorithm was able to classify CNV as absent or present, and secondly the CNV membrane and vessels were successfully segmented. The proposed method accomplished these tasks on a diverse dataset that included both CNV scans and others with different pathologies, and our performance assessment did not exclude any scans due to low image quality. The high sensitivity, specificity, and AROC values reported in these conditions indicate our proposed method achieved robust identification and segmentation.

Since CNV is a vision-threatening development in a common retinal disease, it has been the target of several studies seeking to use OCTA to quantify or visualize its scope. In clinical research, CNV membrane areas are often drawn or segmented by manually adjusted thresholding

[122, 123, 124, 125], but this is time-consuming, particularly since for accurate measurement the effect of artifacts on the OCTA visualization must be carefully considered. At the same time, automation approaches such as the saliency-based approach [70, 98, 105] are readily foiled by the presence of artifacts, which are inevitable in clinical datasets. Because CNV lesions often grow from their periphery, by achieving accurate segmentation of membrane area even when the peripheral vessels are small and dim the algorithm proposed here contributes more to CNV monitoring than the performance metrics evaluated above indicate. Furthermore, to the best of our knowledge, all previous attempts to automate CNV identification have limited their scope to just membrane segmentation. Since CNV vessel morphology is associated with CNV treatment response[126], vessel segmentation is also highly desirable.

We believe that the work presented here represents a significant improvement upon previous CNV detection and segmentation algorithms. We have already discussed the limitations of our saliency-based algorithm [105]. We also previously published a distance mapping approach [127]. This method, in common with the saliency algorithm, was a just an intensity-based algorithm that will necessarily detect some CNV in any input image, and so requires manual classification of images for the presence of CNV. The distance mapping method is also vulnerable to disruptions caused by projection or other artifacts. Our initial efforts on CNV segmentation was conducted on the slab-subtracted outer retinal angiogram [70, 105], and Zhang et al. [71, 128] also proposed a morphology and edge detection based method that relies on slab-subtraction to help mitigate the most egregious effects from projection artifacts. But as noted (Fig. 5.3D), CNV vascular integrity is easily damaged by slab subtraction. Finally, both of these methods, as well as our saliency-based method, relied on hand-crafted features. CNV vascular patterns contain unique features that differentiate them from noise that such approaches cannot, in general, use for segmentation (in contrast to deep learning-based approaches). The use of a CNN can circumvent many of these difficulties. Zhang et al. reported a CNN-based outer retinal structural abnormality detection algorithm that may detect CNV [129]; however, their approach relied exclusively on structural OCT data, which cannot by itself differentiate CNV from other pathologies that cause retinal layer

disorganization. As a result, the specificity of this algorithm for CNV detection in clinical datasets may be compromised.

To the best of our knowledge, we are the first group to diagnose and segment CNV from OCTA using CNNs. By using a varied and information-rich input dataset, including outer retinal volumetric structural data and *en face* angiograms of the inner and outer retina with different levels and methods of error correction, the CNN-based algorithm was able to exclude the remaining projection artifacts and noise from the CNV membrane and vessels. Several other design choices contributed to the high performance of our proposed method. The designed CNNs utilized a modified dense network with atrous kernels in the encoder blocks. Features were extracted across multiple scales by increasing the atrous kernel dilation rate, and parallelized feature extraction across low and high levels helped to accelerate the training progress. The number of kernels was reduced and kept the constant to achieve a deeper networks. Several groups have reported vessel segmentation algorithms [130, 131, 132, 133, 134, 135], including some results based on CNNs[131, 132, 133, 134, 135], these accomplish general vessel segmentation, rather than CNV-specific segmentation. Comparison between these algorithms is therefore misleading, but also difficult due to problems with fairly measuring vessel segmentation against both each other and the ground truth manual segmentation. In particular pixel-scale variation in vascular segmentation for small vessels can lead to low scores for common metrics such as dice coefficient or mean intersection over union, even when the ground truth and algorithm output essentially agree. Furthermore, in such cases there is little reason to prefer either the manually segmented ground truth or any specific algorithm output.

While we achieved highly accurate CNV diagnosis and segmentation, there are several ways that future work could improve upon the results we present here. One issue is that layer segmentation for the ILM, OPL and BM are required in pre-processing. Even though these layers were automatically segmented using a graph-search based algorithm [55, 128], manual correction was sometimes needed to modify the segmentation of BM (for example under large drusen). Future work could focus on improving the automation of this step in order to achieve a fully automated data pipeline. Another issue is quantifying our algorithm's performance. In AMD scans, the entire

CNV membrane area is easily quantified and compared to the manually delineated equivalent to extract, e.g., F1 scores. Similar comparison is difficult for the output vessel masks. Since vessels are thin, small (i.e., pixel scale) discrepancies between the manual graded and CNN outputs can lead to significant differences when evaluating segmentation accuracy. And with small, dim vessels, it is difficult to say which pixels exactly correspond to true flow even for human. It is difficult to tell whether the human graded ground truth or the CNN output is more correct. Quantitative comparisons between solutions generated by manual grading and the CNN are therefore potentially misleading. Still, qualitative comparisons like those presented above speak to reasonable performance.

Despite these limitations, the algorithm proposed in this work accomplishes the essential tasks for which it was intended. Transitioning CNV segmentation to a fully automated approach will not only increase the amount of information available during patient monitoring, but may also reveal previously hidden indicators of CNV progression and prognosis as more data accumulates. Tracing CNV vessels for every patient is not feasible, so the vessel segmentation presented here offers an essential capability if we wish to monitor new and potentially better CNV biomarkers in the clinic.

6 Deep learning for diagnosing and segmenting choroidal neovascularization in optical coherence tomographic angiography in a large real-world dataset

6.1 Abstract

Purpose : To diagnose and segment choroidal neovascularization (CNV) in a real-world multi-center clinical optical coherence tomographic angiography (OCTA) dataset using deep learning.

Methods: A total of 10566 OCTA scans from 3135 eyes, including 4701 with CNV and 5865 without, were collected in 5 eye clinics. Both $3 \times 3 - mm$ and $6 \times 6 - mm$ scans of the central and temporal macula were included. Scans with CNV were collected from multiple diseases, and scans without CNV were collected from both healthy controls and multiple diseases. No scans were removed during training or testing due to poor quality. The trained hybrid multi-task convolutional neural network (CNN) outputs a CNV diagnosis and membrane segmentation, respectively.

Results: The model demonstrated highly accurate CNV diagnosis (area under receiver operating characteristic curve, AROC = 0.97), achieving a sensitivity of 95% at 95% specificity. The model also correctly segmented CNV lesions (F1 score = 0.78 ± 0.19). Additionally, model performance was comparable on both high-definition $3 \times 3 - mm$ scans and low-definition $6 \times 6 - mm$. The model did not suffer large performance variation under different diseases. We also show that a subclinical lesion in a neovascular age-related macular degeneration (AMD) patient can be monitored over a multi-year timeframe using our approach.

Conclusions: The proposed method can accurately diagnose and segment CNV in a large real-world clinical dataset.

Translational Relevance: The algorithm could enable automated CNV screening and quantification in the clinic, which will help improve CNV diagnosis and treatment evaluation.

6.2 Introduction

Choroidal neovascularization (CNV) is pathologic angiogenesis in which abnormal vessels connected to the choroid develop in the outer retina[16, 17, 110, 111, 136]. It can lead to vision loss

This work has been submitted to the Translational Vision Science & Technology.

and blindness, with symptoms including hemorrhage, lipid exudation, fluid exudation, or formation of fibrotic scars[137]. Early diagnosis is key to preventing these outcomes[138]. Gold standard diagnosis currently relies on dye-based angiography, but as an invasive technique this modality is ill-suited for routine examination and screening[139]. Our ability to identify CNV before serious symptoms develop is consequently jeopardized by reliance on dye-based angiography[126].

Recently, optical coherence tomographic angiography (OCTA) has introduced dyeless, depth-resolved *in vivo* imaging of retinal circulatory networks down to capillary scale resolution[43]. In contrast to dye-injection modalities, OCTA procedures are non-invasive, rapid, and inexpensive-each exceptional qualities for a screening technology. Furthermore, OCTA is capable of detecting subclinical CNV[116], and OCTA measurements of CNV lesion complexity and size are predictive of treatment response[114, 126]. Nonetheless, CNV diagnosis using OCTA faces several challenges. CNV identification may require clinicians and graders to review cross-sectional scans[140]. Because a single OCTA data volume typically contains hundreds of cross-sectional scans, manual identification may be time consuming. This issue is exacerbated by the presence of artifacts in OCTA data[34, 48]. In particular, projection artifacts can cause specious flow signal that mimics the morphology of superficial vasculature to appear in the outer retina. Such artifacts can be confused for true CNV or obscure its signal.

Fortunately, these concerns can be alleviated by well-designed software solutions. The reported methods for CNV classification/segmentation were conducted with dye-based indocyanine green angiograph (ICGA)\fluorescein angiograph (FA), optical coherence tomography (OCT), and OCTA[18, 65, 70, 71, 105, 114, 127, 128, 141, 142, 143, 144, 145, 146, 147]. Limitations for CNV analysis using FA and ICGA[18, 142, 143, 144] include (1) a restriction to two-dimensional (2D) imaging modality projects the three-dimensional (3D) features onto a 2D plane, (2) detection reliant on the appearance of hyperfluorescence caused by CNV vessel leakage, which obscures CNV vessels at the capillary level. Reliance on dye leakage also limits the ability of these methods to diagnose and characterize non-exudative CNV lesions. Structural OCT also has important limitations for CNV diagnosis and quantification[145, 146, 147]. While it can display retinal pigment epithelium layer

(RPE) degeneration caused by CNV, pathological features caused by non-exudative CNV appear similar to drusen in structural OCT. More importantly, structural OCT does not provide flow information. OCTA does, and depth resolves them. This capability enables automated typing of CNV lesions in eyes in that have been diagnosed with exudative CNV[145]. However automated OCTA CNV analysis platforms also have limitations[65, 70, 105, 114, 127, 128]. Projection artifacts in uncorrected OCTA can cause CNV diagnosis and segmentation to go awry, although these artifacts can themselves be used to identify CNV[148]. OCTA and structural OCT are best combined so that both RPE loss to exudation and capillary scale vasculature can be directly considered[65, 145]. The reported CNV diagnosis\segmentation methods can also be classified into two categories, rules-based[70, 71, 105, 127, 128, 147] and deep learning-based methods[65, 145, 146]. The relative efficacy of these different approaches remains to be assessed and will of course depend on the nature of the algorithms being compared. However, in our previous study a rules-based method could fail on challenging scans with strong residual artifacts or large CNV lesions, and was incapable of differentiating CNV signal from residual artifacts[105, 114]. On a similar data set and using similar inputs we reported a convolutional neural network (CNN) that avoided these drawbacks. These advantages may be a result of the relative utility of each approach (i.e. deep learning offers greater context sensitivity and can learn complex features that are not easily captured through codified rules), and it should be further noted that deep learning approaches have consistently outperformed rules-based approaches in image analysis tasks for some time[149]. For these reasons it is likely that our experience (deep-learning methods outperforming rules-based) may be usual. However, the previous deep learning-based study was limited to a small dataset consisting exclusively of $3\times3-mm$ macular scans of age-related macular degeneration (AMD) patients[65]. But $3\times3-mm$ scans typically have higher image quality than the larger scan sizes that are also frequently used in the clinic, and CNV is not an AMD-specific pathology.

In this study we developed and validated a hybrid multi-task CNN model for both CNV diagnosis and membrane segmentation. We evaluated performance using a real-world clinical dataset consisting of 10566 OCTA scans from 3135 eyes collected at 5 eye clinics. This dataset included not just eyes diagnosed with neovascular AMD, but also several other diseases in which

CNV is implicated. Likewise, controls without CNV present consisted of not just healthy eyes, but also eyes diagnosed with other common and rare retinal diseases.

6.3 Methods

6.3.1 Dataset

The dataset used in this work was collected from multiple eye institutes, including the Casey Eye Institute, Oregon Health Science University, Portland OR, USA; Shanxi Eye Hospital, Taiyuan, Shanxi, PR China; Zhongshan Ophthalmic Center, Sun Yat-Sen University, Guangzhou, Guangdong, PR China; Tongren Hopital, Beijing, PR China, and the Department of Ophthalmology, Aichi Medical University, Nagakute, Japan. OCTA scans with CNV were identified by retina experts (please see section 2.3) in multiple retinal diseases, including neovascular AMD, pathological myopia, and polypoidal choroidal vasculopathy (PCV). Remaining cases were associated with rare diseases including macular telangiectasia, choroideremia, pattern dystrophies, acute multifocal placoid pigment epitheliopathy, vitelliform macular dystrophy, Doyne honeycomb retinal dystrophy, chorioretinitis, angioid streaks, and familial dominant drusen. Control scans without CNV were collected and identified from healthy eyes and eyes with DR, non-neovascular AMD,branch retina vein occlusion (BRVO), central retina vein occlusion (CRVO), branch retina arterial occlusion (BRAO), central retina vein occlusion (CRVO), retinitis pigmentosa, central serous chorioretinopathy (CSC), or birdshot chorioretinopathy.

This study was conducted in compliance with Declaration of Helsinki. Participants were scanned using a $70 - kHz$ commercial spectral-domain OCTA system (RTVue-XR; Optovue, Fremont, CA) with a central wavelength of $840nm$. Both $3 \times 3 - mm$ and $6 \times 6 - mm$ scans of the central and temporal macula were included. The temporal macular data was included to improve the dataset diversity, as choroidal neovascularization (CNV) can occur at this location as well. Two sets of B-frames were acquired at the same position and the split-spectrum amplitude decorrelation angiography (SSADA) was utilized to generate optical coherence tomographic angiography (OCTA) signal[43]. One X-Fast and one Y-Fast volume were acquired and registered to suppress motion artifacts[76]. In $3 \times 3 - mm$ scans, each optical coherence tomography (OCT)/OCTA volume

included 304 B-frames and each B-frame included 304 A-lines, providing $\sim 10um/$line sampling density. Sampling density was reduced in half ($20um/$line) in $6 \times 6 - mm$ scans. Repeat and follow-up scans centered on the same area were included in the dataset. The follow-up scans were treated as unique samples, since the CNV patterns noticeably changed. No single sample was included in both training and testing. No scans were excluded due to low image quality.

6.3.2 Preprocessing

Projection artifact removal is an essential pre-processing step for generating anatomically accurate angiograms of plexuses beneath the superficial vascular complex (Fig. 6.1 A). In this work the projection-resolved OCTA (PR-OCTA) algorithm[73] removed projection artifacts volumetrically while preserving real flow signal, enabling clear presentation of the choroidal neovascularization (CNV) vasculature. In order to produce structural or angiographic *en face* images or volumes of specific anatomic slabs retinal layer segmentation is also required in preprocessing. Our algorithm requires segmenting the inner limiting membrane (ILM), outer border of the outer plexiform layer (OPL), and Bruch's membrane (BM). This was done using a graph-search based algorithm implemented in our COOL-ART custom-designed optical coherence tomographic angiography (OCTA) reading software[1]. Segmentation errors on the challenging scans were manually corrected using the same software. In this work we distinguish between the inner retina, defined as the slab between the boundaries of the ILM and outer border of OPL, and the outer retina, which is the slab between the boundaries of outer border of OPL and BM. In healthy eyes the inner retina is vascularized, while the outer retina is avascular.

6.3.3 Ground truth label generation

The ground truth CNV diagnosis and membrane segmentation (Fig. 6.1 A) were generated from projection-resolved (PR) outer retinal OCT angiograms graded by two experts. To exclude residual artifacts, the graders also referred to the inner retinal angiogram. The first grader (KT) labeled the CNV scans and also drew the CNV membrane area. The second grader (TTH) reviewed and refined the first grader's labels. Questionable scans were reviewed in collaboration. B-scans were also referenced to confirm the position of CNV in unclear or low-quality scans.

6.3.4 Deep learning model for choroidal neovascularization diagnosis and segmentation

The proposed hybrid multi-task CNN model achieves two tasks: (i) CNN diagnosis and (ii) CNV membrane segmentation (Fig. 6.1 C). The architecture includes several sub-nets: one each for 3D and 2D feature extraction, bridge sub-nets to integrate the 2D and 3D features, and a sub-net each for CNN diagnosis and membrane segmentation. In the 3D to 2D feature compression sub-net, mean and maximum projection operations are applied to extract important and general features from the volume; these features are input into the 2D feature extraction sub-net. This allows the proposed model to learn to identify volumetric features useful for projection on to 2D images. Since the dataset included two different fields of view (3×3 and $6 \times 6 - mm$), we incorporated feature extraction at two different scales (3×3 and 5×5 convolution kernels with depth 4 and 6, respectively). This improved the network's ability to learn relevant features from both input field of view sizes. In the last step, the extracted features were fed into one Res-Net[150] sub-net for CNV diagnosis and into a U-Net[151] sub-net for CNV membrane segmentation. Both the segmentation and diagnosis errors were evaluated by the categorical cross-entropy, and training loss was the average of the segmentation and diagnostic error.

An important part of our algorithm's design is the incorporation of a large but relevant input library consisting of both OCT/OCTA volumes and their 2D projections. For the 2D input arm, the OCTA inputs to our algorithm consist of four *en face* angiograms: (1) the inner and (2) outer retinal uncorrected OCTA angiograms, (3) the slab-subtracted outer retinal angiogram [70, 71, 98], and (4) the projection-resolved (PR) outer retinal angiogram [73] (Fig. 6.1 B). Both slab subtraction and PR-OCTA are processing techniques used to remove projection artifacts. Including both methods, as well as uncorrected angiograms, provides a set of images that can help unambiguously distinguish CNV. The uncorrected inner and outer retinal angiogram can be used to identify projection artifacts, as the projection artifacts in the uncorrected outer retinal angiogram are duplicated in the vascular pattern in the inner retinal angiogram. The uncorrected outer retinal angiogram may also include true flow suppressed by the slab-subtracted or PR solutions. However, in uncorrected angiograms the true CNV signal is often obscured by overlying projection artifacts. In slab-subtraction processing,

the (scaled) inner retinal flow signal is subtracted from the outer retinal angiogram; this preserves the most significant CNV features but less prominent features may be removed. The PR outer retinal angiogram is able to provide a clear image of the CNV vascular pattern, but residual projection artifacts could still be confused with the real CNV signal.

The network also takes 2D structural OCT projections and thickness information as input for the 2D subnet (Fig. 6.1 B). Pathologic changes in reflectivity are associated in particular with exudative CNV, so structural images can also help identify CNV lesions. In order to preserve some depth information for the network to learn, we split the structural volume into 10 equal partitions, using mean projection to obtain the *en face* images. The mean projection of the entire structural volume and inner retina were also included. The width of different anatomic layers is also often modulated by the presence of a CNV membrane. Thickness maps for both the inner and outer retina can therefore also help identify CNV lesions, and these maps were included in the model input. Additionally, thickness maps can further help the network recognize projection artifacts since they often coincide with retinal pigment epithelium elevations [65].

Finally, the 3D input arm accepts the outer retinal structural OCT and PR-OCTA volumes with A-lines were resampled to identical sizes (Fig.6.1 B). These volumes were used enable the network to learn the complete spatial information latent in the data.

6.3.5 Implementation

The loss of both the CNV diagnosis and segmentation were calculated by the cross-entropy function, and the training loss defined as the average of CNV diagnosis and segmentation losses. During the training, the Adam optimizer was utilized to accelerate convergence. Batch normalization was also applied to help prevent over-fitting and improve generalization capability. A learning rate decay of 10^{-1} was used to achieve optimal parameters, and the minimum learning rate was 10^{-6}.

The designed CNN was implemented using TensorFlow with an intel $i9-10980XE@3.0GHZ$, DDR4 $256GB$ RAM, and Nvidia Quadro RTX 8000 graphics card (4608 CUDA cores, $48GB$ GDDR6 memory).

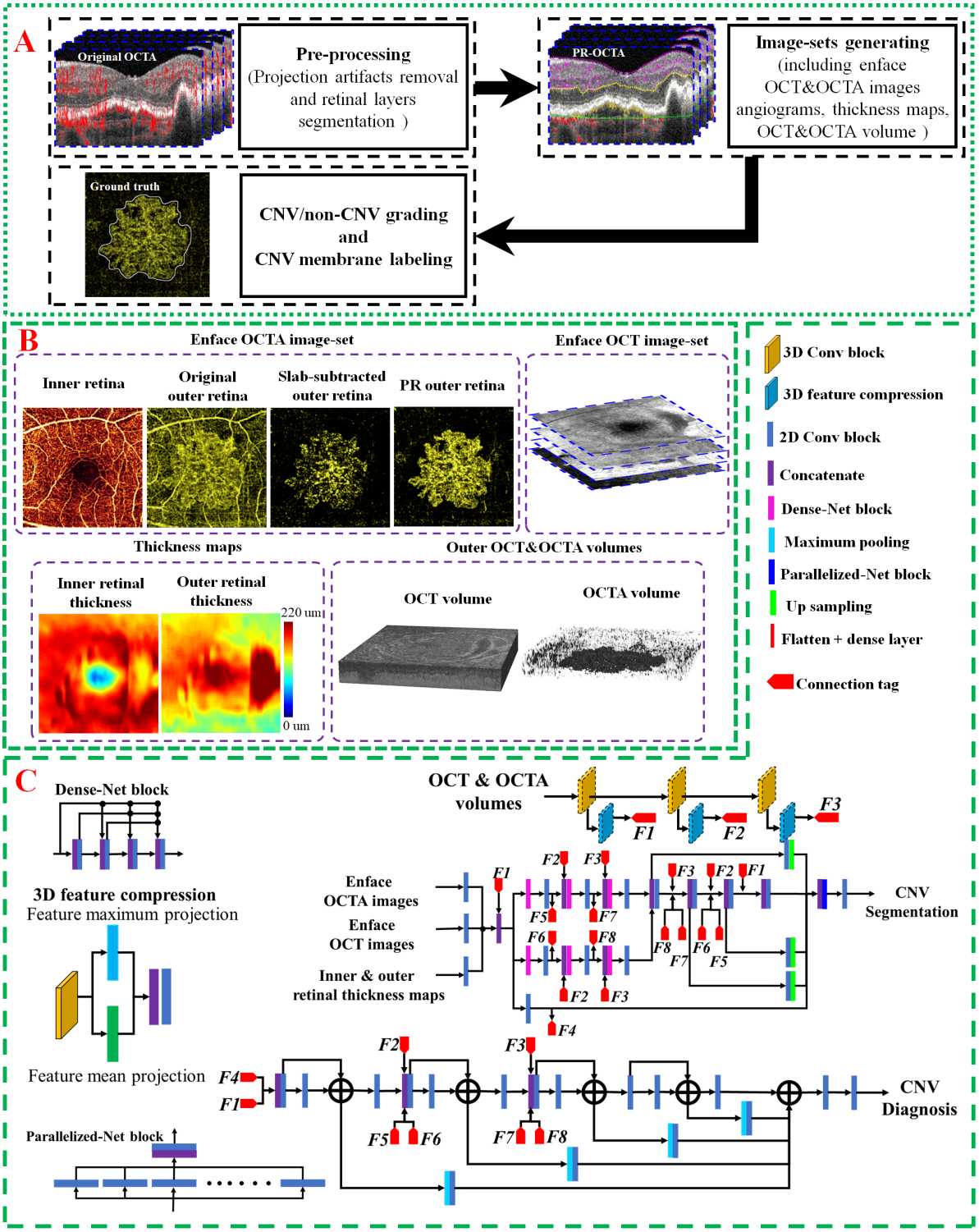


Figure 6.1: Proposed CNV diagnosis and segmentation method. (A) OCTA data is pre-processed by removing projection artifacts and segmenting retinal layers; OCTA scans were further graded as CNV/non-CNV scans and CNV membrane area was outlined in projection-resolved (PR) outer retinal angiogram. (B) Model inputs consist of an *en face* OCTA image-set, thickness maps, an *en face* structural OCT image-set, and outer retinal OCT&OCTA volumes. The OCTA image set consists of uncorrected inner and outer retinal angiograms, a slab subtracted outer retinal angiogram, and a PR outer retinal angiogram, all produced using maximum projection. The structural OCT image set includes *en face* mean projections of ten equal partitions of the entire data volume as well as a mean projection covering just the inner retina, and a mean projection of the entire volume. (C) The proposed hybrid multi-task CNN model combines 3D and 2D convolution; the feature extraction block is shared between the CNV diagnosis and membrane segmentation modules. F1-F8 are tensor connection tags.

6.4 Results

6.4.1 Study population

A total 10566 OCTA scans from 3135 eyes were collected, including 4701 scans with CNV and 5865 without (Table 6.1& 6.2). Repeat and follow-up centered on the same area were included in the dataset. The follow-up scans were treated as unique samples since these scans showed large, apparent changes in the CNV vascular patterns. The enrolled OCTA scans have a wide range of signal strength index (SSI) ($34 \leq$ SSI ≥ 95).

Table 6.1: Dataset enrolled in the study

Disease (scans)	Scan size	Scans	Samples	Eyes	Patients
choroidal neovascularization (CNV)	$3 \times 3 - mm$	2457	1184	362	323
	$6 \times 6 - mm$	2244	1436	519	439
non-CNV	$3 \times 3 - mm$	4606	3589	1664	1078
	$6 \times 6 - mm$	1259	1163	590	472

Table 6.2: Choroidal neovascularization (CNV) data enrollment in retinal diseases

Disease (scans)		nAMD	Pathological myopia	PCV	Rare disease
CNV	$3 \times 3 - mm$	1927	41	273	216
	$6 \times 6 - mm$	1620	298	198	128

nAMD: Neovascular age-related macular degeneration (AMD); PCV: Polypoidal choroidal vasculopathy.

6.4.2 Overall performance evaluation of choroidal neovascularization diagnosis and membrane segmentation

Five-fold cross-validation was applied to test the performance of the proposed model on the entire dataset. Individual samples were included in either only the training or only the testing dataset. Diagnostic sensitivity was 95% and with 95% specificity, and the area under receiver operating characteristic curve (AROC) is 0.97 (Table 3). CNV membrane segmentation performance was evaluated by measuring the intersection over union (IOU) and F1 score defined by:

$$\begin{bmatrix} \text{IOU} = \dfrac{GT \bigcup Out}{GT \bigcap Out} & \text{Precision} = \dfrac{TP}{TP + FP} \\ \text{Recall} = \dfrac{TP}{TP + FN} & \text{F1 Score} = 2\dfrac{\text{Precision} \times \text{Recall}}{\text{Precision} + \text{Recall}} \end{bmatrix} \tag{6.1}$$

where, GT is the ground truth membrane segmentation and Output is the segmentation predicted by the proposed model, TP is a true positive, FP is a false positive, and FN is a false negative. The

IOU measures the overlap between the ground truth and model predictions, precision measures the rate of correctly segmented CNV area in the output, recall measures the rate of correctly segmented CNV area within the ground truth CNV membranes, and F1 score measures the segmentation accuracy by taking into account both precision and recall. In general, there was agreement between the model predictions and the ground truth (Table 6.3). The average IOU was 0.66 and the F1 score was 0.78 (Table 6.3). The F1 score was 0.79 ± 0.23 on both $3 \times 3 - mm$ and $6 \times 6 - mm$ scans with SSI ≥ 50. However, even if we consider low quality scans (SSI < 50), the F1 score was 0.73 ± 0.22, which indicates that the CNV membrane prediction was usually essentially correct. We evaluated the methodological contributions of the proposed model using ablations by excluding the 3D and 5×5 feature extraction sub-nets, separately. Both the 3D sub-net and 5×5 feature extraction sub-nets contribute to both CNV diagnosis (Delong's method[152], $p < 0.01$) and membrane segmentation (t-test, $p < 0.01$).

Table 6.3: Overall performance of choroidal neovascularization (CNV) diagnosis and membrane segmentation

CNV diagnosis		CNV membrane segmentation		
Model	AROC	Sensitivity	IOU	F1 Score
Proposed CNN model	0.97	0.95	0.66 ± 0.24	0.78 ± 0.19
With 5×5 sub-net excluded	0.97	0.91	0.61 ± 0.27	0.72 ± 0.26
With 3D sub-net excluded	0.96	0.89	0.60 ± 0.28	0.70 ± 0.28

AROC: Area under receiver operating characteristic curve, IOU: Intersection over union.

A majority of scans were accurately segmented and diagnosed with high confidence (Fig. 6.2 row 1). Under-segmentation mostly occurred when CNV vessels with weak signal co-occurred with strong residual projection artifacts (Fig. 6.2 row 2). Over-segmentation usually resulted from some confusion with non-CNV pathology (e.g. drusen being included in the segmentation result), or in scans with only indistinct CNV due to either weak signal or strong residual artifacts (Fig. 6.2 row 3). Finally, the major cause for large errors was low contrast between CNV vessels and background (Fig. 6.2 row 4). The cases that in which the network performed poorly often also required time consuming review of cross-sectional scans in order to achieve accurate ground truth segmentations, indicating that these scans were also difficult for human graders to analyze.

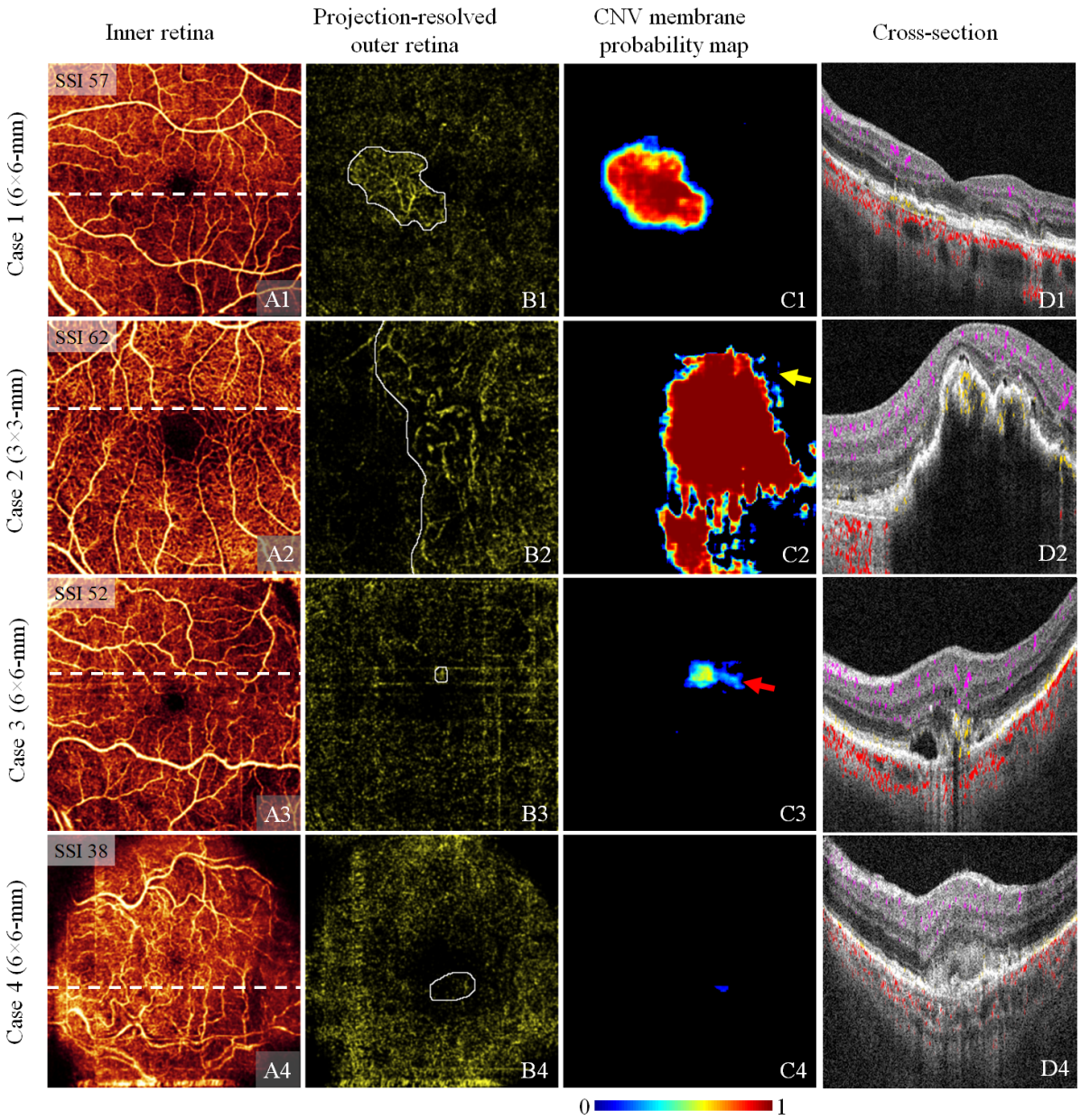


Figure 6.2: Example choroidal neovascularization (CNV) membrane segmentation results. (Column A) Inner retinal angiogram; (B) projection-resolved outer retinal angiogram with CNV membrane ground truth (white outline); (C) output CNV membrane probability map; (D) structural OCT cross-section at the location of the white line in A, with flow signal overlaid (violet: inner retinal; yellow: pathological outer retinal; red: choroidal). Row 1: example in which the network achieved an accurate segmentation. Row 2: example of a under segmentation. The lesion in this scan extended beyond the optical coherence tomographic angiography (OCTA) scan's field of view, which may be difficult for the network to properly analyze due to the truncated nature of the information available at the edge of the image. Row 3: an example of over-segmentation and low prediction confidence in the CNV membrane area. Note that the pathologic flow signal in the outer retina was of similar magnitude to the background in this scan, making analysis difficult. Row 4: an example of a segmentation error in an extremely low-quality scan. This eye exhibits extreme defocus and a large number of residual artifacts. Note that the network did make a low confidence prediction of a CNV membrane in a region that overlapped with the ground truth.

6.4.3 Performance of choroidal neovascularization diagnosis and membrane segmentation on different scan sizes

We evaluated performance separately on both $3 \times 3 - mm$ and $6 \times 6 - mm$ scans that were acquired at the same visit. The CNV diagnostic sensitivities were 99% and 90% in $3 \times 3 - mm$ and $6 \times 6 - mm$ scans with 95% specificity, respectively. Both the CNV diagnosis and membrane segmentation accuracy were higher in $3 \times 3 - mm$ scans (Table 4, $p - value < 0.01$); this could indicate that better image resolution with a more detailed CNV flow signal helped to improve CNV diagnostic and the segmentation accuracy.

Table 6.4: Performance of choroidal neovascularization (CNV) diagnosis and membrane segmentation on different scan sizes

Scan size	CNV diagnosis		CNV membrane segmentation	
	AROC	Sensitivity	IOU	F1 Score
$3 \times 3 - mm$	0.97	0.99	0.69 ± 0.23	0.80 ± 0.19
$6 \times 6 - mm$	0.95	0.90	0.63 ± 0.24	0.76 ± 0.20

AROC: Area under receiver operating characteristic curve, IOU: Intersection over union.

Both scan sizes face challenges for CNV diagnosis and segmentation. Small scans may fail to capture the entire extent of a CNV lesion (Fig. 6.3 case1 B1). On the other hand, $6 \times 6 - mm$ scans in commercial systems are typically obtained with under-sampling, leading to reduced signal-to-noise ratios and an increase in the quantity and severity of artifacts. While our model does suffer some performance decline on larger scans, the segmentation remains accurate on average. The model can therefore be used to effectively evaluate CNV progression even as lesions grow to cover regions larger than typical $3 \times 3 - mm$ scan patterns (Fig. 6.3 C1&C2).

6.4.4 Performance of choroidal neovascularization diagnosis and membrane segmentation on different diseases

We also investigated model performance in different diseases and with different pathologies (Fig. 6.4). The model achieved similar, high performance among the different retinal diseases, including both leading causes of blindness (AMD) [153, 154, 155, 156], a pathology that is difficult to image with OCTA (PCV)[66, 157, 158, 159], and rare diseases. The outputs of the CNV diagnostic probabilities were similar in different diseases (Table 6.5, $p - value > 0.10$). The CNV membrane segmentation accuracy of rare diseases was better than other three diseases ($p - value <$

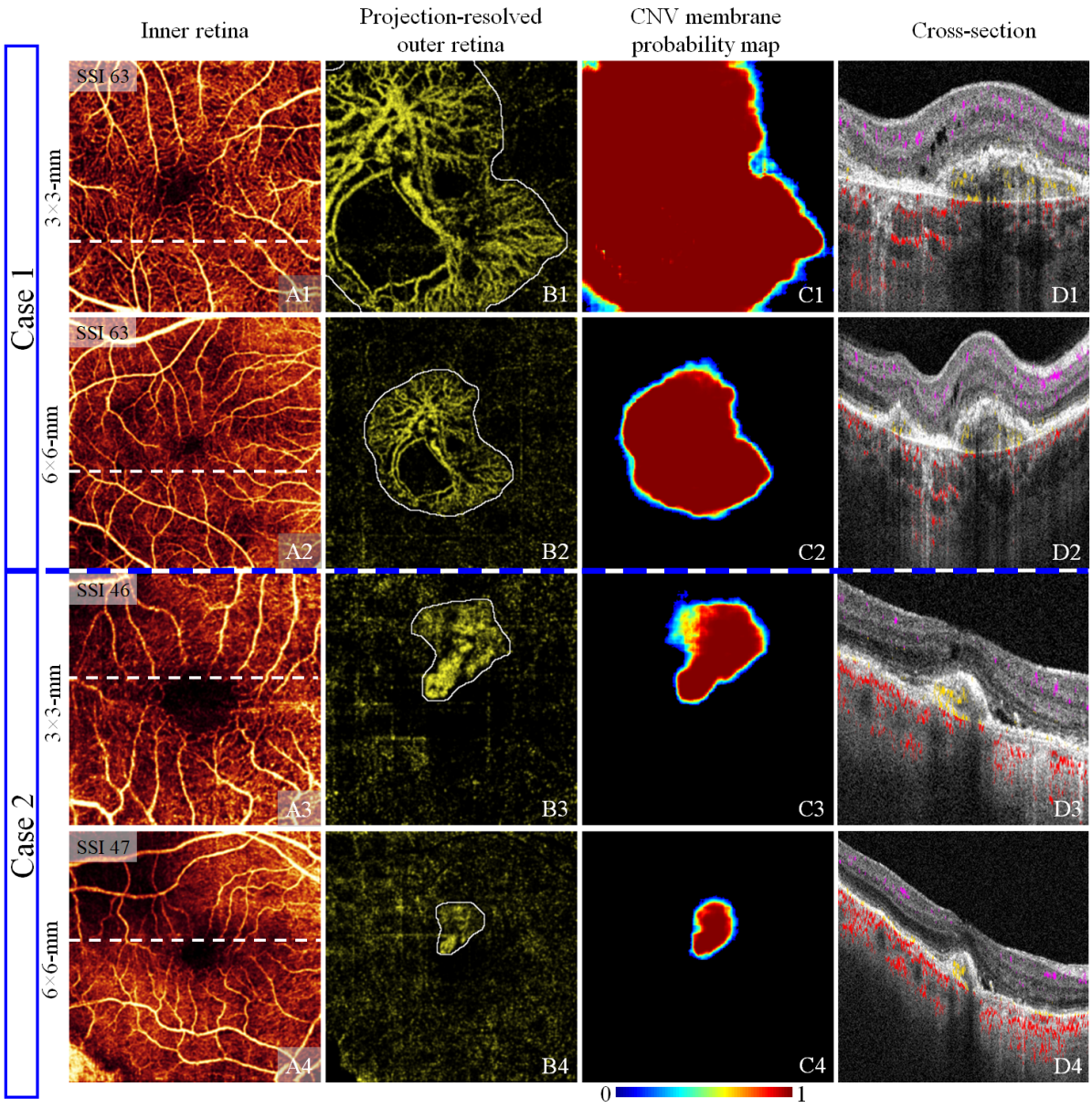


Figure 6.3: Choroidal neovascularization (CNV) membrane segmentation on both $3 \times 3 - mm$ and $6 \times 6 - mm$ scans. (A) Inner retinal angiogram; (B) Projection-resolved outer retinal angiogram with CNV membrane ground truth (white outline); (C) CNV probability map; (D) Structural OCT cross-section at the location of the white line in (A), with flow signal overlaid (violet: inner retinal; yellow: pathological outer retinal; red: choroidal). Case 1 shows a large CNV lesion that cannot be fully imaged using a small scanning window. Case 2 shows a small CNV lesion in a defocused scan with strong residual artifacts. Both cases at both resolutions resulted in correct detections. SSI: Signal strength index.

0.05), which can be explained the best image quality of rare diseases scans ($p - value < 0.01$) helped to increase the CNV segmentation accuracy.

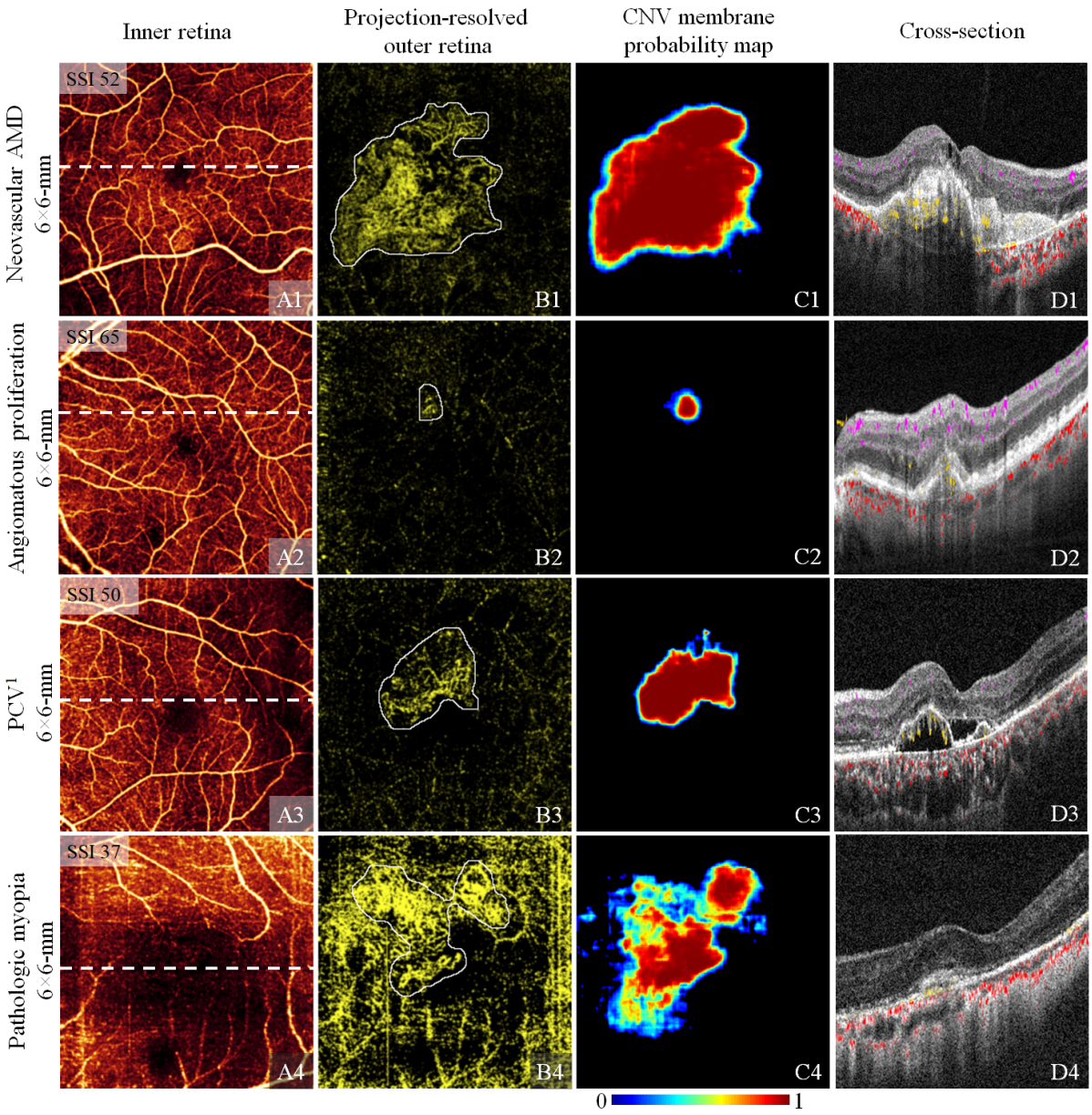


Figure 6.4: Choroidal neovascularization (CNV) membrane segmentation results in several retinal diseases. (A) Inner retinal angiogram; (B) Projection-resolved outer retinal angiogram with CNV membrane ground truth (white outline); (C) CNV probability map; (D) Structural optical coherence tomography (OCT) cross-section at the location of the white line in (A), with flow signal overlaid (violet: inner retinal; yellow: pathological outer retinal; red: choroidal). Row 1: Example segmentation in neovascular age-related macular degeneration (AMD). Row 2: Example segmentation in angiomatous proliferation. The identity of the lesion is best appreciated in the cross sectional image (D2). Despite the small lesion size, this scan resulted in a correct prediction. Row 3: Example segmentation in polypoidal choroidal vasculopathy (PCV). Flow signal in PCV is often very weak, which makes it difficult to distinguish from background (B3). Row 4: Example segmentation in pathologic myopia. Eyes with pathologic myopia often suffer from extreme defocus in optical coherence tomographic angiography (OCTA) imaging (A4, B4). The residual artifacts in these scans probably account for the relatively low performance (C4). SSI: Signal strength index.

Table 6.5: Performance of choroidal neovascularization (CNV) diagnosis and membrane segmentation on different diseases

Diseases	CNV diagnosis		CNV membrane segmentation	
	AROC	Sensitivity	IOU	F1 Score
nAMD	0.97	0.95	0.66 ± 0.24	0.78 ± 0.19
pm-CNV	0.96	0.94	0.64 ± 0.23	0.76 ± 0.20
PCV	0.96	0.96	0.65 ± 0.22	0.77 ± 0.19
Rare diseases	0.94	0.90	0.76 ± 0.17	0.83 ± 0.14

nAMD: Neovascular age-related macular degeneration (AMD); pm-CNV: Pathological myopia CNV; PCV: Polypoidal choroidal vasculopathy; AROC: Area under receiver operating characteristic curve; IOU: Intersection over union.

6.4.5 Clinical application

A growing number of CNV vascular pixels predicts exudation11. Using the proposed method, we segmented CNV membrane areas on $3 \times 3 - mm$ OCTA scans acquired from a neovascular AMD patient who had 46 months of follow-up visits, and also generated CNV vessel masks using the Otsu algorithm[81] within the membrane areas (Fig. 6.5). The CNV membrane and vascular areas were very small when they were first identified but grew rapidly. Conversion to exudative CNV was observed at a $6 - month$ follow-up visit. The patient was subsequently treated with anti-VGEF therapy. Following treatments, the CNV pattern changed dramatically, with the CNV vessel area growing more slowly than the membrane area.

6.5 Discussion and conclusion

In this study, we developed a hybrid multi-task CNN model for CNV diagnosis and membrane segmentation. The proposed model was tested on a realistic clinical dataset and showed reliable CNV diagnosis and membrane segmentation. The overall AROC of segmentation was 0.97 and the primary CNV membrane area was detected with a 0.78 F1 score.

Several novel features contributed to the model's accurate CNV diagnosis and membrane segmentation.

First, the proposed model was trained with a real-world, diverse dataset containing over $10,000$ scans. These scans were collected from multiple eye clinics, included multiple eye diseases, and spanned a large range of image qualities. Since no scans were excluded due to quality, many kinds of artifacts that we might see in the clinic (such as shadows, defocusing, and motion) were apparent

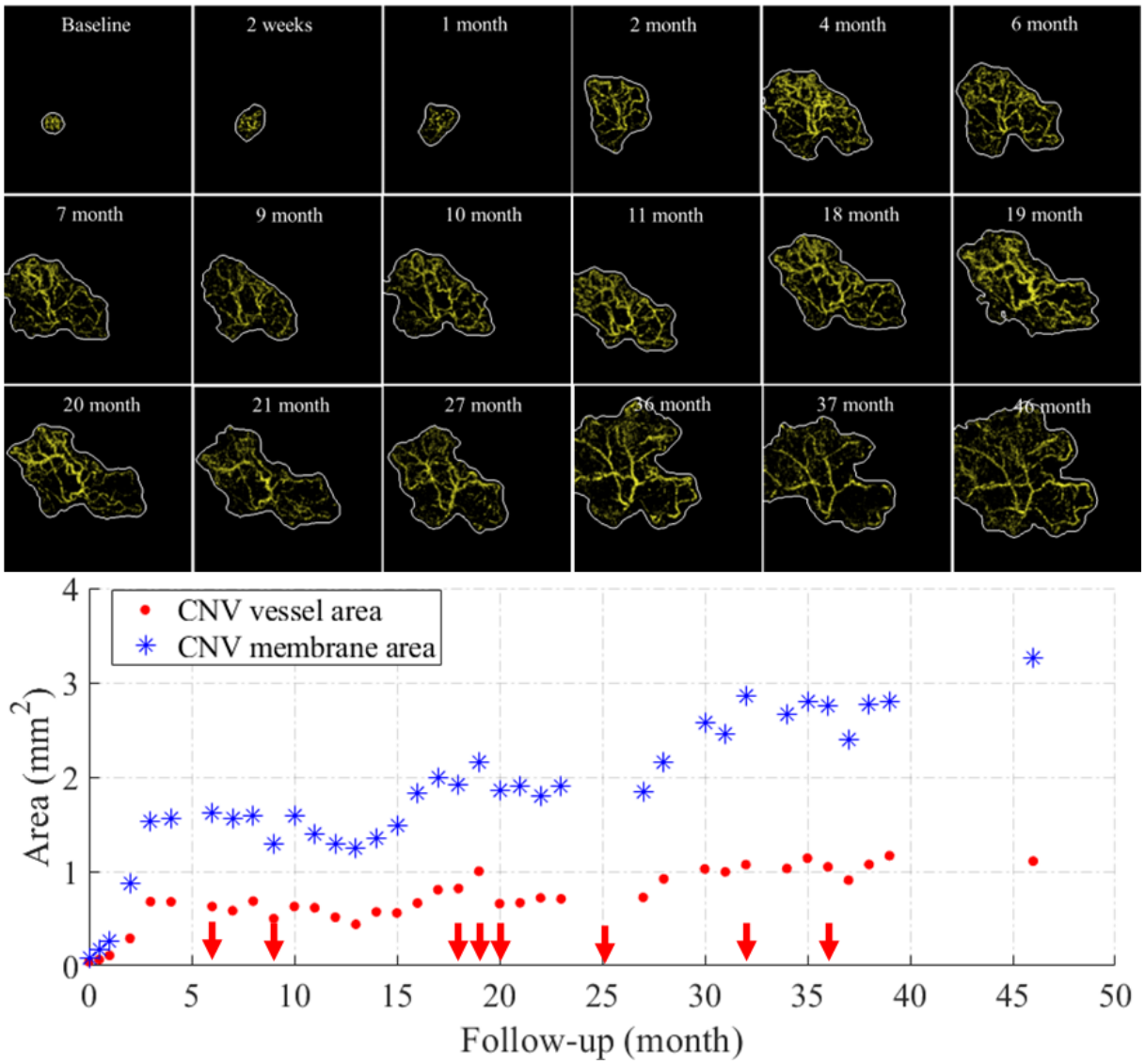


Figure 6.5: Choroidal neovascularization (CNV) growth dynamics illuminated by the proposed detection algorithm. CNV vessels were detected in the segmented CNV membrane area (white outline) using Otsu's algorithm. CNV vascular patterns changed dramatically after treatment. The scatter plot of CNV vessel area and membrane area shows the CNV dynamics following anti–vascular endothelial growth factor (anti-VEGF) treatments (red arrows) in longitudinal follow-ups.

in the dataset. Scans also included many kinds of pathologies, such as geographic atrophy, drusen, macular edema, and hard exudates. While this dataset was consequently more challenging, by using it the model was able to learn more contextual information which could prevent underperformance on artifact-rich scans.

Second, our model contains a large number of carefully chosen inputs. By including several projection artifact correction techniques, the network had access to information that enabled it

to identify the projection artifacts that often plague OCTA studies. This capability is paramount for any automated approaches operating in the outer retina, which is near the strongly reflecting retinal pigment epithelium layer (RPE) and therefore prone to disruption by projection artifacts. Additionally, the *en face* OCT images and thickness maps can identify pathologic regions since exudation can cause changes in retinal thickness and reflectivity. In tandem, these structural OCT and OCTA inputs provide separate information that can be correlated to more readily identify CNV. Finally, the OCT and OCTA volumes include spatial information that can help identify real CNV flow since CNV occurs at specific anatomic depths.

Third, a novel CNN architecture was designed specifically for the tasks in this work. The architecture contains separate pipelines for 3D and 2D information in order to ensure that the structure of each data format can be fully exploited. By separating the diagnosis and segmentation tasks, a Res-Net[150] and a U-Net[151] structure could both be employed. These network architectures are considered state of the art in medical image processing, and have previously shown excellent performance in OCTA imaging in particular[149]. The proposed method also relied purely on deep learning to determine outputs, removing arbitrary feature size thresholding that is used in some OCT feature segmentation architectures[53, 65].

CNV is a significant development in several diseases[16, 66, 157, 158, 159, 160, 161]. However, as indicated by several of the example images shown in this study, it is not always prominently visible in realistic datasets (which will include low quality scans). Performance on pathological myopia exhibited the most variation in IOU, recall and F1 score. In general scans from eyes with pathological myopia were of low quality due to difficulty removing defocus (Fig. 6.4 row 4). It is unsurprising that scans with severe artifacts like those present in pathological myopia were more difficult for the model to analyze. Rare diseases are also challenging, since this category contains a variety of pathologies which may not share similar features. Evaluating performance on each specific pathology could potentially illuminate this variation in performance but the dataset used in this work is not large enough to comment on this in a statistically satisfactory manner.

The proposed algorithm does have some limitations.

The reliance on retinal layer segmentation- even though the proposed work only requires knowledge of the location of the ILM, OPL, and BM- is one such limitation. While automated retinal layer segmentation algorithms do exist[1], manual correction is frequently required to produce accurate layer boundaries on some scans with a large amount of pathology. Future work should include either improved automation of retinal layer segmentation or forego reliance on layer boundaries altogether.

We also did not include a vessel segmentation module in this study. Vessel segmentation has been included in other CNV segmentation platforms[65]; however, in the low-definition scans ($6 \times 6 - mm$) included in this study, CNV vessel width can be as small as a single pixel. And with small, dim vessels, it is difficult to say which pixels exactly correspond to true flow even for a human grader. Under these conditions, it is difficult to generate a ground truth to train a CNN for CNV vessel segmentation, and it is also difficult to gauge performance since metrics like the IOU are sensitive to anatomically irrelevant pixel displacements. However, this limitation should be addressed if vessel metrics such as tortuosity prove useful for analyzing CNV progression.

Due to the unbalanced dataset used in this work we were unable to investigate model performance based on patient identity characteristics. We are collaborating with different clinics to collect balanced sub-datasets in order to explore model performance in different ethnic groups. Similarly, we would like to characterize model performance in specific clinics, but we also lack balanced datasets to make this comparison. This could also be addressed in future work.

Lastly, while it's generally possible to improve network design to enhance performance, errors in model output in this work were usually on scans that were difficult to assess by eye. Clinicians might also miss the CNV in these cases, and the ground truth membrane area is ambiguous anyway (Fig. 6.2 B4). For these reasons, software or hardware enabling improved image quality may be a more fruitful approach improving OCTA analysis of CNV.

Despite these limitations, the proposed model achieved two important tasks: CNV diagnosis and membrane segmentation. These tasks were achieved on a clinically realistic data set that

included over $10,000$ scans from several diseases and healthy eyes from several clinics. Our results indicate the plausibility of automating CNV analysis in the clinic.

7 Invariant features-based automated registration and montage for wide-field optical coherence tomographic angiography

7.1 Abstract

The field of view of optical coherence tomographic angiography (OCTA) images of the retina can be increased by montaging consecutive scans acquired at different retinal regions. Given the dramatic variation in aberrations throughout the entire posterior pole region, it is challenging to achieve seamless merging with apparent capillary continuity across the boundaries between adjacent angiograms. For this purpose, we propose herein a method that performs automated registration of contiguous OCTA images based on invariant features and uses a novel montage algorithm. The invariant features were used to register the overlapping areas between adjacently located scans by estimating the affine transformation matrix needed to accurately stitch them. Then, the flow signal was compensated to homogenize the angiograms with different brightness and the joints were blended to generate a seamless, montaged wide-field angiogram. We evaluated the algorithm on normal and diabetic retinopathy eyes. The proposed method could montage the angiograms seamlessly and provided a wide-field of view of retinal vasculature.

7.2 Introduction

Since the first time-domain optical coherence tomography (OCT) [26] article was published in 1991, OCT technology has developed rapidly. With faster scanning using Fourier-domain modalities, current OCT devices allow acquisition of three-dimensional data representing the retinal layered structure rapidly. Optical coherence tomographic angiography (OCTA) detects the variation of OCT signal reflectance over scans repeated at the same location in order to evaluate the microcirculation flow *in vivo*; allowing sensitive, fast (< 3 seconds), and high resolution volumetric imaging of the retinal flow[43]. This technique has demonstrated utility in key ophthalmic diseases such as diabetic retinopathy (DR), age-related macular degeneration (AMD), and glaucoma, allowing visualization of vascular details. In addition, OCTA allows more reliable quantification of the

This work has been published in Biomedical Optics Express: Jie Wang, Acner Camino, Xiaohui Hua, Liang Liu, David Huang, Thomas S. Hwang, and Yali Jia, "Invariant features-based automated registration and montage for wide-field OCT angiography," Biomed. Opt. Express 10, 120-136 (2019).

vasculature changes[98]. With the improvement of the hardware and the progress of processing algorithms, a current research endeavor in OCTA is to increase the achievable field of view (FOV) of images. Previous studies have shown that wide-field OCTA can reveal more clinically useful information [162, 163].

The availability of faster light sources has allowed acquisition of wide-field OCTA in a single scan[164, 165]. This approach to increase the FOV faces two fundamental challenges. First, the retinal curvature covered by the large FOV and limited focusing depth of OCT result in B-scans that are only in focus centrally, and defocused at the periphery [166]. Secondly, propagation of the scanning beam across a larger FOV induces larger wavefront aberrations that are difficult to compensate for without the assistance of adaptive optics[167]. As a consequence, the beam size at the peripheral retina is large and aberrant, deteriorating the lateral resolution of the instrument and degrading the images. An alternative to wide-field scanning is to montage smaller, but high-quality scans with overlapping areas to create a wide-field image. This approach is more cost-effective and amenable to improvement using the existing equipment.

The main task of mosaicking techniques that reproduce wide-FOV from stitching small-FOV scans is to conceal the seam between individual angiograms by ensuring capillary overlap and background level homogeneity. Previous research on montaging retinal images used fundus images with large vessel patterns and intersections to register overlapping areas as well as post-processing of the edges in order to get a seamless, wider fundus image[168, 169, 170, 171, 172, 173, 174]. Accomplishing the same task in OCTA requires the use of more challenging image processing techniques, given the finer vessel details visualized by OCTA. Moreover, in order to attain a large FOV by mosaicking, the individual scans need to be large enough to not require an unreasonable number of acquisitions from the subject, making $3 \times 3 - mm$ scans impractical. However, the standard $6 \times 6 - mm$ angiograms are not isoplanatic. For that FOV, the retinal curvature in the periphery of posterior pole or in near-sighted eyes already produces a significant deformation, and further image processing is required to correct for an adequate blending with adjacent patches.

In our previous research montaging OCTA images, we developed a parallel-strip registration algorithm in two-dimensional (2D) [175] and three-dimensional (3D) [176]. This method focused on removing motion artifacts and required a large overlapping area. Here, we propose a new mosaicking solution in which patches of the retina with limited overlapping areas are registered by a method based on invariant features [177, 178]. The registered patches are seamlessly stitched by a panoramic image seamless stitching routine [179, 180, 181, 182] using flow signal compensation. This method allows ultra-wide visualization of the retinal flow by OCTA, with a great potential to better assist clinicians in the assessment of retinal diseases.

7.3 Data acquisition and preprocessing

We developed an algorithm to montage separate OCTA images in order to achieve a wide FOV. Although we demonstrated the algorithm mainly on scans centered on the optic disc and macula, it can be applied on the scans through to the back of the eyes. The mean distance between disc and fovea was $4.76 \pm 0.34mm$ [183], and the mean disc-fovea angle was $7.76 \pm 3.63°$[184] . Assuming the distance from the center of the fovea avascular zone (FAZ) to the optic disc is approximately $5mm$ horizontally and about $1mm$ vertically, if the two scans are perfectly centered the overlap between them would be approximately $1mm$ horizontally and $5mm$ vertically, with variations between subjects.

Participants were scanned using a $70-kHz$ commercial AngioVue OCTA system (RTVue-XR; Optovue, Fremont, CA) with the wavelength centered at $840nm$. Scans covered a $6 \times 6 - mm$ area, using a high-definition scan pattern with 400×400 sampling rate ($15um$/pixel). Two repeated B-scans at the same location were acquired and processed by the commercial version of the split-spectrum amplitude decorrelation angiography (SSADA), which is sensitive to capillary flow. A horizontal-priority and a vertical-priority scan of the same area were collected and registered to suppress microsaccadic motions artifacts [76]. Ten eyes diagnosed with DR and 10 normal eyes were scanned at different retinal landmarks to generate the wide-field OCTA. The DR eyes were scanned centering on the disc, fovea and temporal regions, ensuring a certain overlap between

adjacent scans. Normal eyes were scanned centering on the disc and fovea to evaluate the proposed algorithm.

During data preprocessing, retinal layers were segmented by a directional graph search algorithm incorporated in the COOL-ART software for OCTA image processing[1] (Fig. 7.1 A). Applying the projection-resolved (PR) algorithm[72, 73], we could remove projection artifacts and visualize the retinal capillary plexuses in three different slabs located at different depths[9] (Fig. 7.1 B-G), which are defined as the superficial vascular complex (SVC), intermediate capillary plexus (ICP), deep capillary plexus (DCP). The combination of three plexuses formed the inner retinal angiogram. Since the inner retinal angiogram is rich in microvascular details, it was used to detect the invariant features and to further estimate the optimal affine matrix to montage the en face angiograms of SVC, ICP, DCP, and the inner retina itself.

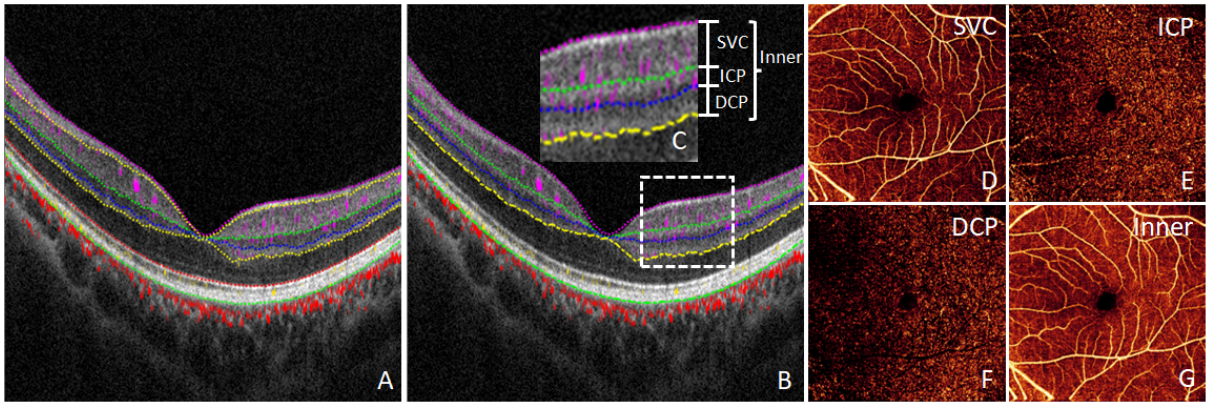


Figure 7.1: Illustration of retinal layer segmentation and angiogram generation on superficial vascular complex (SVC) (inner 80% of the ganglion cell complex (GCC)), intermediate capillary plexus (ICP) (outer 20% of the GCC and inner 50% of the inner nuclear layer (INL)), deep capillary plexus (DCP) (outer 50% of the INL and outer plexiform layer (OPL)), and inner retina (between the inner limiting membrane (ILM) and the OPL).

7.4 Methods

There were three key steps to generate the montaged, wide-field OCTA: accurate estimation of the affine transformation matrix, flow signal compensation, and seamless blending of the edge of overlapping areas. The estimated affine transformation matrix contains the global information used to rotate and shift one image to montage it with the other. The fine registration in the edge area registered the vessels regionally in order to smooth the edges. The flow signal compensation equalized the flow signal to generate a homogenized wide-field OCTA.

7.4.1 Algorithm overview and data pre-processing

The disc angiogram was selected as the target image (I_t) and the macular angiogram was the moving image (I_m). Then, the invariant features were detected and matched by speed-up robust-features (SURF) algorithm[185], and further fine matching in local area followed by random sampling consensus (RANSAC) algorithm [186] were applied to filter the outliers. The remaining paired points were used to infer the affine matrix. Then, in order to generate an even and seamless wide-field angiogram, a post-processing step including flow signal compensation and seamless blending was applied. The algorithm framework is described in Fig. 7.2.

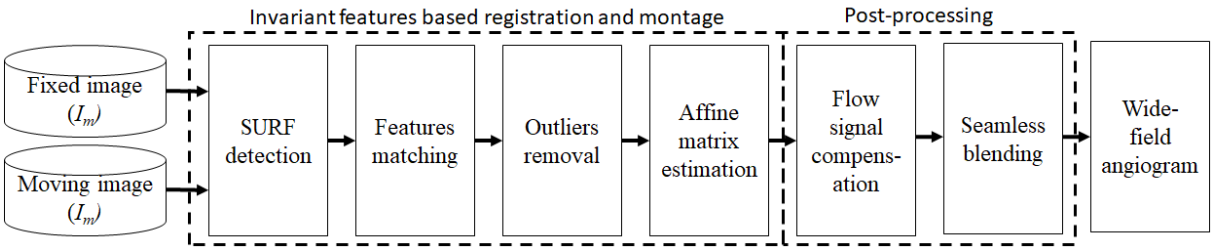


Figure 7.2: Overview of the invariant features-based automated registration and montage algorithm. SURF – Speed-Up Robust Features.

7.4.2 Invariant features-based registration and montage

(1) *Affine transformation and features detection*

Stitching the moving angiogram (I_m) to the target angiogram (I_t) consists of re-arranging the pixels of the moving angiogram to match their equivalents in the overlapping area of the target angiogram. The transformation needed for 2D image stitching can be modeled by the affine transformation matrix:

$$p_1 = Ap_0, A = \begin{bmatrix} a_{11} & a_{12} & a_{13} \\ a_{21} & a_{22} & a_{23} \\ 0 & 0 & 1 \end{bmatrix} \tag{7.1}$$

where, p_0 and p_1 are matching points in I_m and I_t). The affine transformation matrix A includes the parameters for rotation, scaling, shifting, flipping and shear mapping. There are 6 degrees of freedom, hence at least 3 matching points are needed to infer the affine transformation matrix.

Scale-invariant feature transform (SIFT) [187] and SURF are popular local feature detection and descriptor methods in computer vision. Both are invariant with rotation, scaling, and intensity variation. Since SURF is more efficient and robust than SIFT, we chose SURF as the invariant features method to select the matching points used to estimate the affine transformation matrix.

SURF detects the features on points of interest in multi-scales, where the points of interest are detected by the determinant of the Hessian matrix following

$$\det(H) = D_{xx}D_{yy} - (0.9D_{xy})^2 \tag{7.2}$$

where, D_{xy}, D_{xy} and D_{yy} are the approximation second derivative of a Gaussian filter. To ensure the invariability of scaling and rotation, the SURF features were detected in multi-scales, and the dominant orientation of the Haar wavelet features were recorded as the SURF orientation descriptor. Furthermore, the summaries of the Haar wavelet features of the neighbors were used to generate the unique and robust SURF descriptors.

The number of SURF features that can be detected is variable, but usually about 800 of SURF features were detected on the OCTA of healthy eyes, which were presented using green crosses in the optic disc angiogram (Fig. 7.3 A). Each feature contained location, orientation, scale, and feature descriptors (Fig. 7.3 B). In the following step, the SURF descriptors were used to match the detected points, whereas the scale and orientation were used to filter the mismatched pairs.

(2) *Angiograms registration and montage*

Each detected invariant feature had their unique feature descriptor. The key points with same sign $(-/+)$ of the $\det(H)$ would conduct the matching process. We compared the invariant features from It with their corresponding ones in I_m using the sum of squared differences (SSD):

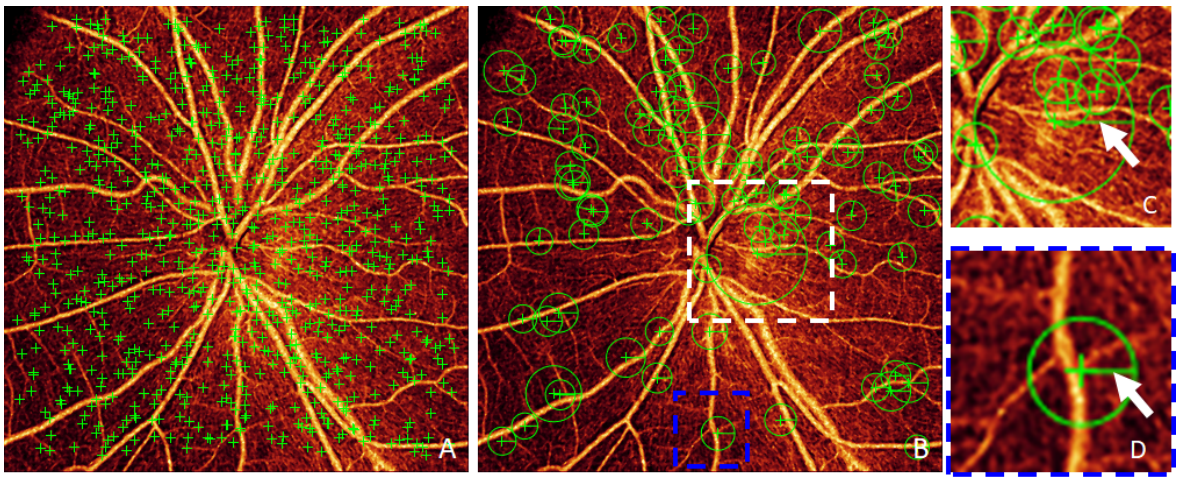


Figure 7.3: Speed-up robust-features SURF detection on OCTA. (A) The green crosses are the locations of detected features on the angiogram. (B) Some of the SURF features in A were selected randomly for clear representation of orientation and scale. The scale of features is represented by the radius of the green circles. The direction of features and scale is represented by the green line highlighted with white arrows in C and D. (C-D) Magnified insets correspond to the regions indicated by black and blue boxes in B.

$$\text{paired}\left[P_t\left(i\right), P_m\left(j\right)\right] = \min_{j\in\forall}\left\{SSD\left[P_t\left(i\right), P_m\left(j\right)\right]\right\} \tag{7.3}$$

where, $P_m(j)$ is the position of $j-th$ SURF feature in I_m, $P_t(i)$ is the position of the $i-th$ SURF feature in I_t. The nearest two points were paired.

OCTA contains a rich vasculature, the image content is monotonic, and the local features are similar. For this reason, if the points of interest were grossly matched based on the feature descriptors only (Eq. 7.2), many of them could be erroneously paired (Fig. 7.4). These mismatches would cause failure of the random sampling consensus (RANSAC) algorithm in trying to infer the affine transformation matrix A. The RANSAC algorithm was designed to find a homograph matrix (H) that could get the greatest number of pairs that can be properly transformed. Therefore, before applying RANSAC, we imposed two additional restrictions to improve the matching accuracy.

For each pair, one point was taken from the moving image (I_m) and represented by Pm whereas the other was taken from the target image (I_t) and represented by Pt. The SURF features of Pm and Pt were represented by (O_m, S_m, D_m) and (O_t, S_t, D_t), where O is the orientation, S is the scale, and D is the feature descriptor. D was already used to grossly pair the SURF points. Then we used the orientation O_m and scale S_m to locally rotate and resize the moving image and calculate

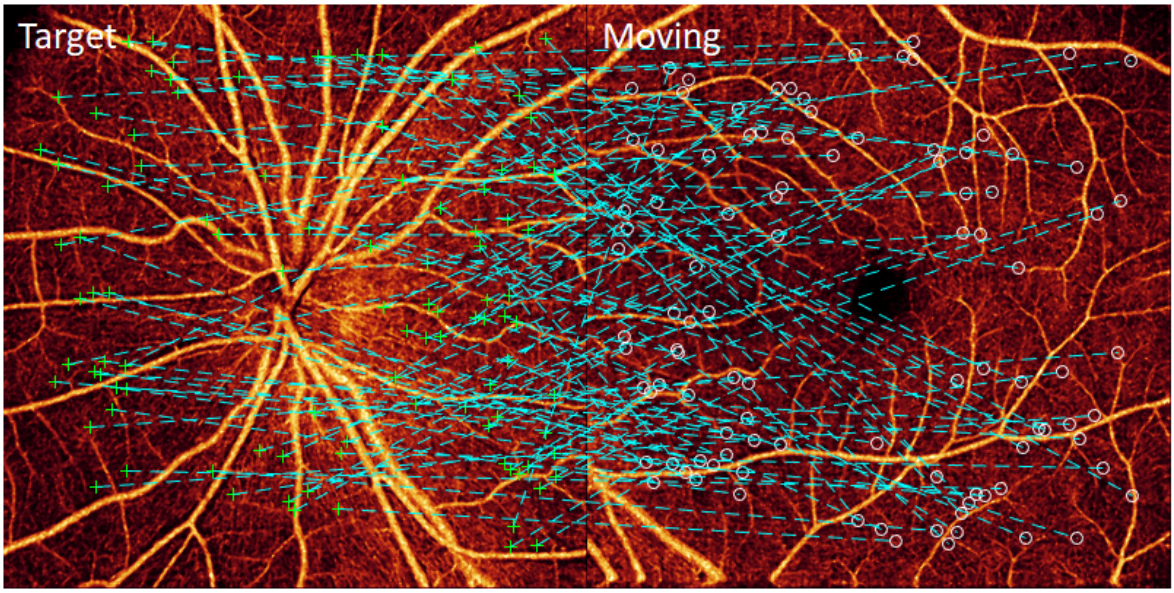


Figure 7.4: Invariant features matching. The paired points were connected using the cyan dashed lines.

the correlation with the target image in the paired local area (Fig. 7.5). The differences of the orientation and scale between the two points of interest were calculated by:

$$\begin{cases} \Delta O = O_m - O_t \\ \Delta S = \dfrac{S_m}{S_t} \end{cases} \tag{7.4}$$

, If $-\pi/8 \leq \Delta O \leq \pi/8$ and $1/2 \leq \Delta S \leq 28$, the points would be kept for the further descriptor comparison using Eq. 7.3. Otherwise, the two points would be marked with an "unmatchable" flag, assuming that scale and orientation should not have changed much between two adjacent scans. Some correctly matched and mismatched points were extracted from Fig. 7.4 to illustrate the differences of scale or orientation between mismatched points (Fig. 7.5).

After the first restriction in Eq. 7.4 is imposed, and for each remaining pair of points, two rectangular areas of size $21 \times 21 -$ pixel were extracted from the target and moving images, surrounding the pixels in the pair. The local areas I^l surrounding the k^{th} pair were represented by $I^l_m(k)$ and $I^l_t(k)$. Then, $I^l_m(k)$ was resized and rotated to register with the $I^l_t(k)$, following

$$I^l_c = T\left[R\left(I^l_m, -\Delta O\right), \Delta S^{-1}\right] \tag{7.5}$$

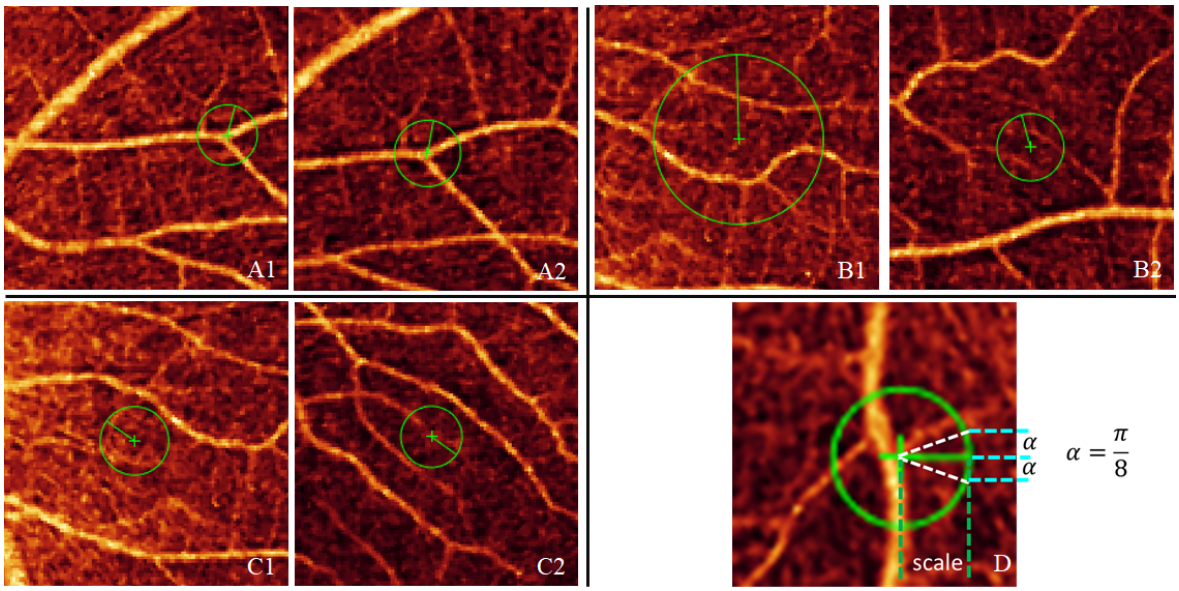


Figure 7.5: Illustration of the scale and orientation of paired points. A1, A2 were correctly paired points of interest; their scale and direction were very similar. B1, B2 were mismatched points, for which both direction and scale were very different. C1, C2 were also mismatched points, where the scale is similar but the difference of direction was great. D is the illustration for the scale and direction restriction for feature matching. The scales of A, B C and D are $1.65 \times 1.65 - mm$, $1.3 \times 1.3 - mm$, $1.65 \times 1.65 - mm$ and $0.9 \times 0.9 - mm$, separately.

where R is the rotation operation, T is the resize operation, ΔO is the rotation parameter, and ΔS is the rescaling parameter. Then, the second restriction was imposed, consisting of evaluating the correlation of the local areas by:

$$C^l = \text{Cor}\left(I_c^l(k), I_t^l(k)\right) \tag{7.6}$$

The areas surrounding truly matching points exhibited high correlation when aligned. The pairs with correlation lower than a threshold value of 0.5 were also filtered out. By doing this, the SURF descriptors and image content of highly matching points were reserved (Fig. 7.6).

After most outliers had been filtered out (Fig. 7.6), the RANSAC algorithm could be employed on reserved pairs to further remove the remaining mismatching pairs (Fig. 7.7) and then recognize the registration matrix. The number of available pairs always exceeded the minimum of 3 points required by RANSAC. The least squares approach was used to infer the affine transformation matrix A At this point, the moving angiogram (I_m) was well montaged onto the target angiogram (I_t), but the whole angiogram exhibited an uneven appearance and the seam was visible (Fig. 7.8).

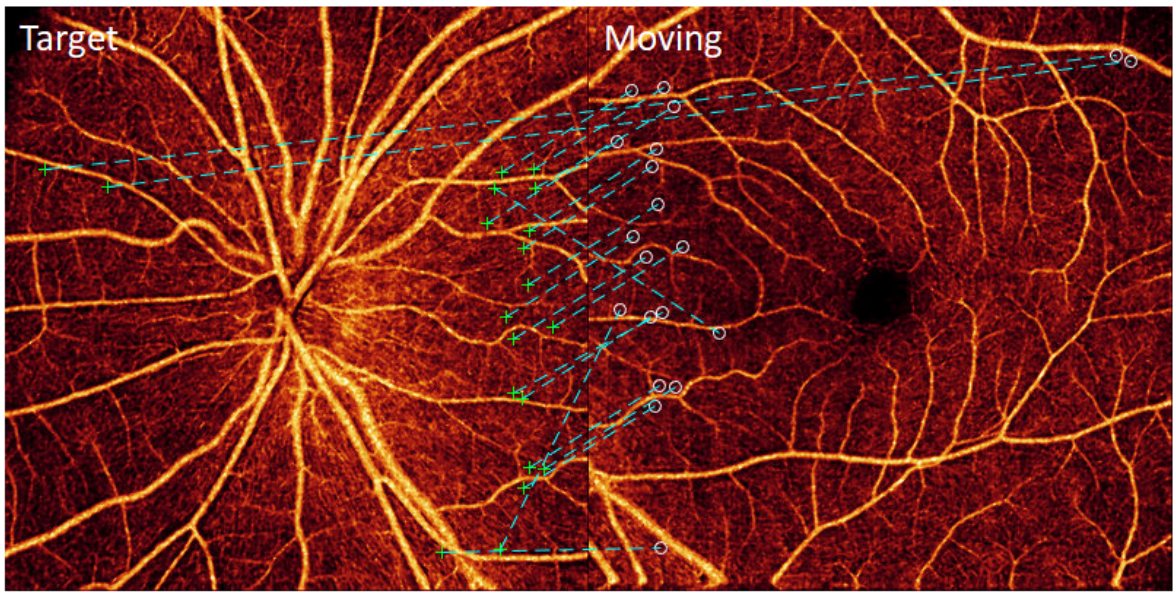


Figure 7.6: Illustration of the pairs reserved for the random sampling consensus (RANSAC) input after local area verification by imposition of the two restrictions described in section of angiograms registration and montage

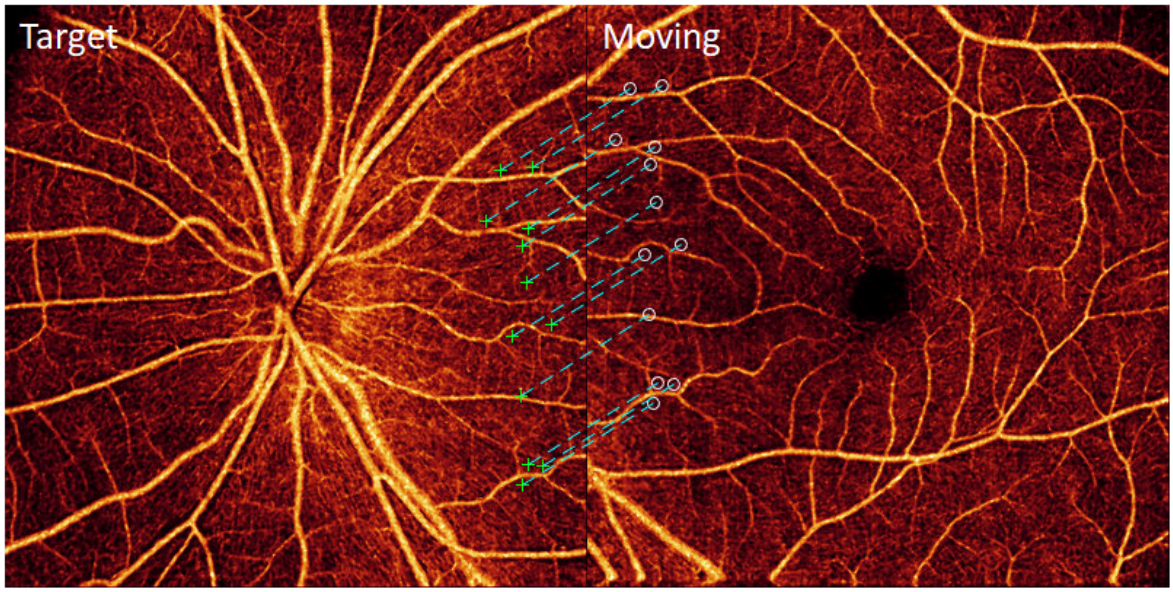


Figure 7.7: Illustration of the pairs reserved after the last step of mismatch removal using random sampling consensus (RANSAC) algorithm.

7.4.3 Flow signal compensation and seamless blending

Aiming at homogenizing the wide-field angiogram, post-processing consisting of flow signal compensation and seamless blending was performed.

Two methods were used to compensate the flow signal: structural reflectance-based compensation and flow signal-based compensation.

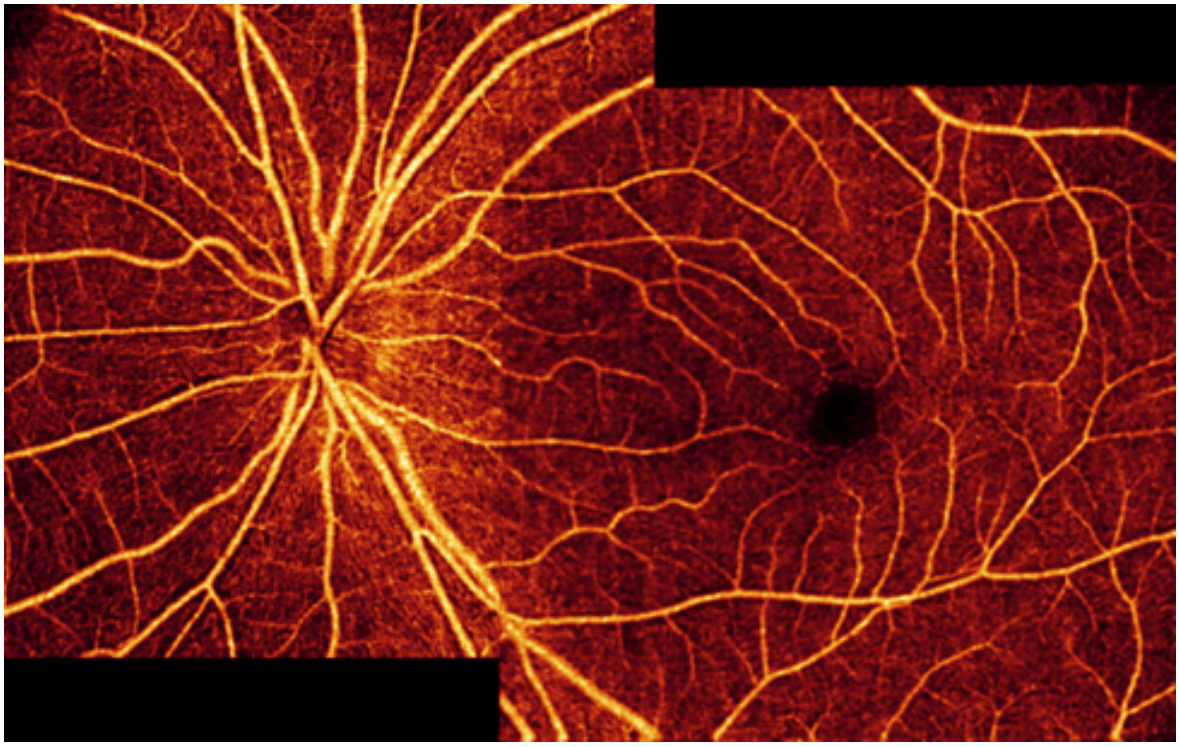


Figure 7.8: Angiography montage with visible seams.

The structural reflectance was obtained from the OCT *en face* projection and used a bias field map to compensate the angiogram:

$$I_{c(A)} = I_A \cdot \frac{\text{Mean}\left(G\left(I_R\right)\right)}{G\left(I_R\right)} \tag{7.7}$$

where, I_A is the original angiogram image, I_R is the en face mean projection of the structural reflectance, and $G(\cdot)$ is the Gaussian filter. The intensity corrected angiogram $I_{c(A)}$ reduced the effect of structural reflectance variation on flow signal.

Then, flow signal based compensation was applied, inspired by the gain compensation algorithm described in [182]. This task was accomplished by minimizing an error function:

$$e = \frac{1}{N} \sum \left[\alpha I_{c(m)}\left(u_m\right) - \beta I_{c(t)}\left(u_t\right)\right]^2 \tag{7.8}$$

where, N is the number of overlapping pixels, u_m and u_t are the overlapping pixels in I_m and I_f with $u_m = Au_t$, and α and β are gain parameters that need to be optimized. In our application, the α and β were restricted, which were both no less than 0.5 and no more than 2.

After compensation, the flow signal exhibited global uniformity. However, the transition of the flow signal from one angiogram to the other was discontinuous and the vasculatures were not perfectly registered at the seams, and hence the edge was visible. Flow signal blending was necessary to obtain a seamless montage angiogram. The multi-band blending algorithm described in[182] was simplified and applied in this study. The flow signal was fused in multi-scale with a fusion weights map decreasing gradually from 1 to 0 from one angiogram to the other across the seam (Fig. 7.9). Weights maps for the target I_t and the moving I_m images were represented by W_t and W_m. The center of the weights map was located on the seam, where the weight is 0.5 on both weights maps. The angiograms were filtered by 2D Gaussian kernels with multiple scales; the high-frequency information was extracted by

$$\begin{cases} \text{Diff}\,(k) = G_{\sigma(k)}\,(I) - G_{\sigma(k+1)}\,(I) \\ \sigma\,(k+1) = 2 * \sigma\,(k) \end{cases} \tag{7.9}$$

When $k = 0$, we assign to $G_{\sigma(k)}\,(I)$ the original image I

The information on the scale was blended by

$$\begin{cases} I_b\,(k) = W_t \times \text{Diff}\,(t_k) + W_m \times \text{Diff}\,(m_k) \\ W_t + W_m = 1 \end{cases} \tag{7.10}$$

where, $I_b(k)$ is the blended image on scale k, W_t is the weights map for the target angiogram, and Wm is the weights map for moving angiogram. The weights maps vary within $[0, 1]$ from the one side of the seam to other. The center of the weights map is 0.5, aligning with the seam. The weights maps were illustrated on Fig. 7.9. Diff (t_k) and Diff (m_k) are the detected Diff values in Eq. 7.9 for the target and moving angiograms separately.

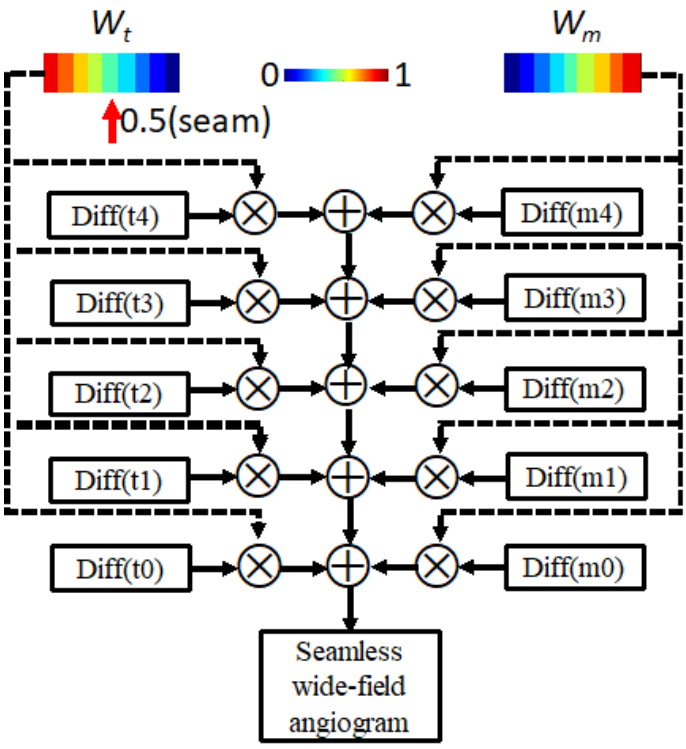


Figure 7.9: Illustration of the seamless blending routine.

On all scales, the blended images were summed up to get the seamless wide-field angiogram:

$$I_{output} = \sum_{k=0}^{N} I_b\,(k) \tag{7.11}$$

Where, N is the number of scales, and I_{output} is final montaged seamless wide-field angiogram. In this study, $N = 4$.

Comparing the montaged image after seamless blending (Fig. 7.10 A) with the montaged angiogram without flow signal compensation in Fig. 7.8, the transition of the first seems smoother. By inspecting local areas about the seam, the vasculature exhibited a continuous appearance across the seam (Fig. 7.10 B-C).

7.4.4 Bundle processing

As mentioned previously, this invariant features-based automated registration and montage algorithm is not limited to two angiograms only. For the merging of multiple angiograms we designed the bundle processing strategy described below.

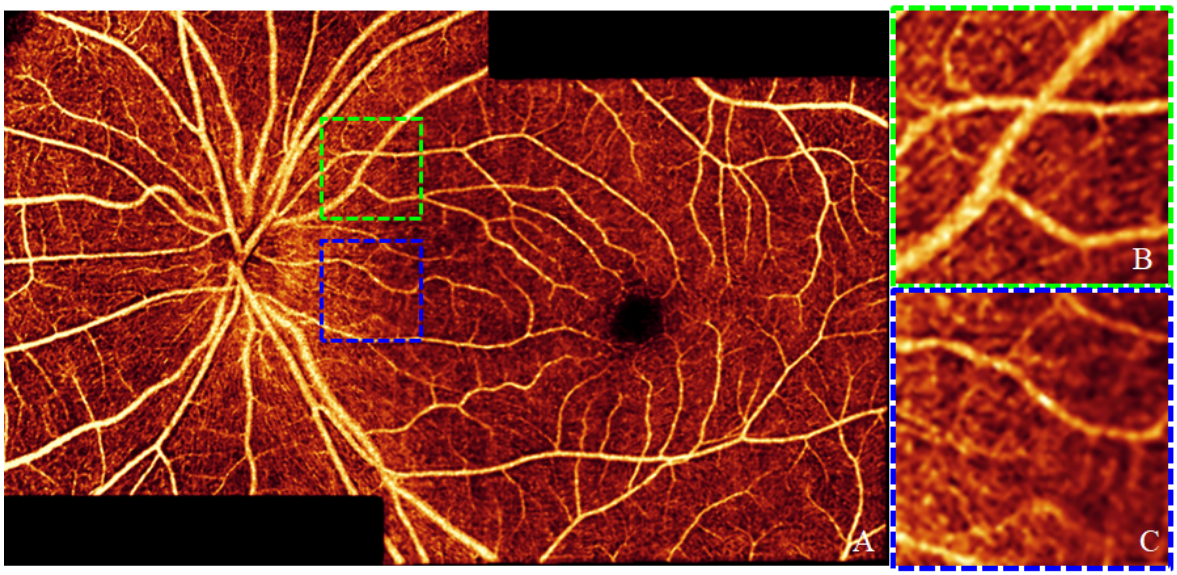


Figure 7.10: The montaged seamless angiogram applying flow signal compensation and seamless blending. (B) and (C) represent the detail capillary network within the green and blue rectangles in (A).

First, a target angiogram needs to be pre-assigned and used as the reference for the montage; all other moving angiograms would be stitched to it one by one. Utilizing the proposed registration method in section of invariant features-based registration and montage, the invariant features of all input angiograms were paired each other. The image connection would be sketched out based on the cluster of the paired points. The pairs only appeared in the overlapping area and were located in a restricted area. The cluster of the paired points in the moving image closer to the target image had priority to be montaged. Once the montage was completed, the resulting angiogram would be updated as the target image, to be further montaged with the following moving angiogram.

7.5 Results

This proposed method was implemented using Matlab $2018a$ (Mathworks, Natick, MA) installed on a computer with Intel (R) Core(TM) $i7-6800K$ CPU @ $3.4GHz$ and DDR4 $64GB$. It could generate a seamless wide-field OCTA by stitching two OCTAs within 15 seconds.

To evaluate the montage accuracy and the continuity of vasculature across the seams, the difference and correlation of flow signal between opposite sides of the seams were calculated on the angiography montage of 10 normal eyes. For evaluation, disc and macular inner retinal angiograms were montaged. As illustrated in Fig.11, the green and cyan thin-slabs contained information from

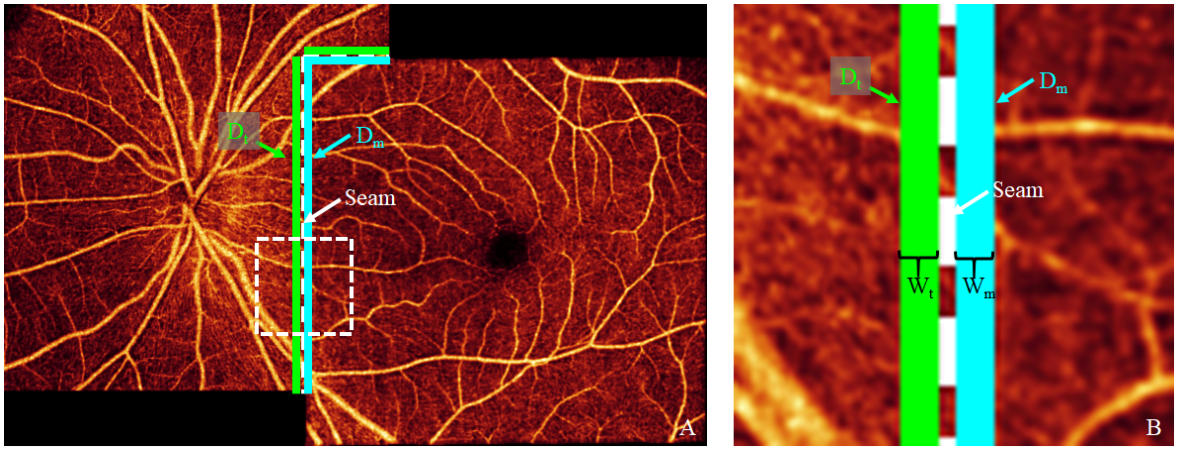


Figure 7.11: Illustration of the algorithm evaluation. Green and cyan lines illustrated both sides of the seam between the target and moving images.

the two sets of flow signals (D_t and D_m) on each side of the seam (dotted white line). The difference ($E\left(D_t, D_m\right)$) and correlation (Cor $\left(D_t, D_m\right)$) between D_t and D_m were calculated by

$$\begin{cases} E\left(D_t, D_m\right) = \frac{1}{L}\sum_{i=1}^{L}\left|M_t\left(i\right) - M_m\left(i\right)\right| \\ \text{Cor}\left(D_t, D_m\right) = \text{cor}\left(M_t, M_m\right) \\ M_t\left(i\right) = \frac{1}{W_t}\sum_{j=1}^{W_t}\left(D_t\left(i,j\right)\right), M_m\left(i\right) = \frac{1}{W_m}\sum_{j=1}^{W_m}\left(D_m\left(i,j\right)\right) \end{cases} \tag{7.12}$$

where, L is the length of the seams, cor $(\cdot)$ is the correlation calculation, $W_t = W_m = 2$ pixels are the width of the slab. $M_t(i)$ and $M_m(i)$ are the flow values of the $i-th$ pixel on the target portion and moving portion, separately. While $M_t(i)$ and $M_m(i)$ are paired on the opposite sides of the $i-th$ position on the seam. The difference evaluates the smoothness of angiogram on the mosaic edge, while correlation evaluates the vasculature continuity.

For comparison, we compared the proposed algorithm with the traditional montage method. Previously, the matched points were obtained based on the invariant feature descriptors and removing the outliers using RANSAC, which means the angiograms were montaged without fine registration in local area, flow signal compensation and seamless blending. Using the traditional approach, the angiograms appeared well montaged (Fig. 7.12 A) but vessels were not continuous across the seams (Fig. 7.12 B). In contrast, after applying the proposed method, the montaged angiogram (Fig. 7.10 A) was more homogeneous, the difference and correlation values were improved (Table 7.1), the

vessels were continuous, and the seam was not visible (Fig. 7.10 vs Fig. 7.12). The vessels were not absolutely perpendicular to the seams, and the vessels patterns were not completely the same at opposite sides of the seam. Taking these two main factors, which are consequence of the scale over which correlation is computed and the amount of detail available, the correlation of the proposed method cannot be particularly high anyways. We would expect it to be considerably higher if the overlapping area was larger. However, the fact that the correlation is improved with respect to the traditional method indicates that vessel connectivity is improved at the stitched area.

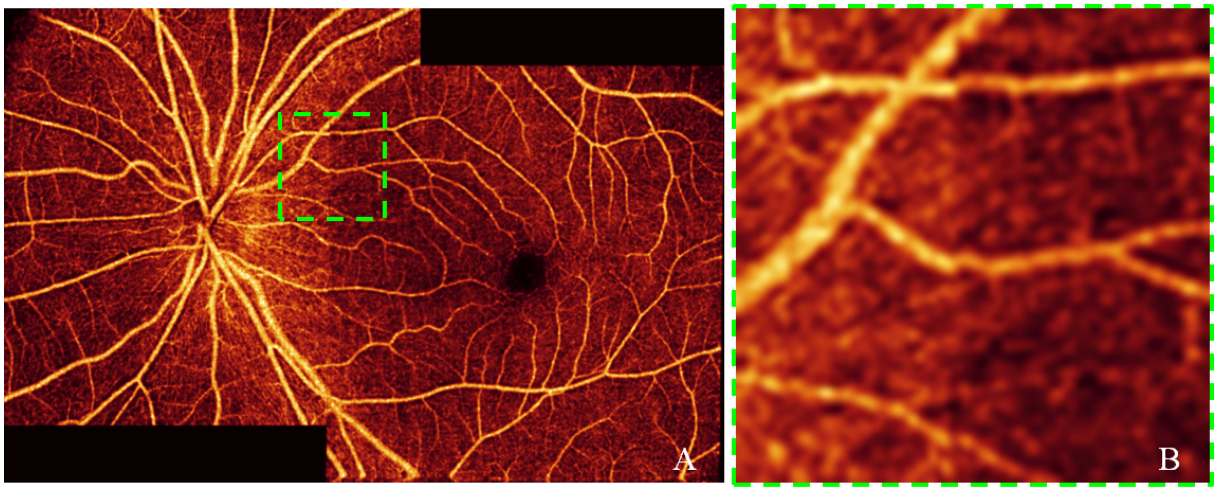


Figure 7.12: Grossly montaged wide-field angiogram before matching verification in local area, flow signal compensation and seamless blending. Five pixel mismatch was demonstrated.

Table 7.1: Evaluation of the performance of the automated montage algorithm on 10 normal eyes by the correlation and mean square errors

	Traditional method	Proposed method	Improvement (%)	$p - value^*$
Correlation (Mean $\pm$ std)	0.26 ± 0.01	0.60 ± 0.04	130	0.008
Correlation (Mean $\pm$ std)	0.036 ± 0.01	0.02 ± 0.002	44	0.008

The affine transformation matrix estimated for the inner retinal angiogram could be used to generate the wide-field angiograms on SVC, ICP, DCP and choriocapillaris (CC) (Fig. 7.13) after projection artifacts were removed by PR-OCTA.

Next, sixteen $6 \times 6 - mm$ HD scans were obtained on a normal eye covering an ultra wide-field of view [Fig. 7.14] and reaching the limit imposed by dilated pupil vignetting. Using the algorithm proposed here, the montaged ultra wide-field angiogram was $15 \times 20 - mm$, and the sampling

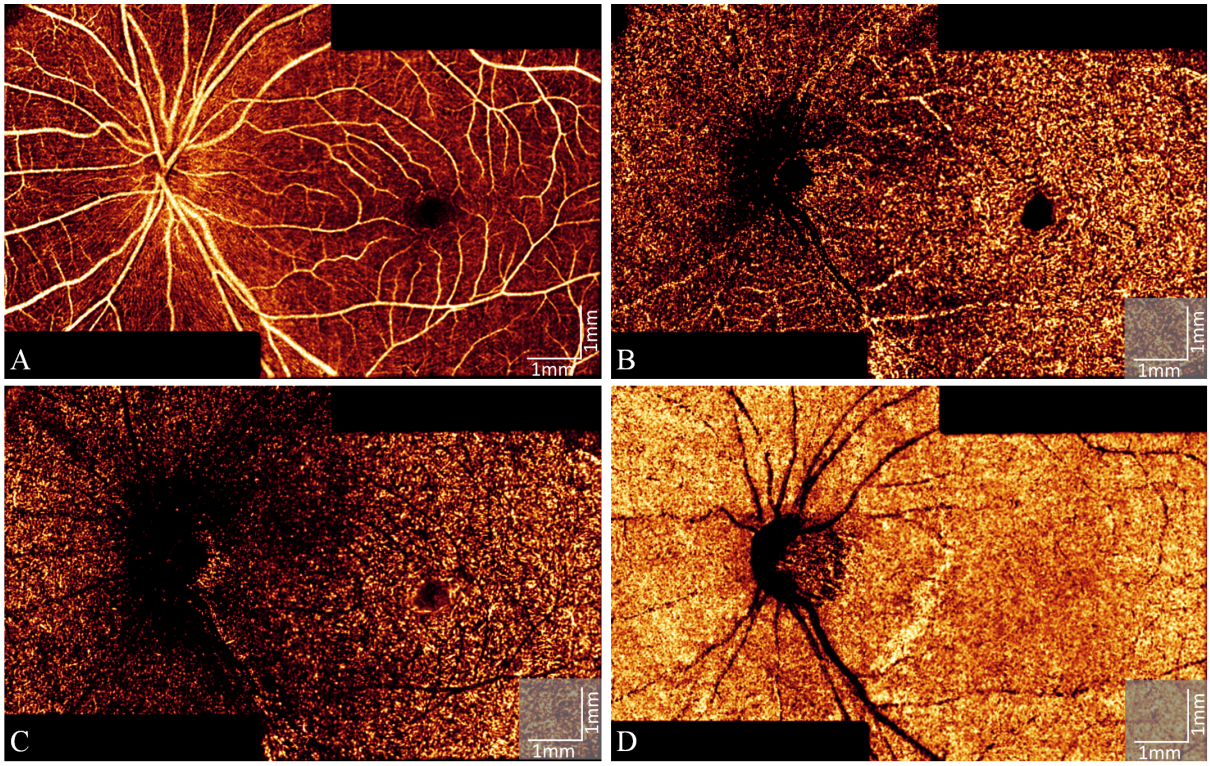


Figure 7.13: Automated montaged angiogram on four slabs of projection-resolved OCTA (PR-OCTA) (2 scans). (A) Superficial vascular complex (SVC). (B) Intermediate capillary plexus (ICP). (C) Deep capillary plexus (DCP). (D) Choriocapillaris (CC).

density was $15um/$pixel. Overviewing the angiogram, the vasculatures were continuous and well connected, which verified the robustness of the bundle of angiograms seamless stitching.

For DR cases (Fig. 7.15), 3 scans centered on the disc, macular, and temporal side of the high-definition (HD) scan pattern were montaged using the proposed algorithm. The montaged wide-field angiogram provided details of the capillary nonperfusion, demonstrating greater extent of abnormalities in the temporal field. The individual scans could not provide equivalent detailed contextualized information for evaluating the progression of vasculopathy.

This method was also applied on the images acquired from DR patients on a $200 - kHz$ prototype swept source OCTA system, with wavelength centered at $1050nm$. Four $10 \times 8 - mm$ scans, each with 800×400 A-scans, centered on the nasal, disc, macular, and temporal areas were merged. Fig. 7.16 demonstrates the four scans stitched seamlessly. The montaged wide-field angiogram presented the detailed pathology, including both capillary loss in nasal and temporal areas as well as the retinal neovascularization.

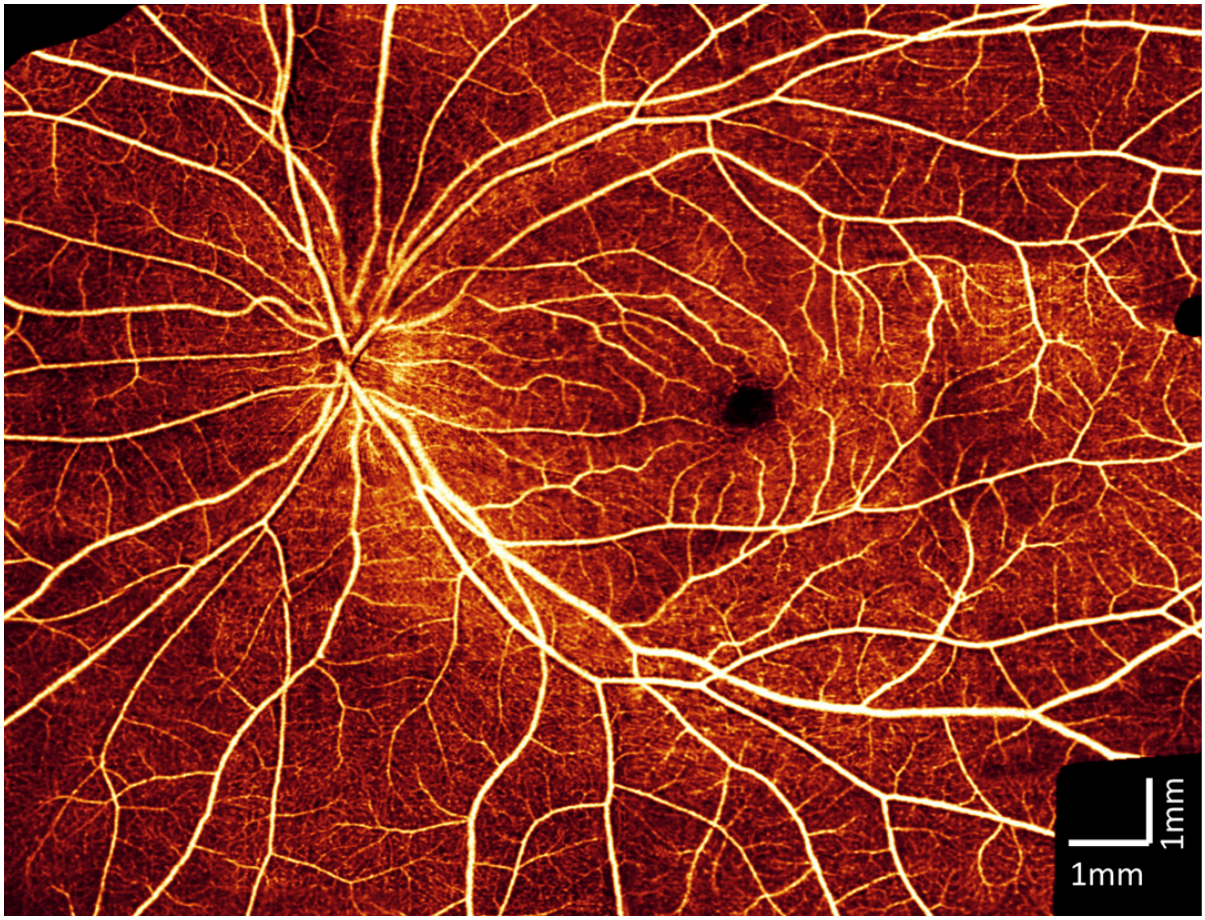


Figure 7.14: Ultra wide-field optical coherence tomographic angiography (OCTA) ($15 \times 20 - mm$) of a healthy eye registered and montaged by sixteen $6 \times 6 - mm$ OCTA scans.

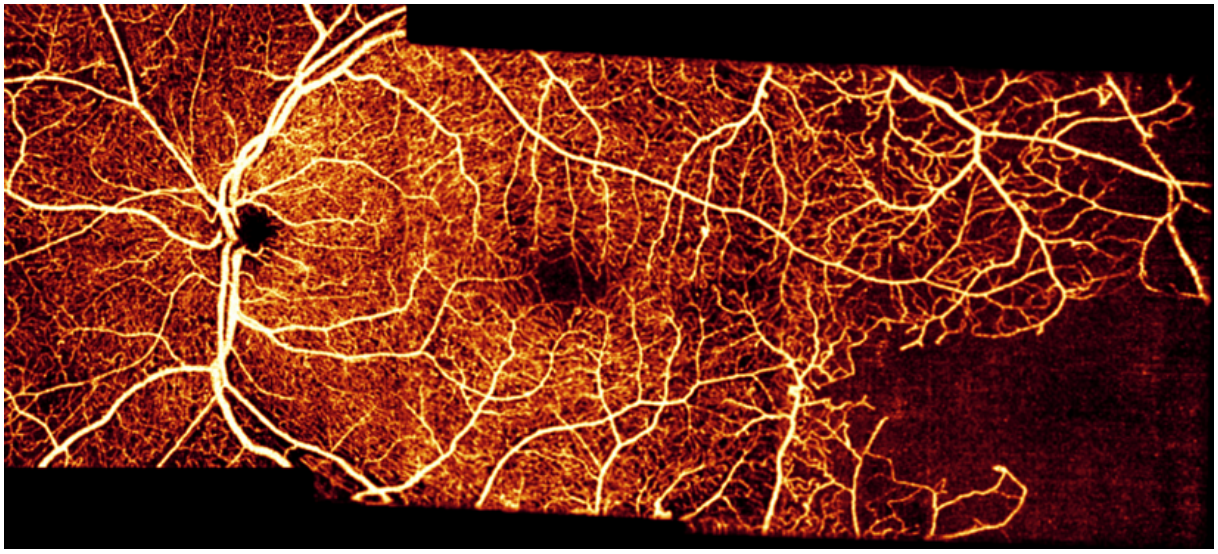


Figure 7.15: Montaged wide-field optical coherence tomographic angiography (OCTA) ($6 \times 15 - mm$, 3 scans) of a diabetic retinopathy (DR) case. Three scans centered on disc, fovea, and temporal were montaged using the algorithm described in the text.

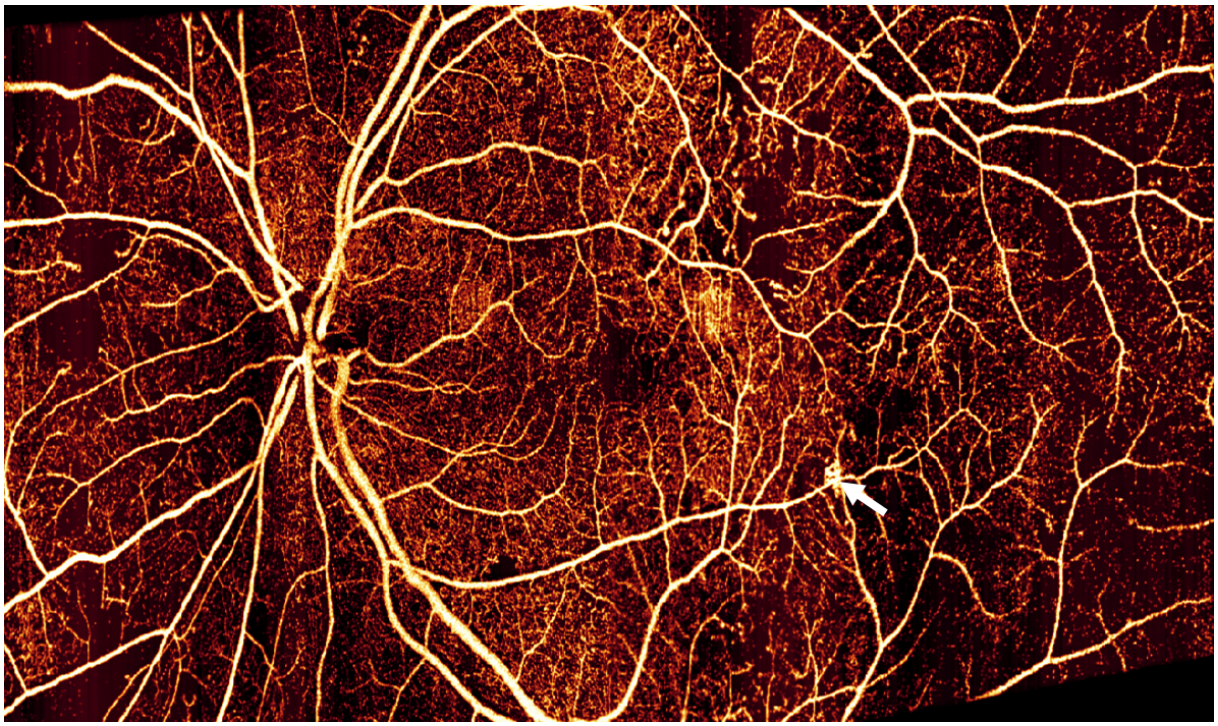


Figure 7.16: Montaged optical coherence tomographic angiography (OCTA) ($10 \times 25 - mm$, 4 scans) of the nasal, disc, macula and temporal regions from an image of a diabetic retinopathy case acquired by a prototype OCTA system. The white arrow highlights the vitreous neovascularization.

7.6 Discussion and conclusion

In this study, we developed an invariant features-based automated registration and montage algorithm for wide-field OCTA, composed of four main steps: (1) detect the invariant features including points of interest and their feature descriptors using the SURF algorithm; (2) match the detected points of interest of the target image with the moving image using their feature descriptors; (3) filter the inaccurate matches and apply the RANSAC algorithm; (4) estimate the affine matrix to stitch the moving image on the target image. The results show that the images were stitched seamlessly and ultra-wide-field OCTAs could be generated.

Clinical studies have validated the benefit of wide-field OCTA over regular FOV[188]. Wide-field OCTA allows clinicians to observe the overall vascular abnormalities, including capillary dropout or neovascularization in the peripheral retina, preserving visualization of the optic disc and macula. To achieve large fields of view by hardware improvements, dynamic compensation of the defocusing on the peripheral retina by adaptive optics would be necessary. The blending

could generate a wide FOV angiogram with a very even appearance. For individual scans, each had different brightness. By presenting them with an even appearance, we don't suggest that some areas have artefactual lower flow speed just because their capillaries show up with lower decorrelation values. While this has been demonstrated in single-scan, wide-field OCT, it has not been accomplished for OCTA thus far. Currently, commercial systems like the RT-Vue XR OCTA have incorporated software solutions to increase the FOV, such as montage of 6×6-mm angiograms of the macula and optic disc only, without the processing necessary to eliminate the apparent seams. To the best of our knowledge, no commercial software has incorporated a seamless montage algorithm for generation of clean wide-field angiograms.

Among the feature descriptor algorithms published in the past decade, e.g. BRISK, FREAK, SURF, KAZE, ORB – SURF descriptors generated using the Haar wavelet were more appropriate to describe vasculature patterns. For invariant features detection, both SIFT and SURF are very popular algorithms because they can locate the points of interest and generate the feature descriptors based on the neighborhood. In practice, SIFT could had also been used to perform the task assigned to SURF in our method. As a prior comparison has indicated [189], SIFT is more robust to the scaling and rotation changes, while SURF is more efficient and performs better on illumination changes. In our application, all scans were well focused and acquired over the same area, minimizing changes owing to scaling and rotation between adjacent scans. On the other hand, the strength of the flow signal is intensity dependent and would change considerably owing to reflectance variations between scans. As Fig. 7.8 demonstrated, the strength of the flow signals on the overlapping area between two scans can produce a very visible seam. Taking into account the factors above, SURF was selected to detect the invariant features.

In the invariant features-based image registration task, RANSAC algorithm is usually used to remove the outliers, but it fails when the number of outliers exceeds the inliers. In this application, the images are composed of very rich vascular patterns and the image features are highly similar, causing plenty of mismatches (as in Fig. 7.4). In this case, when we set an iteration limitation, it is easy to reach to a wrong solution. To address this problem, we did a further verification of

the matches utilizing their scale, rotation and the correlation between the surrounding areas. The number of inaccurate matches was greatly reduced, and only the highly correlated matches were reserved (Fig. 7.6). Then RANSAC could remove the remaining outliers to estimate the accurate affine matrix used to stitch the moving image onto the target image.

There are a few limitations of the proposed automated seamless montage algorithm. An overlapping area is required for registration to estimate affine matrix. The overlapping area of the acquired data was $5 \times 1 - mm$, but this is not the limitation of the proposed method. For the success montage, the overlapping area could be as small as $2 \times 1 - mm$ on normal eye, which was estimated by cropping the images to change the overlapping area. The other limitation is that at least 3 matches were required for the affine transformation estimation. Consequently, an inefficient number of angiograms need to be acquired from the subject in order to generate the wide-field view. For images with low quality on which pair key points could not be detected to match the features automatically, we can manually remove the mismatches or add matches to improve the accuracy of the estimated affine transformation. In this instance, this method would be a semi-automated, the further blending process could also be applied to generate the seamless wide-field montaged angiogram.

In summary, this invariant features-based automated montage algorithm can stitch multiple angiograms to generate a seamless wide-field angiogram, which provides an efficient way to view the vascular changes in a wide FOV without requiring challenging hardware updates or invasive imaging methods using contrast dye.

8 Future work and Conclusion

8.1 Future improvements of technology

Technology improvements propel humanity forward toward a better quality of life. People living 100 years ago could neither have an instant video chat with a doctor a thousand miles away nor diagnosis diseases with precise laboratory tests and high-definition medical images. I am inspired by these accomplishments to remain curious and enterprising in order to develop clinical potentials for optical coherence tomographic angiography (OCTA).

First, artificial intelligence (AI) is a powerful tool to remove projection artifacts. The relationship between signal attenuation and reflectance and optical distance is complex. In the implementation of signal attenuation-compensated projection-resolved OCTA (sacPR-OCTA), this complexity was simplified using a linear model. However a linear model may not fully describe the signal attenuation model on some challenging scans, such as low quality and pathological evaluation. My exploratory works showed that AI is a powerful tool to establish complex non-linear models to further improve projection-resolved OCTA (PR-OCTA)[190].

Second, low perfusion area is an important feature to measure retinal vascular degeneration. Unlike the macular ischemia caused by capillary dropout, low perfusion area is caused by insufficient circulation that can be visualized as flow reduction with OCTA[191]. An advanced convolutional neural network (CNN) can be designed and trained to segment both non- and low- perfusion area for generating reliable measurements of retinal vascular degeneration.

Third, a real-time OCTA data analysis platform is needed to improve clinical utility. Contemporary OCTA reading toolkit software are offline processing platforms that require copying data from commercial devices. In the future, commercial OCTA systems can be equipped with the retinal vascular disorder detection algorithms presented in this disseration for providing real-time OCTA reports to assist diagnosis of retinal vascular diseases.

Fourth, cloud computing provides efficient healthcare services. The algorithms presented in this dissertation have been implemented in a custom-designed OCTA reading toolkit software that

is reliant on the traditional on-site computing. Establishing on-site high-performance workstations involves large investments, and distributing the clinical data to multiple on-site workstations wastes storage by saving duplicate data and also incurs potential risk of patients data breaches. The drawbacks of traditional computing restricts collaboration and OCTA adoption in clinical applications. Cloud computing has compelling benefits for solving the drawbacks of traditional computing mentioned above, with advanced features including (1) platform independence so that Clinicians or researchers can process the data remotely from any devices with an internet connection, (2) cost-effective high performance that reduces hardware requirements in client devices, (3) superior data reliability and security which reduces the risk of patient data breaches and improves the feasibility of large clinical medical image datasets for collaboration, and (4) consistent software management provides standardized bio-markers comparison for easy comparison across OCTA studies.

8.2 Conclusion

This dissertation presented an entire procedure of OCTA analysis that consists of (i) retinal layer segmentation and OCTA angiogram denosing (section 2), (ii) projection artifacts removal (section 3), (iii) macular ischemia detection in specific vascular plexuses in the inner retina (section 4), (iv) CNV disgnosis and detection in the outer retina (section 5&6), and (v) invariant feature-based automated registration and montage for wide-field OCTA (section 7). A user module for automated retinal layer segmentation and intelligent manual correction provides anatomic retinal layers position for generating plexus-specific OCTA angiograms. The denosing module suppresses images noise that can further benefit retinal vasculature visualization and vascular disorder detection. The signal attenuation-compensated projection-resolved OCTA (sacPR-OCTA) algorithm was developed to remove projection artifacts at voxel scale resolution. A fully automated CNV diagnosis and segmentation algorithms based on a CNN were developed, which were able to detect CNV from multiple retinal diseases. Invariant features-based automated registration and montage for wide-field OCTA algorithm was generated. In summary, an advanced OCTA analysis platform for plexus-specific micro-vascular pathologies detection was presented in this dissertation.

9 References

[1] Miao Zhang, Jie Wang, Alex D. Pechauer, Thomas S. Hwang, Simon S. Gao, Liang Liu, Li Liu, Steven T. Bailey, David J. Wilson, David Huang, and Yali Jia. Advanced image processing for optical coherence tomographic angiography of macular diseases. *Biomedical optics express*, 6(12):4661–4675, 2015.

[2] Chandrakumar Balaratnasingam, Dong An, Yoichi Sakurada, Cecilia S Lee, Aaron Y Lee, Ian L McAllister, K Bailey Freund, Marinko Sarunic, and Dao-Yi Yu. Comparisons between histology and optical coherence tomography angiography of the periarterial capillary-free zone. *American journal of ophthalmology*, 189:55–64, 2018.

[3] Gary C Brown. Vision and quality-of-life. *Transactions of the American Ophthalmological Society*, 97:473, 1999.

[4] Melissa M Brown, Gary C Brown, Sanjay Sharma, Brandon Busbee, and Heidi Brown. Quality of life associated with unilateral and bilateral good vision. *Ophthalmology*, 108(4):643–647, 2001.

[5] Mingguang He, Jingjing Xu, Shaozhen Li, Kaili Wu, Sergio R Munoz, and Leon B Ellwein. Visual acuity and quality of life in patients with cataract in doumen county, china. *Ophthalmology*, 106(8):1609–1615, 1999.

[6] Ellen M Mowry, Michael J Loguidice, Anthony B Daniels, Dina A Jacobs, Clyde E Markowitz, Steven L Galetta, M Ligia Nano-Schiavi, Gary R Cutter, Maureen G Maguire, and Laura J Balcer. Vision related quality of life in multiple sclerosis: correlation with new measures of low and high contrast letter acuity. *Journal of Neurology, Neurosurgery & Psychiatry*, 80(7):767–772, 2009.

[7] John V. Forrester, Andrew D. Dick, Paul G. McMenamin, Fiona Roberts, and Eric Pearlman. Chapter 1 - anatomy of the eye and orbit. In John V. Forrester, Andrew D. Dick, Paul G. McMenamin, Fiona Roberts, and Eric Pearlman, editors, *The Eye (Fourth Edition)*, pages 1–102.e2. W.B. Saunders, fourth edition edition, 2016.

[8] Daniel Al Mouiee, Erik Meijering, Michael Kalloniatis, Lisa Nivison-Smith, Richard A. Williams, David A. X. Nayagam, Thomas C. Spencer, Chi D. Luu, Ceara McGowan, Stephanie B. Epp, and Mohit N. Shivdasani. Classifying Retinal Degeneration in Histological Sections Using Deep Learning. *Translational Vision Science & Technology*, 10(7):9–9, 06 2021.

[9] JP Campbell, M Zhang, TS Hwang, ST Bailey, DJ Wilson, Y Jia, and D Huang. Detailed vascular anatomy of the human retina by projection-resolved optical coherence tomography angiography. *Scientific reports*, 7(1):1–11, 2017.

[10] Yali Jia, Joseph M Simonett, Jie Wang, Xiaohui Hua, Liang Liu, Thomas S Hwang, and David Huang. Wide-field oct angiography investigation of the relationship between radial peripapillary capillary plexus density and nerve fiber layer thickness. *Investigative ophthalmology & visual science*, 58(12):5188–5194, 2017.

[11] Eun Jee Chung, Mi In Roh, Oh Woong Kwon, and Hyoung Jun Koh. Effects of macular ischemia on the outcome of intravitreal bevacizumab therapy for diabetic macular edema. *Retina*, 28(7):957–963, 2008.

[12] Dawn A Sim, Pearse A Keane, Javier Zarranz-Ventura, Simon Fung, Michael B Powner, Elise Platteau, Catey V Bunce, Marcus Fruttiger, Praveen J Patel, Adnan Tufail, et al. The effects of macular ischemia on visual acuity in diabetic retinopathy. *Investigative ophthalmology & visual science*, 54(3):2353–2360, 2013.

[13] Fabio Scarinci, Peter L. Nesper, and Amani A. Fawzi. Deep retinal capillary nonperfusion is associated with photoreceptor disruption in diabetic macular ischemia. *American journal of ophthalmology*, 168:129–138, 2016.

[14] Wasim A Samara, Abtin Shahlaee, Murtaza K Adam, M Ali Khan, Allen Chiang, Joseph I Maguire, Jason Hsu, and Allen C Ho. Quantification of diabetic macular ischemia using optical coherence tomography angiography and its relationship with visual acuity. *Ophthalmology*, 124(2):235–244, 2017.

[15] Neville N Osborne, Robert J Casson, John PM Wood, Glyn Chidlow, Mark Graham, and José Melena. Retinal ischemia: mechanisms of damage and potential therapeutic strategies. *Progress in retinal and eye research*, 23(1):91–147, 2004.

[16] Hans E Grossniklaus and W Richard Green. Choroidal neovascularization. *American journal of ophthalmology*, 137(3):496–503, 2004.

[17] Peter A Campochiaro. Retinal and choroidal neovascularization. *Journal of cellular physiology*, 184(3):301–310, 2000.

[18] Jason S Slakter, Lawrence A Yannuzzi, Ulrike Schneider, John A Sorenson, Antonio Ciardella, David R Guyer, Richard F Spaide, K Bailey Freund, and Dennis A Orlock. Retinal choroidal anastomoses and occult choroidal neovascularization in age-related macular degeneration. *Ophthalmology*, 107(4):742–753, 2000.

[19] Jiri Rehak and Matus Rehak. Branch retinal vein occlusion: pathogenesis, visual prognosis, and treatment modalities. *Current eye research*, 33(2):111–131, 2008.

[20] Sohan Singh Hayreh. Classification of central retinal vein occlusion. *Ophthalmology*, 90(5):458–474, 1983.

[21] Craig M Greven, M Madison Slusher, and Richard G Weaver. Retinal arterial occlusions in young adults. *American journal of ophthalmology*, 120(6):776–783, 1995.

[22] Hans E Grossniklaus and W Richard Green. Pathologic findings in pathologic myopia. *Retina (Philadelphia, Pa.)*, 12(2):127–133, 1992.

[23] Saad Shaikh, Alan J Ruby, and George A Williams. Photodynamic therapy using verteporfin for choroidal neovascularization in angioid streaks. *American journal of ophthalmology*, 135(1):1–6, 2003.

[24] Matthew A Thomas and Henry J Kaplan. Surgical removal of subfoveal neovascularization in the presumed ocular histoplasmosis syndrome. *American journal of ophthalmology*, 111(1):1–7, 1991.

[25] Michel Secrétan, Michel Sickenberg, Leonidas Zografos, and Bertrand Piguet. Morphometric characteristics of traumatic choroidal ruptures associated with neovascularization. *Retina (Philadelphia, Pa.)*, 18(1):62–66, 1998.

[26] David Huang, Eric A. Swanson, Charles P. Lin, Joel S. Schuman, William G. Stinson, Warren Chang, Michael R. Hee, Thomas Flotte, Kenton Gregory, Carmen A. Puliafito, and James G. Fujimoto. Optical coherence tomography. *science*, 254(5035):1178–1181, 1991.

[27] Maciej Wojtkowski, Rainer Leitgeb, Andrzej Kowalczyk, Tomasz Bajraszewski, and Adolf Friedrich Fercher. In vivo human retinal imaging by fourier domain optical coherence tomography. *Journal of Biomedical Optics*, 7(3):457–463, 2002.

[28] R. Leitgeb, C.K. Hitzenberger, and A.F. Fercher. Performance of fourier domain vs. time domain optical coherence tomography. *Optics express*, 11(8):889–894, 2003.

[29] Michael A. Choma, Marinko V. Sarunic, Changhuei Yang, and Joseph A. Izatt. Sensitivity advantage of swept source and fourier domain optical coherence tomography. *Optics express*, 11(18):2183–2189, 2003.

[30] James Fujimoto and David Huang. Foreword: 25 years of optical coherence tomography. *Investigative ophthalmology & visual science*, 57(9):OCTi–OCTii, 2016.

[31] Christopher S Brand. Management of retinal vascular diseases: a patient-centric approach. *Eye*, 26(2):S1–S16, 2012.

[32] Glenn J Jaffe and Joseph Caprioli. Optical coherence tomography to detect and manage retinal disease and glaucoma. *American journal of ophthalmology*, 137(1):156–169, 2004.

[33] Matthew A Windsor, Sissi JJ Sun, Kevin D Frick, Eric A Swanson, Philip J Rosenfeld, and David Huang. Estimating public and patient savings from basic research—a study of optical coherence tomography in managing antiangiogenic therapy. *American journal of ophthalmology*, 185:115–122, 2018.

[34] Tristan T. Hormel, David Huang, and Yali Jia. Artifacts and artifact removal in optical coherence tomographic angiography. *Quantitative Imaging in Medicine and Surgery*, 11(3):1120, 2021.

[35] Tristan T Hormel, Yali Jia, Yifan Jian, Thomas S Hwang, Steven T Bailey, Mark E Pennesi, David J Wilson, John C Morrison, and David Huang. Plexus-specific retinal vascular anatomy and pathologies as seen by projection-resolved optical coherence tomographic angiography. *Progress in Retinal and eye Research*, 80:100878, 2021.

[36] Anqi Zhang, Qinqin Zhang, Chieh-Li Chen, and Ruikang K Wang. Methods and algorithms for optical coherence tomography-based angiography: a review and comparison. *Journal of biomedical optics*, 20(10):100901, 2015.

[37] Zhongping Chen, Thomas E Milner, Shyam Srinivas, Xiaojun Wang, Arash Malekafzali, Martin JC van Gemert, and J Stuart Nelson. Noninvasive imaging of in vivo blood flow velocity using optical doppler tomography. *Optics letters*, 22(14):1119–1121, 1997.

[38] Joseph A Izatt, Manish D Kulkarni, Siavash Yazdanfar, Jennifer K Barton, and Ashley J Welch. In vivo bidirectional color doppler flow imaging of picoliter blood volumes using optical coherence tomography. *Optics letters*, 22(18):1439–1441, 1997.

[39] Jeff Fingler, Dan Schwartz, Changhuei Yang, and Scott E Fraser. Mobility and transverse flow visualization using phase variance contrast with spectral domain optical coherence tomography. *Optics express*, 15(20):12636–12653, 2007.

[40] Shuichi Makita, Youngjoo Hong, Masahiro Yamanari, Toyohiko Yatagai, and Yoshiaki Yasuno. Optical coherence angiography. *Optics express*, 14(17):7821–7840, 2006.

[41] Jennifer K Barton and Steven Stromski. Flow measurement without phase information in optical coherence tomography images. *Optics express*, 13(14):5234–5239, 2005.

[42] Adrian Mariampillai, Beau A Standish, Eduardo H Moriyama, Mamta Khurana, Nigel R Munce, Michael KK Leung, James Jiang, Alex Cable, Brian C Wilson, I Alex Vitkin, et al. Speckle variance detection of microvasculature using swept-source optical coherence tomography. *Optics letters*, 33(13):1530–1532, 2008.

[43] Yali Jia, Ou Tan, Jason Tokayer, Benjamin Potsaid, Yimin Wang, Jonathan J. Liu, Martin F. Kraus, Hrebesh Subhash, James G. Fujimoto, Joachim Hornegger, and Huang David. Split-

spectrum amplitude-decorrelation angiography with optical coherence tomography. *Optics express*, 20(4):4710–4725, 2012.

[44] Simon S Gao, Gangjun Liu, David Huang, and Yali Jia. Optimization of the split-spectrum amplitude-decorrelation angiography algorithm on a spectral optical coherence tomography system. *Optics letters*, 40(10):2305–2308, 2015.

[45] Ruikang K Wang, Steven L Jacques, Zhenhe Ma, Sawan Hurst, Stephen R Hanson, and Andras Gruber. Three dimensional optical angiography. *Optics express*, 15(7):4083–4097, 2007.

[46] Lin An and Ruikang K. Wang. In vivo volumetric imaging of vascular perfusion within human retina and choroids with optical micro-angiography. *Optics express*, 16(15):11438–11452, 2008.

[47] Lin An, Jia Qin, and Ruikang K Wang. Ultrahigh sensitive optical microangiography for in vivo imaging of microcirculations within human skin tissue beds. *Optics express*, 18(8):8220–8228, 2010.

[48] Richard F. Spaide, James G. Fujimoto, and Nadia K. Waheed. Image artifacts in optical coherence angiography. *Retina (Philadelphia, Pa.)*, 35(11):2163, 2015.

[49] Liang-Chieh Chen, George Papandreou, Iasonas Kokkinos, Kevin Murphy, and Alan L Yuille. Deeplab: Semantic image segmentation with deep convolutional nets, atrous convolution, and fully connected crfs. *IEEE transactions on pattern analysis and machine intelligence*, 40(4):834–848, 2017.

[50] Alex Krizhevsky, Ilya Sutskever, and Geoffrey E Hinton. Imagenet classification with deep convolutional neural networks. *Communications of the ACM*, 60(6):84–90, 2017.

[51] Karen Simonyan and Andrew Zisserman. Very deep convolutional networks for large-scale image recognition. *arXiv preprint arXiv:1409.1556*, 2014.

[52] Philippe Burlina, Katia D Pacheco, Neil Joshi, David E Freund, and Neil M Bressler. Comparing humans and deep learning performance for grading amd: a study in using universal

deep features and transfer learning for automated amd analysis. *Computers in biology and medicine*, 82:80–86, 2017.

[53] Jie Wang, Tristan T. Hormel, Qisheng You, Yukun Guo, Xiaogang Wang, Liu Chen, Thomas S. Hwang, and Yali Jia. Robust non-perfusion area detection in three retinal plexuses using convolutional neural network in oct angiography. *Biomedical optics express*, 11(1):330–345, 2020.

[54] Yukun Guo, Acner Camino, Jie Wang, David Huang, Thomas S Hwang, and Yali Jia. Mednet, a neural network for automated detection of avascular area in oct angiography. *Biomedical optics express*, 9(11):5147–5158, 2018.

[55] Yukun Guo, Acner Camino, Miao Zhang, Jie Wang, David Huang, Thomas Hwang, and Yali Jia. Automated segmentation of retinal layer boundaries and capillary plexuses in wide-field optical coherence tomographic angiography. *Biomedical optics express*, 9(9):4429–4442, 2018.

[56] Pengxiao Zang, Jie Wang, Tristan T Hormel, Liang Liu, David Huang, and Yali Jia. Automated segmentation of peripapillary retinal boundaries in oct combining a convolutional neural network and a multi-weights graph search. *Biomedical optics express*, 10(8):4340–4352, 2019.

[57] Leyuan Fang, David Cunefare, Chong Wang, Robyn H Guymer, Shutao Li, and Sina Farsiu. Automatic segmentation of nine retinal layer boundaries in oct images of non-exudative amd patients using deep learning and graph search. *Biomedical optics express*, 8(5):2732–2744, 2017.

[58] Thomas S Hwang, Simon S Gao, Liang Liu, Andreas K Lauer, Steven T Bailey, Christina J Flaxel, David J Wilson, David Huang, and Yali Jia. Automated quantification of capillary nonperfusion using optical coherence tomography angiography in diabetic retinopathy. *JAMA ophthalmology*, 134(4):367–373, 2016.

[59] Miao Zhang, Thomas S Hwang, Changlei Dongye, David J Wilson, David Huang, and Yali Jia. Automated quantification of nonperfusion in three retinal plexuses using projection-

resolved optical coherence tomography angiography in diabetic retinopathy. *Investigative ophthalmology & visual science*, 57(13):5101–5106, 2016.

[60] Peter L Nesper, Philipp K Roberts, Alex C Onishi, Haitao Chai, Lei Liu, Lee M Jampol, and Amani A Fawzi. Quantifying microvascular abnormalities with increasing severity of diabetic retinopathy using optical coherence tomography angiography. *Investigative ophthalmology & visual science*, 58(6):BIO307–BIO315, 2017.

[61] A Yasin Alibhai, Lucas R De Pretto, Eric M Moult, Chris Or, Malvika Arya, Mitchell McGowan, Oscar Carrasco-Zevallos, ByungKun Lee, Siyu Chen, Caroline R Baumal, et al. Quantification of retinal capillary nonperfusion in diabetics using wide-field optical coherence tomography angiography. *Retina*, 40(3):412–420, 2020.

[62] Qi Sheng You, Jie Wang, Yukun Guo, Christina J Flaxel, Thomas S Hwang, David Huang, Yali Jia, and Steven T Bailey. Detection of reduced retinal vessel density in eyes with geographic atrophy secondary to age-related macular degeneration using projection-resolved optical coherence tomography angiography. *American journal of ophthalmology*, 209:206–212, 2020.

[63] Handan Akil, Alex S Huang, Brian A Francis, Sirinivas R Sadda, and Vikas Chopra. Retinal vessel density from optical coherence tomography angiography to differentiate early glaucoma, pre-perimetric glaucoma and normal eyes. *PloS one*, 12(2):e0170476, 2017.

[64] Maurizio Battaglia Parodi, Maria Vittoria Cicinelli, Alessandro Rabiolo, Luisa Pierro, Marco Gagliardi, Gianluigi Bolognesi, and Francesco Bandello. Vessel density analysis in patients with retinitis pigmentosa by means of optical coherence tomography angiography. *British Journal of Ophthalmology*, 101(4):428–432, 2017.

[65] Jie Wang, Tristan T. Hormel, Liqin Gao, Pengxiao Zang, Yukun Guo, Xiaogang Wang, Steven T. Bailey, and Yali Jia. Automated diagnosis and segmentation of choroidal neovascularization in oct angiography using deep learning. *Biomedical Optics Express*, 11(2):927–944, 2020.

[66] Min Wang, Yao Zhou, Simon S Gao, Wei Liu, Yongheng Huang, David Huang, and Yali Jia. Evaluating polypoidal choroidal vasculopathy with optical coherence tomography angiography. *Investigative ophthalmology & visual science*, 57(9):OCT526–OCT532, 2016.

[67] Thomas S. Hwang, Ahmed M. Hagag, Jie Wang, Miao Zhang, Andrew Smith, David J. Wilson, David Huang, and Yali Jia. Automated quantification of nonperfusion areas in 3 vascular plexuses with optical coherence tomography angiography in eyes of patients with diabetes. *JAMA ophthalmology*, 136(8):929–936, 2018.

[68] Richard B Rosen, Jorge S Andrade Romo, Brian D Krawitz, Shelley Mo, Amani A Fawzi, Rachel E Linderman, Joseph Carroll, Alexander Pinhas, and Toco YP Chui. Earliest evidence of preclinical diabetic retinopathy revealed using optical coherence tomography angiography perfused capillary density. *American journal of ophthalmology*, 203:103–115, 2019.

[69] Alex C Onishi, Peter L Nesper, Philipp K Roberts, Ganna A Moharram, Haitao Chai, Lei Liu, Lee M Jampol, and Amani A Fawzi. Importance of considering the middle capillary plexus on oct angiography in diabetic retinopathy. *Investigative ophthalmology & visual science*, 59(5):2167–2176, 2018.

[70] Yali Jia, Steven T. Bailey, David J. Wilson, Ou Tan, Michael L. Klein, Christina J. Flaxel, Benjamin Potsaid, Jonathan J. Liu, Chen D. Lu, Martin F. Kraus, James G. Fujimoto, and Huang David. Quantitative optical coherence tomography angiography of choroidal neovascularization in age-related macular degeneration. *Ophthalmology*, 121(7):1435–1444, 2014.

[71] Anqi Zhang, Qinqin Zhang, and Ruikang K Wang. Minimizing projection artifacts for accurate presentation of choroidal neovascularization in oct micro-angiography. *Biomedical optics express*, 6(10):4130–4143, 2015.

[72] Miao Zhang, Thomas S Hwang, J Peter Campbell, Steven T Bailey, David J Wilson, David Huang, and Yali Jia. Projection-resolved optical coherence tomographic angiography. *Biomedical optics express*, 7(3):816–828, 2016.

[73] Jie Wang, Miao Zhang, Thomas S. Hwang, Steven T. Bailey, David Huang, David J. Wilson, and Yali Jia. Reflectance-based projection-resolved optical coherence tomography angiography. *Biomedical Optics Express*, 8(3):1536–1548, 2017.

[74] Simon S Gao, Yali Jia, Liang Liu, Miao Zhang, Hana L Takusagawa, John C Morrison, and David Huang. Compensation for reflectance variation in vessel density quantification by optical coherence tomography angiography. *Investigative ophthalmology & visual science*, 57(10):4485–4492, 2016.

[75] Acner Camino, Yali Jia, Gangjun Liu, Jie Wang, and David Huang. Regression-based algorithm for bulk motion subtraction in optical coherence tomography angiography. *Biomedical optics express*, 8(6):3053–3066, 2017.

[76] Martin F. Kraus, Benjamin Potsaid, Markus A. Mayer, Ruediger Bock, Bernhard Baumann, Jonathan J. Liu, Joachim Hornegger, and James G. Fujimoto. Motion correction in optical coherence tomography volumes on a per a-scan basis using orthogonal scan patterns. *Biomedical optics express*, 3(6):1182–1199, 2012.

[77] Pierre D. Wellner. Adaptive thresholding for the digitaldesk. *Xerox, EPC1993-110*, pages 1–19, 1993.

[78] Derek Bradley and Gerhard Roth. Adaptive thresholding using the integral image. *Journal of graphics tools*, 12(2):13–21, 2007.

[79] Ou Tan, Vikas Chopra, Ake Tzu-Hui Lu, Joel S. Schuman, Hiroshi Ishikawa, Gadi Wollstein, Rohit Varma, and David Huang. Detection of macular ganglion cell loss in glaucoma by fourier-domain optical coherence tomography. *Ophthalmology*, 116(12):2305–2314, 2009.

[80] Alejandro F. Frangi, Wiro J. Niessen, Koen L. Vincken, and Max A. Viergever. Multiscale vessel enhancement filtering. In *International conference on medical image computing and computer-assisted intervention*, pages 130–137. Springer, 1998.

[81] Nobuyuki Otsu. A threshold selection method from gray-level histograms. *IEEE transactions on systems, man, and cybernetics*, 9(1):62–66, 1979.

[82] Karl Pearson. Vii. note on regression and inheritance in the case of two parents. *proceedings of the royal society of London*, 58(347-352):240–242, 1895.

[83] Louisa Lam, Seong-Whan Lee, and Ching Y Suen. Thinning methodologies-a comprehensive survey. *IEEE Transactions on Pattern Analysis & Machine Intelligence*, 14(09):869–885, 1992.

[84] Simon S Gao, Li Liu, Steven T Bailey, Christina J Flaxel, David Huang, Dengwang Li, and Yali Jia. Quantification of choroidal neovascularization vessel length using optical coherence tomography angiography. *Journal of biomedical optics*, 21(7):076010, 2016.

[85] Larry A. Donoso, David Kim, Arcilee Frost, Alston Callahan, and Gregory Hageman. The role of inflammation in the pathogenesis of age-related macular degeneration. *Survey of ophthalmology*, 51(2):137–152, 2006.

[86] Paulo E. Stanga, Jennifer I. Lim, Peter Hamilton, FRCS, and RCOphth. Indocyanine green angiography in chorioretinal diseases: indications and interpretation: An evidence-based update. *Ophthalmology*, 110(1):15–21, 2003.

[87] Early Treatment Diabetic Retinopathy Study Research Group et al. Fundus photographic risk factors for progression of diabetic retinopathy: Etdrs report number 12. *Ophthalmology*, 98(5):823–833, 1991.

[88] Diabetic Retinopathy Clinical Research Network et al. Relationship between optical coherence tomography–measured central retinal thickness and visual acuity in diabetic macular edema. *Ophthalmology*, 114(3):525–536, 2007.

[89] Dawn A Sim, Pearse A Keane, Simon Fung, Michael Karampelas, Srinivas R Sadda, Marcus Fruttiger, Praveen J Patel, Adnan Tufail, and Catherine A Egan. Quantitative analysis of diabetic macular ischemia using optical coherence tomography. *Investigative ophthalmology & visual science*, 55(1):417–423, 2014.

[90] Kumi Sakata, Hideharu Funatsu, Seiyo Harino, Hidetaka Noma, and Sadao Hori. Relationship between macular microcirculation and progression of diabetic macular edema. *Ophthalmology*, 113(8):1385–1391, 2006.

[91] Ronald Klein, Barbara EK Klein, Scot E Moss, Matthew D Davis, and David L DeMets. The wisconsin epidemiologic study of diabetic retinopathy: Ii. prevalence and risk of diabetic retinopathy when age at diagnosis is less than 30 years. *Archives of ophthalmology*, 102(4):520–526, 1984.

[92] Akihiro Ishibazawa, Taiji Nagaoka, Atsushi Takahashi, Tsuneaki Omae, Tomofumi Tani, Kenji Sogawa, Harumasa Yokota, and Akitoshi Yoshida. Optical coherence tomography angiography in diabetic retinopathy: a prospective pilot study. *American journal of ophthalmology*, 160(1):35–44, 2015.

[93] Thomas S. Hwang, Yali Jia, Simon S. Gao, Steven T. Bailey, Andreas K. Lauer, Christina J. Flaxel, David J. Wilson, and David Huang. Optical coherence tomography angiography features of diabetic retinopathy. *Retina (Philadelphia, Pa.)*, 35(11):2371, 2015.

[94] Thomas S. Hwang, Miao Zhang, Kavita Bhavsar, Xinbo Zhang, J. Peter Campbell, Phoebe Lin, Steven T. Bailey, Christina J. Flaxel, Andreas K. Lauer, David J. Wilson, David Huang, and Yali Jia. Visualization of 3 distinct retinal plexuses by projection-resolved optical coherence tomography angiography in diabetic retinopathy. *JAMA ophthalmology*, 134(12):1411–1419, 2016.

[95] Danny Y Lin, Mark S Blumenkranz, Rosemary J Brothers, David M Grosvenor, and The Digital Diabetic Screening Group. The sensitivity and specificity of single-field nonmydriatic monochromatic digital fundus photography with remote image interpretation for diabetic retinopathy screening: a comparison with ophthalmoscopy and standardized mydriatic color photography. *American journal of ophthalmology*, 134(2):204–213, 2002.

[96] Matthew M Wessel, Nandini Nair, Grant D Aaker, Joshua R Ehrlich, Donald J D'Amico, and Szilárd Kiss. Peripheral retinal ischaemia, as evaluated by ultra-widefield fluorescein angiography, is associated with diabetic macular oedema. *British Journal of Ophthalmology*, 96(5):694–698, 2012.

[97] Ceying Shen, Shu Yan, Min Du, Hong Zhao, Ling Shao, and Yibo Hu. Assessment of capillary dropout in the superficial retinal capillary plexus by optical coherence tomography

angiography in the early stage of diabetic retinopathy. *BMC ophthalmology*, 18(1):1–6, 2018.

[98] Yali Jia, Steven T Bailey, Thomas S Hwang, Scott M McClintic, Simon S Gao, Mark E Pennesi, Christina J Flaxel, Andreas K Lauer, David J Wilson, Joachim Hornegger, et al. Quantitative optical coherence tomography angiography of vascular abnormalities in the living human eye. *Proceedings of the National Academy of Sciences*, 112(18):E2395–E2402, 2015.

[99] Rachel C. Patel, Jie Wang, Thomas S. Hwang, Miao Zhang, Simon S. Gao, Mark E. Pennesi, Steven T. Bailey, Brandon J. Lujan, Xiaogang Wang, David J. Wilson, David Huang, and Jia Yali. Plexus-specific detection of retinal vascular pathologic conditions with projection-resolved oct angiography. *Ophthalmology Retina*, 2(8):816–826, 2018.

[100] Justin J Park, Christopher S Chung, and Amani A Fawzi. Visualizing structure and vascular interactions: macular nonperfusion in three capillary plexuses. *Ophthalmic Surgery, Lasers and Imaging Retina*, 49(11):e182–e190, 2018.

[101] Yukun Guo, Tristan T Hormel, Honglian Xiong, Bingjie Wang, Acner Camino, Jie Wang, David Huang, Thomas S Hwang, and Yali Jia. Development and validation of a deep learning algorithm for distinguishing the nonperfusion area from signal reduction artifacts on oct angiography. *Biomedical optics express*, 10(7):3257–3268, 2019.

[102] Jeffrey J Yu, Acner Camino, Liang Liu, Xinbo Zhang, Jie Wang, Simon S Gao, Yali Jia, and David Huang. Signal strength reduction effects in oct angiography. *Ophthalmology. Retina*, 3(10):835–842, 2019.

[103] Steven A Agemy, Nicole K Scripsema, Chirag M Shah, Toco Chui, Patricia M Garcia, Jessica G Lee, Ronald C Gentile, Yi-Sing Hsiao, Qienyuan Zhou, Tony Ko, et al. Retinal vascular perfusion density mapping using optical coherence tomography angiography in normals and diabetic retinopathy patients. *Retina*, 35(11):2353–2363, 2015.

[104] Julia Schottenhamml, Eric M Moult, Stefan Ploner, ByungKun Lee, Eduardo A Novais, Emily Cole, Sabin Dang, Chen D Lu, Lennart Husvogt, Nadia K Waheed, et al. An automatic,

intercapillary area based algorithm for quantifying diabetes related capillary dropout using oct angiography. *Retina (Philadelphia, Pa.)*, 36(Suppl 1):S93, 2016.

[105] Li Liu, Simon S Gao, Steven T Bailey, David Huang, Dengwang Li, and Yali Jia. Automated choroidal neovascularization detection algorithm for optical coherence tomography angiography. *Biomedical optics express*, 6(9):3564–3576, 2015.

[106] Kazuya Morino, Tomoaki Murakami, Yoko Dodo, Shota Yasukura, Tatsuya Yoshitake, Masahiro Fujimoto, and Akitaka Tsujikawa. Characteristics of diabetic capillary nonperfusion in macular and extramacular white spots on optical coherence tomography angiography. *Investigative Ophthalmology & Visual Science*, 60(5):1595–1603, 2019.

[107] The Eye Disease Prevalence Research Group. Causes and prevalence of visual impairment among adults in the united states. *Archives of Ophthalmology (Chicago, Ill.: 1960)*, 122(4):477–485, 2004.

[108] The Eye Disease Prevalence Research Group. Prevalence of age-related macular degeneration in the united states. *Arch Ophthalmol*, 122(4):564–572, 2004.

[109] Rama D Jager, William F Mieler, and Joan W Miller. Age-related macular degeneration. *New England Journal of Medicine*, 358(24):2606–2617, 2008.

[110] Paulus TVM De Jong. Age-related macular degeneration. *New England Journal of Medicine*, 355(14):1474–1485, 2006.

[111] Michael R Hee, Caroline R Baumal, Carmen A Puliafito, Jay S Duker, Elias Reichel, Jason R Wilkins, Jeffery G Coker, Joel S Schuman, Eric A Swanson, and James G Fujimoto. Optical coherence tomography of age-related macular degeneration and choroidal neovascularization. *Ophthalmology*, 103(8):1260–1270, 1996.

[112] MP Lopez-Saez, E Ordoqui, P Tornero, A Baeza, T Sainza, e JM Zubeldia, ML Baeza, and Maria Luisa Baeza. Fluorescein-induced allergic reaction. *Annals of Allergy, Asthma & Immunology*, 81(5):428–430, 1998.

[113] Xiang Wei, Acner Camino, Shaohua Pi, William Cepurna, David Huang, John C Morrison, and Yali Jia. Fast and robust standard-deviation-based method for bulk motion compensation in phase-based functional oct. *Optics Letters*, 43(9):2204–2207, 2018.

[114] Rachel Patel, Jie Wang, J Peter Campbell, Lee Kiang, Andreas Lauer, Christina Flaxel, Thomas Hwang, Brandon Lujan, David Huang, Steven T Bailey, et al. Classification of choroidal neovascularization using projection-resolved optical coherence tomographic angiography. *Investigative Ophthalmology & Visual Science*, 59(10):4285–4291, 2018.

[115] Kavita V Bhavsar, Yali Jia, Jie Wang, Rachel C Patel, Andreas K Lauer, David Huang, and Steven T Bailey. Projection-resolved optical coherence tomography angiography exhibiting early flow prior to clinically observed retinal angiomatous proliferation. *American Journal of Ophthalmology Case Reports*, 8:53–57, 2017.

[116] Steven T. Bailey, Omkar Thaware, Jie Wang, Ahmed M. Hagag, Xinbo Zhang, Christina J. Flaxel, Andreas K. Lauer, Thomas S. Hwang, Phoebe Lin, David Huang, and Yali Jia. Detection of nonexudative choroidal neovascularization and progression to exudative choroidal neovascularization using oct angiography. *Ophthalmology Retina*, 3(8):629–636, 2019.

[117] Mayss Al-Sheikh, Nicholas A Iafe, Nopasak Phasukkijwatana, SriniVas R Sadda, and David Sarraf. Biomarkers of neovascular activity in age-related macular degeneration using optical coherence tomography angiography. *Retina*, 38(2):220–230, 2018.

[118] Ursula Schmidt-Erfurth, Amir Sadeghipour, Bianca S Gerendas, Sebastian M Waldstein, and Hrvoje Bogunović. Artificial intelligence in retina. *Progress in retinal and eye research*, 67:1–29, 2018.

[119] Stefan Maetschke, Bhavna Antony, Hiroshi Ishikawa, Gadi Wollstein, Joel Schuman, and Rahil Garnavi. A feature agnostic approach for glaucoma detection in oct volumes. *PloS one*, 14(7), 2019.

[120] Liang-Chieh Chen, George Papandreou, Florian Schroff, and Hartwig Adam. Rethinking atrous convolution for semantic image segmentation. *arXiv preprint arXiv:1706.05587*, 2017.

[121] Gao Huang, Zhuang Liu, Laurens Van Der Maaten, and Kilian Q Weinberger. Densely connected convolutional networks. In *Proceedings of the IEEE Conference on Computer Vision and Pattern Recognition*, pages 4700–4708, 2017.

[122] Alison D Treister, Peter L Nesper, Alaa E Fayed, Manjot K Gill, Rukhsana G Mirza, and Amani A Fawzi. Prevalence of subclinical cnv and choriocapillaris nonperfusion in fellow eyes of unilateral exudative amd on oct angiography. *Translational Vision Science & Technology*, 7(5):19–19, 2018.

[123] Marco Antonio Bonini Filho, E Talisa, Daniela Ferrara, Mehreen Adhi, Caroline R Baumal, Andre J Witkin, Elias Reichel, Jay S Duker, and Nadia K Waheed. Association of choroidal neovascularization and central serous chorioretinopathy with optical coherence tomography angiography. *JAMA Ophthalmology*, 133(8):899–906, 2015.

[124] Laura Kuehlewein, Mayank Bansal, Tamara L Lenis, Nicholas A Iafe, SriniVas R Sadda, Marco A Bonini Filho, E Talisa, Nadia K Waheed, Jay S Duker, and David Sarraf. Optical coherence tomography angiography of type 1 neovascularization in age-related macular degeneration. *American Journal of Ophthalmology*, 160(4):739–748, 2015.

[125] Maiko Inoue, Chandrakumar Balaratnasingam, and K Bailey Freund. Optical coherence tomography angiography of polypoidal choroidal vasculopathy and polypoidal choroidal neovascularization. *Retina*, 35(11):2265–2274, 2015.

[126] Peter L Nesper, Brian T Soetikno, Alison D Treister, and Amani A Fawzi. Volume-rendered projection-resolved oct angiography: 3d lesion complexity is associated with therapy response in wet age-related macular degeneration. *Investigative Ophthalmology & Visual Science*, 59(5):1944–1952, 2018.

[127] Jie Xue, Acner Camino, Steven T Bailey, Xiyu Liu, Dengwang Li, and Yali Jia. Automatic quantification of choroidal neovascularization lesion area on oct angiography based on density cell-like p systems with active membranes. *Biomedical Optics Express*, 9(7):3208–3219, 2018.

[128] Qinqin Zhang, Chieh-Li Chen, Zhongdi Chu, Fang Zheng, Andrew Miller, Luiz Roisman, Joao Rafael de Oliveira Dias, Zohar Yehoshua, Karen B Schaal, William Feuer, Giovanni Gregori, Sophie Kubach, Lin An, Paul F. Stetson, Mary K. Durbin, Philip J. Rosenfeld, and Ruikang K. Wang. Automated quantitation of choroidal neovascularization: a comparison study between spectral-domain and swept-source oct angiograms. *Investigative Ophthalmology & Visual Science*, 58(3):1506–1513, 2017.

[129] Yuhan Zhang, Zexuan Ji, Yuexuan Wang, Sijie Niu, Wen Fan, Songtao Yuan, and Qiang Chen. Mpb-cnn: a multi-scale parallel branch cnn for choroidal neovascularization segmentation in sd-oct images. *OSA Continuum*, 2(3):1011–1027, 2019.

[130] Renzo Perfetti, Elisa Ricci, Daniele Casali, and Giovanni Costantini. Cellular neural networks with virtual template expansion for retinal vessel segmentation. *IEEE Transactions on Circuits and Systems II: Express Briefs*, 54(2):141–145, 2007.

[131] Huazhu Fu, Yanwu Xu, Stephen Lin, Damon Wing Kee Wong, and Jiang Liu. Deepvessel: Retinal vessel segmentation via deep learning and conditional random field. In *International conference on medical image computing and computer-assisted intervention*, pages 132–139. Springer, 2016.

[132] Avijit Dasgupta and Sonam Singh. A fully convolutional neural network based structured prediction approach towards the retinal vessel segmentation. In *2017 IEEE 14th International Symposium on Biomedical Imaging (ISBI 2017)*, pages 248–251. IEEE, 2017.

[133] Aaron Wu, Ziyue Xu, Mingchen Gao, Mario Buty, and Daniel J Mollura. Deep vessel tracking: A generalized probabilistic approach via deep learning. In *2016 IEEE 13th International Symposium on Biomedical Imaging (ISBI)*, pages 1363–1367. IEEE, 2016.

[134] Chengzhang Zhu, Beiji Zou, Rongchang Zhao, Jinkai Cui, Xuanchu Duan, Zailiang Chen, and Yixiong Liang. Retinal vessel segmentation in colour fundus images using extreme learning machine. *Computerized Medical Imaging and Graphics*, 55:68–77, 2017.

[135] Juan Mo and Lei Zhang. Multi-level deep supervised networks for retinal vessel segmentation. *International journal of computer assisted radiology and surgery*, 12(12):2181–2193, 2017.

[136] Laurence S. Lim, Paul Mitchell, Johanna M. Seddon, Frank G. Holz, and Tien Y. Wong. Age-related macular degeneration. *The Lancet*, 379(9827):1728–1738, 2012.

[137] Arup Das and Paul G. McGuire. Retinal and choroidal angiogenesis: pathophysiology and strategies for inhibition. *Progress in retinal and eye research*, 22(6):721–748, 2003.

[138] Renate Rauch, Birgit Weingessel, Saskia M. Maca, and Pia V. Vecsei-Marlovits. Time to first treatment: the significance of early treatment of exudative age-related macular degeneration. *Retina*, 32(7):1260–1264, 2012.

[139] Christina J Flaxel, Ron A. Adelman, Steven T. Bailey, Amani Fawzi, Jennifer I. Lim, G. Atma Vemulakonda, and Gui-shuang Ying. Age-related macular degeneration preferred practice pattern®. *Ophthalmology*, 127(1):P1–P65, 2020.

[140] Ambar Faridi, Yali Jia, Simon S. Gao, David Huang, Kavita V. Bhavsar, David J. Wilson, Andrew Sill, Christina J. Flaxel, Thomas S. Hwang, Andreas K. Lauer, et al. Sensitivity and specificity of oct angiography to detect choroidal neovascularization. *Ophthalmology retina*, 1(4):294–303, 2017.

[141] Kristen M Meiburger, Massimo Salvi, Giulia Rotunno, Wolfgang Drexler, and Mengyang Liu. Automatic segmentation and classification methods using optical coherence tomography angiography (octa): a review and handbook. *Applied Sciences*, 11(20):9734, 2021.

[142] Walid M Abdelmoula, Syed M Shah, and Ahmed S Fahmy. Segmentation of choroidal neovascularization in fundus fluorescein angiograms. *IEEE Transactions on Biomedical Engineering*, 60(5):1439–1445, 2013.

[143] Syed Mahmood Shah, Sinan Tatlipinar, Edward Quinlan, Jennifer U Sung, Homayoun Tabandeh, Quan Dong Nguyen, Ahmed S Fahmy, Ingrid Zimmer-Galler, RC Andrew Symons, Jesse M Cedarbaum, et al. Dynamic and quantitative analysis of choroidal neovascularization by fluorescein angiography. *Investigative ophthalmology & visual science*, 47(12):5460–5468, 2006.

[144] Micah J Guthrie, Christian R Osswald, Nicole L Valio, William F Mieler, and Jennifer J Kang-Mieler. Objective area measurement technique for choroidal neovascularization from

fluorescein angiography. *Microvascular research*, 91:1–7, 2014.

[145] Kai Jin, Yan Yan, Menglu Chen, Jun Wang, Xiangji Pan, Xindi Liu, Mushui Liu, Lixia Lou, Yao Wang, and Juan Ye. Multimodal deep learning with feature level fusion for identification of choroidal neovascularization activity in age-related macular degeneration. *Acta Ophthalmologica*, 100(2):e512–e520, 2022.

[146] Xiaoming Xi, Xianjing Meng, Lu Yang, Xiushan Nie, Gongping Yang, Haoyu Chen, Xin Fan, Yilong Yin, and Xinjian Chen. Automated segmentation of choroidal neovascularization in optical coherence tomography images using multi-scale convolutional neural networks with structure prior. *Multimedia Systems*, 25(2):95–102, 2019.

[147] Yuchun Li, Sijie Niu, Zexuan Ji, Wen Fan, Songtao Yuan, and Qiang Chen. Automated choroidal neovascularization detection for time series sd-oct images. In *International Conference on Medical Image Computing and Computer-Assisted Intervention*, pages 381–388. Springer, 2018.

[148] Kawther Taibouni, Alexandra Miere, Abdourahmane Samake, Eric Souied, Eric Petit, and Yasmina Chenoune. Choroidal neovascularization screening on oct-angiography choriocapillaris images by convolutional neural networks. *Applied Sciences*, 11(19):9313, 2021.

[149] Tristan T Hormel, Thomas S Hwang, Steven T Bailey, David J Wilson, David Huang, and Yali Jia. Artificial intelligence in oct angiography. *Progress in Retinal and Eye Research*, 85:100965, 2021.

[150] Kaiming He, Xiangyu Zhang, Shaoqing Ren, and Jian Sun. Deep residual learning for image recognition. In *Proceedings of the IEEE conference on computer vision and pattern recognition*, pages 770–778, 2016.

[151] Olaf Ronneberger, Philipp Fischer, and Thomas Brox. U-net: Convolutional networks for biomedical image segmentation. In *International Conference on Medical image computing and computer-assisted intervention*, pages 234–241. Springer, 2015.

[152] Elizabeth R DeLong, David M DeLong, and Daniel L Clarke-Pearson. Comparing the areas under two or more correlated receiver operating characteristic curves: a nonparametric

approach. *Biometrics*, pages 837–845, 1988.

[153] Jonathan L. Prenner, Brett J. Rosenblatt, Michael J. Tolentino, Gui-Shuang Ying, Noreen B. Javornik, Maureen G. Maguire, Allen C. Ho, and CNVPT Research Group. Risk factors for choroidal neovascularization and vision loss in the fellow eye study of cnvpt. *Retina*, 23(3):307–314, 2003.

[154] David M. Brown, Peter K. Kaiser, Mark Michels, Gisele Soubrane, Jeffrey S. Heier, Robert Y. Kim, Judy P. Sy, and Susan Schneider. Ranibizumab versus verteporfin for neovascular age-related macular degeneration. *New England Journal of Medicine*, 355(14):1432–1444, 2006.

[155] Philip J. Rosenfeld, David M. Brown, Jeffrey S. Heier, David S. Boyer, Peter K. Kaiser, Carol Y. Chung, and Robert Y. Kim. Ranibizumab for neovascular age-related macular degeneration. *New England Journal of Medicine*, 355(14):1419–1431, 2006.

[156] CATT Research Group. Ranibizumab and bevacizumab for neovascular age-related macular degeneration. *New England Journal of Medicine*, 364(20):1897–1908, 2011.

[157] Chui Ming Gemmy Cheung, Timothy Y.Y. Lai, Paisan Ruamviboonsuk, Shih-Jen Chen, Youxin Chen, K. Bailey Freund, Fomi Gomi, Adrian H. Koh, Won-Ki Lee, and Tien Yin Wong. Polypoidal choroidal vasculopathy: definition, pathogenesis, diagnosis, and management. *Ophthalmology*, 125(5):708–724, 2018.

[158] Masanobu Uyama, Mitsumasa Wada, Yoshimi Nagai, Takashi Matsubara, Hiroshi Matsunaga, Ichiro Fukushima, Kanji Takahashi, and Miyo Matsumura. Polypoidal choroidal vasculopathy: natural history. *American journal of ophthalmology*, 133(5):639–648, 2002.

[159] Chee Wai Wong, Yasuo Yanagi, Won-Ki Lee, Yuichiro Ogura, Ian Yeo, Tien Yin Wong, and Chui Ming Gemmy Cheung. Age-related macular degeneration and polypoidal choroidal vasculopathy in asians. *Progress in retinal and eye research*, 53:107–139, 2016.

[160] Salomon Y. Cohen. Anti-vegf drugs as the 2009 first-line therapy for choroidal neovascularization in pathologic myopia. *Retina*, 29(8):1062–1066, 2009.

[161] WM Chan, M Ohji, TYY Lai, DTL Liu, Y Tano, and DSC Lam. Choroidal neovascularisation in pathological myopia: an update in management. *British Journal of Ophthalmology*, 89(11):1522–1528, 2005.

[162] Qinqin Zhang, Cecilia S. Lee, Jennifer Chao, Chieh-Li Chen, Thomas Zhang, Utkarsh Sharma, Anqi Zhang, Jin Liu, Kasra Rezaei, Kathryn L. Pepple, Richard Munsen, James Kinyoun, Murray Johnstone, Russell N. Van Gelder, and Ruikang Wang. Wide-field optical coherence tomography based microangiography for retinal imaging. *Scientific reports*, 6(1):1–10, 2016.

[163] Qinqin Zhang, Yanping Huang, Thomas Zhang, Sophie Kubach, Lin An, Michal Laron, Utkarsh Sharma, and Ruikang K. Wang. Wide-field imaging of retinal vasculature using optical coherence tomography-based microangiography provided by motion tracking. *Journal of biomedical optics*, 20(6):066008, 2015.

[164] Takao Hirano, Shinji Kakihara, Yuichi Toriyama, Muneeswar Gupta Nittala, Toshinori Murata, and Srinivas Sadda. Wide-field en face swept-source optical coherence tomography angiography using extended field imaging in diabetic retinopathy. *British Journal of Ophthalmology*, 102(9):1199–1203, 2018.

[165] Masayo Kimura, Miho Nozaki, Munenori Yoshida, and Yuichiro Ogura. Wide-field optical coherence tomography angiography using extended field imaging technique to evaluate the nonperfusion area in retinal vein occlusion. *Clinical Ophthalmology (Auckland, NZ)*, 10:1291, 2016.

[166] James Polans, Brenton Keller, Oscar M Carrasco-Zevallos, Francesco LaRocca, Elijah Cole, Heather E Whitson, Eleonora M Lad, Sina Farsiu, and Joseph A. Izatt. Wide-field retinal optical coherence tomography with wavefront sensorless adaptive optics for enhanced imaging of targeted regions. *Biomedical optics express*, 8(1):16–37, 2017.

[167] James Polans, Bart Jaeken, Ryan P McNabb, Pablo Artal, and Joseph A Izatt. Wide-field optical model of the human eye with asymmetrically tilted and decentered lens that reproduces measured ocular aberrations. *Optica*, 2(2):124–134, 2015.

[168] Ali Can, Charles V. Stewart, Badrinath Roysam, and Howard L. Tanenbaum. A feature-based, robust, hierarchical algorithm for registering pairs of images of the curved human retina. *IEEE transactions on pattern analysis and machine intelligence*, 24(3):347–364, 2002.

[169] Ali Can, Charles V. Stewart, Badrinath Roysam, and Howard L. Tanenbaum. A feature-based technique for joint, linear estimation of high-order image-to-mosaic transformations: mosaicing the curved human retina. *IEEE Transactions on pattern analysis and machine intelligence*, 24(3):412–419, 2002.

[170] Ali Can, Charles V Stewart, and Badrinath Roysam. Robust hierarchical algorithm for constructing a mosaic from images of the curved human retina. In *Proceedings. 1999 IEEE Computer Society Conference on Computer Vision and Pattern Recognition (Cat. No PR00149)*, volume 2. IEEE, 1999.

[171] Sangyeol Lee, Michael D Abramoff, and Joseph M Reinhardt. Validation of retinal image registration algorithms by a projective imaging distortion model. In *2007 29th Annual International Conference of the IEEE Engineering in Medicine and Biology Society*, pages 6471–6474. IEEE, 2007.

[172] Sangyeol Lee, Michael D Abràmoff, and Joseph M Reinhardt. Feature-based pairwise retinal image registration by radial distortion correction. In *Medical Imaging 2007: Image Processing*, volume 6512, pages 701–710. SPIE, 2007.

[173] Charles V. Stewart, Chia-Ling Tsai, and Badrinath Roysam. The dual-bootstrap iterative closest point algorithm with application to retinal image registration. *IEEE transactions on medical imaging*, 22(11):1379–1394, 2003.

[174] Jian Chen, Jie Tian, Noah Lee, Jian Zheng, R. Theodore Smith, and Andrew F. Laine. A partial intensity invariant feature descriptor for multimodal retinal image registration. *IEEE Transactions on Biomedical Engineering*, 57(7):1707–1718, 2010.

[175] Pengxiao Zang, Gangjun Liu, Miao Zhang, Changlei Dongye, Jie Wang, Alex D Pechauer, Thomas S Hwang, David J Wilson, David Huang, Dengwang Li, and Yali Jia. Automated

motion correction using parallel-strip registration for wide-field en face oct angiogram. *Biomedical optics express*, 7(7):2823–2836, 2016.

[176] Pengxiao Zang, Gangjun Liu, Miao Zhang, Jie Wang, Thomas S. Hwang, David J. Wilson, David Huang, Dengwang Li, and Yali Jia. Automated three-dimensional registration and volume rebuilding for wide-field angiographic and structural optical coherence tomography. *Journal of biomedical optics*, 22(2):026001, 2017.

[177] P.V. Lukashevich, B.A. Zalesky, and S.V. Ablameyko. Medical image registration based on surf detector. *Pattern Recognition and Image Analysis*, 21(3):519–521, 2011.

[178] Mustafa Teke and Alptekin Temizel. Multi-spectral satellite image registration using scale-restricted surf. In *2010 20th International Conference on Pattern Recognition*, pages 2310–2313. IEEE, 2010.

[179] Ashley Eden, Matthew Uyttendaele, and Richard Szeliski. Seamless image stitching of scenes with large motions and exposure differences. In *2006 IEEE Computer Society Conference on Computer Vision and Pattern Recognition (CVPR'06)*, volume 2, pages 2498–2505. IEEE, 2006.

[180] Anat Levin, Assaf Zomet, Shmuel Peleg, and Yair Weiss. Seamless image stitching in the gradient domain. In *European conference on computer vision*, pages 377–389. Springer, 2004.

[181] Luo Juan and Gwun Oubong. Surf applied in panorama image stitching. In *2010 2nd international conference on image processing theory, tools and applications*, pages 495–499. IEEE, 2010.

[182] Matthew Brown and David G Lowe. Automatic panoramic image stitching using invariant features. *International journal of computer vision*, 74(1):59–73, 2007.

[183] Rahul Arvo Jonas, Ya Xing Wang, Hua Yang, Jian Jun Li, Liang Xu, Songhomitra Panda-Jonas, and Jost Bruno Jonas. Optic disc-fovea distance, axial length and parapapillary zones. the beijing eye study 2011. *PloS one*, 10(9):e0138701, 2015.

[184] Rahul A Jonas, Ya Xing Wang, Hua Yang, Jian Jun Li, Liang Xu, Songhomitra Panda-Jonas, and Jost B Jonas. Optic disc-fovea angle: the beijing eye study 2011. *PLoS One*, 10(11):e0141771, 2015.

[185] Herbert Bay, Andreas Ess, Tinne Tuytelaars, and Luc Van Gool. Speeded-up robust features (surf). *Computer vision and image understanding*, 110(3):346–359, 2008.

[186] Martin A. Fischler and Robert C. Bolles. Random sample consensus: a paradigm for model fitting with applications to image analysis and automated cartography. *Communications of the ACM*, 24(6):381–395, 1981.

[187] David G. Lowe. Distinctive image features from scale-invariant keypoints. *International journal of computer vision*, 60(2):91–110, 2004.

[188] Qinqin Zhang, Chieh-Li Chen, Zhongdi Chu, and Ruikang K. Wang. Wide field oct angiography by using swept source oct in living human eye. In *Ophthalmic Technologies XXVII*, volume 10045, pages 82–87. SPIE, 2017.

[189] Luo Juan and Oubong Gwun. A comparison of sift, pca-sift and surf. *International Journal of Image Processing (IJIP)*, 3(4):143–152, 2009.

[190] Jie Wang, Tristan Hormel, and Yali Jia. Artificial intelligence-assisted projection-resolved optical coherence tomographic angiography (aipr-octa). *Investigative Ophthalmology & Visual Science*, 63(7):2910–F0063, 2022.

[191] Aiyin Chen, Liang Liu, Jie Wang, Pengxiao Zang, Beth Edmunds, Lorinna Lombardi, Ellen Davis, John C Morrison, Yali Jia, and David Huang. Measuring glaucomatous focal perfusion loss in the peripapillary retina using oct angiography. *Ophthalmology*, 127(4):484–491, 2020.